GHENT UNIVERSITY
FACULTY OF BIOSCIENCE ENGINEERING

Department of Mathematical Modelling, Statistics and Bioinformatics

Fungal growth modelling and assessment: Towards a three-dimensional spatially explicit fungal growth model

Guillermo Vidal Diez de Ulzurrun

Thesis submitted in fulfillment of the requirements for the degree of Doctor (Ph.D.) of Applied Biological Sciences

Academic year 2016-2017

Supervisors:

Prof. dr. Bernard De Baets
Department of Mathematical Modelling,
Statistics and Bioinformatics
Ghent University, Belgium

dr. ir. Jan Baetens
Department of Mathematical Modelling,
Statistics and Bioinformatics
Ghent University, Belgium

Prof. dr. ir. Jan Van den Bulcke
Department of Forest and Water Management
Ghent University, Belgium

Examination committee:

Prof. dr. Anita Van Landschoot (Chairman)

Prof. dr. ir. Joris Van Acker
Prof. dr. Fordyce Davidson
dr. Ruth Falconer
Prof. dr. ir. Monica Höfte
Prof. dr. Mieke Verbeken

Dean:

Prof. dr. ir. Marc Van Meirvenne

Rector:

Prof. dr. Anne De Paepe

Guillermo Vidal Diez de Ulzurrun

Fungal growth modelling and assessment: Towards a three-dimensional spatially explicit fungal growth model

Thesis submitted in fulfillment of the requirements for the degree of

Doctor (Ph.D) of Applied Biological Sciences

Academic year 2016-2017

Dutch translation of the title:

Modellering en evaluatie van schimmelgroei: Op naar een driedimensionaal ruimtelijk expliciet model

Please refer to this work as follows:

G. Vidal-Diez de Ulzurrun (**2016**). Fungal growth modelling and assessment: Towards a three-dimensional spatially explicit fungal growth model, PhD Thesis, Department of Mathematical Modelling, Statistics and Bioinformatics, Ghent University, Ghent, Belgium.

ISBN 978-90-5989-966-7

Guillermo Vidal Diez de Ulzurrun was supported by the Research Foundation Flanders (FWO project 3G.0838.12.N).

Acknowledgements

I would like to start by thanking my three promotors for their invaluable guidance and support during these last four years. You have helped me to grow as a person and as a researcher. Furthermore, I believe this dissertation has been the result of a team effort and I am very proud to have formed a team with people so wonderful at a professional and personal level. Also I would like to thank Liselotte, my successor, for bringing new energy to my research at the moment I needed it the most. I would also like to thank the jury members for making some room in their busy schedules to help me improve my work and learn more about it from a different perspective.

In a more personal level, I would like to express my appreciation to the big family of Ghent University. More particularly, I would like to thank my department, where I have always felt welcome and supported. Of course special thanks to the international crew, you all have taught me how friendship can overcome obstacles like culture and language, and for always being ready for new plans and adventures. Also in this paragraph I would like to thank my office mates, for withstanding my stress, my doubts and more than anything my singing. Jan B, Jan R and Aisling: it has been great sharing an office with you all these years.

Being far from home has been difficult sometimes but luckily I have been able to find, what I felt, like a new family in Ghent. Yingjie, Guangchao and Liv thanks for sharing so important moments with me during these years, being in your life has been an honour. Marc and Carlotta, thank you for so many wonderful memories and for being there always, I will miss you terribly. And finally, Aisling, I cannot believe how people so different can have such a strong connection. I owe you half, if not more of this PhD. Not only for your help and support with my writing and

research, but also for being such an incredible friend and companion during these last four years.

También quiero agradecer a mi familia y amigos. A mis amigos por tenerme siempre presente, a pesar de la distancia nunca me he sentido solo porque sé que haga lo que haga tengo vuestro apoyo incondicional. Sois los mejores y nunca dejáis de demostrármelo. A mis hermanos, les quiero dar las gracias por encargarse de la familia en mi ausencia. Y a mi madre, por ser tan fuerte y ayudarme a no sentirme lejos en los momentos importantes. Maxime, no sé cómo agradecerte toda la ayuda y apoyo que me has dado todo este tiempo. Has aguantado mis momentos malos y compartido mis momentos buenos como si fuesen tuyos. Siempre me has dado la fuerza y el empuje que me falta y nunca habría llegado tan lejos sin ti, te lo debo todo a ti. Juntos somos invencibles y esta ha sido solo la primera de nuestras muchas aventuras.

Por último, le dedico todo este trabajo a mi padre. Me diste mi educación y me enseñaste que la honestidad y el trabajo duro son las herramientas más importantes para conseguir nuestros objetivos. Sé que estarías muy orgulloso de mi por este logro, pero no tanto como lo estoy yo de ser tu hijo.

Guillermo Vidal Diez de Ulzurrun
Ghent, 01 February 2017

Contents

List of Figures

List of Tables

List of symbols

I	Original image
I_{xx}	Horizontal derivative of image I
I_{yy}	Vertical derivative of image I
σ	Standard deviation
G''	1D second order Gaussian kernel
$\hat{G}$	2D Anisotropic Gaussian Kernel
θ	Orientation of the kernel
ρ	Aanisotropy index
F_α	F-measure
ϕ	Smoothing filter
Δ^2	Baddeley's Delta Metric
g	Maximum growth rate [−]
λ	Lag phase duration [−]
R^2	Coefficient of determination
F^t	Array representing the *in silico* fungus at time step t
$S_{i,j}$	Hyphal segment of hypha i emerged at time step j
$X_{i,j}$	End point of segment $S_{i,j}$
$I_{i,j}^t$	Amount of internal substrate [mol] in segment $S_{i,j}$ at time step t
$\Theta_{i,j}$	Growth direction of $S_{i,j}$
$\theta_{i,j}$	Polar angle of the growth direction $\Theta_{i,j}$ [rad]
$\varphi_{i,j}$	Azimuthal angle of the growth direction $\Theta_{i,j}$ [rad]

A^t	Auxiliary anastomosis matrix at time step t
s_1	State of hyphal segment denoting an active segment
s_2	State of hyphal segment denoting an inactive segment
s_3	State of hyphal segment denoting a new segment of a branch
s_4	State of hyphal segment denoting a segment involved in anastomosis
C_k	Boundary condition cuboid
X_k	Position of the center of cuboid C_k
L_k	Dimensions of cuboid C_k
l_k	Side length of cuboid C_k [mm]
w_k	Width of cuboid C_k [mm]
h_k	Height of cuboid C_k [mm]
E_k^t	Amount of external substrate in cuboid C_k at time step t [mol]
T	Number of steps [−]
h_0	Hyphal segment length [mm]
Δt	Time step [d]
ω	Variation of growth direction [rad]
P	Branching probability [−]
c_g	Cost of growth [$\mathrm{mol\,mm^{-1}}$]
D	Diffusion coefficient [$\mathrm{mm\,d^{-1}}$]
M_{cap}	Maximum concentration [$\mathrm{mol\,mm^{-1}}$]
μ_k	Uptake coefficient of cuboid C_k [$\mathrm{mol^{-1}\,d^{-1}}$]
γ_k	Tropism strength of cuboid C_k [−]
τ_k	Resistance [−] of cuboid C_k
δ_k	Durability of cuboid C_k [d]
T	Number of steps [−]
H_0	Initial tips [−]
Ω_0	Initial substrate in the *in silico* fungus [mol]

List of abbreviations

1D	One dimension
2D	Two dimensions
3D	Three dimensions
AGK	Anisotropic Gaussian kernel
AIC	Akaike information criterion
BDM	Baddeley’s Delta Metric
CLSM	Laser scanning confocal microscope
CT	X-ray computed tomography
DVSC	Diffusive vesicle supply center
FCC	Face-centred cubic lattice
FOIGK	First order isotropic Gaussian kernel
GUFI-1	Ghent university fungal images data-set 1
IdE	Integro-difference equation
IGK	Isotropic Gaussian kernel
LoG	Laplacian of a Gaussian
MSE	Minimum squared error
ODE	Ordinary differential equation
OdE	Ordinary difference equation
OFM	Optical fluorescent microscopy
PDE	Partial differential equation
PdE	Partial difference equation

RH	Relative humidity
SA	Sensitivity analysis
SEM	Spatially explicit model
SOIGK	Second order isotropic Gaussian kernel
VSC	Vesicle supply center

1

Introduction

1.1 General overview

Fungi are remarkable organisms that have been populating planet Earth long before humans. The oldest fungal fossil dates from the Paleozoic, suggesting that fungi may have been the first organisms to creep out of the Ocean and live on the Earth's land. Therefore, fungi may be the organisms responsible for accommodating the land for the arrival of animals and plants. Humans have been aware of the existence of fungi for thousands of years. Several civilizations used fungal fruiting bodies as food resource or for their medicinal characteristics. However, fruiting bodies represent only the tip of the iceberg of fungi since most fungal activity happens underground where complex hyphal networks, referred to as mycelia (sing. mycelium), can cover kilometres. For instance, fungi are considered the soul of forests where their mycelium coordinate the distribution of nutrients to the different plant organisms present. Fungi are able to survive in all environments, as they are able able to adapt to the environmental characteristics. The first systematic studies on fungi date back from the 18th century. The appreciation of fungi as a proper subject of study together with the advances in study techniques resulted

in more detailed studies and the discovery of several fungal species. This better understanding revealed some characteristics that made scientists question the genetic relation between fungi and plants. For instance, the composition of the fungal cell wall and the nutrition of fungi appeared more closely related to similar properties in animals than in plants. For these reasons and the high diversity of fungal species discovered, fungi were finally classified as a proper Kingdom in 1969. From this moment, the research on fungi gained even more momentum and more complex processes were studied, including their genetics and their evolutionary relationships.

In parallel to the theoretical discoveries on fungal composition, behaviour and diversity, different industries studied fungi for their commercial potential. Historically, fungi were used in fermentation processes to produce food products such as bread, cheese or beer. However, in 1928 Alexander Fleming discovered that fungi could be used for much more than just the production of food products. His discovery, penicillin, a powerful antibiotic derived from a common fungus, *Penicillium notatum*, triggered the industrial research on fungi. Ever since, industry has profited from fungi. They have been used in the production of diverse products ranging from paper and textile to biofuels and bioremediation agents. In contrast, efforts have also been made in the opposite direction by investigating treatments and products able to stop or at least slow down the action of fungi. The reason for this is that many products can be consumed and degraded by fungi, including most organic materials such as food and building materials. For instance, several fungal species are plant pathogens, as such causing diseases affecting crops, resulting in substantial economic losses in the agricultural sector. In addition, some fungi are also harmful for humans and other living organisms since they induce allergic reactions, diseases and even the death of their hosts.

In summary, fungi have been widely studied to gain a better understanding of their unique characteristics and habits, to improve production processes and generate new products, or to limit their growth in order to protect organic materials and living organisms. These extensive studies have resulted in remarkable contributions to modern society, and as new discoveries were presented, other challenges and possibilities arose, as such demonstrating the importance of research on fungi. However, most established experimental techniques are not able to efficiently produce quality data, as such hindering the study of fungi in general and fungal growth dynamics more specifically.

For instance, most experimental techniques require direct manipulation of the samples, as such being susceptible to human errors and time consuming. Other techniques involve the destruction of the samples which makes it impossible to track growth on the same individual. Even though some techniques are able to overcome some of these problems, they often focus on small regions of the studied fungus, and are therefore unable to characterize the behaviour of the whole mycelium. In addition, experiments have to be performed repeatedly to account

for the natural variability of fungi. For these reasons, new techniques able to produce high-quality data in an automated and non-destructive way are needed to further study the dynamics of mycelia.

Fortunately, the rise of new data acquisition techniques, such as the automated processing of biological imagery, opens new avenues of study which can help to overcome some of these limitations. Image analysis has gained momentum due to the availability of cheap imaging and processing equipment, and the development of dedicated image analysis algorithms. The scale at which fungi grow allows for the extraction of numerous images using basic machinery, making them the perfect subjects to study with such techniques. Furthermore, images can be captured in an automated and non-destructive way, as such overcoming the limitations of existing techniques.

Even though image analysis techniques represent an improvement in comparison with most established techniques, they are still subject to the space and time restrictions of laboratory experiments. In addition, the processes occurring within the mycelium cannot be captured by most imaging devices despite their importance for the development of fungi.

In order to overcome the limitations imposed by laboratories, researchers need to address the study of fungi from a broader perspective, and relying on more abstract concepts and techniques. One powerful option to tackle such limitations resides in the use of mathematical models which are gaining momentum due to the increase in computing power. For instance, different scientific disciplines have benefited from the use of mathematical models, as they were used to complement laboratory experiments and to extend and understand experimental data.

Several mathematical models have already been proposed to mimic fungal growth by relying on different hypotheses, methods, scales and modelling paradigms. Nevertheless most of these models are not able to represent the evolution of fungi realistically or in sufficient detail since they rely on unrealistic space discretizations or restrict growth to two dimensions. Additionally, some modellers neglect the underlying biological processes driving growth or do not include the effect of external factors on the fungal development. Therefore, most models are not able to fully grasp the development of fungi and to simulate realistic fungal growth scenarios.

All models including those accounting for the aforementioned factors require data in order to improve the accuracy of their results. Such data need to be in line with the growth scenarios covered by the model, for instance representing similar scales and initial conditions of those in the model. So mathematical models and experimental techniques can benefit from one another and combining them can help to overcome some of the limitations that hinder the study of fungal growth dynamics.

1.2 Objectives

Motivated by the shortcomings of current experimental techniques and the current advances in technology, this dissertation studies the possibilities that more updated methods can offer to the study of fungi. More specifically, the main objectives of this dissertation are:

1. Develop an experimental technique able to track fungal growth of different fungal species and in different fungal growth scenarios. This technique needs to address the issues of current approaches, therefore being able to track entire mycelia in an automated and non-destructive way. In addition, this technique should be efficiently repeatable, therefore accounting for the natural variability of fungi.
2. Formulate a mathematical model able to realistically simulate fungal growth. Consequently, such a model should be able to represent fungal growth in three dimensions accounting for both the biological processes driving growth and the effect of different external stimuli. Ultimately, this model should be able to replicate similar growth scenarios as those most commonly studied in laboratories in order to allow for comparison between experiments and simulations.

1.3 Outline of this dissertation

This dissertation is organized in four parts. Part I gives the background and provides detailed information on some of the methods and processes used throughout the remainder of this dissertation. Parts II and III describe the main contributions. Finally, Part IV summarizes the most important conclusions and elaborates on possible extensions of the work presented here.

Part I of this dissertation is divided into two chapters. The first chapter (Chapter 2) gives the biological background on fungi and summarizes their most relevant uses in industry, their importance in natural ecosystems and their impact on human and other living organisms. In addition, the morphology and diversity of fungi is briefly discussed, followed by a detailed overview of the processes driving the growth of filamentous fungi. Chapter 3 consists of a detailed discussion and comparison of different mathematical models encoding fungal growth. Some of the most common mathematical paradigms and different modelling approaches are explained in this chapter. In addition, the most relevant fungal growth models are presented according to the scale they operate at.

Part II is divided into three chapters, Chapter 4 focuses on how to transform images of mycelia into simplified versions. For this purpose, an image analysis algorithm

based on Gaussian kernels is introduced and tested. It is able to remove redundant information from the original images, as such allowing for a better analysis of the fungal images. In Chapter 5, an innovative experimental set-up to track fungal growth using basic imaging devices and the mathematical techniques used to extract fungal growth features from the binary images obtained using the algorithm introduced in Chapter 4, are described. Several fungal growth features are then extracted for different fungal species allowing for a mutual comparison of their growth behaviour and a detailed study of their evolution. Chapter 6 uses similar techniques to assess the effect of temperature and relative humidity on fungal growth.

Part III presents an innovative spatially explicit model able to simulate fungal growth in three dimensions occurring under a variety of growth scenarios. Chapter 7 explains the development of the model and includes a sensitivity analysis of the main model parameters. In addition, different scenarios are simulated indicating the importance of the environment on the growth of fungi.

In Chapter 8 the most important conclusions of this dissertation are summarized, while Chapter 9 presents avenues for future research.

PART I

BIOLOGICAL AND MATHEMATICAL BACKGROUND

2 Biological Background

2.1 Introduction

Millions of different fungal species are estimated to inhabit the Earth (Blackwell, 2011), some of which include the largest and oldest living organisms. Fungi have been collected and harvested as food and exploited for product development, such as alcoholic beverages and antibiotics. They are crucial in nutrient cycles in forests for litter decomposition and live in symbiosis with trees and plants, as such facilitating the redistribution of nutrients through the ecosystem. They are, however, detrimental in human ecosystems as the main decaying organisms of building materials and the main cause of food spoilage.

For all of these reasons, fungi have been widely studied, still some of their main features are not yet well understood. For instance, the total number of fungal species is still an open debate. While some studies estimate the number of species at 1.5 million based on ratios of known fungi to plant species (Hawksworth, 2001), other studies based on analyses of environmental DNA of soil samples predict that more than 5 million fungal species exist (O'Brien et al., 2005). However, only

around 99.000 fungal species have been formally described (Blackwell, 2011). In this chapter, the motivation and framework of fungal research will be discussed. The main fungal structures and processes are introduced together with a brief review on fungal morphology. This will be followed in Section 2.4 by an in-depth study of fungal growth focusing on mycelial growth including the different environmental conditions and nutrient requirements needed for growth.

2.2 Motivation and framework

Fungi populate most known ecosystems, even those with extreme environmental conditions or a lack of nutrients (Magan, 2007). For instance, fungal activity has been found in deserts (Stutz et al., 2000), the Arctic (Robinson, 2001), in the deep ocean (Le Calvez et al., 2009), and even in man-made structures such as nuclear reactors (Zhdanova et al., 2000). The reason for this resides in the unique body of most fungi, the mycelium, which allows them to redistribute nutrients across large distances and consequently to survive in inhospitable environments (Boddy, 1999). In addition, fungal nutritional needs are easy to meet, which means that most organic materials are a potential target for fungal decay (Adan and Samson, 2011), and consequently most ecosystems can be colonized by fungi.

In natural ecosystems, such as forests, fungi are the main organisms in charge of organic matter degradation and therefore they are also essential in nutrient recycling (Krivtsov et al., 2006). Fungi are able to degrade organic matter by releasing enzymes targeting different chemical components. They are the only organisms able to degrade lignin, one of the main components of both plants and trees. Different fungal species are able to degrade moist wood of dead and living trees (Figure 2.1(a)) in different ways, which are referred to as brown rot, white rot and soft rot (Schwarze, 2007). While in brown rot and soft rot the cellulose of wood is broken down by the attacking fungus, other fungal species are specialized in the breakdown of lignin causing white rot.

In addition to their degrading behaviour, fungi are key to the formation of symbiotic relationships with plants and trees in natural ecosystems (Gadd et al., 2007). The most well-known symbiotic relationship between plants and fungi is the one between roots and fungi, referred to as mycorrhizal symbiosis (Dickson and Kolesik, 1999) (see Figure 2.1(b)). Fungi fuse with the roots of their symbiotic partners, as such being able to redistribute nutrients from the plant to themselves and vice versa. In exchange, the hyphae of fungi extend into the soil, increasing the absorption potential for water and nutrients of the host plant. Furthermore, these mycorrhizal associations have been proven to protect the plants from root pathogens, such as nematodes and other fungi. Fungi are able to produce antibiotic substances in order to protect their symbiotic partners (Brimner and Boland, 2003). Other fungi create symbiotic relationships with other parts of the plant such

(a) Fungi growing on a death tree

(b) Mycorrhizal symbiosis between plant and fungus

Figure 2.1: Examples of the action of fungi in natural ecosystems. (Source: Aberdeen Mycorrhiza Research Group)

as the leaves or the stem. These fungi are referred to as endophytes and they protect their host from harmful fungi, insects and mammals (Faeth and Fagan, 2002; Sun and Guo, 2012).

The presence of fungi in human ecosystems is also crucial. Different industries benefit from the action of fungi as they are used to develop products ranging from medicines to food products (Grimm et al., 2005). Fungi such as truffles and mushrooms are harvested and consumed as nutritious food. In addition, some fungi have been used for centuries as fermenting agents to develop products as bread and alcohol (Papagianni, 2004). Fungal metabolites can be used to develop antibiotics (Berdy, 2005) and plant growth stimulators (Sahasrabudhe and Sankpal, 2001). In addition, enzymes are extracted from fungi to produce dairy products, such as yogurt (Gougouli et al., 2011), in paper production (Torres et al., 2012) and biofuel generation (Vicente et al., 2009). Fungi are also used as biological control agents against insects, nematodes and fungi harming plants and crops (Brimner and Boland, 2003). The use of fungi in industry and their impact on humans and other organisms is summarized in Figure 2.2.

During the last years, fungi have also been used as climate change and global warming indicators (Boddy et al., 2014). This use is motivated by the fact that fungi are present all over the world and most fungal species are susceptible to temperature and humidity changes making them the perfect indicators to study climate change. For instance, mycologists have recently identified a change in host affinity in certain fungal species associated with changes in environmental conditions (Gange et al., 2011). In addition, a shift in the timing of the spring fruiting of different fungal species as a consequence of climate change has been observed (Kauserud et al., 2010), as such providing an indicator of the evolution

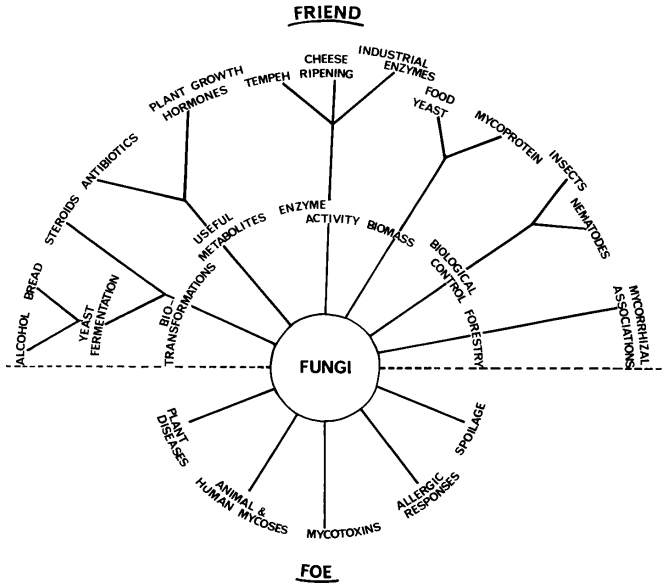

Figure 2.2: Summary of the beneficial and detrimental activities of fungi. (Source: Moss (1987))

of the climate conditions in the studied areas.

Fungi can also have detrimental effects on both natural and human ecosystems. In contrast to their ability to develop symbiotic relationships with plants, many fungal species are plant pathogens (Dean et al., 2012). In nature, most plant species are susceptible to fungal diseases (Hansen, 2008). As their natural counterparts, plants harvested in man-made ecosystems are also vulnerable to the action of plant pathogen fungi. Fungal diseases affect key crops for humans, such as rice (Couch et al., 2005), wheat (Bolton et al., 2008) and potato (Secor and Gudmestad, 1999). Therefore, the action of fungi results in substantial economic losses in the agricultural sector. For instance, the fungus *Magnaporthe oryzae*, present in 85 countries worldwide, is responsible for the rice blast disease which causes 10 to 35% loss of harvest (Fisher et al., 2012).

In response, different industries use and develop fungicides in order to prevent fungal attack. Fungicides are not only used for crops, but also to protect building materials since they are also affected by fungi (Adan and Samson, 2011). Building structures can be damaged by the action of fungi due to the presence of moisture or water (Viitanen et al., 2010b). Unfortunately, indoor plumbing problems, condensation or leaky roofs are common situations that lead to the degradation of building materials. In addition, some building parts such as the façade are often exposed to long periods of condensation bringing along optimal conditions for fungal growth (Gobakken and Westin, 2008). Due to these problems, preventing the deterioration of buildings by fungi is extremely difficult.

Fungal decay does not only affect building structures but also the different living areas. Indoors, fungi spoil food and other organic products (Adan and Samson, 2011). The environmental conditions needed for fungi to grow prevail in many buildings, due to structural or insulation problems (Pasanen et al., 1992). For instance, air currents promote the propagation of spores, while areas with low ventilation are more suitable to sustain the conditions required for fungal growth (Cooley et al., 1998). In addition to food spoilage (Samson, 1989), indoor fungi generate mycotoxins that cause several diseases for humans and domestic animals, referred to as mycoses. A prolonged exposure to certain fungi can result in severe illnesses and even death (Thornton, 2011). Fungal mycotoxins can access the human body through inhalation or wounds causing diseases affecting internal organs known as systemic mycoses. Even though most mycoses only affect immune-depressed patients, certain fungi have proven to increase allergic reactions and respiratory conditions such as asthma in healthy individuals (Denning et al., 2006). Therefore, preventing the action of fungi is a health issue and, consequently, it is a priority for the research community.

In summary, fungi play an important role in most known ecosystems either in a positive or in a negative way. For this reason fungi have been widely studied in different scientific fields such as forestry and engineering. Nevertheless, some aspects of fungi and their development remain a mystery due to the narrow scope of current experimental techniques for tracking the evolution of fungi. Therefore, the study of fungi and fungal development is a critical issue for the whole society.

2.3 Fungal diversity and morphology

Fungi are present all over the world in a wide range of shapes and sizes, some of which represent the largest and oldest living organisms on Earth (Anderson, 1992). Fungi are grouped in their own taxonomic kingdom, within the supergroup Opisthokonta of the taxon Eukaryota (Adl et al., 2005), in the light of their unique features such as the structure of their cell walls, composed of glucans and chitin (Adams, 2004), substances found in the cell wall of plants and arthropods, respectively. As is the case for plants (kingdom Plantae), fungi are immobile and growth is their only way of moving. Additionally, fungi and plants share growth habitats and the fruiting bodies of some fungi resemble plant structures, which explain why they were initially classified as part of the plant kingdom (Whittaker, 1969). In contrast to plants, fungi are heterotrophs and they are not able to fix carbon from inorganic compounds implying that they need to obtain carbon from their environment, similar to animals (kingdom Animalia). On the other hand, fungal digestion differs significantly from animal digestion since the former takes place outside the fungal body while the latter usually takes place inside the animal body. Hence, even though the kingdom of fungi shares features with other king-

doms, it also has unique characteristics that distinguish it clearly from the other kingdoms.

Historically, there are two ways of classifying organisms, either according to their morphological characteristics or their ability to reproduce with individuals of the same species (biological species). These two classifications are not the best option for fungi since most species reproduce through asexual reproduction and several fungal species are unicellular whose morphological characteristics are not easy to differentiate. Therefore, genetics are mostly used to classify fungi in phylogenetic trees, thereby showing the evolutionary relations between different organisms. These trees are constructed using DNA sequence analysis and they group the organisms sharing certain ancestors. For instance, the fungi kingdom is divided in five so-called phyla (sing. phylum), referred to as basidiomycetes, ascomycetes, zygomycetes, chytrids and glomeromycota. Table 2.1 shows the different phyla of the concerned kingdom, together with their main characteristics and some of the species included.

Table 2.1: Key characteristics and most representative species of each of the four fungal phyla. (Sources:Webster and Weber (2007); Blackwell (2011)).

Phylum	Key characteristics	Typical examples	Number of species
Basidiomycota	Reproduce mainly sexually via the formation of specialized club-shaped end cells called basidia	Mushrooms, puffballs, boletes and rusts	31,515
Ascomycota	Form non-motile spores in a microscopic sexual structure called ascus as part of sexual reprodution	Yeasts, truffels *Fusarium* and morels	64,163
Zygomycota	Reproduce mainly asexually and lack septa	Black bread mold (Rhizopus stolonifer)	1,065
Chytridiomycota	Predominately aquatic and produce zoospores	Allomyces	1,500
Glomeromycota	Form arburscular mycorrhizae with plants	Arbuscular mycorrhizal fungi	169

Fungi can be typified according to their cellular structure as unicellular fungi or yeasts and filamentous fungi, also known as moulds (Wendland, 2001). The former consist of a single cell that grows new cells by asexual and/or sexual reproduction. The most common form of asexual reproduction in yeasts is by budding. In this case, a new organism arises as an outgrowth of the mother cell, as such resulting in a smaller genetic clone of the mother cell (Balasubramanian et al., 2004). Asexual reproduction of yeast can also occur by fission, where two identical daughter cells originate from the mother cell's division. Under stress, yeasts are able to produce haploid spores able to fuse with other spores, as such creating diploid cells able to survive even under stress conditions (Wagstaff et al., 1982).

Filamentous fungi are multicellular organisms formed by thread-like structures referred to as hyphae (sing. hypha). The hyphae of a filamentous fungus form a network referred to as mycelium (plur. mycelia) or fungal colony. A fungal hypha consists of one or more cells surrounded by a thin tubular cellular wall. All the cells in the hypha are connected allowing for the redistribution of nutrients, water and organelles within the whole fungus. The hyphae of some fungal species are separated in different compartments by cross-walls (Barnett and Hunter, 1972), referred to as septa (sing. septum). These septa have pores allowing for the communication between adjacent compartments of neighbouring hyphae. Other fungal species are mainly composed of aseptate hyphae and have septa only at the bases of reproductive structures. The structure and functions of the hyphae will be further discussed in Section 2.4.

A last kind of fungi is referred to as dimorphic since it is able to exist both as hyphae and single cells. They are able to change their morphology depending on the environmental conditions. For example, some plant, human and animal pathogens grow as hyphae outside their hosts and take a yeast form once inside the host (Gauthier, 2015).

Different morphological characteristics can be observed across the fungal species comprising the fungi kingdom. Even simple unicellular fungi show different colours, shapes and sizes (Agarwal et al., 2011). The morphological characteristics among the filamentous fungi also differ substantially. Even though the tubular structure is common to all filamentous fungi, the shape and thickness of the cells composing the hyphae can differ significantly (Alexopoulos et al., 1996). In addition, the morphology of the asexual spores produced by fungi and the pigmentation of the hyphae also varies among species. From a mesoscopic point of view, a fungus can be characterized in terms of the morphology of its colony. Growing filamentous fungi produce different shapes as the result of the extension and branching behaviour of their hyphae, ranging from really condense circular colonies to sparse irregular mycelia. One of the most common ways to identify fungi from a macroscopic point of view is by means of their fruiting bodies. The fruiting bodies of fungi, also referred to as sporocarps, formed by the more evolved groups (ascomycetes and basidiomycetes) are used to produce and store the spores needed for sexual reproduction (Alexopoulos et al., 1996). The shape and size of fruiting bodies differ widely between different fungal species (see Figure 2.3). The best known fungal fruiting body is the agaric, a mushroom-like structure characteristic of most edible mushrooms. There are sporocarps resembling corals, cups or flasks (Alexopoulos et al., 1996) (see Figure 2.3 for some examples of fungal fruiting bodies).

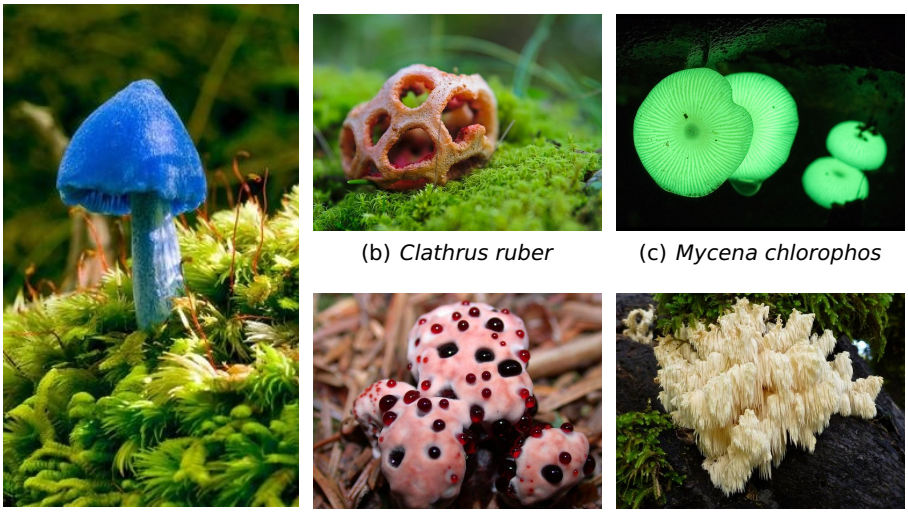

(a) *Entoloma hochstetteri* (b) *Clathrus ruber* (c) *Mycena chlorophos*

(d) *Hydnellum peckii* (e) *Hericium erinaceus*

Figure 2.3: Different fungal fruiting bodies. (From Creative Commons)

2.4 Fungal growth

We will focus on filamentous fungi since most fungi belong to this group Gadd et al. (2007). The most remarkable characteristic of filamentous fungi is their growth. These fungi are able to gain biomass only by extending existing hyphae. Moreover, filamentous fungi are able to create new hyphae by branching. The processes involved in both the generation of new hyphae and the extension of existing hyphae have been studied at different scales. Growth only occurs under certain environmental and nutritional conditions which differ among fungal species making the study of fungal growth even more challenging.

2.4.1 The life cycle of fungi

The fungal life cycle is divided in different phases. In the first phase, fungi take the form of spores. Spores are haploid structures that are dispersed in the environment by mature fungi for sexual or asexual reproduction. They are usually able to survive in unfavourable conditions and they develop into a new mycelium under favourable environmental conditions (Ayerst, 1969). The transition between spore and mycelium is called germination and during this stage the fungal spore loses its spore-specific characteristics and generates new hyphae (see Figure 2.4).

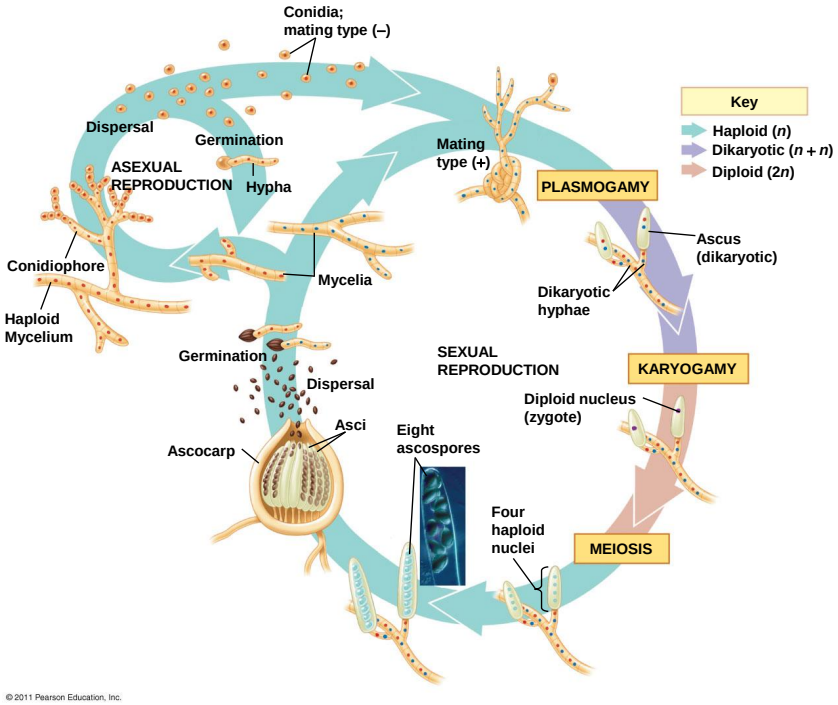

Figure 2.4: Summary of the life cycle of an ascomycete.

The hyphae developed from the spores are of a specific mating strain and are able to form a mycelium, referred to as primary mycelium or haploid mycelium (Webster and Weber, 2007) (Figure 2.4). The primary mycelium is able to grow on independently and to produce new individuals either by fragmentation of hyphae or by generating new asexual spores, referred to as conidia.

When different mating strain mycelia meet, first their hyphae fuse in a process referred to as plasmogamy, resulting in a combined mycelium (Figure 2.4). This new mycelium is composed of cells with two haploid nuclei and is referred to as secondary mycelium or dikariotic mycelium (Webster and Weber, 2007). The secondary mycelium of usually grows in soil and in some fungal species it is able to form compact masses just below the soil surface. These compact masses of hyphae are known as mushroom primordia and are able to develop into fruiting bodies (also known as mushrooms or sporocarps). The nuclei of certain cells of the secondary mycelium can fuse in a process referred to as karyogamy as such resulting in diploid cells able to produce sexual spores via meiosis. These spores are usually stored in the fruiting bodies and can be released in the environment, ultimately giving rise to new fungi as such closing the cycle.

2.4.2 A closer look into the hypha

A hypha is composed of one or more cells organized in a thread-like structure with connected protoplasm surrounded by a thin tubular wall. Hyphae are usually composed of different types of cells that can be classified in terms of their morphology and function (Bistis et al., 2003; Riquelme et al., 2011). There are hyphal cells whose primary function is the growth of the mycelium, for instance leading hyphae situated at the periphery of the colony. Leading hyphae are very active and are able to grow and generate new hyphae by branching (Bistis et al., 2003). Other hyphal cells, referred to as fusion hyphae, are specialized in making new connections within the mycelium. These cells create bridges between different parts of the mycelium improving the connectivity of the hyphal network (Bistis et al., 2003). Hyphae involved in the sexual reproduction of fungi are able to sense and react to each other. For instance, trichogyne are hyphae exhibiting positive tropisms towards cells of the other mating type (Bistis et al., 2003). Hyphae can also react to their environment by growing towards or away from certain materials. An example of this behaviour are aerial hyphae showing a negative tropism towards the growth medium surface in order to disperse asexual spores more efficiently (Bistis et al., 2003).

The fungal cell wall is common to all fungal cells and is responsible for the characteristic shape of the hyphae (Alexopoulos et al., 1996). It is composed of chitin, glucan and glycoproteins and protects the fungus from the environment by acting as a filter controlling what enters and exits the cell protoplasm (Dijksterhuis, 2011). The fungal wall is rigid enough to safely contain turgor pressure inside the hyphae and to maintain the shape of the hyphae under environmental stress (Bowman and Free, 2006). However, it is also a dynamic and malleable structure able to change throughout the fungal cycle, as such allowing for hyphal branching, fusion and extension (Bowman and Free, 2006). The mechanisms involved in the remodelling of the fungal wall in order to accommodate branch formation and extension remain one of the most intriguing mysteries in mycology (Riquelme et al., 2011).

Inside a fungal cell, the same organelles present in most eukaryotic cells can be found (see Figure 2.5). However, the distribution of these organelles in the case of hyphae is stratified, i.e. the organelles are distributed along the whole hypha (Dijksterhuis, 2011). A typical fungal hypha can be divided in different regions, each of which contains several cells and different organelles (Roberson et al., 2010). Even though not all organelles are present in each region of the hypha, they are able to migrate within the hypha in order to cover the needs of a specific region. This migration of organelles and vesicles occurs along the cytoskeleton (Steinberg, 1998), a dynamic structure composed of microtubules and actin microfilaments. The cytoskeleton supports the shape of the hypha and controls the cell movements. In addition, the cytoskeleton has proven to be crucial for fungal cellular division and the spatial regulation of organelles in growing tips (Riquelme et al., 2011). For

instance, actin is abundantly present in growing hyphal tips and the inhibition of the compounds of the cytoskeleton has a direct negative impact on the growth of tips (Bartnicki-García, 2002).

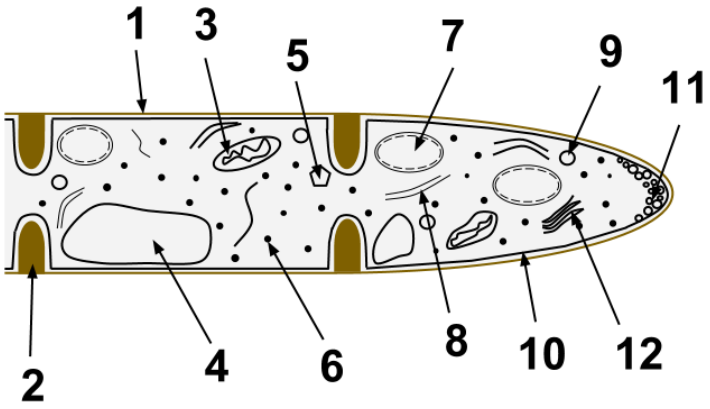

Figure 2.5: Fungal cell and organelles. 1. Hyphal wall. 2. Septum. 3. Mitochondrion. 4. Vacuole. 5. Ergosterol crystal. 6. Ribosome. 7. Nucleus. 8. Endoplasmic reticulum. 9. Lipid body. 10. Plasma membrane. 11. Spitzenkorper. 12. Golgi apparatus. (From Creative Commons, original artist - AHiggins12)

From all the organelles present in the protoplasm of a hypha, the most interesting is the Spitzenkörper due to its important role in fungal growth and its unique structure. The Spitzenkörper contains macrovesicules, microvesicules, ribosomes and cytoskeletal components (Bartnicki-García, 2002). This structure is believed to function as a vesicle supply centre regulating the delivery of fungal cell wall-building vesicles to the apex, as such inducing growth. The Spitzenkörper is always located at the tip of growing hyphae and its position inside the tip determines the growth direction (Riquelme et al., 1998). Due to the importance of this structure for both apical growth and branching, its role will be further discussed in the following sections.

2.4.3 Apical growth

Apical growth occurs at the tips of the hyphae, also known as apices, and results in the elongation of existing hyphae. The tip of a hypha has a different structure than the rest of the hypha since it contains mostly vesicles, assembled into the Spitzenkörper, and its cell wall is weaker than elsewhere in the hypha (Harold, 1997). During apical growth, the vesicles containing the components needed for tip extension are manufactured in different parts of the mycelium and then carried through the microtubules to the tips (Riquelme et al., 2011). There, the vesicles are transported to the Spitzenkörper that acts as a vesicle supply center deliv-

ering the cell-wall building vesicles to the tip (Bartnicki-Garcia et al., 1995). At the tip, the cell-wall is thin and structurally weak (Harold, 1997), so turgor pressure exerted on the wall of the tip causes its deformation (Lew et al., 2004). This deformation enables the insertion of new wall material in the existing wall, thus resulting in the extension of the cell wall and the hypha (Wessels, 1986; Steinberg, 2007).

As the tip extends, the Spitzenkörper moves keeping its location at the end of the tip. Its position within the hyphal tip is not fixed and determines the growth direction of the hypha (Bartnicki-García, 2002). For instance, a Spitzenkörper placed at the axis of a growing tip makes the hypha extend straight ahead, whereas off-centre displacement of the Spitzenkörper precedes a change in the growth direction of the hypha. Even though the trajectory of the Spitzenkörper mostly follows the existing cell axis leading to straight growth (Riquelme et al., 1998), this trajectory often shifts resulting in changes of the growth direction.

The Spitzenkörper has proven to be the main intracellular factor determining the growth direction of a hypha but external factors such as light, chemicals or oxygen also have an impact (Brand and Gow, 2009). Thus, the Spitzenkörper is repositioned in response to these external stimuli resulting in reorientation (Riquelme et al., 2011), known as tropism. For instance, growing tips within the same fungal colony are able to sense and avoid each other to maximize the colonization of substrate (Brand and Gow, 2009). Chemotropisms, i.e tropisms towards chemical substances can be observed when hyphal tips re-orient in response to pheromones secreted by hyphae of the opposite mating type. Fungi are able to react to other organisms such as certain plant pathogen fungi able to grow towards their hosts in a plant-directed tropism (Brand and Gow, 2009).

The elongation of hyphae does not occur at a steady rate even under constant environmental conditions (Lopez-Franco et al., 1994). Apical growth is a pulsatile phenomenon, i.e. periods of fast and slow growth alternate, for some species ranging from 2.7 to 14 pulses/min (Bartnicki-García, 2002). The rate at which a hypha elongates depends on its genetic characteristics and the environmental conditions (Boddy, 1983). Extension rates vary significantly even within strains of the same fungal species.

2.4.4 Branching

Fungi are able to generate new hyphae from existing ones in a process known as branching. The result of branching is a new tip that is able to grow apically, thus generating new fungal biomass. The formation of new branches results in exponential biomass growth of the fungal colony, an increase of the surface area of the colony and a better exploitation of the substrate in the environment (Riquelme et al., 2011; Harris, 2008). In addition, the branching behaviour of fungi plays an

important role in their interactions with other organisms (Akiyama et al., 2005) and even among hyphae of the same colony (Hickey et al., 2002).

Two branching processes can be observed in most fungi, namely lateral and apical branching (Harris, 2008). Both processes result in a new tip, but the mechanisms differ significantly. Apical branching (also referred to as dichotomous branching) occurs at the tip of the parental hypha and seems to be the result of an abnormal accumulation of vesicles at the tip. Apical branching is often associated with periods of rapid hyphal growth during which the supply of vesicles exceeds the capacity to be incorporated into the existing tip, as such leading to the formation of new tips (Harris, 2008). One of the main characteristics of apical branching is the disappearance of the Spitzenkörper. During apical branching the Spitzenkörper disappears temporally, as such disturbing the growth and morphology of the parental tip (Harris, 2008). In contrast, lateral branching occurs at sites distant to the original hyphal tip. It has been hypothesized that the location of lateral branches in the hypha away from the growing tip illustrates a phenomenon referred to as apical dominance (Webster and Weber, 2007). It is a well-known phenomenon, also observed in plants and other organisms, where the growing tip suppresses the development of lateral branches in its vicinity (Harris, 2008). Another difference with apical branching is that lateral branching is triggered by the appearance of a new Spitzenkörper (Harris, 2008). Therefore, the production of lateral branches does not impact the growth rate and morphology of the parental hypha. New lateral branches can be formed at any position within the existing hypha (Riquelme et al., 2011). Spontaneous polarization is the most accepted theory explaining the emergence of new branch sites (Harris, 2008). It states that a new branch is formed when the local level of polarity determinants on a site exceeds a certain threshold. The local levels of polarity determinants fluctuate randomly and, consequently, the location of new branches is also random.

Any new branch is formed in different consecutive steps (Riquelme et al., 2011). Once a new branching site is selected, the components required for fungal extension need to be transferred to the branching site. This process is known as recruitment, since the morphogenetic machinery (i.e. the components and vesicles required for cell and cell wall expansion) is recruited from different places in the hypha to the branching site. During the second step, referred to as polarization, the morphogenetic machinery functions in order to create the new branch. The final step is the maturation of the new branch during which the new tip attains its maximal extension rate. After maturation the new hypha is able to grow apically as described in Section 2.4.3.

Even though branches can occur at any position, some external factors have proven to influence their formation. For instance, environmental factors such as light (Lauter et al., 1998), temperature (Watters and Griffiths, 2001) and substrate distribution (Watters et al., 2000) have a direct effect on the branching behaviour of fungi. Furthermore, branching is also induced by external organisms such as

plants and algae. For instance, in mycorrhizal associations between fungi and plant roots (see Figure 2.1(b)), root exudates are able to trigger profuse fungal branching (Akiyama et al., 2005). Other hyphae can induce the formation of new branches in order to promote the fusion of hyphae (see Section 2.4.5), as such allowing for the communication between neighbouring hyphae. This can be observed when a hyphal tip gets close to an existing hypha, where it induces the formation of a new Spitzenkörper, as such triggering the formation of a new lateral branch at the former (Glass et al., 2004).

2.4.5 Anastomosis

Fusion of hyphae has been observed in filamentous fungi. Hyphal fusion occurs at different stages of the life cycle of fungi and serves different purposes (Alexopoulos et al., 1996). Connections between hyphae of the same fungus make the mycelium more efficient, allowing for a better translocation of nutrients, water and fungal organelles inside the fungus (Glass et al., 2004). In addition, hyphal fusion between opposite mating hyphae is crucial for sexual reproduction (Coppin et al., 1997). Unfortunately, the frequency, spatial and temporal distribution of fusions are not yet well understood (Hickey et al., 2002). Anastomosis occurs in different parts of the mycelium, but all fusions require at least one hyphal tip (Hickey et al., 2002). Therefore, two types of anastomosis can be observed: tip-to-tip anastomosis, where two hyphal tips fuse, and tip-to-side anastomosis, when a tip fuses with a part of the hypha different than the tip (Hickey et al., 2002).

Both kinds of anastomosis occur in three different stages, namely, pre-contact, post-contact and post-fusion (Glass et al., 2004). In tip-to-side anastomosis, the tip approaching the hypha secretes a signal during the first stage of hyphal fusion. This signal induces the formation of a new Spitzenkörper at the site of the upcoming fusion and therefore the formation of a new lateral branch. Then, similar to tip-to-tip anastomosis, the two tips grow towards each other until they make contact, which is the starting point of the post-contact phase. During this phase, the hyphal tip extension ceases (growth arrest) and the tips secrete an adhesive substance in order to stick together. Once glued together, they start to dissolve their fungal walls until the cytoplasm of both tips is in contact. In the last stage, the two former tips combine their cytoplasm and their Spitzenkörpers disappear. The result of this fusion is a hyphal cell connecting the two initial hyphae that is no longer able to grow.

Within the same fungal colony, anastomosis occurs at the interior of the fungal colony rather than the periphery (Glass et al., 2004). The reason for this is that hyphae at the periphery of the colony avoid other hyphae, i.e. exhibit negative autotropism. In contrast, the hyphae at the interior show positive autotropism (Glass et al., 2004).

2.4.6 Fungal nutrition

Fungi are able to use almost any carbon source (Alexopoulos et al., 1996). However, the specific nutritional needs differ from species to species. For instance, while some species are able to utilise anything that contains organic matter, other species have restrictive nutritional needs and can only feed on very specific substrates. Fungi are often classified according to their nutrition in three groups: saprobes, parasites and mutualists (Alexopoulos et al., 1996). The former use dead or decaying organic material, such as leaves, branches and animals. Parasitic fungi obtain their food by attacking living organisms. They damage their host and can eventually cause its death. Finally, mutualistic fungi are able to obtain food from living organisms without causing any damage to their hosts. In some cases, the presence of fungi in animals and plants can even be advantageous for the host, such as protection or additional sources of substrate. For instance, the relationship between algae and fungi in lichens is an example of a mutualistic relationship, where the fungi use the carbon obtained by the photosynthesis of the algae, while the algae get protection and moisture from the fungi.

Fungi need extracellular sources of organic material, for their maintenance, growth and reproduction (Alexopoulos et al., 1996). The nutrients have to be absorbed through the fungal cell wall, so that only small particles are able to enter the fungus. Since most nutrients are not able to pass through the fungal wall, the fungus needs to break down the nutrients in the environment into soluble molecules that can then be absorbed (Jennings, 1995). Hence, the fungal digestion occurs outside the fungus.

Fungal digestion is carried out by enzymes released by the fungus into the environment. Since fungi have many different vacuoles, they are able to generate enzymes targeting a wide range of substrates. For instance, most fungi are able to produce all the enzymes needed for exploiting the substrates present in their natural environments (Jennings, 1995). During fungal digestion, fungi decompose simpler compounds first and then move to more complex compounds. The simplest compounds present in the environment of most fungi are sugars. Glucose is ready to use by all fungi and it can pass almost intact through the fungal wall. Therefore, fungi target first glucose and once the glucose is depleted they release enzymes able to degrade other molecules, such as cellulose or lignin. Cellulose is the most common complex carbohydrate available in the environment and therefore many fungi specifically target its breakdown. It is broken down by special enzymes known as cellulases. In natural ecosystems cellulose is often associated with lignin, the second more common organic polymer in the environment (Dashtban et al., 2010). Some fungi are able to degrade lignin, but this process is often much slower and more complex than the degradation of cellulose (Jennings, 1995). Furthermore, the degradation of lignin demands a lot of energy and therefore it usually requires a co-substrate to provide the extra energy for lignin degradation.

For these reasons, the degradation of lignin takes place only in the absence of better nutrient sources. In addition to the above-mentioned compounds, almost any molecule able to release energy on digestion can be completely or partially degraded by one or more fungal species (Alexopoulos et al., 1996). However, the breakdown of some molecules requires the action of additional microorganisms, and their digestion rate may be much slower than in the case of cellulose, glucose and lignin.

The products of fungal digestion are absorbed by the fungus in a process referred to as uptake. Only small molecules are able to pass through the plasma membrane and wall of the hyphae, so mainly simple sugars, amino acids and fatty acids can be taken up following digestion (Jennings, 1995). These molecules are absorbed in solution, so water is needed in the environment in order to enter the fungal cell (Alexopoulos et al., 1996). Some nutrients are able to be absorbed faster than others. Hence, the affinity of the uptake process depends on the type of nutrient and the fungal species, and it is quantified using an affinity constant of the fungus for a particular nutrient (Jennings, 1995). Consequently, the amount of a particular nutrient taken up depends on its affinity constant and the environmental concentration and saturation of the nutrient. The flux of a particular nutrient into a fungus can be used to determine the competitive ability of the fungus for that nutrient (Jennings, 1995).

One of the main characteristics of fungi is their ability to redistribute nutrients within the mycelium. This redistribution mechanism or translocation allows solutes and water to travel within the hyphae across long distances, as such covering the specific needs of different parts of the mycelium. Translocation is particularly important in habitats with an irregular spatial distribution of nutrients and minerals (Fricker et al., 2008). Due to translocation, fungi are also able to grow and survive in oligotrophic and polluted habitats, by exploiting the resources available in other parts of the mycelium (Boswell et al., 2002).

Translocation is a combination of different processes, such as mass flow, diffusion, cytoplasmatic streaming and specific vesicular transport (Tlalka et al., 2007). Translocation is usually divided in two distinct mechanisms; passive translocation and active translocation. While the former is usually characterized by diffusion of substrate within the network, the latter is described as metabolically driven (Boswell et al., 2002). In the case of active translocation the nutrients travel mainly through the cytoskeleton, usually in the direction of the growing tips. In contrast, diffusion usually follows the opposite direction and occurs as a consequence of the concentration gradient within the fungus (Jennings, 1995). Long-distance nutrient translocation is mainly driven by mass flow and shows a strong pulsatile behaviour (Fricker et al., 2007). The mechanisms governing the mass flow within the network are not yet well understood, but it has been hypothesized that the flow of water entering and exiting the mycelium could be the main factor steering the mass flow (Fricker et al., 2007).

The speed and direction of translocation depend on different factors. For instance, the position, size and quality of the available resources affect the flow direction (Fricker et al., 2008). Translocation is a bidirectional process since nutrients can be redistributed in both directions within the mycelium (Tlalka et al., 2007). For instance, when a fungal colony grows starting from a nutrient source, the translocation of nutrients occurs towards the growing margin of the colony in order to promote growth (Fricker et al., 2007). However, when the growing hyphae reach additional resources, they can be redistributed in order to cover the local needs of areas in the absence of nutrients (Fricker et al., 2007). In addition, the structure of the mycelium also plays an important role in translocation since the number of connections in the network, its length and the number of branches and tips have a direct impact on the translocation strategy of the fungus (Fricker et al., 2007).

2.4.7 Other factors affecting fungal growth

Aside from substrate, also other external factors influence the growth of fungi. One of the main factors is moisture (Pasanen et al., 1992). Even though moisture requirements vary considerably between different fungal species, the fungal wall of all fungi is susceptible to desiccation (Alexopoulos et al., 1996). Water is needed to dilute the solutes resulting from the digestion in order to pass them through the fungal wall (Alexopoulos et al., 1996). Therefore, water needs to be present in a fungus' environment in order to sustain its growth. Moreover, the study conducted in Ayerst (1969) to assess the effect of humidity on fungal growth, established the optimal moisture content to be above 90% for all studied species.

The second most important external factor affecting the growth of fungi is temperature. Temperature is crucial for the development of mycelia since each fungal species is able to grow only in certain temperature ranges (Tommerup, 1983). Wood rotting fungi grow only under temperatures between 5° and 40° and reach optimum growth rates between 20° and 30° (Boddy, 1983). In contrast, other species are able to grow only under very low temperatures or in environments with temperatures up to 100°C (Magan, 2007).

Most fungi are aerobes and need oxygen to survive (Webster and Weber, 2007). It has been reported that hyphae sense and grow towards oxygen and therefore oxygen also determines the overall shape of the mycelium (Brand and Gow, 2009). Fungal growth is also influenced by the pH of the environment (Sundari and Adholeya, 2003) and, as in the case of temperature, the optimal range of pH depends on the fungal species (Alexopoulos et al., 1996).

Finally, the last factor affecting fungal growth is light (Lauter et al., 1998). Even though light is not required for fungal growth, it is often important for sexual and asexual reproduction (Alexopoulos et al., 1996). Certain fungal species require a

light source in order to produce asexual spores (Bayram et al., 2008), since light is involved in the orientation of spore-bearing structures and spores are usually discharged toward the light (Pöggeler et al., 2006).

3

Overview of mathematical models in mycology for fungal growth

3.1 Introduction

The recent increase of computing power and the decrease of computing cost have advanced the field of mathematical modelling, resulting in more efficient and accurate models. A mathematical model is a description of a part of reality using mathematical constructs. Mathematical models are widely used to complement studies on biological phenomena. In contrast to lab experiments, simulations are non-destructive, inexpensive and often faster than their experimental counterparts. Therefore, mathematical models are the perfect tool to extend results obtained in laboratories and to test hypotheses raised from experiments. For instance, mathematical models have been employed to predict the spread of infectious diseases in order to minimize their impact on society (Funk et al., 2010). Other models are able to reproduce the dynamics of different populations of organisms

resulting in a better understanding of the factors driving these dynamics (Grimm, 1999). In contrast, some models focus on the dynamics of a single individual or even on only one of its parts, such as those representing the growth of individual plants (Prusinkiewicz, 2004) or the extension of their roots (Dupuy et al., 2010), respectively.

Mathematical models in biology usually describe the evolution of biological processes as a function of time and/or space. Space, time and the characteristics of the modelled entity (state) can be represented in different ways, resulting in different modelling paradigms. For instance, time is often discretized using time steps of the same duration, while the discretization of space is done using grids of equally sized cells. In the case of the state set, features such as population size can be modelled in a continuous or a discrete way. For example, a system of differential equations can be used to model the biomass of a community of plants. In this case, time and space are continuous, as well as the state, which here is the average biomass. Therefore, the average biomass can take any value and it is known for every point in time and space. In contrast, a cellular automaton would model the same phenomenon using discrete time steps and a grid of cells dividing the space, where each cell can take one of a finite number of states, representing different biomass values. Hence, a cellular automaton is able to represent the spatial spread of the community accurately but not the exact biomass value since it models presence or absence rather than amount. In this way, models can be classified according to whether space, time and state are discrete or continuous (Table 3.1).

In addition to this classification, models can also be classified depending on their space dimension, into one, two and three-dimensional models. Besides, most biological phenomena can be studied at different scales, resulting in macro-, meso- and microscopic models. For instance, the growth of most organisms can be modelled at population, individual or cellular level using macro-, meso- and microscopic models, respectively.

The field of mycology has also benefited from mathematical models. Mathematical models in this field focus on different features of fungi and their interactions with their environment. The scope of these models is wide and their use manifold. They can be used to study biological processes occurring in natural ecosystems or to optimize production processes involving fungi in industries, such as the dairy (Valík et al., 1999) and pharmaceutical industry (Geng and Yuan, 2010), and the building (Hukka and Viitanen, 1999) and the agricultural sector (Jeger et al., 2008).

An example of a widely modelled fungal phenomenom occurring in natural ecosystems is the symbiosis between roots and fungi, captured in several models (Schnepf et al., 2008; Declerck et al., 2001). Some of them focus on the effect of the mycelium on the uptake potential of its symbiotic partner. For instance, the model presented in Schnepf et al. (2008) combines a fungal growth model with a model for the phosphorus concentration in the soil surrounding the roots. By mimicking

Table 3.1: Typification of spatio-temporal models based upon the structure, discrete (D) or continuous (C), of the involved space-time region and the state space. (Adapted from: Berec (2002))

Time	Space	State	Common label	Constructs[1]
C	C	C	PDE-based model	PDEs
C	D	C	Spatially implicit model	ODEs
D	C	C	Reaction-diffusion model	IdEs
D	D	C	Coupled-map lattice	PdEs
C	C	D	Spatial point model	Set of rules
D	C	D	Agent-based model	Set of rules
C	D	D	Interacting particle system	Set of rules
D	D	D	Cellular automata	Set of rules

[1] PDE: partial differential equation; IdE: integro-difference equation; ODE: ordinary differential equation; PdE: partial difference equation

three different fungal growth patterns and two possible uptake strategies for the depletion of phosphorus, this model leads to results similar to those obtained in experiments, as such shedding some light on the possible processes leading to phosphorus uptake by mycorrhizal fungi. Another related example can be found in Declerck et al. (2001). In this paper, experimental data on the evolution of spores of an arburscular mycorrhizal fungus over time is used to compare three possible growth models representing sporulation dynamics, leading to the conclusion that the sporulation of the studied fungal strains follows a sigmoidal pattern.

Mathematical models have also been used to study fermentation processes of fungi, due to their importance for different industries. In dairy industry, different models have been developed to determine the optimal conditions for the production of cheese (Valík et al., 1999) and yoghurt (Gougouli et al., 2011). Despite their simplicity, such models capture the effects of factors such as temperature, water potential or pH, on fungal features including the growth rate and lag time. For example, the fed-batch fermentation of *Penicillium chrysogenum* has been modelled to improve its yield and productivity in the pharmaceutical industry (Geng and Yuan, 2010). In Vázquez and Martin (1998) the use of peat in the fermentation process of *Phaffia rhodozyma* is simulated in order to optimize the fermentation time and biomass yield, and to study the affinity of the fungus for peat.

Different building materials are prone to the attack of fungi. For instance, mould fungi are able to grow on the surface of several materials, as such affecting the permeability and the aesthetical performance of the attacked material. For these reasons, in Hukka and Viitanen (1999), the effects of temperature and relative humidity on a healthy wood sample are modelled. Their model introduces the concept of mould index, a numerical scale representing mould growth as the percentage of the sample that is covered by fungus. Other fungal species do not

restrict their growth to the surface and can also grow inside different materials. This often results in more severe damage and even the decomposition of the attacked building material. Despite the importance of this problem in the building sector, only few models, such as the one described in Fuhr et al. (2011), have simulated the decay of building materials by fungi.

The spoilage of food has also been modelled at various scales and using different modelling paradigms (Gibson and Hocking, 1997; Dantigny et al., 2005). These models focus mainly on the presence and germination of spores by calculating the probability of a product to become infected by fungi, and allow to determine the effectiveness of specific food preservation methods.

Still, most of the established models are those representing the growth of fungi due to their relevance for all processes involving fungi. Microscopic fungal growth models study the processes driving growth at cellular level, i.e. representing small hyphal regions. On the other hand, macroscopic models study the spread of entire populations of fungi by relying on models similar to those mimicking the spread of diseases. In addition, some macroscopic models are able to describe the colonization of substrates by fungi, and the genotypic evolution of different fungal strains. Finally, mesoscopic models simulate the growth of a single colony. They use information from microscopic studies without restricting growth to a single cell or hyphal region. They are also able to represent large colonies and can be scaled up to provide information similar to that obtained using macroscopic models. The data extracted by current experimental techniques can be easily incorporated into such models, thereby resulting in more realistic models (Falconer et al., 2010). For these reasons, mesoscopic models are the most abundant ones. In the remainder of this chapter, the most relevant models for fungal growth will be reviewed, according to the scale they operate at.

3.2 Macroscopic models for fungal growth

Macroscopic fungal growth models describe the evolution of fungal populations over time and through space. While some of these models are able to represent the spread of fungi in response to the available resources, most of them simulate the spread of pathogen fungi (Davidson, 2007) given their impact on the agricultural industry. An example of the former is given in Jeger et al. (2008) where a model, relying on a system of ODEs, representing the colonization of a certain substrate and the decomposition of carbon by the fungus *Rhizoctonia solani* is used to identify the key factors driving fungal invasion.

Most macroscopic models aim at representing the dynamics of fungal pathogens in crops or the efficiency of fungicides against fungal diseases (van den Bosch and Gilligan, 2008). For instance, the stochastic model described in Milgroom

et al. (1990) simulates the evolution of a pathogen and its capacity to become resistant to a certain fungicide. The results obtained using this model include the probability that the fungicide resistance of the population reaches a certain threshold and the final host population size by the end of an epidemic period. The model described in Oliveira et al. (2004) also addresses the effects of fungicides, but in contrast to the one of Milgroom et al. (1990), this model focuses on the leaves of the host plant. This model is spatially implicit and relies on a system of ODEs that represents the evolution of the populations of resistant and susceptible plants. Instead of using a fixed growth rate, Oliveira et al. (2004) formulate a growth rate that changes over time, thereby being able to represent the effects of temperature on fungal growth. This model proved its worth for the agricultural sector since it can be used to calculate the optimal time to apply a fungicide in order to minimize crop loss.

Apart from studying the dynamics within a single crop field, macroscopic models can be used to model the spread of fungi at larger scales. For instance, in Parnell et al. (2006), a spatially implicit model is used to study the regional spread of a pathogen fungus. The model is based on a system of ODEs representing the evolution of infected and non-infected fields over time. The former contain spores that can be blown to healthy fields, thereby infecting them. The action of fungicides is included by allowing parts of the fields to be treated against the pathogens during the course of the simulation, resulting in resistant-infested and sensitive-infested field fractions. Four parameters drive the spread of the pathogen, namely the fraction of fields treated with fungicide, the effectiveness of the treatment, the cost of resistance of the pathogen, and the capacity of the pathogen to infest other fields.

The model presented in Stacey et al. (2004) goes one step further since it is capable of representing the invasion and spread of rhizomania, a disease transmitted by the soil borne fungus *Polymyxa betae*, affecting beetroot in farms throughout the United Kingdom. The model includes two phases: expansion during which the disease and the beetroot evolve mainly on a local scale (within the same field), and dispersion, representing the movement of infectious material within and between farms. The dynamics of each field is simulated by a system of ODEs representing: the total population of roots (n), the susceptible population of roots (s) and the new inoculum (M):

$$\begin{cases} \dfrac{dn}{dt} = r\,(1-n), \\ \dfrac{ds}{dt} = r\,(1-n) - \lambda(T)\,M_i\,s - m\,s, \\ \dfrac{dM}{dt} = Q\,\lambda(T)\,M_i\,s, \end{cases} \tag{3.1}$$

where r, m, and Q represent the root growth rate, the inverse of the susceptible

period for the roots, and the amplification of inoculum within infected root tissue, respectively. $\lambda(T)$ is the force of infection per unit inoculum initially present in the vicinity of the plant M_i, depending on temperature T. The inoculum spreads within a field as the result of cultivation. In addition, rhizomania travels from infested fields to fields of the same and other farms due to the movement of shared machinery. A farm shares machinery only with a certain number of farms, represented by a contact network over which infested materials can be distributed. The model was calibrated using historical data on the disease spread and then used to predict the state of the epidemic in subsequent years, and to compare the outcome of different control strategies. The results of such simulations can be found in Figure 3.1.

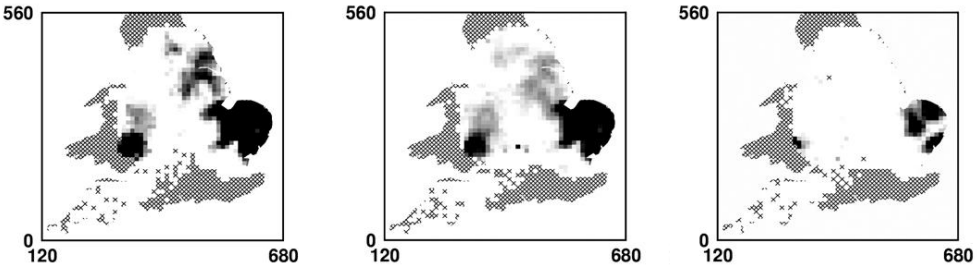

(a) (b) (c)

Figure 3.1: Maps representing the predicted state of the epidemic in the year 2050 in different scenarios: (a) containment implemented from the year 2000, (b) restriction of within-farm transmission from the year 2000, (c) restriction of between-farm transmission to 10% of its standard level from the year 2000. Darker shades indicate that a larger proportion of farms in a region are symptomatic. Cross-hatching indicate regions where beet is not grown. (Source: Stacey et al. (2004))

The model presented in Cunniffe and Gilligan (2008) also represents the spread of fungal infections, but in contrast to the models described by Parnell et al. (2006) and Stacey et al. (2004), this model predicts the spread of the infection by scaling up the growth dynamics of fungi. First, the evolution of the mycelium density $B(x,t)$ is computed as:

$$\frac{\partial B}{\partial t} = \gamma N(t) \nabla^2 B + \alpha N(t) B, \tag{3.2}$$

where $\gamma N(t)$ and $\alpha N(t)$ represent the functional responses of the spread and bulking-up to time-varying nutrient availability $N(t)$. Then a system of ODEs is used to track the total biomass evolution $C(t) = \int_{x \in \mathbb{R}^n} B(x,t)\, \mathrm{d}^n x$ and the depletion of substrate $N(t)$:

$$\begin{cases} \dfrac{dC}{dt} = \alpha\ N(t) C(t), \\ \dfrac{dN}{dt} = -\beta \alpha N(t) C(t) - \gamma \epsilon N(t) C(t). \end{cases} \tag{3.3}$$

where β and ϵ relate the rate of consumption of nutrients to the amount of bulking-up and spatial spread by diffusion, respectively. This simulation of the growth of the mycelium is similar to the one used in continuous mesoscopic models (see Section 3.4). System of equations (3.3) is first solved and its analytical solution is used in Eq. (3.2) to calculate $B(x,t)$. Finally, the evolution of the cumulative probability $p_L(t)$ of infection over time of a target host, at a distance L from the mycelium, is given by:

$$\frac{dp_L}{dt} = \lambda\, e^{-\mu t}\, N(t)\, B(L,t)\, (1 - p_L(t)), \tag{3.4}$$

where the initial rate of infection λ decays at rate μ as the host becomes progressively more resistant to infection. Therefore, this probability depends on the fungal disease efficiency and the amount of fungal biomass. This model allows to determine a pathozone, i.e. a map representing the probability of infection of a host anywhere in space. Hence, this model succeeds in scaling up fungal growth from the colony level to fungal infection dynamics at the population level.

Generally speaking, macroscopic models are a suitable option for studying and combatting the spread of fungal diseases in crops. Unfortunately, their scale limits their ability to represent fungal growth realistically. For instance, it has been proven that the morphology of the early mycelium has a direct impact on later growth phases, but macroscopic models are not able to account for this (Blackledge and Barry, 2011). Besides, macroscopic quantities such as the number of infected hosts or the fraction of infected crops do not provide information on the total fungal biomass yield or the structure and properties of the mycelium, so they cannot capture fungal growth explicitly.

3.3 Microscopic fungal growth models

Microscopic fungal growth models describe growth within a single fungal cell or a small hyphal region. They have been widely used to validate growth hypotheses derived from experimental observations. Several microscopic models investigate the role of separate hyphal components, such as the cytoskeleton or the cell wall, on the overall growth. Similarly, other growth-related processes such as the turgor pressure and the effect of external factors have been studied through the use of such models. In the remainder of this section we will discuss some of the most relevant microscopic models.

Two main fungal growth theories at cellular level have been studied using microscopic models. The first one considers the extension of cells as the result of the turgor pressure inside the cell and the elastic properties of the cell wall (Wessels,

1986; Money, 1997; Steinberg, 2007). Ortega (1985) describes a model representing tip extension as the result of the aforementioned processes, based on an early model for plant cell elongation by Lockhart (1965). The latter model consists of a single ODE representing the cell elongation as the result of turgor pressure and the plastic cell wall extension, i.e. the irreversible wall extension:

$$\frac{dV}{V\,dt} = \Phi\,(P - P_c), \tag{3.5}$$

where V is the volume of the cell, Φ is the extensibility of the cell wall, and P and P_c represent the turgor pressure and the critical turgor pressure, respectively. Ortega (1985) extended the Lockhart equation (1965)to include elastic stretching of the cell wall, as such resulting in a simple, yet realistic, extended model of the extension of cells. Using a similar set of assumptions, the model proposed in Goriely and Tabor (2003) represents a single hyphal tip as a three-dimensional membrane using a system of PDEs. The membrane is composed of two materials, one able to stretch, placed at the apical dome, and a rigid material, resulting from the ageing of old wall material (also referred to as lysis). The membrane is filled with a viscous fluid under pressure that stresses the elastic material of the membrane, resulting in the expansion of the tip. The composition of the membrane is constantly reparametrized in order to keep elastic material at the apical dome which can then stretch further (see Figure 3.2(a)). By changing the reparametrization process at the membrane, this model is able to replicate different hyphal shapes observed *in vivo*, including those resulting from apical swelling (Figure 3.2(b)) and beading (Figure 3.2(c)).

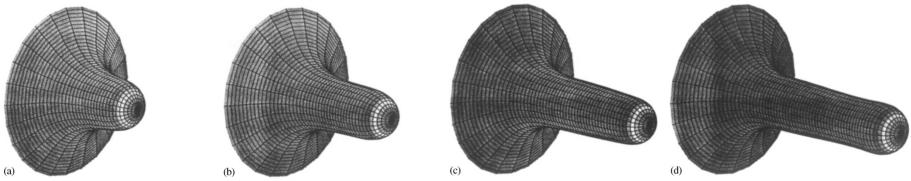

(a) Growth sequence

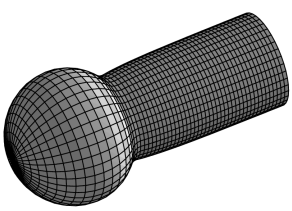

(b) Apical swelling

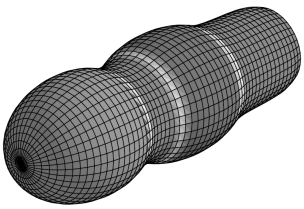

(c) Beading

Figure 3.2: Three-dimensional hyphal shapes simulated using the model proposed by Goriely and Tabor (2003): (a) growth sequence obtained from an initial spherical shape, (b) apical swelling and (c) beading obtained as the result of turgor preassure variations. (Source: Goriely and Tabor (2003))

A second growth theory relies on the concept of the vesicle supply center (VSC), introduced by Bartnicki-Garcia et al. (1989) (see Section 2.4.3) to simulate fungal tip growth. This theory states that the Spitzenkörper (see Section 2.4.2), placed at the tip of growing hyphae, acts as a VSC delivering wall-building vesicles to the tip wall. In order to test their hypothesis, Bartnicki-Garcia et al. (1989) constructed a mathematical model representing the VSC. This model simulates a single fungal cell evolving on a two-dimensional square grid. The VSC delivers vesicles to the cell wall, in all possible directions and as they impact the cell wall they are immediately added to it, as such increasing the cell surface. The VSC can either stay at a fixed location or move along a straight line. While the former results in an expanding circle, the latter generates a tubular shape (see Figure 3.3). The combination of both types of growth allows the replication of different parts of the fungus such as the sporangium, a sexual structure characteristic of some fungi, and growth processes such as fungal germination. Furthermore, Bartnicki-Garcia et al. (1989) provide evidence for the hypothesis about the role of the Spitzenkörper on the tip formation.

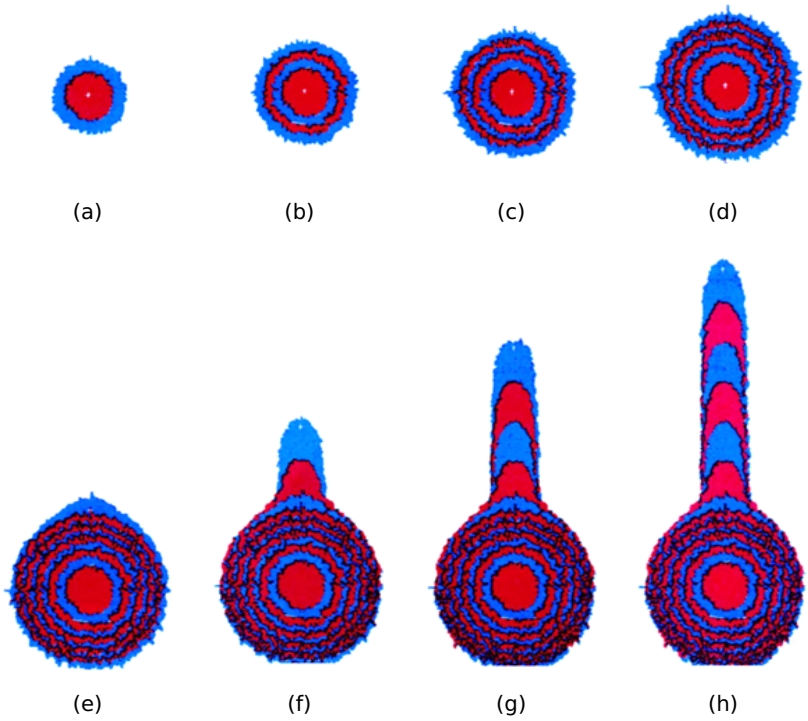

Figure 3.3: In silico spherical (a-d) and hyphal morphogenesis (e-h) obtained using the VSC model of Bartnicki-Garcia et al. (1989): (a-d) spherical growth simulated by random discharge of vesicles from a fixed VSC, (e-f) emergence of germ tube obtained by displacing the VSC toward the periphery, (f-h) elongation of the hyphal tube as the result of the continuous advance of the VSC. Each color band shows the growth obtained from the release of 8000 new vesicles. (Source: Bartnicki-Garcia et al. (1989))

A three-dimensional version of the VSC was modelled in Gierz and Bartnicki-Garcia (2001). This model relies on the same assumptions as its two-dimensional predecessor. The advance to three dimensions requires the imposition of a pattern of expansion on the cell wall. The three-dimensional derivation led to an indetermination whose solution required defining a priori the pattern of expansion of the cell wall, i.e. the overall spatial movement of the wall as new wall materials displace the existing wall. Consequently, three possible expansion patterns were studied, namely orthogonal, isometric and rotational (see Figures 3.4(b) and 3.4(c)). Orthogonal growth forces the new wall material to grow perpendicular to the existing wall surface. In the isometric expansion pattern, a new wall is forced to displace an existing wall evenly in all directions. The rotational pattern is obtained by imposing a fixed shape throughout the growth of the tip. The results obtained from the different expansion patterns suggest that *in vivo* hyphal growth falls in the category of the orthogonal expansion growth. The orthogonal growth pattern promotes growth at the very end of the tip which could be the result of the turgor pressure inside the cell, as such aligning the results of Gierz and Bartnicki-Garcia (2001) with other studies pointing to turgor pressure as driving fungal extension (Lockhart, 1965; Ortega, 1985; Goriely and Tabor, 2003).

The three-dimensional VSC model is further extended in Tindemans et al. (2006). Tindemans et al. (2006) claim that some of the assumptions made in the original VSC model are unrealistic. For instance, the isotropic behaviour of the VSC, supplying the same number of vesicles in all directions, would imply a ballistic vesicle motion contrary to experimental observations of *in vivo* hyphae. In addition, in the original VSC model, vesicles fuse immediately with the cell wall which seems to contradict *in vivo* observations. In response, Tindemans et al. (2006) developed the diffusive VSC (DVSC) model. Now, the vesicles diffuse freely in the cytoplasm of the cell after leaving the VSC (see Figure 3.4(a)). The DVSC model also includes a constant rate for vesicle fusion with the cell wall, referred to as the exocytosis constant. The tip shapes obtained with this new model are blunter when compared to those obtained using the original VSC model. In addition, the action of the exocytosis constant results in tips located closer to the VSC, compared to the VSC model where tips grow farther from the VSC. Therefore, the inclusion of these two new features results in a more realistic model still able to represent the essential features of tip growth.

In Eggen et al. (2011), the effects of turgor pressure and cell wall elongation are coupled with the VSC, as such combining both growth theories. The resulting model simulates the effects of cell wall ageing on tip growth in three dimensions. In this model, each part of the cell wall expands independently according to an expansion propensity that ultimately depends on its age. The expansion propensity extends the two cell-wall components, elastic and rigid, introduced in Lockhart (1965) and Goriely and Tabor (2003). Wall material becomes older over time but it can rejuvenate when it is in contact with new wall-building materials. This material

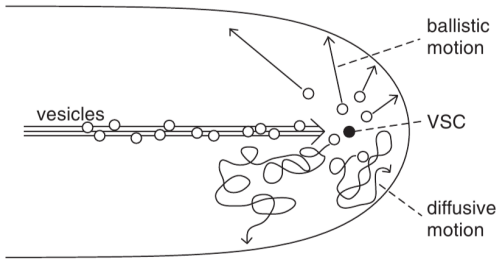

(a) Schematic representation of the VSC

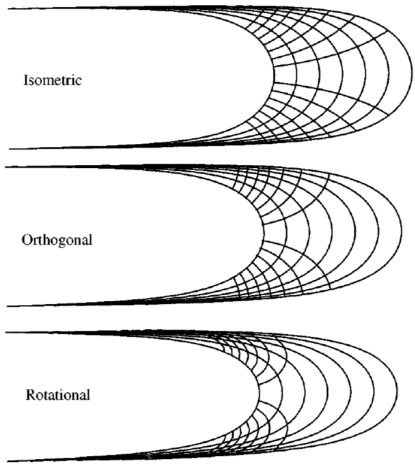

(b) Two-dimensional expansion patterns

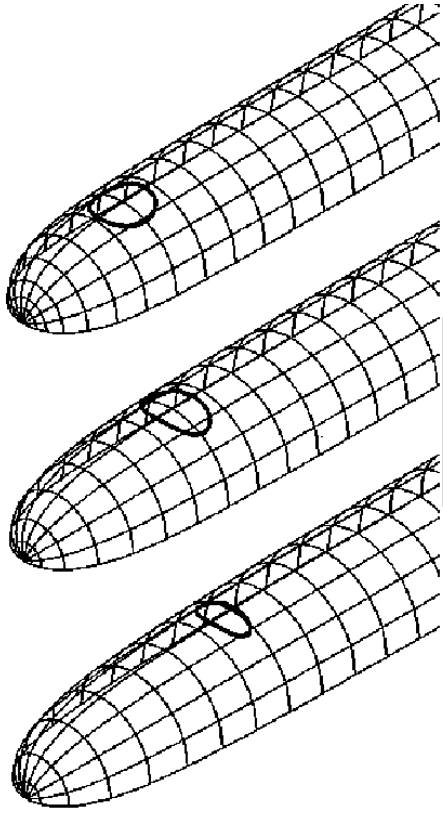

(c) Three-dimensional expansion patterns

Figure 3.4: Visual description of the theories used to develop three-dimensional VSC models: (a) schematic representation of the VSC and comparison of the ballistic and diffusive VSC models, (b) point trajectories and hyphal displacement for the isometric, orthogonal and rotational extension patterns in two dimensions (from top to bottom) and (c) growing hyphae obtained using these patterns of expansion. (Sources: (a) Tindemans et al. (2006) and (b-c) Gierz and Bartnicki-Garcia (2001))

is supplied to the cell wall in two different ways: using a simple geometrical model based on the curvature of the cell wall (more material is supplied to more strongly curved areas), and using a simplified version of the VSC model (more material is delivered to the surroundings of the VSC). Hence, still mimicking cell extension as the result of the vesicles supplied to the cell wall (Bartnicki-Garcia et al., 1989) instead of being just the result of turgor pressure. The results of this model show that by using this combined approach it is possible to obtain a wider variety of tip shapes than those obtained using other three-dimensional models (Gierz and Bartnicki-Garcia, 2001; Goriely and Tabor, 2003; Tindemans et al., 2006) (see Figure 3.5), as such demonstrating that the combination of both growth theories is not only possible but also more realistic.

Figure 3.5: Shapes obtained using the simple geometrical model proposed in Eggen et al. (2011) for different parameter combinations. (Source: Eggen et al. (2011))

A very different theoretical approach is presented in Denet (1996). In this model, the elongation of a single cell is simulated in response to a morphogen diffusing in the environment. For this purpose, a system of PDEs is employed and its numerical solutions lead to cylindrical shapes similar to the ones observed in fungal hyphae and cells such as neurons, as such suggesting that external factors also play a role in the fungal cell elongation.

Processes other than growth can also be mathematized using microscopic models. For instance, the transport of wall-building vesicles is modelled in Regalado and Sleeman (1999). It is known that the vesicles required for fungal growth are produced in different parts of the hyphae and then transported to the fungal tip along the cytoskeleton (see Sections 2.4.2 and 2.4.3). Therefore, Regalado and Sleeman (1999) model the cytoskeleton as a viscoelastic fluid responsible for the transport of wall-building vesicles. The cytoskeleton is represented as an elastic body whose deformation results in advective forces affecting the position of surrounding vesicles. A conservation equation represents the viscoelastic forces in the cytoskeleton:

$$m\frac{\partial^2 \mathbf{u}}{\partial t^2} = 0 = \nabla\left\{\left[\eta\,\tilde{\epsilon_t} + \xi\,\theta_t\tilde{I}\right] + \frac{E}{(1+\nu)}\left[\tilde{\epsilon} + \frac{\nu}{(1-2\,\nu)}\,\theta\tilde{I}\right] + \zeta\,c\tilde{I}\right\}, \tag{3.6}$$

where m is the cytoskeleton mass contained in a unit volume and $\mathbf{u}$ is the displacement vector of the cytoskeleton. η and ξ are the shear and bulk viscosity, respectively. E is the stiffness and ν measures how a strip of cytoskeleton compresses in one direction when it is stretched by a unit length in the perpendicular direction. $\tilde{\epsilon}$ is the strain tensor, θ is the dilation and $\tilde{I}$ is the unit tensor. ζ measures the intensity of the elastic deformation resulting from the interaction between the vesicles and the cytoskeleton. Finally, c represents the vesicles density which evolution is simulated using the following PDE:

$$c_t = \Delta D(\tilde{\epsilon})\, c - D_2 \nabla \mathbf{v}\, c. \tag{3.7}$$

Here, D is the diffusivity of the vesicles and $\mathbf{v} = \frac{\partial \mathbf{u}(r,t)}{\partial t}$ is the advective velocity. The number of vesicles displaced by the adjective forces is proportional to the vesicle density with proportionality constant D_2. The simulations with this model are able to replicate well-known hyphal phenomena such as aggregation (see Figure 3.6(a)) and the collapse of vesicles at the tips. Moreover, some of the studied scenarios result in the formation of two vesicles aggregation peaks (see Figure 3.6(b)), which confirms hypotheses on the formation of new apical branches after the loss of the Spitzenkörper (Harris, 2008).

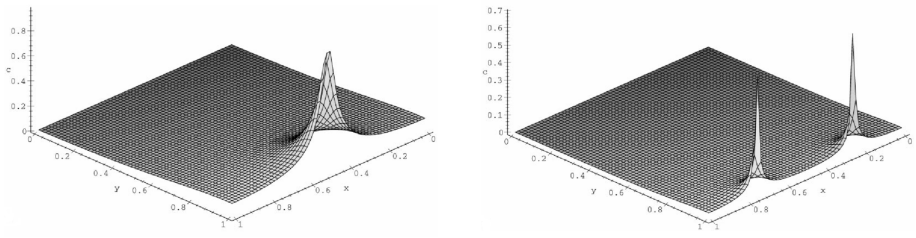

(a) Single vesicle aggregation peak (b) Two vesicle aggregation peaks

Figure 3.6: Stationary solutions obtained for the conservation equation introduced by Regalado and Sleeman (1999) representing the density of vesicles in two dimensions. (Source: Regalado and Sleeman (1999))

Finally, it is worth mentioning that microscopic models can also be employed to mimic fungal structures other than growing tips. For instance, a model representing the infection of rice by the fungus *Magnaporthe grisea* is introduced in Tongen et al. (2006). This fungus develops a characteristic structure that sticks to the rice leaves, the appressorium, in which an enormous pressure leads to a penetration peg through the rice cell walls, thereby infecting the rice plant. This model is able to reproduce some of the mechanical principles observed in the appressorium, which is represented as an elastic shell subject to turgor pressure.

Different microscopic models are capable of representing fungal cell extension mainly at the growing tip. These models are useful for the study of the role of microscopic processes driving the extension of tips, but are not able to capture the complexity of apical growth even at the hyphal level. For instance, the shape of the entire mycelium, the fungus' environment and the amount of substrate within the mycelium are key factors affecting fungal growth that can not be represented at the microscopic level. In addition, most microscopic models focus only on apical growth, as such not accounting for other important growth processes, like branching and anastomosis. Therefore, the scope of microscopic models is limited and they cannot be scaled up to represent the growth dynamics of even individual

fungal colonies.

3.4 Mesoscopic models of fungal growth

Growth at the level of the fungal colony has been studied using many mesoscopic growth models. Mesoscopic models study the evolution of the mycelium and the growth and interaction of all the hyphae composing the network. The features of fungal colonies at the mesoscopic scale can be captured with most imaging devices resulting in a significant amount of data that can be used to reinforce, calibrate and validate mesoscopic models. In addition, most mesoscopic models simulate growth as the result of several microscopic fungal processes, so they combine the knowledge obtained from different microscopic models. Furthermore, the morphology of the mycelium has an important role in macroscopic phenomena (e.g. infections (Stacey et al., 2001)), which can only be studied at the mesoscopic scale.

Two types of mesoscopic models can be distinguished. A first group of modellers envisions the fungal colony as a continuum, mimicking average features of the colony and its biomass evolution, while a second makes use of spatially explicit models. In this section we will summarize the most relevant mesoscopic models.

3.4.1 The fungus as a continuum

The foundation of continuous fungal growth models was established by Edelstein (1982). Her model combines apical growth, branching and hyphal lysis. Hence, the gain of biomass takes place only at the tips of the hyphae, where the tips diffuse and leave a trail of biomass. The fungus can generate new tips by lateral and/or apical branching, whereas the number of tips decreases due to tip-to-tip anastomosis, tip-to-hypha anastomosis and natural tip death. In addition, the hyphal biomass decreases as the result of hyphal lysis following from hyphal autolysis (natural hyphal death) and death as the result of an overcrowded environment. These processes are coupled in a system of two ODEs:

$$\begin{cases} \dfrac{\partial p}{\partial t} = n\,v - d, \\ \dfrac{\partial n}{\partial t} = -\dfrac{\partial n\,v}{\partial x} + \sigma. \end{cases} \tag{3.8}$$

where the first equation reflects the evolution of the hyphal density $p(x,t)$, in units of filament length per unit area, as the result of the tip extension with rate v, and the death of hyphae with rate d. The second equation represents the tip density

$n(x,t)$ (number per unit area) evolving as the result of tip diffusion and branching, formalized through the function $\sigma(n,p)$. By using different branching functions the model allows the replication of several fungal growth patterns resembling those observed *in vivo*. Yet, this model does not account for the interactions of the colony with the environment and the growth of the colony is steered by constant growth rates instead of the underlying biological processes.

The model formulated in Davidson et al. (1997) takes a completely different approach, modelling the spatial spread of the fungal colony in response to the nutrient concentration in the environment. For this purpose, Davidson et al. (1997) constructed a reaction-diffusion model representing the interaction between an activator $a(x,t)$ and a generic substrate placed in the environment $s(x,t)$. The activator is responsible for the conversion of substrate into energy, and subsequently into biomass, and decays at a constant rate μ. The activator also diffuses (D_a) and its production is autocatalytic, depends on the substrate and is computed using the constant conversion rate c_1. Substrate is replenished at a constant rate computed from the initial substrate s_0 and a constant g. It diffuses through the environment with diffusion constant D_s and is converted into activator based on a conversion constant c_2. All these processes are coupled in the following system of PDEs:

$$\begin{cases} a_t = D_a \Delta a + c_1 a^2 s - \mu a, \\ s_t = D_s \Delta s - c_2 a^2 s + s_0 - g s, \end{cases} \tag{3.9}$$

where $a_t = \frac{\partial a(x,t)}{\partial t}$ and $s_t = \frac{\partial s(x,t)}{\partial t}$, represent the evolution of activator and substrate, respectively. Different parameter combinations lead to steady state solutions of the reaction-diffusion system, typically representing oscillatory patterns. These growth patterns resemble those generated by fungi in nature (see Figure 3.7), assuming that the peaks of the activator correspond to peaks in fungal biomass. Despite its simplicity, this model is able to demonstrate the importance of the environment and the diffusion of substrate in the development of growth colonies. However, the model assumes that peaks of activator correspond to peaks in biomass, without a complete justification. In fact, Davidson et al. (1997) find limitations in this model, such as the inability to sustain uniform growth without reducing the capacity for substrate use in the interior.

Davidson (1998) further investigated the role of fungal nutrition on the overall shape of the mycelium. The fungus is now represented as a continuum of biomass, so the activator concentration is replaced by the fungal biomass density. In this new model, the substrate is divided into two categories: external substrate, available in the environment, and internal substrate, contained within the fungus. The external substrate can be taken up by the fungus, thereby becoming internal substrate. Within the mycelium, the internal substrate is translocated to meet the nutritional needs of the fungus and to produce new biomass. These assumptions

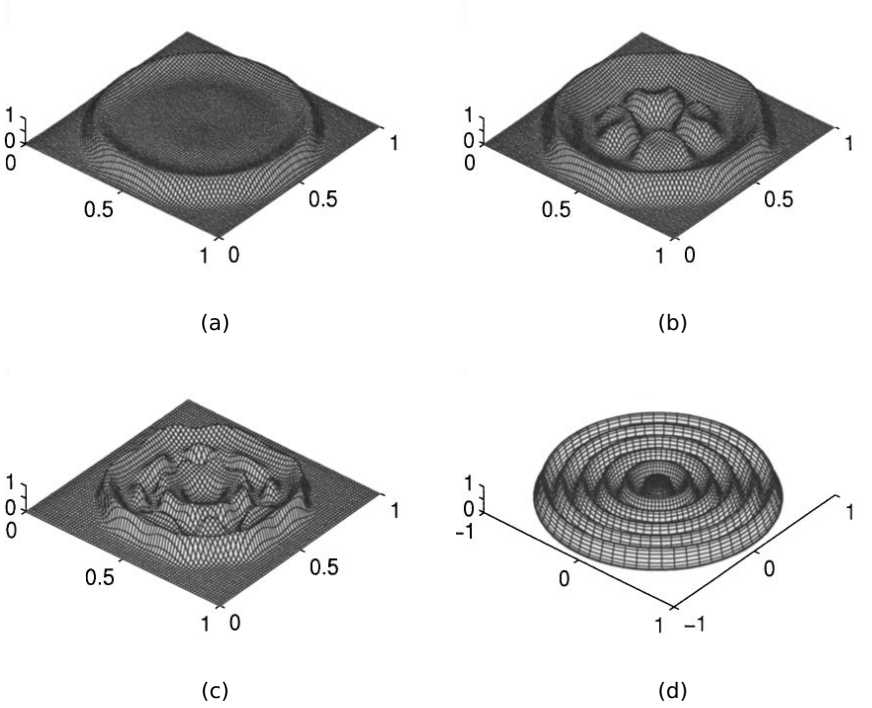

Figure 3.7: Different activator concentration patterns obtained with the model described in Davidson et al. (1997) for different parameter combinations. (Adapted from:Davidson et al. (1997))

are described by a system of three PDEs representing the evolution of the biomass density $m(x,t)$, the internal substrate concentration $s_i(x,t)$ and the external substrate concentration $s_e(t)$:

$$\begin{cases} \dfrac{\partial m}{\partial t} = \nabla(D_m s_i \nabla m) + c_1 m^2 \left(\dfrac{s_i}{k_1 + s_i} - m\right), & \text{(3.10a)} \\ \dfrac{\partial s_i}{\partial t} = \nabla(D_i m \nabla m) - c_2 m^2 \dfrac{s_i}{k_1 + s_i} + c_3 s_i \dfrac{s_e}{k_2 + s_e} - c_4 m (s_i - s_e), & \text{(3.10b)} \\ \dfrac{\partial s_e}{\partial t} = D_e \Delta s_e - c_5 \left(c_6 s_i \dfrac{s_e}{k_2 + s_e} - c_4 m (s_i - s_e)\right). & \text{(3.10c)} \end{cases}$$

In Eq. (3.10a), the transformation of internal substrate into biomass is expressed using Michaelis-Menten kinetics with constant k_1 and a conversion constant c_1. This equation also accounts for the biomass flux, which depends on the amount of internal substrate and takes place from regions with high to low hyphal concentration according to a diffusion constant D_m. The remaining two equations represent the change in internal and external substrate concentration, respectively.

In Eq. (3.10b), diffusion occurs inside the mycelium and therefore depends on the biomass density and diffusion constant D_i, while in Eq. (3.10c) the external substrates diffuses free in the environment according to D_e. Eq. (3.10b) and (3.10c) also account for the uptake of substrate, which is computed on the basis of the biomass density, since hyphae are responsible of substrate uptake, and depends on the amount of internal and external substrate with constants c_4 and c_5. In addition, the uptake process has a cost in internal substrate proportional (with constant c_4) to the amount of substrate taken up. Finally, the transformation of external substrate into internal substrate is calculated using Michaelis-Menten kinetics with constants c_3, c_6 and k_2. By using this model in an environment where the substrate concentration is spatially heterogeneous, Davidson (1998) are able to predict readily observable aspects of the development of mycelia. Furthermore, the numerical simulations replicate the growth patterns obtained in Olsson (1995), thereby providing further grounds to the hypothesis that mycelial growth in heterogeneous environments depends on substrate uptake and nutrient redistribution within the fungus.

The model proposed in Boswell et al. (2002) builds on the best of the Edelstein (1982) and Davidson (1998) models. For instance, it simulates the density of hyphae and tips as the result of fungal growth biological processes as in Edelstein (1982), while it also includes the effects of external and internal substrate as proposed in Davidson (1998). In addition, the model introduces the concept of inactive hyphae, an intermediate stage between fully active hyphae and dead hyphae. Hence, hyphal degradation occurs in two subsequent stages. The model consists of a system of PDEs representing the evolution of active hyphae m and inactive hyphae m', both expressed in $\mathrm{cm\,cm^{-2}}$, tips p expressed in number of tips per $\mathrm{cm^{-2}}$, and internal substrate s_i and external substrate s_e ($\mathrm{mol\,cm^{-2}}$):

$$\frac{\partial m}{\partial t} = v\, s_i\, p - d\, m, \tag{3.11a}$$

$$\frac{\partial m'}{\partial t} = d\, m - r\, m', \tag{3.11b}$$

$$\frac{\partial p}{\partial t} = -\frac{\partial}{\partial x}\left(v\, s_i\, p\right) + b\, s_i\, m - f\, m\, p, \tag{3.11c}$$

$$\frac{\partial s_i}{\partial t} = \frac{\partial}{\partial x}\left(D_i\, m\, \frac{\partial s_i}{\partial x} - D_a\, m\, s_i\, \frac{\partial p}{\partial x}\right) + c_1\, s_i\, m\, s_e - c_2\, v\, s_i\, p - c_4\, D_a\, m\, s_i \left|\frac{\partial p}{\partial x}\right|, \tag{3.11d}$$

$$\frac{\partial s_e}{\partial t} = D_e\, \frac{\partial^2 s_e}{\partial x^2} - c_3\, s_i\, m\, s_e. \tag{3.11e}$$

In the first equation, the generation of new active biomass is modelled via apical growth, which depends on the availability of internal substrate, the number of tips and a constant v. The active biomass becomes inactive at rate d and inactive biomass dies at rate m'. Tip density is modelled as in Edelstein (1982). Tips diffuse in order to generate new biomass and new tips are generated by branching. This process depends linearly on the amount of internal substrate and the total active biomass with rate b. In addition, tips can disappear due to anastomosis, which depends on the number of tips, active biomass and an anastomosis constant f.

To model substrate, Boswell et al. (2002) use a slightly different approach than Davidson (1998). Instead of using Michaelis-Menten kinetics, they argue that the amount of substrate taken up by the fungus depends linearly on the size of the mycelium, the internal and the external substrate concentration, modelled using a constant c_3 determining the amount of substrate taken up and a constant c_1 representing the cost of this process. In addition, internal substrate is partly translocated actively, and partly passively. While passive translocation is modelled as normal diffusion inside the mycelium (using constant D_i), active translocation occurs in the direction of higher tip density in order to deliver substrate to the more active areas of the mycelium using the diffusion coefficient D_a. Active translocation has a cost in internal substrate (c_4). Finally, as in Davidson (1998), external substrate diffuses free in the environment with diffusion coefficient D_e. In view of the results obtained by including passive and active translocation in the model, Boswell et al. (2002) are able to differentiate between two kinds of tips: exploring tips, at the periphery of the colony, and resource-exploiting tips. Hence, the model results suggest that passive translocation is used for exploration, while active translocation supports resource exploitation, as such agreeing with observations.

In Boswell et al. (2003), the model presented in Boswell et al. (2002) is adapted to represent fungal growth in two dimensions. This model succeeds in replicating the experimental results obtained in Jacobs et al. (2002) representing two growth scenarios: spatially homogeneous and heterogeneous substrate concentrations (see Figure 3.8). So, this model represents the best approach so far for simulating continuous fungal growth in heterogeneous environments.

The model constructed in Falconer et al. (2005) starts from the hypothesis of biomass recycling by fungal mycelia. This hypothesis states that fungi are capable of taking locally immobilized internal resources and remobilizing them, in order to redistribute and reuse these resources. The mycelium is represented by two types of biomass: immobile and mobile. The former is split between non-insulated hyphae, representing active hyphae able to take up substrate, and insulated, inactive hyphae hardly capable of taking up substrate. Non-insulated biomass increases by diffusion and it leaves a trail of insulated biomass as it grows. Mobile biomass is redistributed within the fungus by diffusion and it is produced as the result of substrate uptake. In addition, mobile biomass becomes immobile and vice versa according to constant rates. This approach results in a system of PDEs

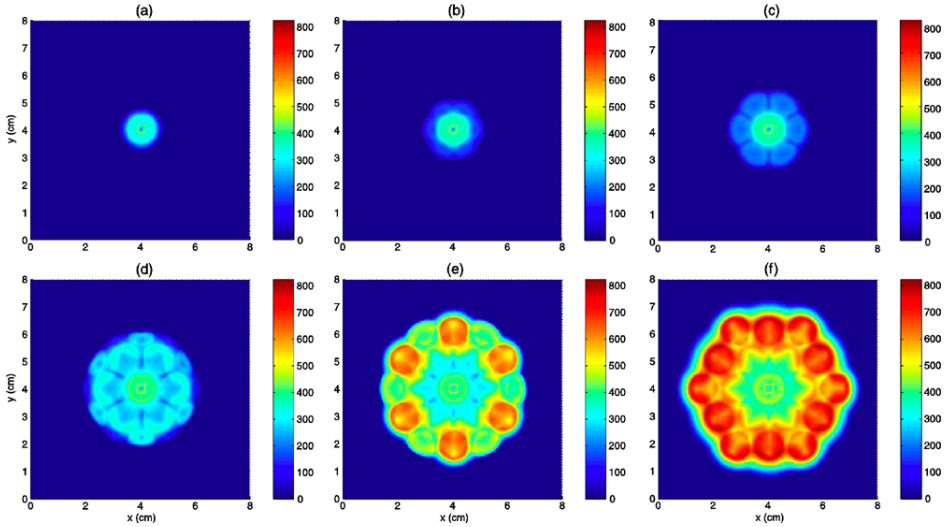

Figure 3.8: Total hyphal density (sum of active and inactive hyphal densities) in cm hyphae cm^{-2} computed from the model by Boswell et al. (2003) at (a) t = 1, (b) t = 2, (c) t = 3, (d) t = 4, (e) t = 5 and (f) t =6 days. The model equations were solved using initial data representing a substrate tessellation of 19 agar droplets. (Source: Boswell et al. (2003))

representing the dynamics of the non-insulated and insulated immobile biomass, mobile biomass and substrate.

This system of equations is solved across a two-dimensional grid representing a constant substrate replenishment scenario. Falconer et al. (2005) conclude that colony-scale features can be reproduced solely by fungal biomass recycling and colony-scale transport. In Falconer et al. (2008) the above mentioned model is extended in such a way that it includes a new PDE representing the evolution of a growth inhibitor secreted by the *in silico* fungus. Due to this extension, Falconer et al. (2008) are able to replicate the interactions between two fungal colonies over time in both two and three dimensions (see Figure 3.9). The interactions replicated include well-known phenomena such as coexistence and diffusion of different fungal strains, and domination and engulfment of a fungal colony over another. In addition, this model is used to predict the impact of different environments on fungal competition processes, such as deadlock and intermingling.

Models representing the mycelium as a continuum can be used to gain insights into the evolution of the fungal biomass over time and space. These models are often based on systems of ODEs or PDEs and mostly represent growth processes using reaction-diffusion equations. Their main advantage is that the underlying equations are well known and widely used to simulate similar biological processes. In addition, the results of these models are usually simpler than their explicit counterparts and can often be adapted to different dimensions without having to tune the equations. On the other hand, the equations used in mesoscopic continuous

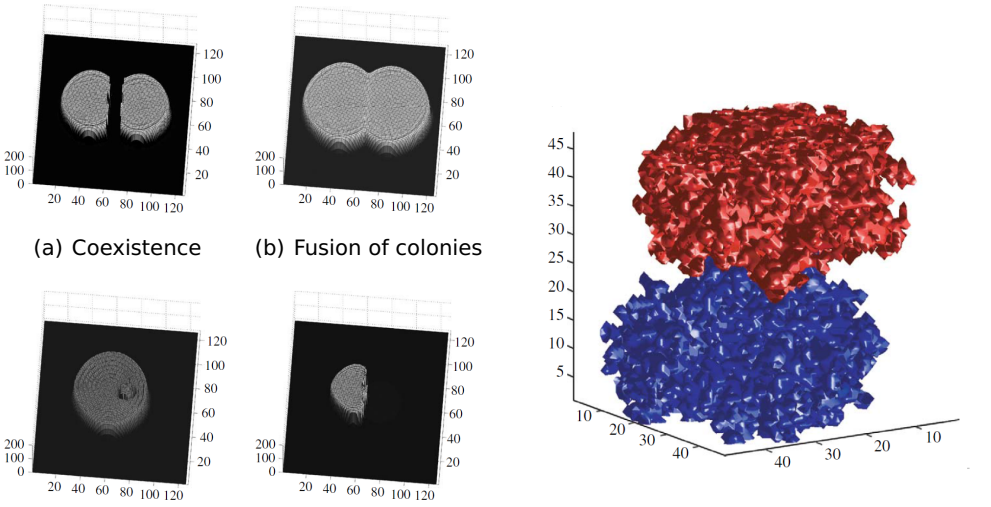

(a) Coexistence (b) Fusion of colonies

(c) Engulfment (d) Domination (e) Three-dimensional interaction of two fungal colonies

Figure 3.9: Fungal colony interactions obtained using the model by Falconer et al. (2008) using different parameter sets: (a) coexistence, (b) fusion of fungal colonies, (c) engulfment and (d) domination of a colony over the other, (e) mycelial distributions of two fungal colonies interacting in three dimensions. (Source: Falconer et al. (2008))

models are often difficult, if not impossible, to solve analytically, so one must turn to numerical methods. Since numerical methods rely on discretizations of space and/or time, using them to solve continuous models contradicts the principles of this modelling approach (Toffoli, 1984).

Some of the processes commonly simulated by mesoscopic continuous models strongly depend not only on the distribution of the fungal biomass, but also on the shape of the mycelium. For example, the shape of the mycelium is crucial to the translocation of nutrients occurring inside the fungal hyphae (Heaton et al., 2010). Finally, continuous models rely on densities and averages that not represent the shape of the fugal colony in full detail.

3.4.2 Spatially-explicit fungal growth models

Spatially explicit models represent the growth of fungal colonies by tracking the interaction and evolution of all the hyphae in the colony. These models often rely on a lattice to represent the growing hyphae and/or the growth environment as discrete entities. Other spatially explicit models represent hyphae as growing and interacting freely in two or three dimensions. These lattice-free models usually

divide each hypha into hyphal segments of the same length, and are also referred to in literature as vectorial models.

In Regalado et al. (1996) a model combining the principles from continuous and explicit approaches is presented. In this model a system of ODEs represents the evolution of a growth activator and an inhibitor diffusing in the two-dimensional space. The interaction of these two factors results in new biomass. The model also includes a source of substrate, which is converted into activator by the fungus, as such contributing to the biomass generation. By solving the system of ODEs over a two-dimensional square grid, Regalado et al. (1996) are able to explicitly represent the morphology of the mycelium (see Figure 3.10(a)). The sites of the grid that reach a certain biomass concentration are considered hyphae.

The fractal structure of the *in silico* mycelium is used to compare the results with *in vivo* fungal growth behaviour. Even though the fractal dimension of the simulated mycelium agrees with that observed for real world fungi, the square lattice jeopardises any resemblance with *in vivo* fungi. The model introduced in López and Jensen (2002) improves the mycelium representation by using a triangular lattice. Each cell in this lattice is either empty or occupied by hyphae, and occupied cells spread inhibitors by diffusion. At each time step, neighbouring cells of an occupied cell can become occupied depending on the growth probability. The latter is computed using the age of the neighbouring cells and the amount of inhibitor material in the cell. Despite its simplicity, this model is able to reproduce the dense colonies developed by *Aspergillus oryzae* (see Figure 3.10(b)), as such further demonstrating the possibilities of spatially explicit models.

The evolution of the mycelium is also studied in Boswell et al. (2007). In this model, the growth surface is meshed using hexagonal cells. The cells represent the initial configuration of external substrate on top of which hyphal growth is simulated. The hyphae are divided into hyphal segments of equal length connecting the centres of neighbouring hexagonal cells. Accordingly, apical growth is simulated as the adhesion of one hyphal segment to an existing tip. New segments grow predominantly along straight lines, but slight changes of the growth direction occur by the use of a biased random walk. New tips can be generated by dichotomous branching, resulting in the addition of two new segments. In order to account for the inactivation of hyphae, the model distinguishes between active and inactive hyphae. The former are able to translocate and uptake substrate but have a maintenance cost, whereas the latter take part in the translocation and die slowly, leaving space for new hyphae. Apart from the maintenance cost, growth processes also consume internal substrate. The change of internal substrate concentration in a cell is then the result of the uptake of external substrate, the consumption by the hyphae present in the cell (in order to grow and survive) and the translocation of internal substrate within the mycelium. Translocation is partly active, towards the tips, and partly passive, normal diffusion between neighbouring cells like in Boswell et al. (2002, 2003). By using this model, Boswell et al. (2007) simulate the

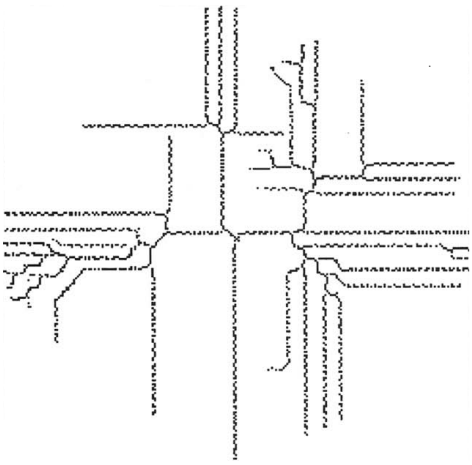

(a) Square lattice

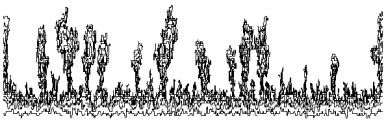

(b) Triangular lattice

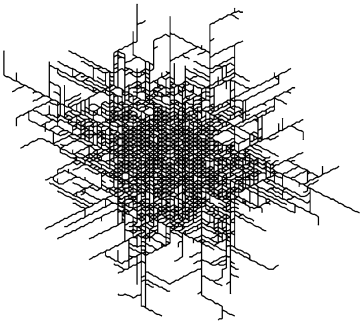

(c) Hexagonal lattice

Figure 3.10: *In silico* fungal mycelia obtained using lattice-based models in two dimensions: (a) model by Regalado et al. (1996), (b) by López and Jensen (2002) and (c) by Boswell et al. (2007). (Sources: (a) Regalado et al. (1996), (b) López and Jensen (2002) and (c) Boswell et al. (2007))

evolution of the mycelium in a more precise way than with their continuous model and succeed in evolving more realistic *in silico* fungal colonies than those obtained with the models by Regalado et al. (1996) and López and Jensen (2002). However, the restriction to two dimensions and the rigid structure imposed by the hexagonal lattice still leads to unrealistic results (see Figure 3.10(c)), hence leaving room for improvement. Therefore, this model is extended to represent three-dimensional growth in Boswell (2008).

This three-dimensional model is based on the same processes and assumptions, but uses a three-dimensional lattice based on layers of equally sized balls, named the face-centred cubic lattice (FCC). The balls are arranged in such a way that each ball has exactly twelve neighbours whose centres are located at the same distance from the original ball, i.e. two times the radii of a ball. As in the two-dimensional model, hyphae are represented by segments extending between the centres of neighbouring balls. By using this approach, Boswell (2008) succeeds in simulating growth in different environments (see Figure 3.11), and in complex soil structures. Even though this model represents the best attempt so far representing fungal growth using a lattice-based model, it is still inflexible due to the imposed lattice. It cannot be adapted to replicate different growth strategies or fungal species.

In the models implemented by Fuhr et al. (2011, 2012), the available substrate takes a central role, since it is used to construct an irregular lattice. Substrate

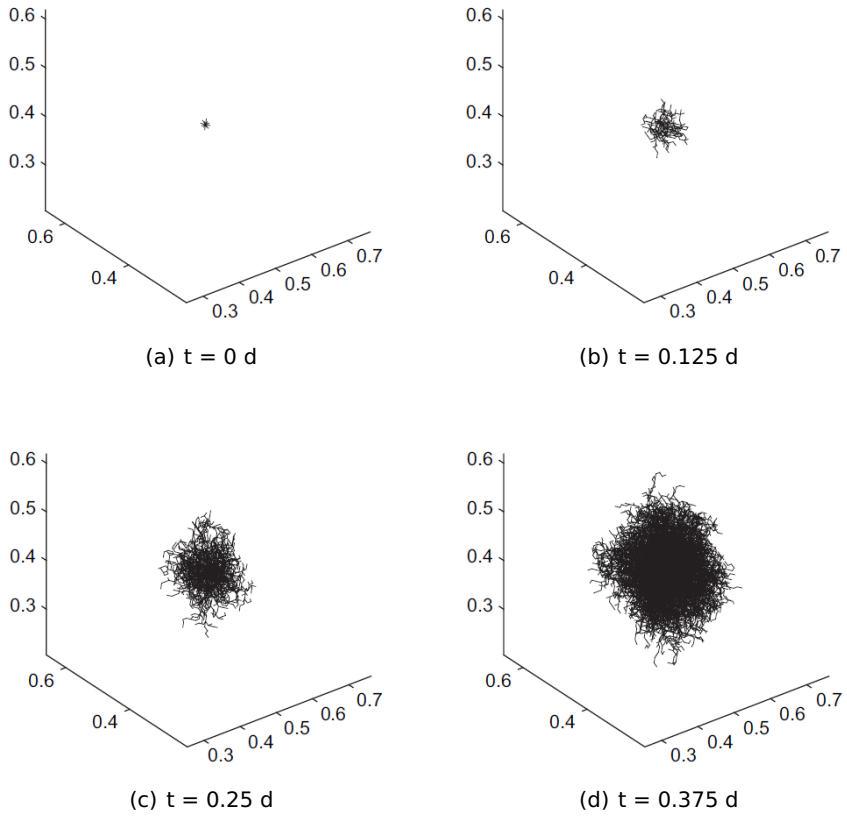

Figure 3.11: Hyphal biomass in an environment with uniformly distributed substrate and volume approximately 1 cm^3 evolved using the model by Boswell (2008) at t= 0 (a), 0.125 (b), 0.25 (c) and 0.375 days (d). (Source: Boswell (2008))

is represented as a set of nodes, placed in the environment and hyphae are represented as edges connecting neighbouring substrate nodes (see Figure 3.12(a)). Hence, the irregular lattice is constructed using the nodes representing the position of nutrients. At each time step, one hypha is able to grow, leading to the colonization of a new node. This growth event has a cost in terms of substrate that is subtracted from the node where the growth process started. In addition, a maintenance substrate cost is also subtracted from each colonized node. The direction of hyphal growth depends on the distance and orientation of the node containing the growing fungus to the reachable substrate nodes. Using this approach, Fuhr et al. (2012) are able to simulate two-dimensional growth on agar (Fuhr et al., 2012) (see Figure 3.12(b)) and inside a three-dimensional wood block (Fuhr et al., 2011). In the latter case, the wood block is represented as a square lattice of wood tracheids connected by pits full of nutrients represented by substrate nodes

(see Figure 3.12(c)). Therefore, fungal growth inside the wood block is restricted to the path created between neighbouring pits. Despite the simplicity of some of the model assumptions, the model constitutes a first attempt to simulate wood degradation and fungal growth explicitly in three dimensions (see Figure 3.12(d)). However, it is only able to describe general growth trends and not the detailed hyphal growth that can be expected from spatially explicit models.

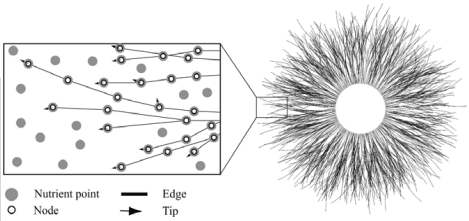

(a) Two-dimensional nutrient-based lattice representing agar

(b) *In silico* mycelium on a Petri dish

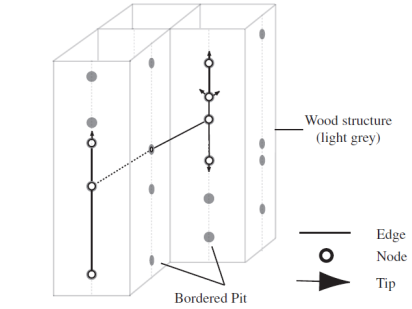

(c) Three-dimensional lattice based on wood structure

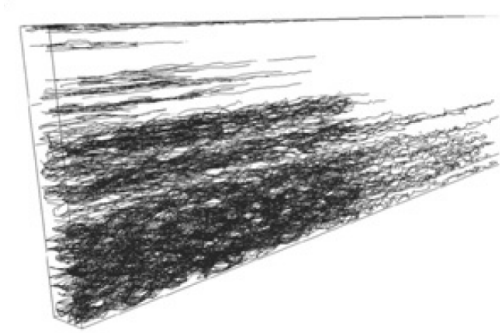

(d) *In silico* mycelium inside a wood block

Figure 3.12: Summary of irregular lattice-based modelling approaches for fungal growth in two and three dimensions by Fuhr et al. (2011, 2012). (a) scheme showing the elements of the two-dimensional lattice, (b) model results showing hyphal expansion after 0, 12 and 24 hours, (c) wood-based lattice and (d) *in silico* mycelium in a wood block after 2.5 days. (Source: (a-b) Fuhr et al. (2012),(c-d) Fuhr et al. (2011))

Established spatially explicit modelling approaches to study organisms like plants have also been used to simulate the growth of fungal colonies. For instance, in Soddell and Soddell (2005) a L-system, similar to those employed to model the growth of plants, was developed in order to simulate fungal growth. Here, an initial string (also known as an axiom) is rewritten at every discrete time step using a set of rewriting rules. Each symbol of the string represents a real object and its characteristics allow for its translation and consequent representation. In the case of the Soddell and Soddell (2005) model, the branching, extension and change of direction of hyphae are represented using a set of 15 rules, some of which are stochastic. In this way, the model imposes a growth path based on fixed rules. These rules are based on parameters extracted from growth experiments of *Geotrichum*,

a filamentous fungus. Despite its simplicity, this model is able to evolve fungal-like networks and to account for the fractal nature of fungal growth. Unfortunately, this model does not account for the effect of important processes such as fungal nutrition or anastomosis, as such resulting in unrealistic simulation outcomes.

An early lattice-free model simulating the growth of a filamentous fungus in a submerged culture was developed in Lejeune and Baron (1997). This model mimics the dynamics of individual tips that are able to extend freely in the three-dimensional space, while lateral branching is simulated as a stochastic process. Oxygen in the environment is consumed by the fungus only for growth, as such affecting the extension rate of the tips. Finally, the porosity of the environment is included in the model as a growth constraint. All together, this model amounts to a three-dimensional random walk of tips. It is able to describe the formation of a fungal colony from one or more fungal spores in three dimensions. Although this model neglects some crucial factors affecting fungal growth, especially those concerning fungal nutrition, it demonstrates the advantages of resorting to a lattice-free approach.

A more elaborated three-dimensional lattice-free model was introduced in Meškauskas et al. (2004b). This model simulates the growth at the tips using the so-called field concept. The field concept states that each point of the mycelium generates different fields as the result of autotropisms (such as tip avoidance) and tropisms generated by external factors (such as gravity or toxic metals). The tropisms affect the orientation of the growing tips that are attracted and repelled by different forces. In addition, tips are able to branch. This process depends mainly on branching parameters that can change during the course of the simulation, but also on the hyphal density of the surroundings. This model is capable of reproducing the most realistic growth patterns, according to the authors, who highlight the need for statistical methods to compare *in silico* and *in vivo* fungal colonies. By tuning the model parameters it is possible to obtain almost any imaginable fungal pattern including fungal fruiting bodies (see Figure 3.13). Although the patterns obtained with this model are impressive, the model overlooks almost all biological processes occurring within the mycelium, therefore simulating fungal growth as the result of parameter tuning instead of biological processes.

In Carver and Boswell (2008), a lattice-free two-dimensional model based on the biological processes driving fungal growth is constructed using the assumptions of Boswell et al. (2007). In order to get rid of the lattice, this model fixes the hyphal segment length and models the fungus as a collection of identical connected segments. Apical growth is simulated as the addition of new segments to existing tips. The position of a new segment is computed by only considering the growth direction of the parent segment and a noise term. Branching is modelled as a stochastic process and it results in the addition of two new segments These growth processes have a substrate cost. The substrate is constantly replenished at the centre of the colony and reaches the fungal hyphae via diffusion between neighbouring

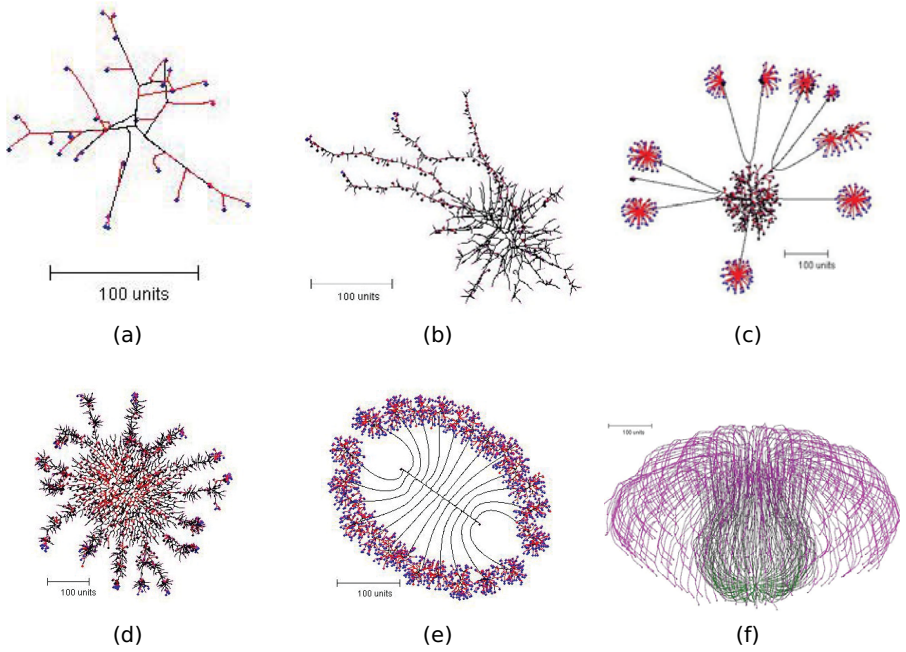

Figure 3.13: Diverse fungal patterns obtained with the lattice-free model introduced in Meškauskas et al. (2004b), including a fruiting body (f). (Source: Meškauskas et al. (2004b))

segments. Hence, this model does not include the external substrate, nor the active translocation or inactivation of hyphae included in Boswell's previous models (Boswell et al., 2007; Boswell, 2008). The simulations result in more realistic hyphae than those obtained with lattice-based models. Even though this model overlooks some crucial aspects of fungal development, especially the effects of the environment on the mycelium development, it demonstrates the possibilities of biologically-based lattice-free models.

A more advanced lattice-free model also based on the one of (Boswell, 2008) is presented in Hopkins and Boswell (2012). This model also represents the mycelium as a collection of connected segments, extending by apical growth and branching. Besides, it incorporates external substrate in the environment, which diffuses and can be taken up by the fungus and transformed into internal substrate. Internal substrate is translocated within the hyphal network by normal diffusion and active translocation in the direction of the growing tips as in Boswell et al. (2002, 2003). In addition, internal substrate is used to create new segments, and depending on the amount of internal substrate branching occurs or not. The growth direction of new segments is chosen using a velocity jump model where the tip velocity undergoes a biased circular random walk. A new feature of this model as compared to Carver and Boswell (2008) is the inclusion of an inhibitor secreted

by the fungus in order to represent hyphal avoidance. Therefore, the final growth direction is computed in two steps: first a preliminary value is obtained from the circular random walk, and then this value is corrected according to the inhibitor concentration in its surroundings. With this model, Hopkins and Boswell (2012) are able to simulate the effects that additional substrate has on the network shape (see Figure 3.14). According to the authors, several tropisms can be represented by changing the parameters of the random walk. This model is able to replicate fungal growth and substrate uptake as a result of biological processes, as such constituting one of the best approaches to date. Unfortunately, it restricts growth to two-dimensional space, contrary to *in vivo* fungal growth.

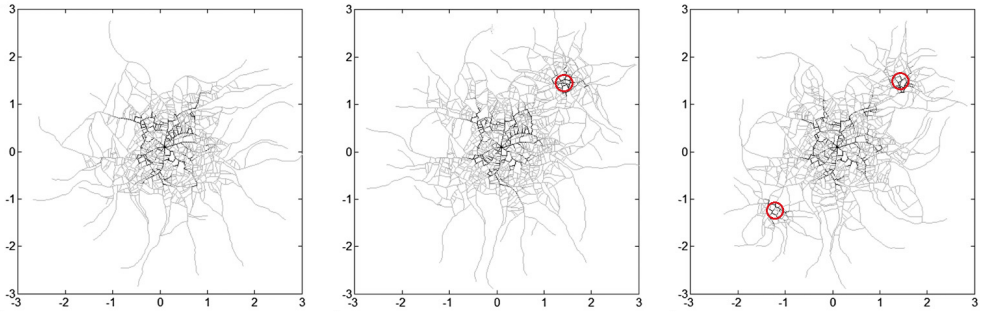

Figure 3.14: *In silico* mycelia obtained by Hopkins and Boswell (2012) model after two days: (a) without additional substrate sources, (b) with an additional substrate source placed at the top-right corner of the mycelium and (c) with two equidistant additional substrate sources. Darker line segments denote higher internal substrate concentrations and red circles denote supplementary resource sites. (Source: Hopkins and Boswell (2012))

In conclusion, spatially-explicit mesoscopic fungal growth models represent the best option to study fungal growth at colony level. These models lead to explicit representations of mycelia with more detail and accuracy than continuous models. Unfortunately, these models often rely on lattices that confine growth to unrealistic shapes (Regalado et al., 1996; López and Jensen, 2002; Boswell et al., 2007). Lattice-free models do not require the use of lattices, and are therefore able to replicate realistic growth patterns. However, these models often neglect crucial biological processes occurring in the mycelium (Meškauskas et al., 2004a; Lejeune and Baron, 1997), as such resulting in incomplete models. Moreover, most lattice-free models are constructed in only two dimensions even though growth is a three-dimensional process (Carver and Boswell, 2008; Hopkins and Boswell, 2012). Even those lattice-free models accounting for most fungal processes occurring within the mycelium are unable to reproduce the effects of external stimuli on the overall growth of the fungi, therefore leaving significant room for improvement.

PART II

EXTRACTING DATA FROM FUNGI

4

Unsupervised ridge detection using second order anisotropic Gaussian kernels

4.1 Introduction

Line detection is one of the most fundamental procedures of low-level image processing. Ridges (bright lines on a dark background) and valleys (the opposite) usually hold critical information for the analysis of images, especially for the extraction of graph-like structures. Such treatment plays a prominent role in many automated processes, such as photogrammetry and remote sensing (Tupin et al.,

This chapter has been published as: C. Lopez-Molina, G. Vidal-Diez de Ulzurrun, J.M. Baetens, J. Van den Bulcke, B. De Baets (2015). Unsupervised ridge detection using second order anisotropic Gaussian kernels. Signal Processing 116, 55-67.

1998; Laptev et al., 2000). Line detection is also relevant for the analysis of biological or biomedical structures, including vessels or bronchi profiling and measurement (Staal et al., 2004; Sluimer et al., 2006). Although such applications demand high-level information for accomplishing their goals, they usually rely on an initial phase of line characterization. In the remainder of this work, we refer to line detection as ridge detection, in order to align with the established nomenclature in the literature. Nevertheless, the adaptation of any ridge detection algorithm to valley detection is usually straightforward (see e.g. Cornelis et al. (2013)).

Together with edges and corners, ridges are the most studied low-level features in literature. The analysis of these three features is often coupled (Prewitt, 1970; Lindeberg, 1998). Also in this work we exploit the relationship between edges and ridges. This connection can be seen in many different ways, the most evident one being that a ridge is composed, at a very small scale, of two locally parallel step edges (Laptev et al., 2000; Paton, 1979; Chaudhuri et al., 1989). From an analytical point of view, edges are local maxima of the first order partial derivative of a signal, while ridges (respectively valleys) are local maxima (respectively minima) of the second order derivative[1]. Both notions can be formulated in similar terms through the local analysis of the Jacobian or Hessian matrices of an image, leading to an evident relationship between both features (Lindeberg, 1998; Jacob and Unser, 2004). An exhaustive analysis of this relationship can be found in Eberly et al. (1994); Haralick (1983) from a mathematical perspective, and in López et al. (1999) from a topological perspective. From this fundamental relationship, it seems clear that the strategies used for detecting edges and ridges basically differ in the order of differentiation applied to the original signal. In this work we elaborate on this relationship to produce a flexible ridge detector inspired by well-known first order differentiation kernels.

The analysis of edges and lines is so similar that there is some controversy on whether they are different concepts. This is partially due to the fact that no clear definition has been agreed upon for edges, leading to *ad hoc* or ground-truth-based characterizations (Lopez-Molina et al., 2013a). For example, Papari and Petkov assumed that the edges in an image are *the set of lines that human observers would consent on to be the contours in that image* (Papari and Petkov, 2011). Since some humans actually mark up lines as edges, they conclude that *every line in the image should be regarded as a contour, although none of the lines is a boundary between two regions of different colors or textures* (Papari and Petkov, 2011). Also relevant is the fact described by Canny that boundaries between polyhedral objects manifest themselves as lines (Canny, 1986), which is also demonstrated by the hybrid edge profiles presented by Perona and Malik (Perona and Malik, 1990). Similar observations have been reported for specific types of images, such as ultrasound scans (Czerwinski et al., 1999), in which edges between tissues mani-

[1] More detailed definitions of ridges can be found in the literature. We refer to (Lindeberg, 1998) or (Eberly et al., 1994) for deeper insights.

fest themselves as peaks in brightness. Despite such controversy, we adhere to the widely accepted assertions by Lindeberg (Lindeberg, 1998) on the characterization of edges and lines as maxima of the first and second partial derivative, respectively.

Ridge detection methods often rely on the analysis of the first or second derivative of the images, which is usually extracted by filtering the image with kernels (Haralick, 1983; Vlachos and Dermatas, 2010). Other ridge detection techniques impose certain conditions on the processing or the images, or even demand the intervention of humans (Laptev et al., 2000). For example, path optimization or tracking techniques call for either the semi-supervised introduction of the endpoints of the segments, or the inclusion of a critical initial phase of endpoint selection (Benmansour and Cohen, 2011; Rouchdy and Cohen, 2013). Although some authors advocate the need for human intervention (Laptev et al., 2000), we believe that this induces a severe, and often undesired, limitation for applied researchers. Alternatively, transformation-based methods (such as those using the Hough transformation) are not well conditioned to analyze complex scenes with intricate networks in which ridges merge, break and branch. An example of this can be seen in the LSD method by Grompone von Gioi et al. (Grompone von Gioi et al., 2008), in which edges are detected as relevant line segments in gradient magnitude images using the Hough transformation. Despite the visually impressive results, the detected edges do not match the exact position of the silhouettes in the original images, since the Hough transformation results in a simplification of their traces. In this work we elaborate on the use of elongated kernels for the characterization of the second partial derivative of an image. These kernels, created as a second partial derivative of the Anisotropic Gaussian Kernels introduced by Shui and Zhang (Shui and Zhang, 2012), are able to adapt to the local conditions of the ridges in terms of width, roundness and orientation. Moreover, we introduce a multiscale procedure that permits the fusion of the local results obtained with several kernels, so that the ridges at each region of the image are characterized by the most suitable kernels. Note that most authors of practical applications combine a phase of line detection with a subsequent phase of problem-aware line discrimination, which incorporates contextual knowledge. Such discrimination can be done in terms of the length of the ridge segments, their width or any other contextual hint, and involves very different classification techniques (see, e.g. Tupin et al. (1998); Staal et al. (2004); Zana and Klein (1999)). In our case, we propose a context-unaware method for line detection, which is further customized for its application to fungal branch delineation for in vitro growth tracking. This customization is tested on a new dataset containing 100 images of fungi with hand-made ground truth.

The remainder of this chapter is organized as follows. In Section 4.2, we review the use of Isotropic Gaussian Kernels (IGKs) of different orders in the literature. Section 4.3 covers the use of Anisotropic Gaussian Kernels (AGKs), which are further applied to a multiscale ridge detection algorithm in Section 4.4. Section 4.5

includes an experimental validation with a new dataset of in vitro fungal images. Finally, Section 4.6 discusses some conclusions.

4.2 Gaussian kernels for low-level feature detection

Gaussian kernels are one of the most employed tools for image processing, and have proven useful for a number of different tasks. The reasons for using such kernels range from their isotropy, steerability or decomposability properties (Freeman and Adelson, 1991; Poli and Valli, 1997) to the special characteristics related to their integration or differentiation. Additionally, the fast computation of their multidimensional extensions was given as an argument for their use during the early years of image processing (Canny, 1986). It is generally agreed upon that Gaussian kernels are a very convenient option for the robust computation of both the first and the second derivative of a discrete signal, and consequently for the computation of its Jacobian and Hessian.

The study of Gaussian kernels can be subdivided according to their order of differentiation. The zero-th order kernels (*i.e.* Gaussian kernels) are used for regularization prior to signal processing. The reasons are diverse, and include their ability to eliminate Gaussian noise (Canny, 1986) and the fact that they produce no new artefacts (maxima or minima of the first derivative) in the image (Babaud et al., 1986). They form the core of the most employed scale-space in the literature, the Gaussian Scale-Space (Lindeberg, 1998; Witkin, 1983; Lopez-Molina et al., 2014), and they have also been linked to other scale-spaces (Weickert, 1998). Another use is, for example, the approximation of the Laplacian of a signal by a difference of Gaussians (see Marr and Hildreth (1980)).

First Order Isotropic Gaussian kernels (FOIGKs) have been used extensively as well, especially after the results obtained by Canny (Canny, 1986). In his paper, Canny observed that the optimal kernel for 1D step edge detection under additive white Gaussian noise is similar to the negative first derivative of a Gaussian kernel[2]. Note that FOIGKs are not the only Gaussian kernels used for edge characterization. (e.g. the Laplacian of a Gaussian (LoG) kernel and its approximation (Marr and Hildreth, 1980)) A detailed review on the variety of usages of Gaussian kernels in the context of edge detection is included in Basu (2002).

Also Second Order Isotropic Gaussian Kernels (SOIGKs) are relevant for low-level feature computation. Apart from the aforementioned methods, the most evident use is the localization of ridges as maxima of the second derivative of an image.

[2]In fact, Canny quantified the difference of performance between the optimal 1D kernel and the negative first derivative of a Gaussian to be about 20% (Canny, 1986), in terms of his penalty criteria.

An early work by Chaudhuri *et al.* (Chaudhuri et al., 1989) elaborates on the idea of finding a pattern for blood vessel characterization and involves the convolution of the image with a range of oriented kernels created from Gaussian pulses. This work has been expanded by studying variations of the kernels (Liu and Haralick, 2002) or making a more elaborated use of the pixel-based information (Staal et al., 2004).

There are several known problems in the use of SOIGKs for the computation of the second partial derivative of a signal, which manifest themselves in the manner ridges are characterized. These problems, illustrated in Fig. 4.1, can be subdivided in two categories:

(i) Crossings and junctions: Filtering with SOIGKs reduces to computing the weighted difference between an oriented central segment and its parallel, neighbouring areas (Jacob and Unser, 2004). Hence, they rely on the idea that there should be background at both sides of the ridge candidate. However, such a background is not present in the case of crossings (Fig. 4.1, upper row) or junctions (Fig. 4.1, middle row), which might lead to broken or ragged edges. This effect manifests as near-zero second derivatives at the positions of the ridges.

(ii) Blobs: Circular, noticeable visual structures are relatively common in real images, either due to existing artefacts or contamination. Because of the isotropy of the SOIGKSs, blobs can fit in the positive region of the kernels, leading to very strong evidence of the presence of lines. An evident solution for this problem is to compute the presence of a line as the difference between the result of a filter in two orthogonal directions (see, e.g. Lindeberg (1998)). However, this solution would even further complicate the detection of crossings and junctions, as can be inferred from the image in the *Blob image* in Fig. 4.1, where the derivatives seem to indicate the presence of a vertical line.

We identify a common root for both problems, namely the non-elongated nature of the SOIGKs. Evidently, any kernel-based method must rely on the local manifestations of a global structure, which in this case is a line, but should also characterize the semi-local properties in the best possible manner. In the case of ridge detection, the semi-local properties relate to the straightness and continuity of line segments. We claim that kernels elongated in the (estimated) direction of the line segment are good candidates for capturing these semi-local properties.

There exists yet a third problem in ridge detection, which relates to the scale (width) of the ridges. Although ridges are possibly monoscalar in synthetic imagery, or very controlled scenarios, this is usually not the case in real images. Following the ideas of Bowyer *et al.* for edge detection (Bowyer et al., 2001), we assert that the essence of the complexity of a real image is that it typically contains

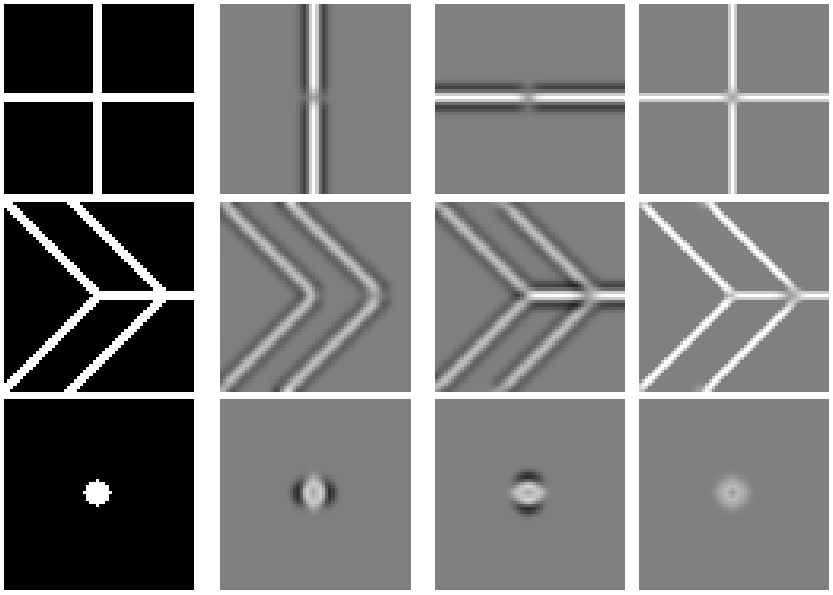

Figure 4.1: Example of images for which the Isotropic Gaussian Kernels produce an unsatisfactory characterization of the second derivative. The leftmost column contains the images (I), which are referred to from top to bottom as *cross image*, *junction image* and *blob image*. The central columns contain the visualization of the second derivative of the images in the horizontal (I_{xx}) and vertical (I_{yy}) direction, computed using second order isotropic Gaussian Kernels with standard deviation $\sigma = 1.0$. The rightmost column contains the maximum value in any possible orientation in $[0, 2\pi[$.

ridges of many different types, scales and curvatures. However, using non-optimal scales is less destructive for edge detection than it is for ridge detection. While in the former the poor fitting of the scale of a kernel leads to an imperfect interpretation of a signal variation (too sensitive, or too unresponsive), in the latter the interpretation can be absolutely unsuited. As an example, in Fig. 4.3(a) we observe a 1D signal containing three ridges of different width, as well as a double (twin) ridge. Figures 4.3(b)-(d) show the results of filtering the signal with three kernels of different scales, shown in Fig. 4.2. When using a high frequency kernel (such as $G''_{2.0}$), we obtain double maxima for the wide ridges, making it difficult to distinguish them from true double ridges. Alternatively, when using a low frequency kernel (such as $G''_{6.0}$), we are unable to individually locate each of the components of the double ridge in the right end of the signal. These problems are even more of an issue in the case of real signals, which might (and probably will) include imperfections and contamination. From this simple example, we may infer that the use of inadequate scales may lead to a poor interpretation of the ridges of an image. Since we anticipate the presence of ridges of different scales in any natural image, multiscale methods appear to be the only option to perform ridge detection in a reliable way.

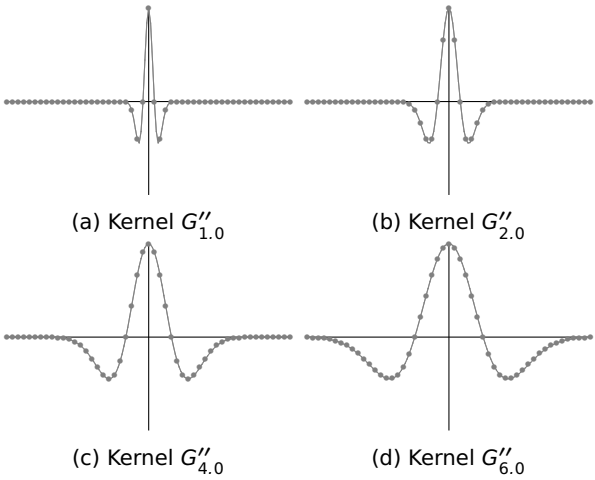

Figure 4.2: One-dimensional second order Gaussian kernels (G''_σ) generated with different standard deviations σ. The plotted lines represent the continuous function, while the dots illustrate the discrete filter selected from it.

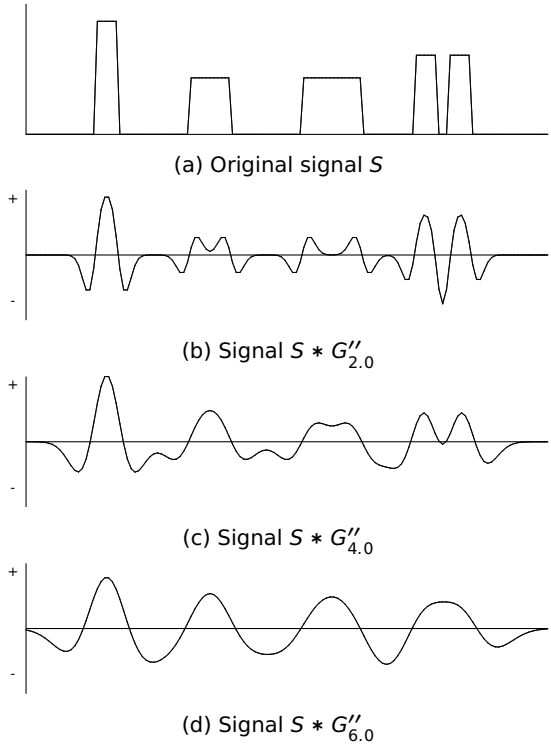

Figure 4.3: Visual example of the problem in misadjusting the scale of a line detection operator. The upper plot contains a signal with four ridges of different scales, while the lower ones include its filtering with the second order Gaussian operators in Fig. 4.2.

4.3 Anisotropic Gaussian kernels and their application in second order differentiation

Notwithstanding the influence of Canny's developments, he also lists some improvements that could be made to his own work, albeit not giving a detailed description of how to realize them. All of them involve the local adaptation of kernels to the particular conditions of each region of (or object in) the image. For example, Canny states that a differentiation kernel *should be oriented normal to the direction of an edge to be detected*, despite that information being, *a priori*, unknown. Additionally, Canny mentions the combined use of Gaussian kernels with different standard deviations, whose output would be later fused to create a single edge map. This idea is very similar to other proposals for feature synthesis in multiscale image processing (Witkin, 1983; Bergholm, 1987; Lopez-Molina et al., 2013b). Additionally, Canny also considers the use of elongated masks, which would exploit the fact that edges in an image are usually locally straight. In fact, in Canny (1986) it is forecast that *highly directional operators will give better results than operators with a circular support*.

In Shui and Zhang (2012), Shui and Zhang introduce a class of Gaussian differentiation kernels that support the ideas of Canny. This class of kernels, which the authors refer to as Anisotropic Gaussian Kernels (AGKs), generalize IGKs, and embody the improvements proposed by Canny (Shui and Zhang, 2013). The objective in Shui and Zhang (2012) is to create a class of kernels with non-circular support and to use their first order derivative to compute gradients in an edge detection procedure (we refer to the original paper for considerations on the noise robustness and contiguous edge detection). Two different aspects of the kernel are customized: the roundness of the kernel and its orientation. Moreover, since they are based on Gaussian kernels, their size can be controlled by the standard deviation of the underlying distribution.

A 2D Anisotropic Gaussian Kernel (AGK) in the two-dimensional Euclidean space is given by:

$$\hat{G}_{[\sigma,\theta,\rho]}(x,y) = \frac{1}{2\pi\sigma^2} e^{-\frac{\phi}{2\sigma^2}}, \tag{4.1}$$

with

$$\phi = \begin{bmatrix} x & y \end{bmatrix} M_{-\theta} \begin{bmatrix} \rho^2 & 0 \\ 0 & \rho^{-2} \end{bmatrix} M_{\theta} \begin{bmatrix} x \\ y \end{bmatrix},$$

and

$$M_{\theta} = \begin{bmatrix} \cos\theta & \sin\theta \\ -\sin\theta & \cos\theta \end{bmatrix},$$

where σ is the standard deviation of the Gaussian distribution, θ is the orientation

of the kernel and ρ is the so-called anisotropy index. Figure 4.4 contains several examples of such kernels. Although Geusebroek et al. (Geusebroek et al., 2003) introduced an alternative definition of AGKs by considering different standard deviations in two orthonormal directions (e.g. σ_x and σ_y), we employ the definition of Shui and Zhang (Shui and Zhang, 2012). This choice is due to the fact that the latter authors include an explicit representation of the roundness and orientation of the kernel, which facilitates its interpretation.

Shui and Zhang proposed to compute the partial derivatives of an image using First Order AGKs (FOAGKs), *i.e.* directional derivatives of the kernel in Eq. (4.1). In this way, the derivative of an image I in the direction θ is computed as

$$\frac{\partial I}{\partial v_\theta}(x,y) = -I * \frac{\partial \hat{G}_{[\sigma,\theta,\rho]}}{\partial v_\theta}(x,y) = -I * \frac{(x\cos\theta + y\sin\theta)}{\rho^{-2}\sigma^2}\hat{G}_{[\sigma,\theta,\rho]}(x,y)\,, \qquad (4.2)$$

where $*$ represents the convolution operation and v_θ represents the unit vector in direction θ. It should be mentioned that the differentiation in Eq. (4.2) is an ill-posed problem in the sense of Hadamard, since it depends on external parameters (σ, θ and ρ), and hence is likely not to yield a unique solution. This is a typical assumption in signal processing for discrete signals (Torre and Poggio, 1984; Poggio et al., 1989). Note also that, for $\rho \neq 1$, this class of kernels is not steerable, so that the differentiation in an arbitrary direction θ cannot be computed from the combination of kernels in fixed orthonormal directions (see Freeman and Adelson (1991) for further details on the concept of steerability). It is necessary to filter the image with a set of k kernels oriented in a variety of directions, as such leading to the characterization of the partial derivatives in k different orientations (asymmetry makes it unnecessary to apply filters in opposite directions). The most evident option to produce a single output from that information is to retain the result produced by the oriented kernel with the maximum absolute value, in contrast to Shui and Zhang's proposal to use the arithmetic mean of the derivatives computed with isotropic and anisotropic kernels (Shui and Zhang, 2012). Figures 4.4 and 4.5 contain several examples of FOAGKs with $\rho \neq 1$.

Given the applicability of FOAGKs to differentiation for edge detection, we argue in this paper that higher order AGKs can also be used for other tasks in image processing. More specifically, we propose the use of Second Order AGKs (SOAGKs) to produce second order derivative approximations that will subsequently be used to detect ridges in images. This idea follows the ridge definition by Lindeberg (Lindeberg, 1998), and hence identifies ridges from the analysis of the Hessian of the

Figure 4.4: 2D Representation of Anisotropic Gaussian Kernels (AGKS) with $\sigma = 1.0$. For each value of ρ we display the kernels with $\theta = 0$ (left) and $\theta = \frac{\pi}{4}$ (right).

Figure 4.5: 2D Representation of Anisotropic Gaussian Kernels (AGKS) with $\sigma = 2.0$. For each value of ρ we display the kernels with $\theta = 0$ (left) and $\theta = \frac{\pi}{4}$ (right).

images. The second derivative of an image I in the direction θ is computed as

$$\frac{\partial^2 I}{\partial v_\theta^2}(x,y) = -I * \frac{\partial^2 \hat{G}_{[\sigma,\theta,\rho]}}{\partial v_\theta^2}(x,y) = -I * \frac{\rho^2}{\sigma^2}\left(\frac{(x\cos\theta + y\sin\theta)^2}{\rho^{-2}\sigma^2} - 1\right)\hat{G}_{[\sigma,\theta,\rho]}(x,y)\,, \tag{4.3}$$

where the meaning of the parameters is as in Eqs. (4.1) and (4.2). The previous comments on the non-steerability of the FOAGKs, as well as those related to the ill-possedness of the problem, also hold for SOAGKs.

Note that some authors have employed Gaussian-based elongated filters for similar purposes. An example is the class of filters proposed by Poli and Valli (Cornelis et al., 2013; Poli and Valli, 1997), which are created by overlapping several Gaussian kernels shifted in a fixed direction. However, we believe that AGKs provide a simpler and more powerful basis for the study of ridge-like structures, avoiding non-evident parameters (number of filters, granularity of the shifting) and empowering the representativity of the properties of the ridge (orientation, roundness, size). In fact, if the parameters are meticulously tuned, the discrete kernels generated with SOAGKs and the filters in Poli and Valli (1997) become fairly similar, despite being constructed on the basis of different methods and having different objectives in mind.

Figure 4.6 includes a repetition of the results in Fig. 4.1 using anisotropic kernels instead of isotropic kernels. It is noticeable how the problems with the characterization of the crossing and the junction are reduced, while the blob produces a lower response than in Fig. 4.1.

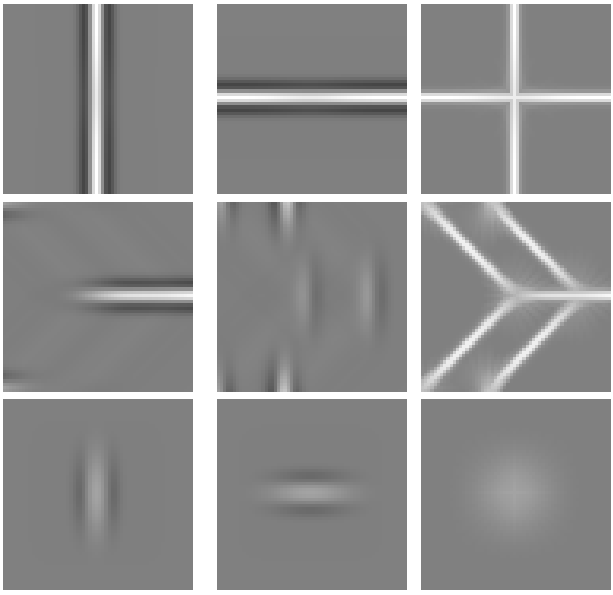

Horizontal der. (I_{xx}) Vertical der. (I_{yy}) Max. der.

Figure 4.6: Visualization of the second derivative of the images in Fig. 4.1 (I) in the horizontal (I_{xx}) and vertical (I_{yy}) direction, computed using second order anisotropic Gaussian kernels with $\sigma = 2.0$ and $\rho = 2$. The rightmost column contains the maximum value in any possible orientation in $[0, 2\pi[$.

4.4 A multiscale algorithm for line detection based on AGKs

This section describes a ridge detection algorithm based on second order differentiation. More specifically, it relies on non-steerable kernels as presented in the previous section. Let I be any scalar-valued (grayscale) image. A ridge candidate is a pixel (x, y) at which the second derivative in the direction ψ is a local maximum, where the direction ψ corresponds to that of the eigenvector associated with the largest eigenvalue of the Hessian of the image at that pixel (Lindeberg, 1998).

Hence, three tasks should be performed at pixel level: (a) locating the most likely direction of a ridge, (b) determining whether the pixel is a ridge center, and consequently a ridge candidate, and (c) estimating a ridge strength. Since we assume that the final output of a ridge detection algorithm should be a thin, binary map of ridges, a final phase of thresholding should follow, so that only the most relevant ridges are selected.

Let D, S and A be the sets of considered directions, scales and anisotropy indices for the generation of the SOAGKs, respectively. That is, $D = \{\theta_1, \ldots, \theta_k\}$, with $\theta_i \in [0, \pi[$, $S = \{\sigma_1, \ldots, \sigma_m\}$, with $\sigma_i > 0$, and $A = \{\rho_1, \ldots, \rho_n\}$, with $\rho_i > 1$. Our algorithm involves the following steps:

(S1) Filtering the image with each possible kernel created from the combination of θ_i, σ_i and ρ_i.

(S2) Retaining, for each pixel, the direction of the kernel producing the strongest response, as well as its value. These values are referred to as the *ridge orientation* and *ridge intensity* at each pixel, respectively.

(S3) Determining which pixels have a local maximum ridge intensity in their ridge orientation. Suppress all the pixels that have not. This operation is commonly known as Non-Maxima Suppresion, and is due to Rosenfeld and Thurston (Rosenfeld and Thurston, 1971).

(S4) Determining two thresholds for binarization using the double threshold determination technique by Liu et al. (Liu et al., 2013), which roughly consists of a dual, sequential application of the Rosin method (Rosin, 2001). This technique is preferred over more frequently used alternatives (as Otsu's method (Cornelis et al., 2013; Otsu, 1979)) since it is able to deal with monomodal histograms, instead of bimodal ones.

(S5) Applying hysteresis to generate the binary, thin ridge map.

A critical decision in the design of the algorithm is to retain uniquely the response and orientation of the filter generating the strongest response. This implies gathering, at each pixel, the result obtained by the filter which best matches a potential ridge, but at the same time it also maximizes (amplifies) the response to noise and image imperfections. An alternative consists in the use of an ordered weighted aggregation of the orientations in such a way that filters with stronger responses are assigned larger weights. Although this operator could be adapted from the regularization operators introduced by Kass and Witkin (Kass and Witkin, 1987), no author has tackled the development of such operators. Hence, we decided to stick to the selection of the result obtained by the filter with the strongest response.

An interesting point in the algorithm above is the fact that the same number of orientations is used irrespective of ρ_i, though this might in some cases cause a computational burden. For instance, if $\rho_i = 1$ the SOAGKs are steerable, and so the results in any orientation can be obtained as a linear combination of those of any other orthogonal ones. Yet, there is a threefold reason why our algorithm always uses the same number of orientations. Firstly, although we can intuitively link the need for more directional filters to the increase of ρ_i, there is no clear way of grading steerability with regard to that parameter. Secondly, setting a variable

number of directions depending on the value of ρ_i would increase the complexity of the algorithm. Thirdly, the current formulation simplifies the algorithm as much as possible, and enables clear options for parallel computing.

Our algorithm has some clear advantages stemming from combining the results of different filters, which can be configured in terms of size, orientation and anisotropy. Firstly, it considers a wide variety of ridge widths and curvatures, in an attempt to adapt to the local conditions of the image. As an example, Fig. 4.7 shows the result of applying a multiscale fusion procedure to the results of the three kernels used in Fig. 4.3. We observe that the combination by means of the maximum yields better results than those obtained by using individual kernels, since each of the ridges generates a unique maximum in the resulting filtered signal. Moreover, not requiring a unique kernel for computing the second derivative simplifies the configuration by non-expert users. Secondly, the algorithm is computationally cheap, since matrix filtering procedures are greatly accelerated by hardware, and can be easily distributed on parallel machines. Thirdly, it is worth noting that our algorithm generalizes other proposals in the literature. For example, by fixing a single scale ($|S| = 1$) and avoiding anisotropic kernels ($A = \{1\}$), we recover the proposal by Chaudhuri (Chaudhuri et al., 1989).

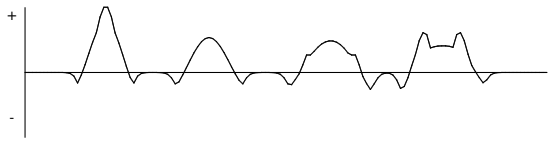

Figure 4.7: Replication of the results in Fig. 4.3 using a multiscale procedure. In this case the results using three filters ($G''_{2.0}$, $G''_{4.0}$ and $G''_{6.0}$, as in Fig. 4.3(b)-(d)) are combined using the maximum.

4.5 Experimental validation

In this experiment we validate our proposed ridge detection algorithm. More specifically, we measure the impact of using anisotropic, multiscale Gaussian kernels for ridge detection in real imagery, i.e. whether the use of non-isotropic kernels at different scales leads to significant improvements over established procedures based on monoscale, isotropic Gaussian kernels.

Here, the result of a ridge detection method has to be expressed as thin, binary lines. Note that other tasks or applications impose different representations of the results, which might enclose information other than the presence and location of a ridge. For example, in Benmansour and Cohen (2011); Rouchdy and Cohen (2013) the width of vessels (or, equivalently, the position of their boundaries) is of major importance, to the point that their success is measured as the overlapping of their results with hand-made segmentations. In our case, we focus on line

detection for tracking the growth of fungi, and the only information of interest is the position of the centerline (i.e. the presence of the ridge) and the preservation of the interlacing structure (junctions, crossings, short tips, etc.).

4.5.1 Automated characterization of fungal structure

The automated processing of biological imagery has gained momentum in the past years (Peng, 2008). The main reason is, as in many other applied fields, the availability of cheap imaging and processing equipment. One such field is fungal technology (see the review by Falconer et al. (Falconer et al., 2010)). For instance, the scale at which fungi grow allows for the extraction of numerous high definition images using standard flatbed scanners. However, experts often encounter difficulties in selecting or customizing methods to effectively and efficiently process the imagery obtained in the labs (Obara et al., 2012).

Most fungi are composed of a vegetative body, called the mycelium, formed by a network of cylindrical thread-like structures, referred to as hyphae. The complex organization of these networks allows for an efficient internal transport of nutrients within the fungus. Both the productivity of industrial processes involving fungi and the decay rate of the different species of fungi depend on the morphology of the network (Barry et al., 2009b; Fuhr et al., 2011; Grimm et al., 2005; Papagianni, 2004). Consequently, there exists a strong demand for robust methods that are able to extract these networks without fine-tuning. Some of the techniques currently in use involve manual labeling of the hyphal network (Heaton et al., 2010; Trinci, 1974), local techniques (Diéguez-Uribeondo et al., 2004; Bolton and Boddy, 1993) or invasive techniques, which do not allow scientists to follow the evolution of the entire hyphal network (Barry et al., 2009a). These techniques are also highly time-consuming and tedious.

For this experiment, we introduce a dataset of 100 images, referred to as Ghent University Fungal Images 1 (GUFI-1), which were extracted from fungi grown in vitro. Each of the images has a resolution of 300×300 pixels, and comes together with their hand-labeled solution, which is taken as ground truth. Images from five fungal species at different growth stages were taken. These species include some of the main organisms responsible for wood decay (*Coniophora puteana*); plant pathogens (*Phanerochaete velutina*, *Rhizoctonia solani*); and fungi commonly used in industry (*Penicillium chrysogenum*) and bioremediation (*Trichoderma viride*). From the perspective of ridge detection, these images constitute a challenge since they contain a diversity of ridges with different widths, different degrees of contamination (often related to the growth stage) and frequent overlaps/junctions. Moreover, images often include large regions without edges. In Fig. 4.8 we depict the first 12 images in the dataset, together with their ground truth. In this subset one can already observe a large variety in ridge width, overlapping, density, etc.

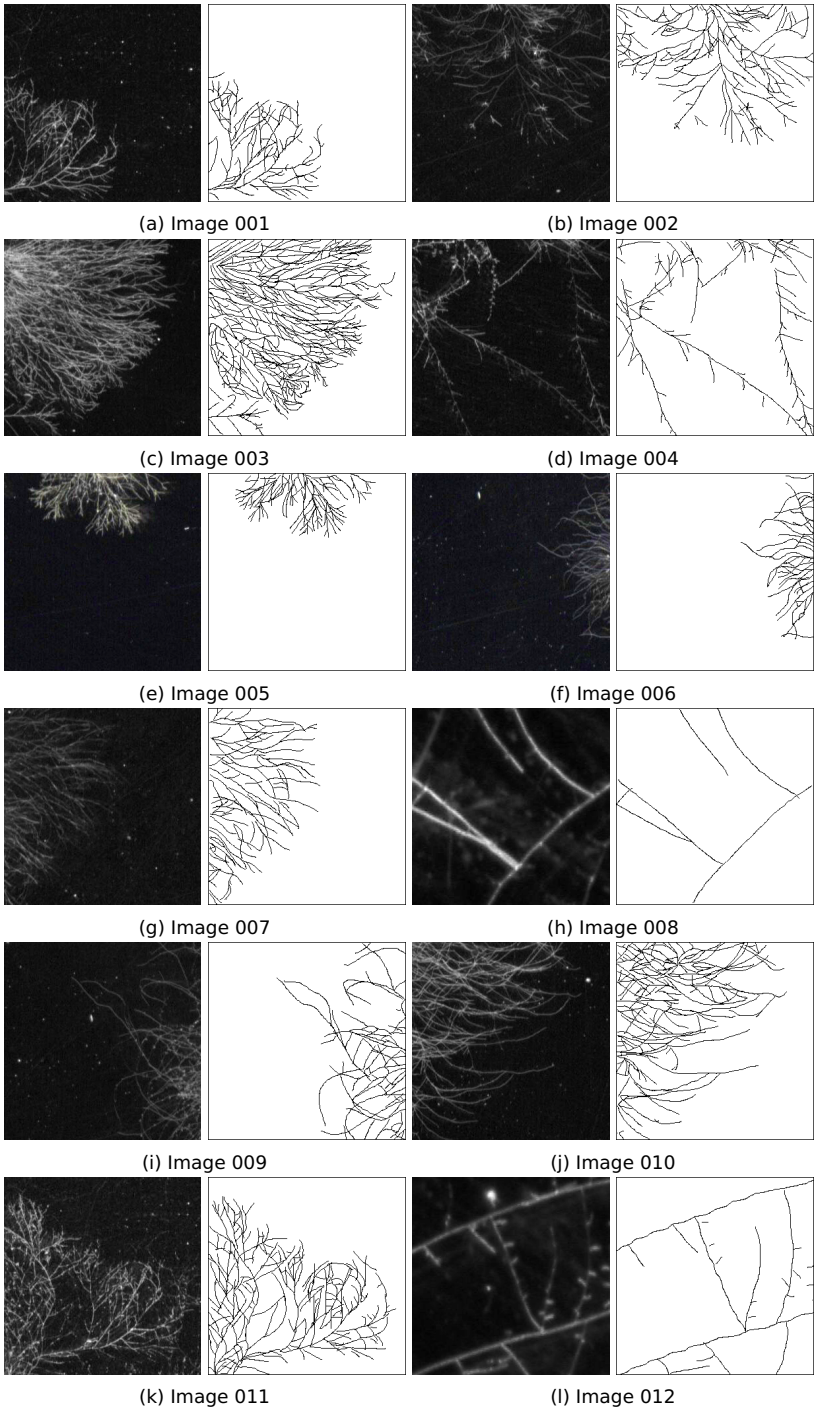

(a) Image 001 (b) Image 002

(c) Image 003 (d) Image 004

(e) Image 005 (f) Image 006

(g) Image 007 (h) Image 008

(i) Image 009 (j) Image 010

(k) Image 011 (l) Image 012

Figure 4.8: Some of the images in the Ghent University Fungal Images 1 (GUFI-1) dataset, together with their hand-labelled solutions, which are to be taken as ground truth. The original images are normalized for better visualization.

4.5.2 Error quantification

Quality evaluation of binary feature imagery is not an obvious task. Although it reduces to comparing a given ground truth image (I_{gt}) with a candidate image (I_{cd}), the task is strongly dependent on the interpretation of the images (see, e.g., the monographs on segmentation (Zhang, 1996) or edge detection (Lopez-Molina et al., 2013a; Peli and Malah, 1982)). Since no single measure is able to cope with all the requirements needed to meaningfully measure the quality of this type of image (see the results in (Lopez-Molina et al., 2013a)), we have opted to combine two different measures:

(i) Firstly, we use the approach by Martin et al. (Martin et al., 2004), which is grounded in the fact that any binary feature image can be seen as the result of a binary classification problem. Hence, the comparison between I_{gt} and I_{cd} can be formulated in terms of success and failure in the detection of ridges. However, the ridges in the automatically generated image might be slightly displaced from their position, and this should not result in both a false positive and a false negative. In order to overcome the problem of displacements, Martin et al. use a stage of pixel-to-pixel correspondence (with a certain spatial tolerance) between the ridges in the automatically generated image and the ground truth image[3]. From this correspondence a proper binary confusion matrix is computed, from which the *precision* (Prec) and *recall* (Rec) evaluations are computed as

$$\mathrm{Prec} = \frac{\mathrm{TP}}{\mathrm{TP}+\mathrm{FP}} \quad \text{and} \quad \mathrm{Rec} = \frac{\mathrm{TP}}{\mathrm{TP}+\mathrm{FN}}\,, \tag{4.4}$$

where TP, FP and FN are the percentages of true positives, false positives and false negatives, respectively. The overall quality of a solution can be expressed in terms of the F-measure (F_α), given by

$$\mathrm{F}_\alpha = \frac{\mathrm{Prec}\cdot\mathrm{Rec}}{\alpha\,\mathrm{Prec}+(1-\alpha)\,\mathrm{Rec}}\,, \tag{4.5}$$

for which we have considered the common $\alpha = 0.5$. Other values of α can be considered when intending to emphasize the penalization of FP or FN.

(ii) Secondly, we use Baddeley's Delta Metric (BDM) on the space of binary images. This measure considers the dissimilarity of the subsets of *featured* points in the image, which are usually represented by the value 1. As we assume the ridges to be expressed as binary lines, this measure can be used

[3] We have used the pseudo-optimal implementation of the Cost Scaling Algorithm (Goldberg and Kennedy, 1995) provided within the BSDS (Martin et al., 2004; Arbelaez et al., 2011).

for our purposes. Assuming I_{gt} and I_{cd} have the same dimensions $M \times N$ (with $\Omega = \{1, \ldots, M\} \times \{1, \ldots, N\}$), and given a value $1 < k < \infty$, the k-BDM between I_{gt} and I_{cd} (denoted $\Delta^k(I_{gt}, I_{cd})$) is given by:

$$\Delta^k(I_{gt}, I_{cd}) = \left[\frac{1}{|\Omega|} \sum_{p \in \Omega} \left| w(d(p, I_{gt})) - w(d(p, I_{cd})) \right|^k \right]^{\frac{1}{k}}, \tag{4.6}$$

where $d(p, X)$ represents the distance from the position p to the closest *featured* point of the image X and $w : [0, \infty] \rightarrow [0, \infty]$ is a concave, increasing function used for weighing. In our experiments, we use the Euclidean distance in the computation of d. Hence, $d(p, X)$ stands for the minimum Euclidean distance from the position p to a ridge in X. Moreover, we use $w(x) = \min(x, t)$, where t is the maximum displacement allowed in a ridge, and $k = 2$, as in Medina-Carnicer et al. (2009).

Note that both techniques involve a common parameter: the displacement a ridge can suffer before it becomes a false detection. In the case of $F_{0.5}$, this manifests itself as the maximum distance allowed in the pixel-to-pixel correspondence, while in BDM it is represented by the parameter t. Here, we have set such distance to 2% of the length of the image diagonal.

4.5.3 Experimental procedure

Any real-world application demands a customization of standard algorithms, such as the one in Section 4.4. In fact, application-oriented works tend to include customizations such as problem-aware regularization (Weickert, 1999) to, e.g., machinery-dependent brightness correction (Lam et al., 2010) or context-aware topological considerations for irrelevant feature removal. We have avoided any treatment other than Gaussian smoothing in order not to obscure the impact of the differentiation filters. For this experiment we have adapted the procedure in Section 4.4, giving rise to Algorithm 1. The purpose of this algorithm is threefold. First, the algorithm must produce a thin, binary ridge image in a fully unsupervised manner. Second, the bright ridges must have prevalence over the dark ones. Third, the connectedness of the extracted graph must be maximized. Consequently, broken or isolated edges must be avoided. The necessity of this third step is directly related to the quality of the data, especially to the appearance of contaminated pixels. Because of the characteristics of the images in the GUFI-1, we employ a morphological closing operation (to fill one-pixel long discontinuities) followed by a clean-up of the segments shorter than 10% of the image diagonal. Despite this clean-up might look drastic, it should be noticed that the appearance of short or broken branches might hinder the analysis of the overall fungal structure, and hence are better removed.

Algorithm 1: Algorithmic representation of the proposed multiscale ridge detection algorithm.

Data: An image I, parameter sets D, S and A, a smoothing parameter ϕ
Result: A binary ridge map B
$I_{\text{ridge}} \rightarrow$ Zero-valued image;
$I_{\text{ori}} \rightarrow$ Null-valued image;
$I * G_\phi \rightarrow I_s$ (Smoothed image);
for *each combination of* $\theta \in D$, $\sigma \in S$ *and* $\rho \in A$ **do**
  Compute $\frac{\partial I_s}{\partial v_\theta}$ as in Eq. (4.2);
  for *each pixel* p **do**
    if $|\frac{\partial I_s(p)}{\partial v_\theta}| \cdot I_s(p) > I_{\text{ridge}}(p)$ **then**
      $I_{\text{ridge}}(p) \leftarrow |\frac{\partial I_s(p)}{\partial v_\theta}| \cdot I_s(p)$;
      $I_{\text{ori}}(p) \leftarrow \theta$;
  Suppress non-local maxima from I_{ridge};
  Compute thresholds T_{high}, T_{low};
  Apply hysteresis on I_{ridge} using T_{high}, T_{low};
  Apply morphological closing with 3×3 structuring element;
  Delete segments shorter than 10% of the length of the image diagonal;

In this experiment we have compared eight different configurations of Algorithm 1, featuring various instances of the parameter sets A and S, as shown in Table 4.1. These configurations include combinations of mono- and multiscale kernels, as well as isotropic and anisotropic ones. The set of discrete directions is kept the same for all configurations $D = \{0, \frac{pi}{16}, \ldots, \frac{15\pi}{16}\}$.

Method	Scales	Anisotropy indices
SI_1	$S = \{1\}$	$A = \{1\}$
SI_2	$S = \{2\}$	$A = \{1\}$
SI_3	$S = \{3\}$	$A = \{1\}$
SI_4	$S = \{4\}$	$A = \{1\}$
MI	$S = \{1, \ldots, 4\}$	$A = \{1\}$
SA_1	$S = \{1\}$	$A = \{1.3\}$
SA_2	$S = \{2\}$	$A = \{1.3\}$
SA_3	$S = \{3\}$	$A = \{1.3\}$
SA_4	$S = \{4\}$	$A = \{1.3\}$
MM_1	$S = \{1, \ldots, 4\}$	$A = \{1.0, 1.1, \ldots, 1.5\}$
MM_2	$S = \{2, \ldots, 4\}$	$A = \{1.0, 1.1, \ldots, 1.5\}$

Table 4.1: Configurations of Algorithm 1 used in the experimental comparison.

4.5.4 Analysis of the results

The results of comparing different configurations of the algorithm are shown in Table 4.2, organized according to the value of the standard deviation of the smoothing filter (ϕ). For each configuration and ρ, we display the results in terms of Baddeley's Delta Metric (Δ^2), F-measure ($F_{0.5}$), precision (P) and recall (R).

There are several conclusions to be drawn from the data in Table 4.2. First, we observe that monoscale, isotropic methods perform worse than any other possible configuration of the algorithm, especially for low values of σ. This holds either in terms of Δ^2, which accounts for the location of the ridges in the image, or in terms of $F_{0.5}$, which penalizes broken or ragged ridges. This is explained by the facts discussed in Section 4.2, and also by the relatively low quality of the real imagery. It is noteworthy that kernels with a low σ, more specifically those based on $\sigma = 1.0$, perform the worst, mostly due to the impact of noise and blurred ridges, which lead to a significant number of false positives and negatives, respectively.

The incorporation of multiscale kernels into the algorithm has a positive influence, as can be seen in the results for the configuration MI. The combination of the isotropic kernels at multiple scales leads to better results than those at any individual scale, both for Δ^2 and $F_{0.5}$. The only exception to this trend occurs for large values of ρ, since the combination of heavy smoothing and large isotropic Gaussian kernels induces a loss of performance. We can observe that the loss of performance of MI is similar to that of SI_4, which indicates that it is caused by the pernicious influence of such large scale kernels.

The influence of the anisotropy of the kernels is brought out by the comparison of the results of the SA_i with their scale-equivalent SI_i. The anisotropic kernels greatly improve the results of their corresponding isotropic configurations, which confirms the fact that anisotropy has a positive effect when filtering images for ridge detection.

Finally, we have the MM_i configurations, which combine the results of filters at different scales with different indices of anisotropy. The quantitative results in Table 4.2 illustrate the fact that these configurations lead to very good results, but not significantly better than other configurations, more specifically SA_2 and SA_3. This is due to the fact that the inclusion of a variety of kernels also increases the possibility of including unfit ones. As happened for the combination of large values of ρ with multiscale isotropic kernels, certain combinations of parameter values might not only lead to no improvement in the final results, but also to a decrease in the performance. The kernels producing such undesired behaviour are, in general, those having low values of σ and ρ, since they lead to the interpretation of noise and contamination as small, non-elongated ridges, often connected to longer ones. Nevertheless, their inclusion might be unavoidable if small, round ridges appear in the image. In those cases, more delicate postprocessing procedures are

		Methods										
		SI_1	SI_2	SI_3	SI_4	MI	SA_1	SA_2	SA_3	SA_4	MM_1	MM_2
$\rho = 0.0$	Δ^2	0.89	0.84	0.84	0.86	0.84	0.90	0.82	0.82	0.83	0.83	0.82
	$F_{0.5}$	.84	.85	.85	.83	.85	.84	.87	.87	.85	.85	.86
	P/R	.95/.78	.97/.79	.97/.78	.97/.75	.97/.77	.94/.81	.96/.81	.96/.81	.97/.79	.97/.79	.97/.80
$\rho = 0.5$	Δ^2	0.87	0.84	0.85	0.86	0.83	0.87	0.82	0.82	0.84	0.84	0.82
	$F_{0.5}$	.85	.85	.84	.83	.85	.86	.87	.87	.85	.86	.86
	P/R	.96/.79	.97/.79	.97/.77	.97/.75	.97/.78	.95/.81	.96/.81	.96/.81	.96/.79	.96/.79	.96/.80
$\rho = 1.0$	Δ^2	0.85	0.85	0.86	0.88	0.84	0.84	0.82	0.83	0.85	0.85	0.83
	$F_{0.5}$	.85	.85	.84	.82	.85	.86	.86	.86	.85	.85	.86
	P/R	.96/.79	.97/.79	.97/.77	.97/.74	.97/.77	.96/.80	.96/.81	.96/.80	.96/.78	.96/.78	.96/.79
$\rho = 1.5$	Δ^2	0.86	0.86	0.88	0.89	0.87	0.86	0.85	0.86	0.87	0.87	0.86
	$F_{0.5}$	.85	.85	.83	.82	.84	.85	.86	.85	.84	.84	.85
	P/R	.96/.79	.97/.78	.97/.76	.97/.74	.97/.76	.96/.79	.96/.80	.96/.79	.96/.77	.96/.77	.96/.77
$\rho = 2.0$	Δ^2	0.87	0.88	0.89	0.91	0.89	0.86	0.87	0.87	0.89	0.89	0.88
	$F_{0.5}$	.84	.84	.83	.81	.83	.85	.85	.84	.83	.83	.83
	P/R	.96/.78	.97/.77	.97/.75	.97/.73	.97/.74	.96/.79	.96/.78	.96/.78	.96/.76	.96/.76	.96/.76

Table 4.2: Quantitative results obtained by each of the configurations included in Table 4.1, in terms of average BDM (Δ^2), F-measure ($F_{0.5}$), and Precision-Recall (P/R) on the GUFI-1 dataset. The results are subdivided according to the standard deviation in the Gaussian smoothing used prior to differentiation.

recommended.

The problems found for parameter setting indicate that some form of *a priori* analysis has to be performed on the images (and the structures to be detected), even when the algorithm considers a wide variety of kernels. In general, the recommendations for the configuration of the algorithm are straighforward. Firstly, S has to encompass as many values as possible, with the extreme values determined by the maximal and minimal width of the ridges to be detected. Secondly, D needs to be as large as possible, considering the time and computing constraints in the specific context. Thirdly, A demands a problem-specific setting, a meaningful option being the use of a unique anisotropy index other than ρ, as in the SA_i configurations.

Nevertheless, it is worth noting that when setting of A and S, the most important decision is on their extreme values, rather than the density of the values between them. While this density is important for optimally fitting each of the ridge conditions in the images, it is in fact the extreme values that make a significant difference in terms of false positive or negative detections.

As a final conclusion, we can enunciate that the inclusion of anisotropic and/or multiscale kernels improves the results by the monoscale, isotropic ones. Although the improvement seems subtle, we must consider the context in which it appears. First, we have that the SI_i methods already perform quite well (around 0.84 in terms of $F_{0.5}$), and consequently the margin for improvement is limited. Secondly, we note that the performance gain is coherent with the improvements expected from the use of SOAGKs, which are: (a) the adequate modelling of crossings and junctions and (b) the avoidance of false positives due to blob-like structures. The former does have a limited impact in terms of $F_{0.5}$, since these artefacts account for a very small number of pixels. The latter does have a significant impact on the evaluation in terms of Δ^2, which heavily penalizes FPs, but its impact on $F_{0.5}$ is again reduced due to the limited number of affected pixels. In Fig. 4.9 we display the results obtained by applying SI_2, SA_2 and MM_2 on the first six images of the GUFI-1 dataset. We observe that the results by SA_2 and MM_2 contain small (although relevant) improvements with respect to those by SI_2, as expected from the results in Table 4.2.

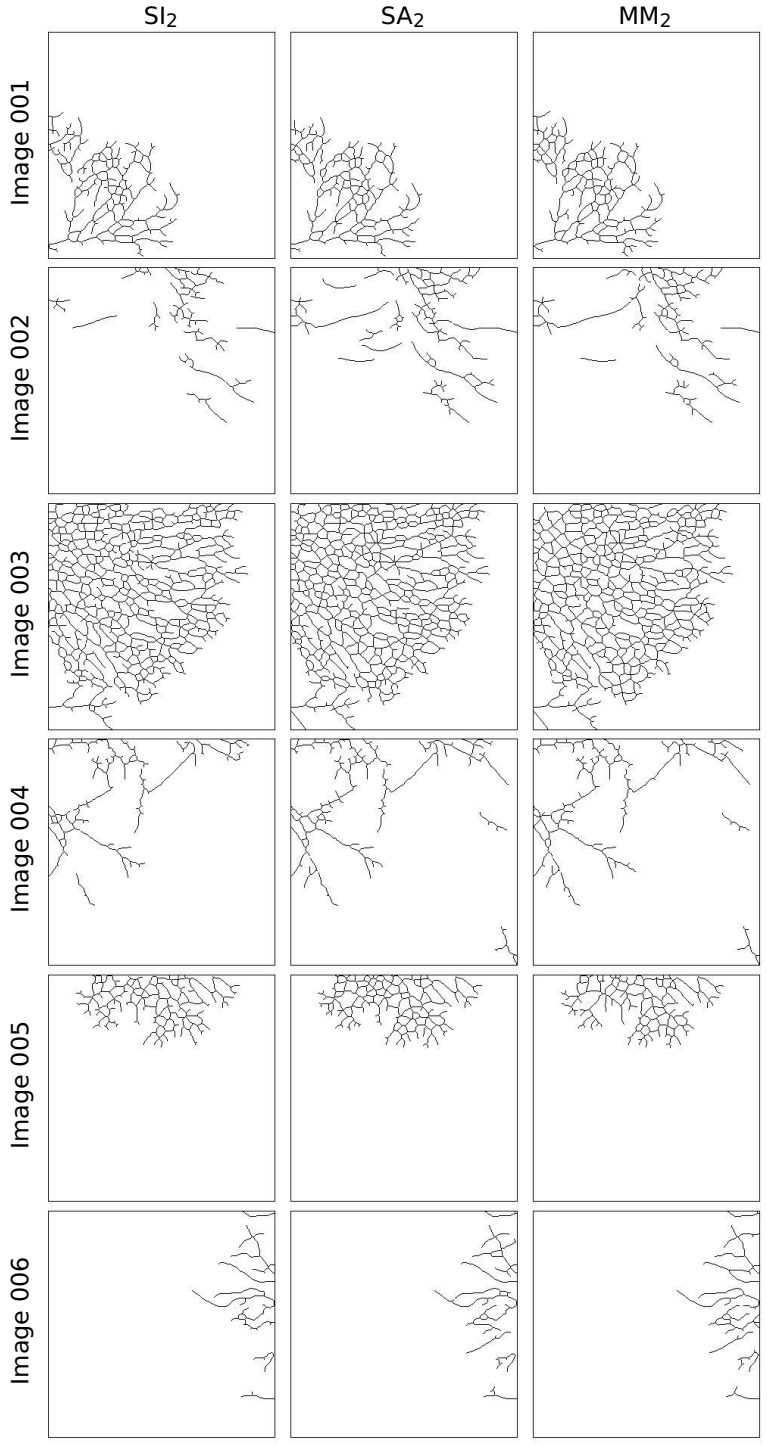

Figure 4.9: Results gathered by three different configurations of the procedure in Algorithm 1 on the first six images of the GUFI-1.

4.6 Conclusions

We have proposed the use of anisotropic, multiscale kernels for second order image differentiation. These kernels have already proven useful in zero-th or first order differentiation, and are also supported by recent trends in local kernel adaptation for image processing. We have presented an expression for such kernels, together with an algorithm for ridge detection based on such second order differentiation. Our algorithm, which allows for the use of multiple scales and anisotropy indices, has been further customized for a real-world application. Specifically, we have focused on the extraction of the structure of in vitro fungi in biological imagery, for which we have introduced a new dataset with 100 images. The images have been taken at the Faculty of Bioscience Engineering of Ghent University, and are publicly available at the KERMIT research unit website[4] under the name Ghent University Fungal Images (GUFI-1). We have run quantitative experiments on this dataset illustrating the fact that using multiscale filters, as well as anisotropic ones, has positive effects on the results of the ridge detection algorithm.

[4] http://www.kermit.ugent.be

5

Automated image-based analysis of spatio-temporal fungal dynamics

5.1 Introduction

Fungi are present in and affect most natural, agricultural and urban environments. In forests, fungi are the primary decomposers of organic matter (Krivtsov et al., 2006), where they also form mycorrhizal associations with tree roots allowing for an effective distribution of nutrients across long distances (Boddy et al., 1999; Dickson and Kolesik, 1999). In addition, pharmaceutical and food industries benefit from fungi considerably, as they are used to create products ranging from

This chapter has been published as: G. Vidal-Diez de Ulzurrun, J.M. Baetens, J. Van den Bulcke, C. Lopez-Molina, I. De Windt, B. De Baets (2015). Automated image-based analysis of spatio-temporal fungal dynamics. Fungal Genetics and Biology 84, 12-25.

alcohol and bread to industrial enzymes and antibiotics (Grimm et al., 2005). Furthermore, fungi are used in biocontrol to fight plant pathogens affecting crops, such as insects and other fungi (Weinzierl and Henn, 1991; Alvindia and Natsuaki, 2008). Nevertheless, fungi are also responsible for wood decay (Schwarze, 2007); therefore, wooden material (Wadsö et al., 2013) and plants (Henkel et al., 2012) are subject to their attack, causing economic losses in construction and agricultural industries.

For all these reasons, fungi have been studied extensively over the years (Boswell et al., 2003; Gadd et al., 2007; Schwarze, 2007). They are characterized by a unique structure, which allows for an efficient internal transportation of nutrients and a rapid expansion in a multitude of different environments, even in extreme conditions (Magan, 2007). Fungi are composed of a vegetative body, called the mycelium, formed by a network of cylindrical thread-like structures, referred to as hyphae. Through these hyphae, nutrients are absorbed and distributed. Fungal growth takes place at the tips of the hyphae (Edelstein, 1982), which are referred to as apices. This gain in biomass can be observed when existing hyphae elongate or when new tips emerge along an existing hypha, a process known as branching (Edelstein, 1982). As hyphae grow and explore their surroundings, they may encounter other hyphae, which sometimes leads to fusion of hyphae, called anastomosis, thereby increasing the efficiency of the nutrient cycle and altering the shape of the network (Simonin et al., 2012).

There have been many efforts spent to understand the dynamics of fungal growth. Some researchers focus on local features, like the diffusion of nutrients within the mycelium (Tlalka et al., 2007) or the way fungal tips extend (Bartnicki-Garcia et al., 1995). Others consider the mycelium as a single entity and study its macroscopic characteristics, such as its density and the total area it covers (Davidson, 1998; Falconer et al., 2005). Alternatively, a third group of researchers focuses on the individual hyphae (Boswell, 2008; Carver and Boswell, 2008; Hopkins and Boswell, 2012), as such studying the fungi from a mesoscopic perspective.

A major concern with these different approaches is the evaluation of the results. Laboratory experiments are expensive and time consuming (Fricker et al., 2009), and typically lead to results that depend on the specific experimental conditions and that make it difficult to compare with other experimental set-ups (Jacobs et al., 2002). Furthermore, some of the *in vitro* methods are destructive and do not allow for tracking the growth process through time (Wadsö, 1997), implying that experiments have to be repeated in order to account for the natural variability among individuals. As a consequence of these limitations, many researchers use data from literature to evaluate their experiments (Meškauskas et al., 2004a; Boswell, 2008; Fuhr et al., 2012), mostly in a qualitative way. Unfortunately, the availability of this kind of data is limited and it is usually decades old (Trinci, 1974; Hutchinson et al., 1980), as such constraining studies to a few growth scenarios, environmental conditions and/or fungal species.

Given the increasing availability of image-capturing techniques (see (Falconer et al., 2010)), an interesting alternative is the use of image analysis. Capturing images is easy and does not require expensive equipment. Image analysis has already been used for the study of fungal growth, but most studies involve manual labelling of the hyphal network (Trinci, 1974; Heaton et al., 2010), tracking of individual hyphae (Bolton and Boddy, 1993; Diéguez-Uribeondo et al., 2004) or invasive techniques (Barry et al., 2009a), which do not allow for tracking the network through time. These techniques are also time consuming and tedious.

In response, this work presents an automated procedure combining image analysis and graph theory to track fungal growth through space and time. The only experimental input needed is a time series of images of a developing mycelium. Hence, direct interaction with samples during the growth phase is not necessary and deterioration of the samples is therefore avoided. The images are automatically processed and transformed into simpler binary representations of the entire mycelium, rather than restricting to a relatively small, unrepresentative part of the network. In this way, the issues of manual labelling, restriction to local scales, and destructive techniques are overcome by this method.

These binary images are composed of thin connected lines and can therefore be easily mapped to mathematical graphs. Using properties of these graphs, we are able to track some of the most relevant mesoscopic fungal growth characteristics through time. In order to study the growth efficiency of fungi, we track measures such as the evolution of the number of tips, the total length of the mycelium (Trinci, 1974; Prosser and Trinci, 1979; Boswell, 2008) and the fractal dimension, which indicates the ability of the fungus to fill the space available (Bolton and Boddy, 1993; Boddy et al., 1999; Blackledge and Barry, 2011). Since the morphology of hyphal networks is crucial for the productivity of industrial processes involving fungi (Barry et al., 2009a), we also quantify some morphological characteristics, such as the growth angle and the mean internodal length. Hence, the output of the proposed method includes the most commonly studied topological measures of mycelia. In addition, an innovative experimental set-up is presented in order to test the image analysis procedure. These experiments result in time series of five different fungal species from five different genera, as such allowing for a mutual comparison of their growth dynamics.

5.2 Materials and Methods

5.2.1 Selected organisms

In this study, we aim at analyzing the dynamics of fungal growth. For this purpose, five different fungal species were selected based on their growth characteristics

and their impact on human health and industrial processes. Mother cultures of *Coniophora puteana* (Basidiomycota causing brown rot commonly found on timbers and other wood construction materials (Green III and Highley, 1997; Viitanen et al., 2010a)), *Phanerochaete velutina* (plant pathogen often used in image analysis studies (Heaton et al., 2010; Obara et al., 2012) from the Basidiomycota), *Trichoderma viride* (Ascomycota used in commercial production (Barry and Williams, 2011) and bioremedation (Joshi et al., 2011)), *Rhizoctonia solani*, Basidiomycota recently renamed as *Thanatephorus cucmeris* (plant pathogen with a vast number of hosts worldwide (Bailey et al., 2000; Jacobs et al., 2002; Boswell et al., 2003)) and *Penicillium lilacinum* also known as *Purpureocillium lilacinum* (Ascomycota used in the pharmaceutical industries as a source of antibiotics (Geng and Yuan, 2010)) were maintained on 4% malt agar (2% agar Bacteriological No. 1 (Oxoid), 4% malt extract) for one week at 23°C ±2°C and 65% ± 5% relative humidity in a temperature-controlled room.

5.2.2 Experimental microcosms

Since we attempt to replicate a scenario for fungal growth with a limited number of external factors, the substrate was limited to a maximum of 0.3 g malt agar in the entire Petri dish with a diameter of 90 mm. In order to maintain the environmental conditions needed for sustaining fungal growth, we added a droplet of substrate in the centre of a Petri dish and some additional droplets along the edge of the disk, as shown in Figure 5.1. An inoculum of size 6 mm by 3 mm, cut from the periphery of the mother culture, was placed on top of the central droplet. Since images obtained with classical devices are two-dimensional, we must limit the space inside the Petri dish in such a way that its vertical dimension may be neglected. This was achieved by placing the sample on the Petri dish lid and then sealing it with the bottom half of the Petri dish (Figure 5.1). In this way, the surface of the lid and the bottom were almost in contact, thereby limiting the maximal growing height to approximately 0.6 mm.

The samples were kept during 24 hours in a conditioned cabinet, after which they were transported to another dark cabinet with similar environmental conditions (23°C ±2°C and 65% ± 5% relative humidity) and positioned on a flatbed scanner (Epson Perfection V750-M Pro Scanner). Images were captured automatically using VueScan (VueScan 9.4, Hamrick Software, USA) every 30 minutes for 75 hours, as such producing a total of 150 images per sample.

The images have a resolution of 1,200 dpi. A maximum of six samples could be scanned simultaneously, resulting in images of 10,000 × 14,040 pixels. These images were cropped automatically to focus on the growth area of interest. The final images have dimensions of 2,125 × 2,125 pixels per sample, corresponding to approximately 4 cm × 4 cm and representing the central area of the Petri dish

containing the initial inoculum.

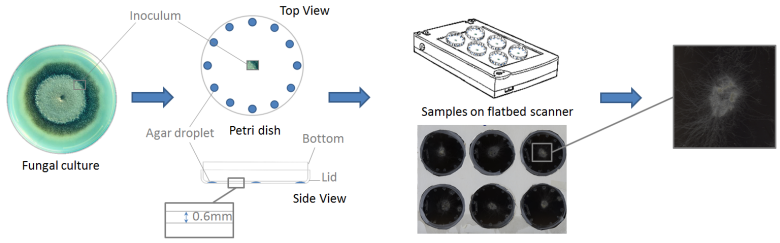

Figure 5.1: Scheme of the experimental set-up. First an inoculum is taken from the periphery of the mother culture. The inoculum is then placed on a Petri dish, where 13 agar droplets were previously arranged in a circular configuration. Finally, the Petri dishes are transported to the flatbed scanner where images are captured every 30 minutes.

In order to prevent the presence of possible erroneous information, the droplets of agar and the initial inoculum were removed from the images. Consequently, a mask of the initial configuration (before any growth had taken place) was subtracted from the other images in the time series.

5.2.3 Image processing

Image processing demands a careful consideration of the conditions in which imagery is acquired, since some factors can have a negative impact on extracting relevant information. In the case of fungal images, the tracking of hyphae is complicated by contamination such as dust particles or spores. Problems also arise due to the poor image quality of some areas and as a consequence of contextual light which might heterogeneously illuminate the background. In addition, fungal growth is not fully two-dimensional and therefore some areas are out of focus due to overlapping hyphae and the varying distance to the scanner plate. In order to overcome these issues, we developed an image processing algorithm that can be adapted to the local conditions of the fungal images in terms of visibility, contamination and the structural properties of hyphae.

We used the algorithm proposed in Chapter 4 to process the raw images. The algorithm is a generic ridge detection algorithm, but can be tuned to meet research-specific needs. It was designed for excelling at junction detection, which is crucial when studying hyphal networks, and it performs a hysteresis-based ridge tracking, instead of a pixel-based discrimination. This algorithm is outlined below.

First, the images are filtered using zero-th order isotropic Gaussian kernels in order to attenuate noise, without creating any new artefacts (Lindeberg, 1994). Then, the second partial derivatives of the images are computed by filtering them with a range of second order anisotropic Gaussian kernels, whose responses are then combined. These derivatives are analyzed to determine the most likely orientation

and visibility of a ridge at each pixel. All the previous information is combined to produce a preliminary binary ridge map in which only the most salient ridges are visible. This step involves non-maxima suppression (Rosenfeld and Thurston, 1971), hysteresis (Canny, 1986) and double-threshold determination (Liu et al., 2013). Finally, ridge cleaning is used to minimize the impact of spurious responses. An example of the results obtained using this workflow for four of the studied fungal species can be found in Figure 5.2 and for the fifth species in Figure 5.3.

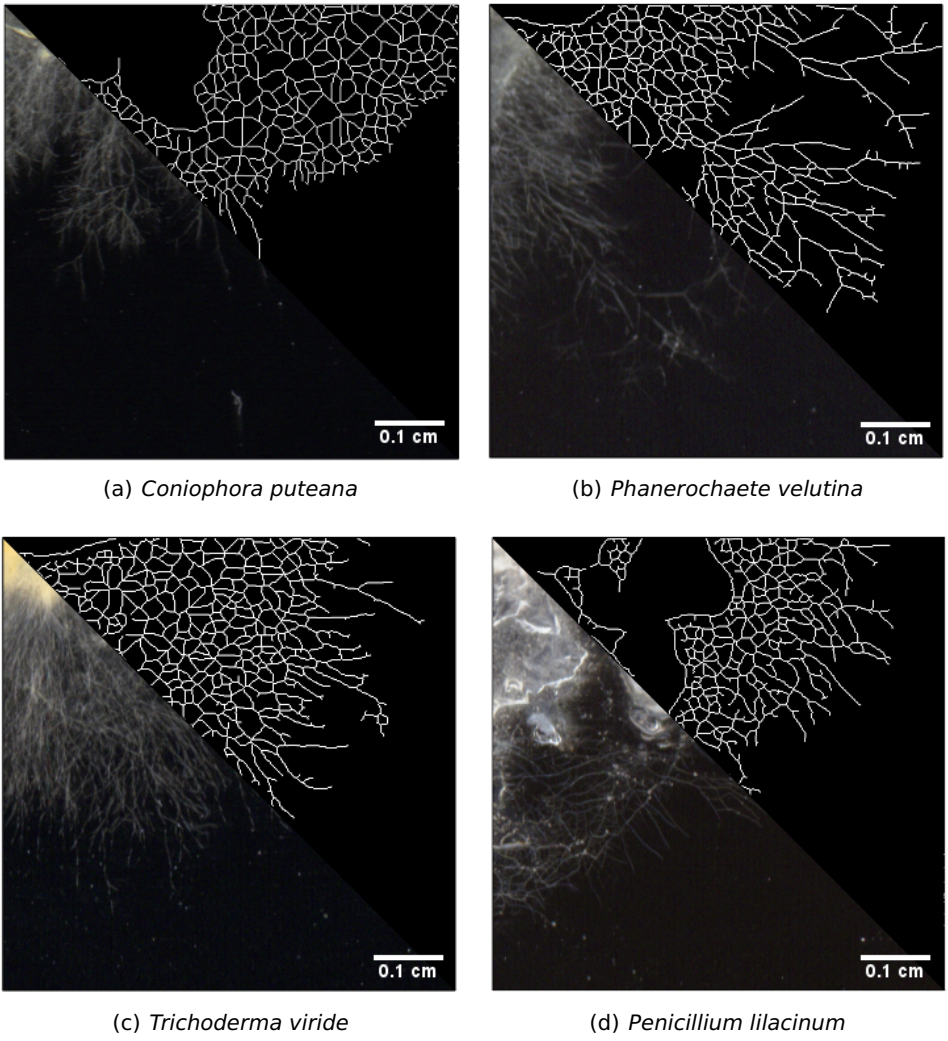

(a) *Coniophora puteana* (b) *Phanerochaete velutina*

(c) *Trichoderma viride* (d) *Penicillium lilacinum*

Figure 5.2: In vitro images and extracted binary ridge maps of the mycelia of different fungal species after a period of 62.5 hours.

Graph theory is commonly used to study networks of line segments. A graph is a mathematical structure that represents a set of objects and their associations.

More specifically, a graph consists of a set of vertices (also known as nodes) and a set of edges. Usually, the vertices represent the studied objects and the edges formalize the relationships between them (Gibbons, 1985). To facilitate the study of the relationships between objects, each vertex is assigned a degree that reflects the number of edges connected to it. In the case of mycelia, the vertices of the corresponding fungal network graph may be envisaged as the junctions and apices of the mycelium (Obara et al., 2012). Consequently, the edges indicate the presence of a geometrical connection between the vertices, i.e. a hyphal segment.

The `MorphologicalGraph` function of Mathematica (Version 10.0, Wolfram Research Inc., USA) enables the translation of images into graphs. This function converts an image into a set of intersections (vertices) and a set of line segments (edges). An example of a fungal network graph obtained using this function, together with the original fungal image and the binary ridge map, is shown in Figure 5.3 for a sample of *Rhizoctonia solani* that was grown for 25 hours.

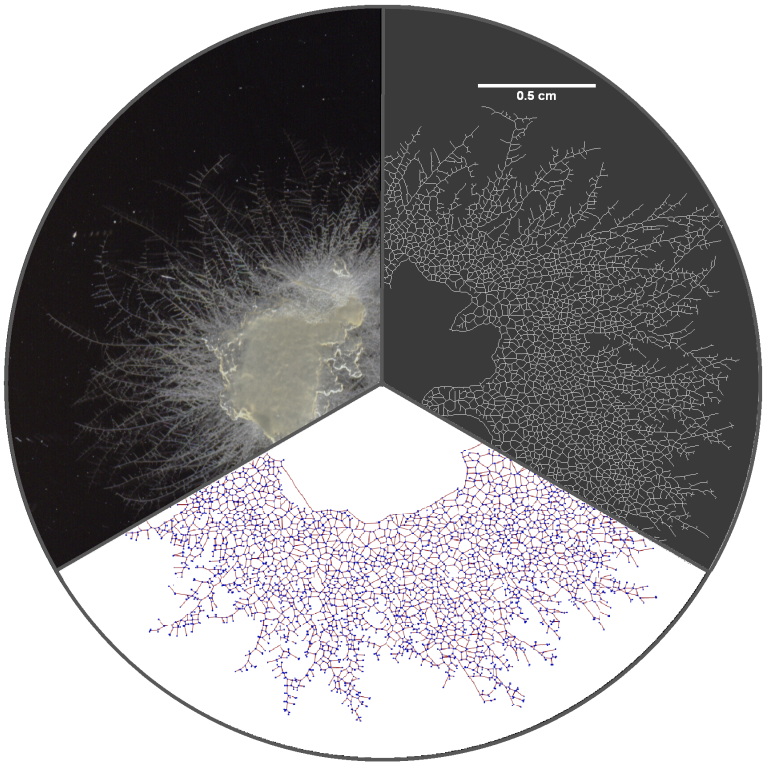

Figure 5.3: *Rhizoctonia solani* growing *in vitro* (left), extracted binary ridge map of the mycelium (right) and corresponding graph (bottom) after a period of 25 hours of growth.

After applying the same process to each of the 150 images per sample, we obtain a time series of fungal network graphs. Since the images were captured every 30 minutes, the resulting time series captures the spatio-temporal dynamics of the

mycelium over a period of 75 hours.

5.2.4 Extraction of fungal growth features

In this section we describe in detail how certain graph characteristics are translated into quantifiers of fungal growth. The different measures are divided in three groups. The first group consists of those that quantify fungal growth and expansion, such as the total length of the mycelium, the area covered by the mycelium and the fractal dimension. The second group encloses measures such as the number of tips, the evolution of the node degree and the node density that give insight into the compactness of the mycelium. Finally, the average internodal length and the growth angle capture the structure of the mycelium. Other features commonly used to describe mycelia are listed in Table 5.2 (Section 5.3).

5.2.4.1 Growth

An edge contains information about its vertices and their coordinates. Since we know the coordinates of the endpoints of the edges, we can calculate the Euclidean distance between them, i.e. the length of the hypha connecting the corresponding points in two-dimensional space. Using the definition of total hyphal length given in (Trinci, 1974), the total length is computed as the sum of the lengths of all the edges composing the graph, which can easily be obtained from the graph.

The coordinates of the vertices are also used to calculate the area covered by the mycelium. The area is computed as the convex hull of the node set, i.e. the smallest convex set that contains all the nodes of the fungal network graph. This measure accounts for the spatial coverage of the fungus and can be combined with other topological measures, such as the number of nodes or the total length, to gain insight into the density of the network.

The last growth feature that is extracted from the graph is the fractal dimension, which is motivated by the fact that fungi have been reported to give rise to fractal structures (Barry et al., 2009a). Fractals are geometric patterns that are repeated at ever smaller scales; the fractal dimension quantifies how often a pattern is repeated. Essentially, it constitutes a space-filling measure. Here, we use the box counting method, where the two-dimensional space is first divided using a non-overlapping grid of squares of increasingly smaller size. Then, for every box size the number of boxes containing a part of the original image is computed (Barry et al., 2009a). The fractal dimension D follows from:

$$D = \lim_{s \to 0} \frac{\log n}{\log 1/s},$$

where n represents the number of boxes containing a section of the fungus and s the box side length. The algorithm was initialized with a box of side length equal to the length of the image (S_0). At each time step i the side length of the boxes used to create the non-overlapping grid was set to S_0/i and D was calculated by considering boxes as small as 10×10 pixels, since we assume this to be the minimum box size that can contain a significant part of hyphae. Therefore the fractal dimension was calculated using 200 different box sizes.

5.2.4.2 Compactness

For each vertex of the fungal network graph, we know its degree, its location in the two-dimensional space, its vertex-vertex adjacencies (i.e. all the vertices connected to it by edges), and the edges incident to it. Since tips are the endpoints of hyphae, these are vertices connected only to a single edge. Consequently, the number of tips in the mycelium is easily calculated by determining all vertices of degree one. A possible issue, although rare, could be the presence of cycles, which are edges starting and ending at the same vertex. However, since the image processing algorithm recognizes such vertices as being of degree two, cycles do not affect the accuracy of the method. The accuracy of this tip detection method can be seen in Figure 5.4 where the tips of *Rhizoctonia solani* are superimposed both on the original image and on the extracted mycelium shown in Figure 5.3.

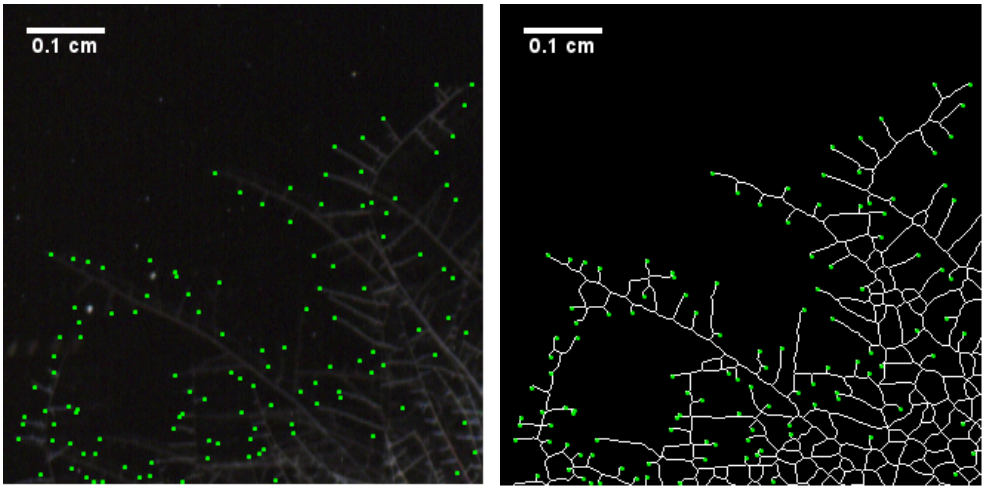

(a) Tips on top of the original image (b) Tips on top of the binary ridge map

Figure 5.4: Detail of the detected tips in part of the mycelium of *Rhizoctonia solani* presented in Figure 5.3.

The number of nodes is computed immediately from the output of the `MorphologicalGraph` function (Mathematica, Version 10.0, Wolfram Research Inc., USA),

while the node density is computed as the ratio of the number of nodes to the area covered by the mycelium (previously explained in Section 5.2.4.1).

5.2.4.3 Morphology

The structure of a mycelium is the main factor determining the efficiency of the internal nutrient translocation. In order to capture this structure, we extract two more features also relying on the graph obtained with the `MorphologicalGraph` function (Mathematica, Version 10.0, Wolfram Research Inc., USA), namely the average growth angle and the average internodal length (fusions, branches and extensions). The growth angle is defined as the difference between the angle of a segment and the angle of its preceding segment. Since a segment can have multiple predecessors, we assume that the predecessor is the one with the smallest angle. This value is obtained for each tip in the fungal network graph, since apical growth and branching occur at the tips present both in the interior and the periphery of the colony. A low value of this measure indicates that there are almost no changes in the growth direction, while larger values possibly imply a complex network full of branches. The average internodal length is computed as the average length of the edges in the fungal network graph. This measure is also related to the complexity of the mycelium, in the sense that large internodal lengths indicate a simple network without much activity other than linear growth, while short lengths imply an active network with many branches and fusions.

The complete source code for the image processing and fungal growth feature extraction algorithms can be found at www.kermit.ugent.be.

5.3 Results

The growth of five fungal species was tracked for 75 hours by capturing images every 30 minutes. All together, seven cultures of every species were tracked, as such yielding seven time series per fungal species to derive the results presented in this section. More cultures were initially prepared, but those that were contaminated or showed excessive condensation in the Petri dish were discarded for further analysis.

5.3.1 Intra species variability

As for most living organisms, fungi present a large variability of growth behaviours, even among individuals of the same species that are growing under the same environmental conditions. This variability is shown in Figure 5.5 for the total length

per species. In order to enable a convincing comparison among the fungal species, we generated a mean curve for each species by averaging the tracked measures over the seven cultures. These curves were generated by averaging the corresponding time-stamped measure across the cultures of a given species. However, it should be noted that the natural intra-species variability of the selected fungi, the presence of outliers and the limited number of samples impact the amount of noise present in the curves.

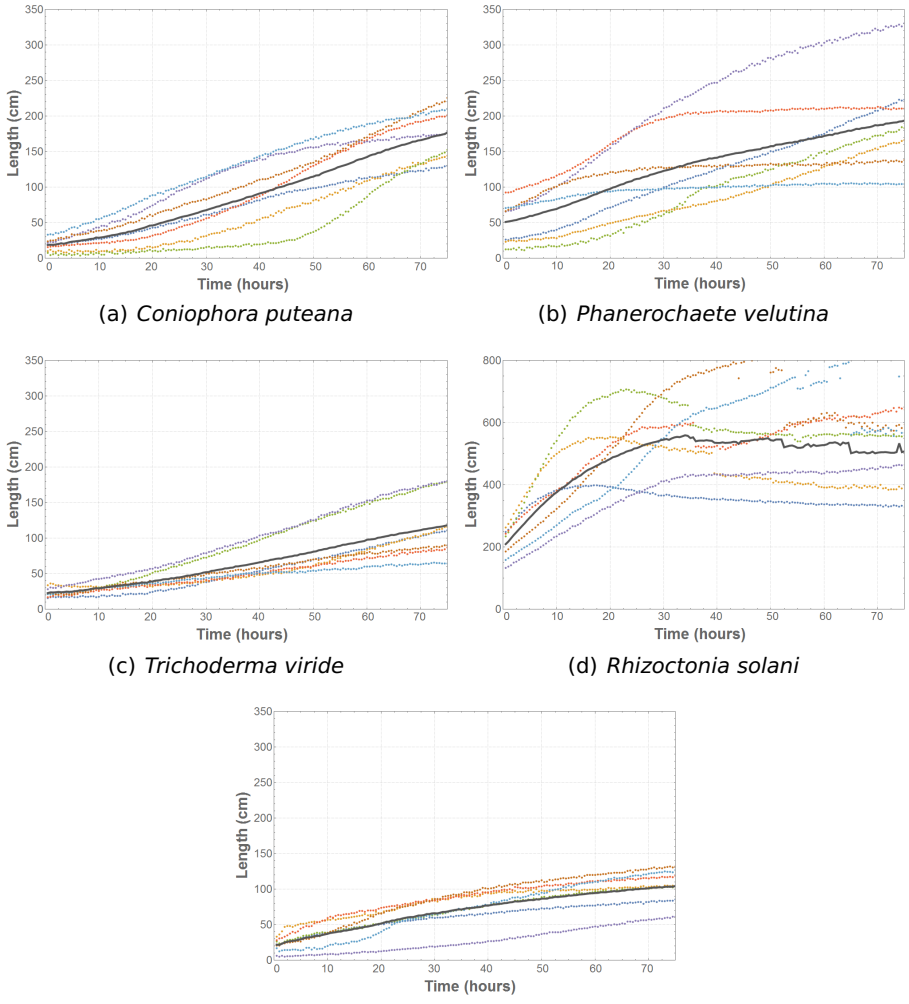

(a) *Coniophora puteana* (b) *Phanerochaete velutina*

(c) *Trichoderma viride* (d) *Rhizoctonia solani*

(e) *Penicilium lilacinum*

Figure 5.5: For each fungal species, evolution of the total length of each sample (dotted lines) and the corresponding mean curves (solid line).

5.3.2 Topological measures quantifying fungal dynamics

In this subsection some of the most relevant topological measures quantifying fungal dynamics are presented. The different measures are classified using the three categories introduced in Section 5.2.4.

5.3.2.1 Growth

The total mycelium length is one of the most important measures when studying fungal growth since it provides insight into the extension of the fungus under study. Figure 5.6a shows the mean evolution of this topological measure over time for the different species. All species show positive growth curves, which is reasonable since decay of biomass was not observed in the time period covered by the experiments. Note that the growth rate varies across species, with especially *Rhizoctonia solani* clearly differing from the other species. The growth of *Rhizoctonia* saturates as soon as the fungus fills the surface of the analysed region. In contrast, the growth curves of other fungal species increase monotonically and at a slower pace, in particular at the beginning of the experiments. Such behaviour in early stages agrees with studies on *Mucor spinosus* presented by Indermitte (1994), while the exponential behaviour of *Rhizoctonia* at early stages agrees with the dynamics observed in other fungal species (Trinci, 1974; Prosser and Trinci, 1979).

The area covered by the mycelium (Figure 5.6b) is calculated as the convex hull of all nodes present in the fungal network graph (Indermitte et al., 1994; Fricker et al., 2007; Boddy et al., 2010). The average area covered by *Rhizoctionia solani* evolves rapidly, because it covers almost the total analysed surface during its first phase of growth. The area covered by the other species also increases over time, yet more slowly; most species are not able to double their initial area by the end of the growth period and all of them cover less than half of the total analysed surface. This measure is especially sensitive to the specificities of the experimental set-up, since not only the environmental conditions, but also the distribution of nutrients plays a significant role. Consequently, it is not possible to fully compare our results with those obtained in other studies.

The fractal dimension of the different species can be found in Figure 5.6c. For all five species the fractal dimension increases over time, a behaviour that has been reported previously (Barry et al., 2009a). This measure has been studied by many researchers (Barry et al., 2009a; Crawford et al., 1993; Lejeune and Baron, 1997), since it reflects the efficiency of occupying space by the fungus. Even though there are many ways to compute this measure, which have a direct effect on the final value, our results are within the same range as those obtained in other

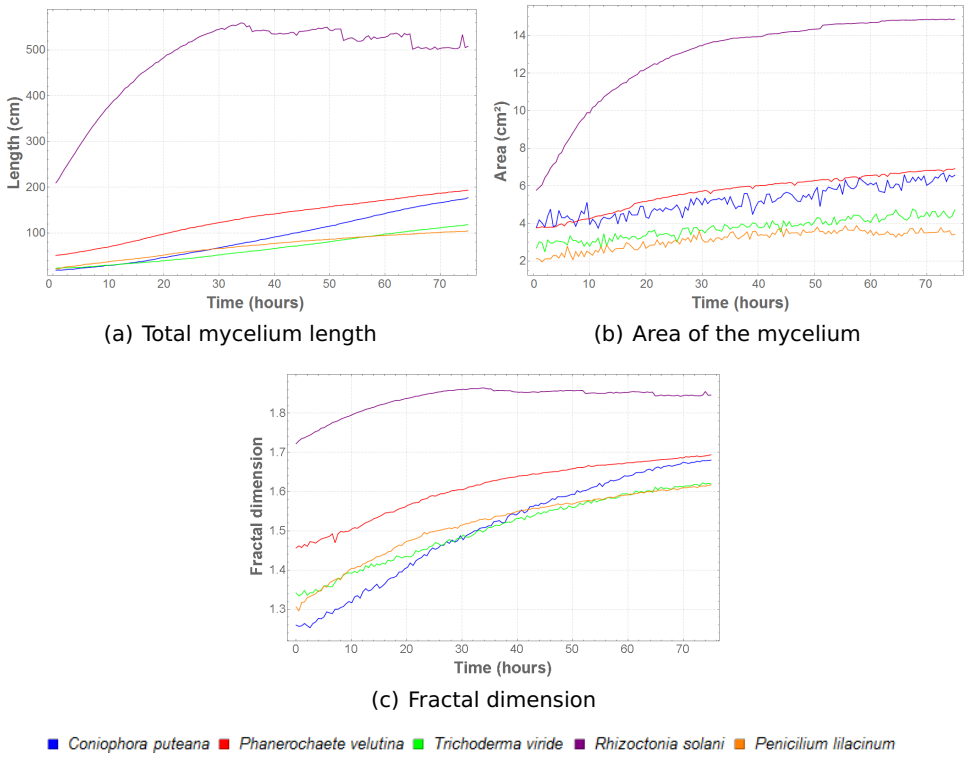

(a) Total mycelium length

(b) Area of the mycelium

(c) Fractal dimension

Figure 5.6: Mean curves of the topological measures quantifying growth over time, computed from seven time series per species capturing 75 hours of growth.

studies using the box counting method and similar experimental inputs (Boddy et al., 1999; Boswell et al., 2007).

5.3.2.2 Compactness

The evolution of the total number of tips is presented in Figure 5.7a. As has been postulated before, the total number of tips is strongly correlated with the total length (Trinci, 1974; Prosser and Trinci, 1979), which is confirmed in this figure where we can distinguish the same types of behaviour as observed for the total length in Figure 5.6a. For *Rhizoctonia solani*, the total number of tips initially increases exponentially, after which its growth slows down and the number of tips remains almost constant. For all other species the number of tips increases more slowly during the course of the experiment. It should be mentioned that tips growing beyond the borders of the studied region are not taken into account when computing the total number of tips. Even though most species did not extend beyond this region, this might however impact the steady state observed for *Rhizoctonia solani*, since all samples of this species reached the borders of the studied region.

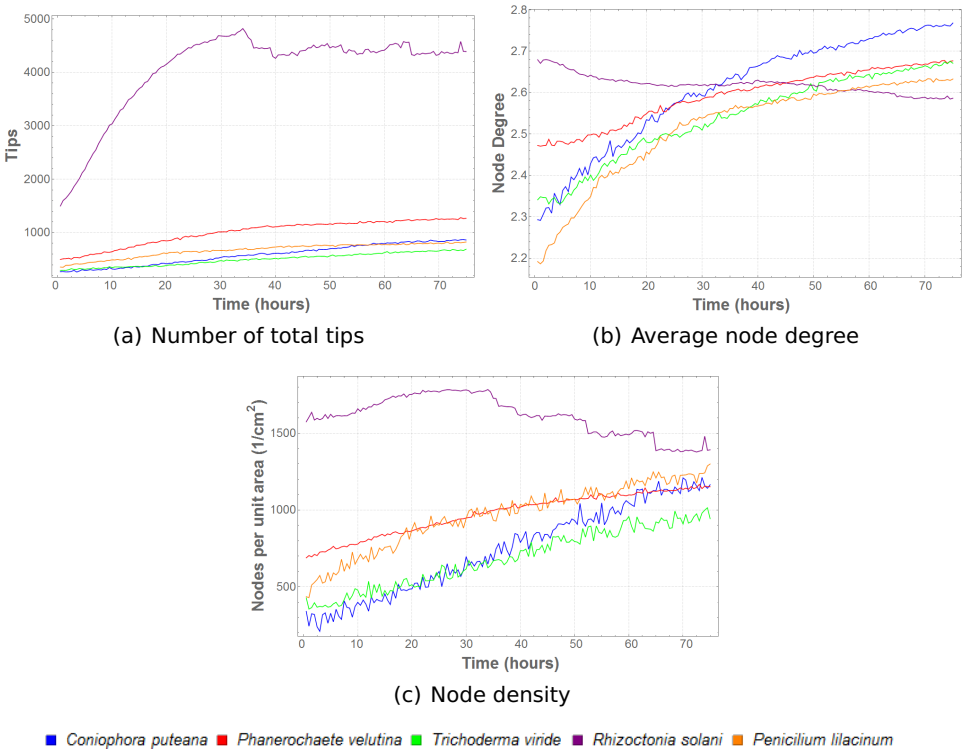

(a) Number of total tips

(b) Average node degree

(c) Node density

Figure 5.7: Mean curves of density-related topological measures over time, computed from seven time series per species capturing 75 hours of growth.

The evolution of the average node degree is presented in Figure 5.7b. This measure is often used to represent the connectivity of networks and can be related to hyphal fusions. A high node degree reflects the presence of several fusion points of multiple hyphae, while a low node degree implies the presence of a tip or a change of direction of an individual hypha. All species studied in this experiment, except *Rhizoctonia solani*, show an increase in the average node degree over time, converging to values of about 2.70 connections per node. A similar value has already been found by other researchers (Fricker et al., 2009). However, in the case of *Rhizoctonia solani*, a small decrease can be observed. The latter can be explained by the fact that the growth was tracked starting only after 24 hours of initial growth, during which *Rhizoctonia* was already able to develop a complex mycelium. As such, the mean node degree for this species is already higher from the beginning of the tracking period than for the other fungi.

The node density increases for all the species except *Rhizoctonia solani* (see Figure 5.7c). The increase of this measure indicates that the mycelium produces new nodes, by branching or extending its apices, faster than it colonizes space. On the other hand, a decrease denotes either a rapid colonization of space or a ces-

sation of growth events. Both facts play a role during the growth of *Rhizoctonia solani*. This measure is usually computed in later growth stages and over longer time scales (Fricker et al., 2007; Boddy et al., 2010), and the time series depicted in Figure 5.7c can therefore not easily be compared with results presented in literature.

5.3.2.3 Morphology

The average growth angle over time, shown in radians in Figure 5.8a, incorporates the angle of apical growth and the branching angle. This angle does not differ significantly between the different species and does not manifest a strong time dependency. *Rhizoctonia solani* is of special interest, as it is characterized by the 90° angle formed by its branches (Kamel et al., 2009), which can be seen in Figure 5.3. However, it is observed that its average growth angle does not reach this extreme value although it is still larger than for all other species. Apical growth has been reported to be almost linear with few changes of direction (Reynaga-Peña et al., 1997; Riquelme et al., 1998), therefore we have also computed the value of the branching angle in order to test this hypothesis. This value can be found in Table 5.2, and concurs with those found in literature for other species (Hutchinson et al., 1980). The low value of the growth angle as compared to the branching angle suggests that most of the biomass originates from apical growth.

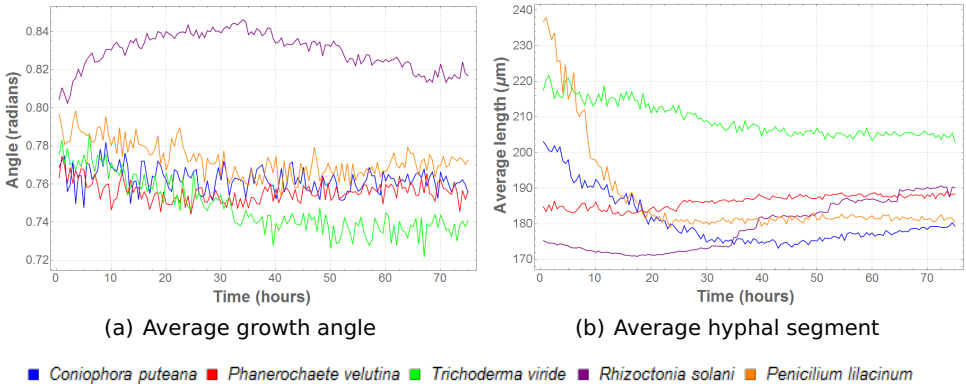

(a) Average growth angle (b) Average hyphal segment

Figure 5.8: Mean curves of morphological measures of fungal networks over time (computed from seven time series per species capturing 75 hours of growth).

The average internodal length over time is shown in Figure 5.8b. The average internodal length decreases for most species, increases for *Rhizoctonia solani* and stays constant for *Phanerochaete velutina*. When a fusion event occurs, a new node is created, as such dividing the intersected edge into two smaller ones. Therefore the decrease of the average internodal length could be the result of an increase in the number of fusions, as was hinted by the average node degree in Figure 5.7b. Conversely, the increase of the internodal length of *Rhizoctonia*

solani could be related to the initial state of its mycelium, already full of fusions, and to the saturation point. From this point on most apical growth occurs outside the study area and therefore mainly fusions are recorded. Moreover, the steady state of *Phanerochaete velutina* also agrees with the results obtained for the node degree, yet with a much lower variation. The average internodal length is one of the main parameters in many spatially explicit models (see the review by Boswell and Hopkins (2008)). Even though the values of this measure do not differ considerably among the different species, the chart shows a clear time dependency. However, this time-dependent behaviour is usually neglected by modellers (Fricker et al., 2007; Boswell and Hopkins, 2008).

5.3.3 Functional description of fungal growth dynamics

The experiments presented in this work were performed on a time series of images, therefore we can report on how the quantifiers of mycelia change over time. We use the data obtained for each topological measure to fit one of the classical sigmoidal growth functions shown in Table 5.1. Such functions have been used historically to model the growth of both populations (Zwietering et al., 1990) and individuals of different species (Zullinger et al., 1984; Weiner and Thomas, 2001), including fungi (Adan, 2011; Barry and Williams, 2011).

Name	Equation
Weibull model	$a - b\,e^{-c\,t^d}$
MMF model	$\frac{a\,b + c t^d}{b + t^d}$
Gompertz model	$a\,e^{-e^{b-c\,t}}$
Richards model	$a\left(e^{b-\mathrm{c\,t}}+1\right)^{-1/d}$
Logistic model	$\frac{a}{b\,e^{-\mathrm{c\,t}}+1}$

Table 5.1: Sigmoidal growth functions with parameters a, b, c and d.

Most of the tracked topological measures fit one of these growth curves, as can be observed in Table 5.2, which includes a summary of the topological measures, the best fitting sigmoidal function with its corresponding parameter values and correlation coefficient. Yet, as mentioned in Section 5.3.2, there are some measures, such as the average growth angle, that do not show a clear time dependency and, therefore do not match any of the sigmoidal curves. Since their evolution

over time is not meaningful, their distributions are shown in the table as the mean value plus/minus the standard deviation of the observations.

For each species and measure, we look for the sigmoidal function and parameter values that best fit the observations obtained from the seven cultures. For this purpose, we performed for each sigmoidal function a weighted least squares regression, which searches for the parameter values that minimize a weighted sum of squared residuals (where each weight is equal to the reciprocal of the variance). For this purpose, we used the `NonLinearModelFit` function of Mathematica (Version 10.0, Wolfram Research Inc., USA). Table 5.2 presents the best fitting function for each species and measure.

In most cases, when a sigmoidal function could be fitted, the correlation coefficients are higher than 70%, which can be considered a good fit (Saltelli et al., 2004). This is the case for the number of nodes (junctions and endpoints of the network), the number of edges (hyphal segments) and the total length. In contrast, measures such as the node density or the volume density cannot be described very accurately by means of a sigmoidal function, since they are not directly related to growth.

Surprisingly, the average area covered by the mycelium presents a poor fit for most species. It has been reported that this measure follows a logistic curve at larger time scales (Adan, 2011), but at the time scale and growth phases covered in this paper, it seems to exhibit a different behaviour. This could also be caused by the use of the convex hull, which is extremely sensitive to false positives in the identification of fungal material.

Finally, for some combinations of species and measures, it is not even possible to fit a sigmoidal curve, which is the case for *Rhizoctonia solani*. As mentioned before, this fungus started its growth before the other species, which implies that its initial growth phase is not reflected in this work. Since sigmoidal functions describe the entire growth cycle, neglecting the initial phase might lead to a mismatch between the sigmoidal curve and the observed time series.

5.4 Discussion

5.4.1 Experimental set-up

We have presented an innovative experimental set-up to track fungal growth in two dimensions over time, which can be reproduced in most laboratories. It is quite versatile since it can be used for various fungal species without any tuning required. This set-up neither requires expensive machinery nor complicated procedures, and permits the tracking of different samples simultaneously, as such

producing a large amount of data. Even though this set-up presents a valid alternative to established procedures for generating data on fungal dynamics, the number of growth scenarios is still rather limited. This follows from the fact that growth should be restricted to two dimensions as much as possible and the need for high contrast between the hyphae and the background. Therefore, growth in more complex environments, such as soil (Morgan et al., 1993; Boddy et al., 1999; Pajor et al., 2010), in three dimensions or within opaque structures such as wood (Hale and Eaton, 1986; Fackler et al., 2007), cannot be captured using such a set-up. Some possibilities for studying such scenarios are X-ray computed tomography (Van den Bulcke et al., 2009) and confocal microscopy (Dickson and Kolesik, 1999; Bago et al., 2002; Fricker et al., 2008). These techniques deliver three-dimensional representations of the interior of opaque structures, while the latter even allows to follow the processes occurring within the fungi (Fricker et al., 2008).

Despite the shortcomings of our set-up to track fungi in complex environments, it can easily be extended to larger surfaces, up to the surface of the entire flatbed scanner. This would allow the study of fungal growth across large areas and longer periods. The results shown in this study are inferred from a small region in order to minimize the impact of the substrate droplets and the computational cost. This was sufficient for most fungal species, but in the case of *Rhizoctonia solani* also a larger region was studied. The results obtained in this way are similar to those reported for *Rhizoctonia solani* in Section 5.3. However, in this case the saturation point is reached later in time. The results obtained for the extended region provide only a minor improvement in the representation of *Rhizoctonia solani*. Therefore they were not included in order to make a consistent comparison between the species. Since the growth process of the other fungal species differs greatly from the one observed for *Rhizoctonia solani*, we think that fixing the tracking duration of the experiment to be equal to the saturation time of *Rhizoctionia* would imply a neglection of the growth of the other species. On the other hand, decreasing only the tracking duration of *Rhizoctonia solani* implies that the different species would be tracked over periods of different length, thereby a comparison across the species would no longer be possible on an equal footing. Therefore we believe that this mismatch should be addressed by changing the experimental set-up rather than treating the data differently.

Even though seven cultures can be considered a representative data set size for the purposes of this work, especially compared to those previously used in the same field (Wadsö, 1997; Heaton et al., 2010; Obara et al., 2012), it is still limited from a statistical point of view. In addition, the techniques used to derive the results shown in this work are quite simple, and with such a small sample size the results might be affected by outliers. Fitting sigmoidal curves to the experimental data is indeed sensitive to outliers (Hastie et al., 2009). This was verified by deleting for each species the culture displaying the most extreme behaviour. In

this way the correlation coefficients improved in most cases, for some species obtaining an improvement of 0.20. This demonstrates the sensitivity of the method to outliers, which could be addressed by changing the regression technique to one which better fits the specific problem setting (Hastie et al., 2009).

5.4.2 Image acquisition

One of the main advantages of the image analysis method presented in this chapter is that it is completely automated. Therefore, this method does not require direct interaction with the samples, allowing to follow the entire growth of a fungus. It is also possible to study interactions with other organisms and/or substances widely studied in this field, such as plants (Schubert et al., 2008), building materials (Pasanen et al., 1992; Nielsen et al., 2004; Fackler et al., 2006) and other fungal species (Falconer et al., 2008; Boswell, 2012). Yet, it should be emphasized that the image analysis method is extremely sensitive in detecting as many hyphal segments as possible. This might affect the resulting images, since the algorithm can also interpret scratches or condensation as being part of the mycelium. This kind of contamination is almost impossible to recognize at a local level during the image analysis stage and should therefore be avoided during the experimental stage.

The quality of the images can be improved by using higher resolution imaging devices. The main issue relates to the blurry regions occurring in the images of the mycelium. This blurriness is caused by the hyphal growth not occurring exactly at the scanner's glass surface. Even though this distance can be extremely small, this causes out-of-focus areas, which could be overcome by using auto-focus scanners. Although using them should not require major changes in the experimental set-up, it could result in an improvement of the image quality. Alternatively, a digital camera in combination with a microscope (Boddy et al., 1999; Barry and Williams, 2011; Blackledge and Barry, 2011) could be used, resulting in high-quality images, with the disadvantage that such a set-up does not easily allow for the tracking of the whole mycelium, or of several samples at once. The translation from the ridge map to the graph would also benefit from a better image quality. The algorithm searches first for junctions and endpoints, and then generates straight lines that connect them, which may not accurately represent the rounded nature of some hyphae. Even though results could be improved by using higher resolution images, the current errors do not appear to differ considerably between the cultures and species in this study. Therefore any bias is consistent across species, allowing for a valid mutual comparison.

Clearly, there exists some correlation between the consecutive images in the time series, since new biomass is generated at the tips of that which was present before (Prosser and Trinci, 1979; Diéguez-Uribeondo et al., 2004; Grimm et al., 2005;

Mouriño Pérez et al., 2006). This fact has been neglected so far. Taking it into account could result in an improvement of the overall results, but this would also require assumptions regarding the correlation between consecutive images, which could in turn affect the objectivity of the procedure.

5.4.3 Scope

The results in this chapter present, to our knowledge, one of the most complete comparisons between fungal species over time reported in literature, and the first achieved in a completely automated way. Although improvements are ongoing, it is already objective and able to capture the dynamics of various fungi. By relying on such an approach, we have shown the time-dependent nature of certain topological measures, in contrast to previous studies (Fricker et al., 2007; Boswell and Hopkins, 2008).

The application shown here is only one example of a large variety of possibilities and extensions. For example, by using proper masks on the original images, it could be possible to study local behaviour within the colony, such as the difference in growth behaviour and morphology between the central region (where more branching and anastomosis occur) and the peripheral region (where hyphae avoid contact and generate less branches and fusions), a behaviour already observed in several studies (de Bekker et al., 2011; Hickey et al., 2002). Our algorithm could be also of use to study other organisms and systems that develop a thin network, such as algae (Kaestner et al., 2006), leaf veins (Fu and Chi, 2003; Li et al., 2006) and plant roots (Kaestner et al., 2006; Perret et al., 2007). The only necessary experimental input is a high contrast picture of the organism or system. The same procedure can be applied to images obtained with devices other than flatbed scanners, if the quality and contrast criteria are fulfilled, and even to the output produced by mathematical models (Boswell, 2008; Carver and Boswell, 2008; Hopkins and Boswell, 2012).

Finally, it should be stressed that similar comparisons are also possible for other species, topological measures and growth scenarios. By using the workflow presented in this chapter, it would be possible to update the data in literature and to make customizable comparisons depending on researchers' needs. However, our approach aims at a general quantification of fungal dynamics and is therefore complementary to other techniques that study certain growth processes in more detail, such as the studies of the Spitzenkörper in order to determine the tip extension (Zhuang et al., 2009) and the growth direction (Riquelme et al., 1998).

5.5 Conclusions

This chapter presents a procedure to quantify fungal dynamics, using image analysis and graph theory. This procedure is entirely automated and addresses the main disadvantages of previous procedures, such as the destructive nature of experiments, the high cost and the need for manual labelling. In order to evaluate the performance of the procedure, we have developed a new experimental set-up that does not require expensive or complex equipment. Despite its simplicity, this set-up allows for the measurement of growth kinetics for various fungal species. Here, we have tracked the growth of five fungal species over time, leading to a quantitative comparison of different growth behaviours. This comparison concurs with key fungal growth assumptions and suggests a good performance of our method, since it was able to capture a variety of different behaviours. In addition, the versatility of this procedure allows for the study of other organisms and phenomena, without the need for significant tuning. Overall, this method offers an updated and broader alternative to classical and narrowly focused studies, thus opening new avenues of investigation in the field of fungal growth research.

Topological measure	Symbol	Description	Units	Fungal species				
				Coniophora puteana	*Phanerochaete velutina*	*Trichoderma viride*	*Rhizoctonia solani*	*Penicillium lilacinum*
Number of nodes	N	Total number of vertices (nodes) in the mycelium, i.e. the number of tips, fusions and branching points	Number of nodes	Gompertz model: $a = 1,16E+04$ $b = 1,04E+00$ $c = 1,19E-02$ Correlation coefficient: 0.8190	Richards model: $a = 8,53E+03$ $b = -5,71E+00$ $c = 1,66E-02$ $d = 2,30E-03$ Correlation coefficient: 0.5837	Logistic model $a = 6,14E+03$ $b = 6,24E+00$ $c = 1,79E-02$ Correlation coefficient: 0.7921		MMF model: $a = 9,55E+02$ $b = 2.38E+02$ $c = 6.45E+03$ $d = 1.18E-00$ Correlation coefficient: 0.7338
Number of edges	M	Total number of edges in the mycelium, i.e. the total number of hyphal segments	Number of edges	Gompertz model: $a = 1,60E+04$ $b = 1,10E+00$ $c = 1,23E-02$ Correlation coefficient: 0.8201		Gompertz model: $a = 1,38E+04$ $b = 9,91E-01$ $c = 7,60E-03$ Correlation coefficient: 0.7845		Gompertz model: $a = 6,19E+03$ $b = 5,07E-01$ $c = 1,89E-02$ Correlation coefficient: 0.7509
Node degree	k	Average node degree	Degree	Gompertz model: $a = 2,82E+00$ $b = -1,57E+00$ $c = 1,62E-02$ Correlation coefficient: 0.8232	MMF model: $a = 2,47E+00$ $b = 1,53E+03$ $c = 2,72E+00$ $d = 1,74E+00$ Correlation coefficient: 0.5629	MMF model: $a = 2,32E+00$ $b = 2,38E+02$ $c = 2,86E+00$ $d = 1,21E+00$ Correlation coefficient: 0.7910	MMF model: $a = 2,73E+00$ $b = 2,29E+01$ $c = 1,76E+00$ $d = 2,56E-01$ Correlation coefficient: 0.3547	MMF model: $a = 2,18E+00$ $b = 1,18E+02$ $c = 2,69E+00$ $d = 1,34E+00$ Correlation coefficient: 0.7977
Connected subgraphs	g	Number of connected subgraphs contained in the mycelium	Number of subgraphs	3.939 ± 1.98	3.371 ± 2.92	4.155 ± 2.23	3.145 ± 2.27	2.799 ± 2.51
Spatial extent	A	Area covered by the mycelium	$10^{-2}m^2$	Logistic model: $a = 1,65E+01$ $b = 3,10E+00$ $c = 4,71E-03$ Correlation coefficient: 0.3107	Logistic model: $a = 6,98E+00$ $b = 9,40E-01$ $c = 2,26E-02$ Correlation coefficient: 0.4831	Logistic model: $a = 5,48E+00$ $b = 9,46E-01$ $c = 1,02E-02$ Correlation coefficient: 0.3306	Logistic model: $a = 1,46E+01$ $b = 1,38E+00$ $c = 4,85E-02$ Correlation coefficient: 0.7503	Logistic model: $a = 3,64E+00$ $b = 8,41E-01$ $c = 2,95E-02$ Correlation coefficient: 0.3501
Node density	NA^{-1}	Number of nodes per unit area covered by the mycelium	Number of nodes/$10^{-2}m^2$	Logistic model: $a = 1,40E+03$ $b = 4,27E+00$ $c = 2,12E-02$ Correlation coefficient: 0.6855	Logistic model: $a = 1,22E+03$ $b = 7,73E-01$ $c = 1,72E-02$ Correlation coefficient: 0.3159	Logistic model: $a = 1,19E+03$ $b = 2,39E+00$ $c = 1,60E-02$ Correlation coefficient: 0.5994		MMF model: $a = 3,87E+02$ $b = 5,38E+01$ $c = 2,87E+03$ $d = 6,66E-01$ Correlation coefficient: 0.6825
Volume density	VA^{-1}	Amount of mycelium per unit area. Where V is computed as a function of the total length (L), assuming all hyphae to be cylinders of equal diameter (10^{-6}m)	$10^{-2}m/10^{-2}m^2$	Logistic model: $a = 3,74E+01$ $b = 4,84E+00$ $c = 1,94E-02$ Correlation coefficient: 0.6839	Logistic model: $a = 3,12E+01$ $b = 9,39E-01$ $c = 1,66E-02$ Correlation coefficient: 0.3502	Logistic model: $a = 3,29E+01$ $b = 2,62E+00$ $c = 1,64E-02$ Correlation coefficient: 0.5945		Logistic model: $a = 3,10E+01$ $b = 1,62E+00$ $c = 2,17E-02$ Correlation coefficient: 0.7116
Average angle of growth	ρ	Average apical growth and branching angle, calculated over all the tips of the mycelium	Radians	0.76 ± 0.02	0.75 ± 0.01	0.74 ± 0.02	0.82 ± 0.02	0.773 ± 0.02
Mean hyphal segment length	l	Mean internodal length	10^{-6}m	180.67 ± 13.80	186.30 ± 7.38	209.13 ± 12.22	179.29 ± 11.27	186.88 ± 23.72
Average branching angle	ϑ	Average angle of branching angle	Radians	1.40 ± 0.05	1.40 ± 0.04	1.37 ± 0.05	1.43 ± 0.02	1.38 ± 0.06
Total number of tips	T	Total number of nodes with degree 1	Number of tips	Logistic model: $a = 1,03E+03$ $b = 3,09E+00$ $c = 1,92E-02$ Correlation coefficient: 0.7639030	Logistic model: $a = 1,27E+03$ $b = 1,69E+00$ $c = 3,14E-02$ Correlation coefficient: 0.5551	MMF model: $a = 3,08E+02$ $b = 1,84E+03$ $c = 1,08E+03$ $d = 1,49E+00$ Correlation coefficient: 0.8083	MMF model: $a = 1,78E+03$ $b = 9,33E+03$ $c = 4,50E+03$ $d = 3,03E+00$ Correlation coefficient: 0.5964	Gompertz model: $a = 8,25E+02$ $b = 1,85E-01$ $c = 2,34E-02$ Correlation coefficient: 0.5251
Total length	L	Sum of the lengths of individual hyphal segments	10^{-2}m	Gompertz model: $a = 3,31E+02$ $b = 1,10E+00$ $c = 1,05E-02$ Correlation coefficient: 0.8292	Gompertz model: $a = 2,20E+02$ $b = 4,23E-01$ $c = 1,55E-02$ Correlation coefficient: 0.6164	Gompertz model: $a = 2,95E+02$ $b = 9,79E-01$ $c = 7,23E-03$ Correlation coefficient: 0.7664	Weibull model: $a = 5,32E+02$ $b = 3,04E+02$ $c = 5,11E-03$ $d = 1,62E+00$ Correlation coefficient: 0.5701	Gompertz model: $a = 1,16E+02$ $b = 4,83E-01$ $c = 1,72E-02$ Correlation coefficient: 0.7512
Fractal dimension	FD	Fractal dimension		Weibull model: $a = 1,88E+00$ $b = 5,19E-01$ $c = 7,91E-04$ $d = 1,51E+00$ Correlation coefficient: 0.6978	MMF model: $a = 1,48E+00$ $b = 3,66E+02$ $c = 1,85E+00$ $d = 1,53E+00$ Correlation coefficient: 0.7113	MMF model: $a = 1,41E+00$ $b = 8,43E+02$ $c = 2,03E+00$ $d = 1,32E+00$ Correlation coefficient: 0.7898	Weibull model: $a = 2,09E+00$ $b = 3,03E-01$ $c = 5,94E-02$ $d = 9,33E-01$ Correlation coefficient: 0.6978	Weibull model: $a = 1,67E+00$ $b = 2,54E-01$ $c = 6,45E-03$ $d = 1,15E+00$ Correlation coefficient: 0.5325

Table 5.2: Topological measures of fungal growth dynamics, together with associated Sigmoidal functions and corresponding Pearson correlation coefficients.

6

Evaluation of the effect of environmental conditions on the growth of *Coniophora puteana*

6.1 Introduction

Fungi grow in most environments including those with extreme conditions. Their nutritional needs can be met by most substrates and materials present in both human and natural environments. Under similar nutritional conditions, their growth is determined by the environmental conditions (Bonner and Fergus, 1960). Each fungal species grows under a certain range of environmental conditions and most species achieve their maximal growth rate under very specific environmental circumstances only (Mislivec and Tuite, 1970), referred to as the optimal growth conditions. Defining these ranges has been frequently done, since they allow

to optimize industrial processes (Valík et al., 1999) and study climate change trends (Kauserud et al., 2010).

Fungal growth results in damage or spoilage of materials and its effects can be reinforced by humidity and temperature, the most relevant environmental factors determining fungal growth which unfortunately cannot always be controlled. For example, outdoor materials are constantly exposed to changing environmental conditions making them vulnerable to fungal attack (Brischke and Thelandersson, 2014). In response, new building and construction materials and coating products are developed in order to improve the resistance. This is especially important in the case of building materials since they insulate the interior of buildings, as such protecting them from weathering, and consequently from fungal attack. Fungi are also responsible for food spoilage. Furthermore, some fungi produce toxic spores that can lead to severe health problems, so preventing their growth is crucial.

For these reasons, several researchers have studied the relationship between fungal growth and environmental conditions. This can be done from two different points of view. Studies in experimental mycology investigate these effects on the mycelium by tracking the changes of the fungal dynamics in response to changing environmental conditions. On the other hand, building mycology focuses on the host, i.e. the substrate (Pardo et al., 2005; Ibrahim et al., 2011) or material (Brischke and Thelandersson, 2014), hence monitoring the properties of the material in order to assess its resistance to fungal attack under different environmental conditions.

The resistance of materials is often measured in terms of the total biomass loss (Meyer and Brischke, 2015; Brischke and Rapp, 2008; Osono, 2015), or the change in its moisture content (Brischke and Lampen, 2014). This requires drying of the sample, which is a destructive method. In contrast, isothermal calorimetry is able to track the thermal activity of fungi, i.e. the heat produced by the fungal metabolism over time without destroying the fungus (Li and Wadsö, 2013; Bjurman and Wadsö, 2000). However, its results are difficult to interpret and not trivial to correlate to growth rates (Bjurman and Wadsö, 2000). Other techniques assess decay by visual inspection of the samples, computing the area covered by the fungus at the end of the experiment (Nielsen et al., 2004) or counting the fungal spores on the sample (Pasanen et al., 2000). Most of them use standard decay scales (Brischke et al., 2013), like EN252 (1989) or EN350-1 (1994), which allow to assign levels of degradation depending on the appearance of the studied sample as assessed by a field expert. So, the current visual methods are subjective, and only allow to track decay on the surface of the studied materials.

The effects of the environmental conditions on fungal growth can also be studied directly by considering changes of the mycelium. These studies rely on simple experimental set-ups where all but one environmental condition are fixed. The techniques used in these assessments often involve microscopes and/or imaging devices to capture images or videos of the growing fungi (Bonner and Fergus,

1960; Pasanen et al., 1991; Ayerst, 1969; Gock et al., 2003; Magan and Lacey, 1984; Boddy, 1983; Huang et al., 2001; Etheridge, 1957). Topological measures, such as the colony radius (Pasanen et al., 1991; Boddy, 1983; Etheridge, 1957), the growth rate (Bonner and Fergus, 1960; Ayerst, 1969; Gock et al., 2003; Magan and Lacey, 1984) or the number of germinated spores (Tommerup, 1983; Huang et al., 2001) can be directly derived from such images. Unfortunately, up to this day the analysis of such data is done manually rendering it impossible to account for more detailed topological measures, such as the total length, the inter-nodal length of the mycelium or the number of tips, even though the latter measures provide crucial information about fungal growth. Furthermore, the resources needed to conduct such analyses hinder the repetition of experiments, such that the natural variability of fungi is typically neglected. Besides, most relevant studies often only focus on small growth areas (Ramakrishna et al., 1993; Laarhoven et al., 2015; Siripatrawan and Makino, 2015; Gougouli and Koutsoumanis, 2013), following the growth of only a few hyphae whose dynamics cannot be considered representative of the entire mycelium.

The method presented here has already been used to extract and compare growth features of different fungal species over time (see Chapter 5). It is completely automated and allows to extract most studied fungal growth features by analysing the whole mycelium without destroying the samples or requiring any human interpretation. By repeating this workflow for several combinations of temperature and relative humidity (RH), it is possible to track their effect on the fungal dynamics. For this purpose, an experimental set-up is designed to study the effect of the environmental conditions on fungal growth. This set-up can be reproduced in most laboratories and produces time series of images representing the evolution of the mycelium over time. These time series can then be used as input for the algorithm described in Chapter 4, resulting in a complete characterization of fungal growth over time.

This chapter is organized as follows. In Sections 6.2.1 the experimental set-up is introduced. The resulting time series of images are then turned into binary ridge maps, using the algorithm described in Chapter 4, and subsequently translated into graphs from which topological measures can be extracted (Section 6.2.2 and Section 6.2.3, respectively). The effect of the environmental conditions on the extracted topological measures is studied by inspecting growth curves of *Coniophora puteana* in Section 6.3.1. In Section 6.3.2, several predictive models are developed, computed from the observed data, in order to study the effects of temperature and relative humidity on different growth parameters. Finally, the main findings and conclusions are presented and discussed in Sections 6.4 and 6.5, respectively.

6.2 Materials and Methods

6.2.1 Experimental microcosms

We have chosen one of the most frequently studied fungal species, namely *Coniophora puteana*. It is a common brown rot fungus responsible for the degradation of wood and building materials. Cultures of this fungus were maintained on 8% malt extract agar (2% agar Bacteriological No. 1 (Oxoid), 8% malt extract) for three days before the start of the actual experiment at 23°C ±2°C and an RH of 65% ± 5% in a climate cabinet (CTS Pharma climatic test chamber Series CP, CTS GmbH, Germany).

In order to study the effect of the environmental conditions on the mycelium by means of image analysis, specific criteria have to be met. For instance, they need to have a high contrast, in order to translate them into meaningful binary ridge maps. In addition, vertical growth has to be limited to ensure a proper representation of fungal growth. Finally, the environmental conditions need to be controlled and the effects of other external factors should be reduced as much as possible. For this purpose, we have developed a new experimental set-up meeting these criteria which is based on the experimental set-up described in Chapter 5.

In order to ensure growth, we have used 8% malt extract agar as substrate in Petri dishes of 9 cm diameter and 0.6 mm height. These disks were used to cultivate mother cultures from the ones described above. After three days of growth, a disk-shaped inoculum of about 1 cm diameter was cut from the periphery of the mother culture. So, the inoculum had the same height as the original agar disk, i.e. 0.6 mm. Then, the inoculum was placed at the centre of the bottom lid of a Petri dish, surrounded by 12 substrate disks (0.5 cm diameter and 0.6 mm height). This allows to keep the environmental conditions inside the Petri dish constant. Finally, the top lid of the Petri dish was placed on top of the bottom lid, as such restricting the height between the lids to 0.6 mm. Using thin agar disks instead of droplets (as in Chapter 5) leads to better images since the former keep their shape and position even after closing the Petri dish, in contrast to the droplets where the substrate can get displaced after closing the Petri dish. Each disk contains the same amount of substrate and since they are placed at the same positions on the lid, we may conclude that the substrate was spatially distributed in the same way in each sample. In addition, the agar disks also maintain their shape during the course of the experiments and these shapes can be easily detected by dedicated image analysis algorithms, as such allowing for the automatic generation of masks.

Images of the growing fungi were captured using a flat bed scanner on top of which the Petri dishes were mounted. The samples were placed on the scanner right after they were prepared, in order to capture early growth, and growth was tracked for

72 hours. During this period, images were scanned automatically every 15 min. The images have a resolution of 1200 dpi and were automatically cropped to the Petri dish, leading to images of 9 cm × 9 cm.

In order to assess the effects of the environmental conditions on fungal growth, we placed the flat bed scanner in a climate chamber where temperature and RH values could be adjusted. The specific values for our experiments were selected in order to cover those used in similar experiments (e.g. Meyer and Brischke (2015); Brischke and Rapp (2008); Tommerup (1983); Magan and Lacey (1984); Boddy (1983); Trinci (1969); Bjurman and Wadsö (2000); Ekesi et al. (1999)). Temperature was varied from 15° to 30° C in steps of 5° C, while RH was varied between 65% to 80%, with steps of 5% as in Bonner and Fergus (1960); Pasanen et al. (1991); Pardo et al. (2005); Bonner (1948). Although studies often investigate scenarios with RH close to 100%, this was not possible with our set-up because the scanner cannot operate at an RH higher than 80%.

In summary, four different temperatures and four different relative humidities were considered giving a total of 16 environmental conditions. The growth of four replicates was followed during a period of 72 hours, resulting in 269 images per sample, i.e. a total of 17, 216 images.

6.2.2 Image processing and quantification of fungal growth

First, the inoculum and the substrate were subtracted from the images since growth within these regions cannot be captured. For this purpose, masks were constructed automatically and subtracted from each image using Mathematica (Version 10.0, Wolfram Research Inc., USA). We used the algorithm introduced in Chapter 4 on the aforementioned images in order to obtain binary ridge maps of the growing fungus. Then, the binary ridge maps were translated into graphs as described in Chapter 5. Different graph characteristics can be obtained from these graphs in order to investigate fungal growth. For instance, measures quantifying fungal growth and expansion, such as the total length of the mycelium and the area covered by the mycelium can be easily computed from them. In addition, measures such as the number of tips and the node density that give insight into the compactness of the mycelium can be calculated. Finally, other measures accounting for the morphology of the fungi can also be obtained including the average internodal length and the growth angle. For more details, we refer the reader to Chapter 5.

These topological measures were tracked during 72 hours for each environmental condition and replicated four times, resulting in 64 curves per measure. In the remainder of this chapter, the topological measures are those computed from

mean curves that were generated by averaging the corresponding time-stamped measure over the four replicates of each condition.

6.2.3 Mathematical and statistical analysis

Clearly, varying temperature and RH might also have an interactive effect on the different topological measures. In order to account explicitly for the impact of temperature, RH and their combined effect on the different topological measures, we constructed several predictive models. The models were constructed using mean curves in two stages, referred to as primary and secondary modelling.

6.2.3.1 Primary modelling

In this modelling stage, a growth function depending only on time is fitted to the growth data. At the end of this stage, a growth function representing the growth data with fitted parameters is obtained.

Here, we fitted both the Gompertz function (Gompertz, 1825; Zwietering et al., 1990) and the growth function of Baranyi (Baranyi and Roberts, 1994) to the values obtained for each of the topological measures. The former function belongs to the family of sigmoidal curves widely used to model biomass growth (Adan, 2011; Barry and Williams, 2011). Besides, Chapter 5 concluded that this function is capable of representing the evolution of several fungal growth features over time. The Gompertz function is given by:

$$y(t) = y_0 + (y_{max} - y_0)\, e^{-e^{1+g\,e\,\frac{(\lambda - t)}{(y_{max} - y_0)}}}, \tag{6.1}$$

where $y(t)$ typically represents the biomass, y_0 and y_{max} represent the initial and the maximum biomass, respectively, g represents the maximum growth rate and λ the duration of the lag phase.

The growth function of Baranyi and Roberts (1994) was originally developed to describe bacterial growth in food as the evolution over time of the cell concentration of a given bacteria. However, it has been widely used to predict the expansion of fungal colonies under different environmental conditions (Samapundo et al., 2005, 2007; Mousa et al., 2016). Moreover, this function has been used to describe the evolution of the diameter of fungal colonies and is given by:

$$y(t) = y_0 + g\,A(t) - \ln\left(1 + \frac{e^{g\,A(t)} - 1}{e^{y_{max} - y_0}}\right), \tag{6.2}$$

where

$$A(t) = t + \left(\frac{1}{g}\right) \ln\left(e^{-g\,t} + e^{g\,\lambda} - e^{-g\,t - g\,\lambda}\right), \tag{6.3}$$

and $y(t)$ represents the colony diameter, g the maximum growth rate, y_0 the initial diameter of the fungal colony at time $t = 0$, y_{max} the maximum colony diameter and λ the duration of the lag phase. In the remainder of this chapter, $y(t)$ will be used to denote any of the topological measures introduced in Section 6.2.2.

6.2.3.2 Secondary modelling

In this stage, the parameters obtained from Eqs. (6.2) and (6.1) fitted to the obtained data (6.2.3.1) are modelled as functions of temperature, RH or both. Here, we will focus on the maximum growth rate and the duration of the lag phase since these parameters appear in both the Gompertz and the Baranyi growth function.

In order to assess the effect of the environmental conditions on the aforementioned growth parameters, we use a polynomial of second degree (see Eq. (6.4)) since it has been shown that such a construct allows to describe the effect of temperature, humidity and their combination (Samapundo et al., 2005, 2007; Mousa et al., 2016). Consequently, in order to assess the effects of either temperature or RH on the maximum growth rate g, we use:

$$\ln(g) = C_0 + C_1 T + C_2 T^2, \tag{6.4}$$

$$\ln(g) = C_0 + C_1 H + C_2 H^2, \tag{6.5}$$

and similarly for the lag phase duration λ. T (° C) represents temperature and H (%) represents RH. The combined effect of temperature and RH is studied using the following second-order polynomial function:

$$\ln(g) = C_0 + C_1 H + C_2 H^2 + C_3 T + C_4 T^2 + C_5 T H, \tag{6.6}$$

and similarly for the lag phase duration λ. The coefficients of Eqs. (6.4), (6.5) and (6.6) were determined by fitting them to estimated maximum growth rates and lag phase durations, as obtained in the primary modelling stage (Section 6.2.3.1). For that purpose, the Nonlinearmodelfit function, based on the Quasi-Newton method, was used in Mathematica.

6.3 Results

6.3.1 Fungal growth curves

Several measures can be used to track the growth and evolution of fungi (see Chapter 5), but in the remainder we focus on four measures summarizing the

extension and the compactness of the mycelium, namely the total length, the area covered by the mycelium, the total number of tips, and the node density. In addition, two measures summarizing the morphology of the mycelium (the growth angle and the mean hyphal length) are also computed, but due to the lack of correlation with either temperature or RH, they will be only briefly discussed.

The evolution of the total length of the mycelium over time for each of the environmental conditions (Section 6.2.1) is shown in Figure 6.1. Two different types of behaviour can be observed. For most environmental conditions, growth starts almost immediately and increase is always monotone until a plateau is reached, after which it levels off, a behaviour observed for several other fungal species (Trinci, 1974; Prosser and Trinci, 1979; Pasanen et al., 1991). In contrast, for some environmental conditions, mainly those with low temperature, the total length increases during the entire period. This behaviour has been also reported for the total length of *Mucor spinosus* (Indermitte et al., 1994) and is consistent with our previous findings (Chapter 5). The maximum total length of *Coniophora puteana* is reached at an RH of 75% and a temperature of 20° C, which agrees with the optimal growth conditions for this species, defined as 22° C and 70 — 80% RH (Adan and Samson, 2011). The minimum total length is observed at 75% RH, and 25° C. Figures 6.2(a) and 6.2(b) show the total length grouped by temperature and RH, averaged over the different temperatures and RH, respectively. The maximum total length as a function of temperature shows that, generally speaking, lower temperatures result in higher total length of the mycelium (Figure 6.2(a)). In the case of RH, most observed hyphae are created at an RH of 75%, followed by 80%, 70% and 65% (Figure 6.2(b)).

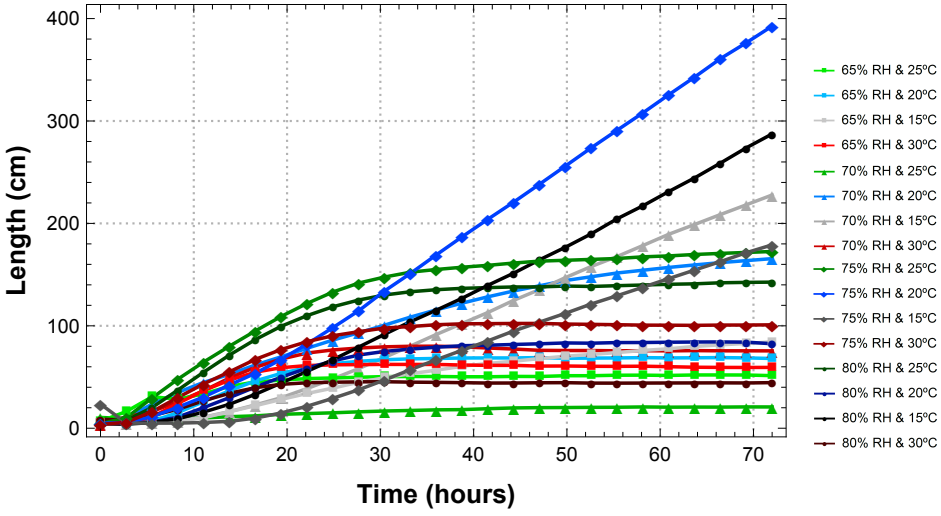

Figure 6.1: Average total length over time for different environmental conditions.

In Figure 6.2(c) the evolution of the total number of tips over time per tempera-

ture is shown. The same growth trends as for the total length (Figure 6.2(a)) can be discerned. Indeed, the number of tips levels off after a few hours when temperature is higher than 25° C, while cultures growing at lower temperatures grow continuously and produce a higher numbers of tips. In Figure 6.2(d), as in the case of the total length, an RH of 75% leads to more tips. Moreover, the greater the difference in RH with the optimum of 75%, the lower the number of tips.

The evolution of the area covered by the mycelium as a function of temperature and RH can be found in Figure 6.2(e) and 6.2(f), respectively. The maximum area is obtained in the scenarios with a temperature of 20° C, where the area increases linearly over time during the entire period. Although a similar growth behaviour can be observed at 15° C, the remaining two temperatures exhibit an almost exponential growth only at the beginning of the experiment after which a plateau is reached and growth stabilizes. This measure is an extension of the colony diameter, a widely studied measure for which similar behaviour has been reported in literature (Pasanen et al., 1991; Samapundo et al., 2005). In view of Figure 6.2(f), we may conclude that the lowest area corresponds to the lowest RH. The samples grown at 80% and 70% lead to similar areas at the end of the experiment, which are almost the double of the ones grown at 65% RH. Finally, the largest mycelium, with an area of approximately 5.5cm^2, is obtained at an RH of 75%. These findings suggest that the maximum area covered by *Coniophora puteana* is obtained for temperatures between 15° C and 20° C and an RH of 75%.

The node density (Figures 6.2(g) and 6.2(h)) is often used to assess the compactness of mycelia. An increase of this measure indicates that the mycelium produces new nodes, by branching or extending its apices, faster than it colonizes space, while a decrease denotes either a rapid colonization of space or a cessation of growth. As can be observed in Figure 6.2(g), the node density increases over time, irrespective of the temperature reaching values within the range of those observed for other species (see Chapter 5). Yet, while it increases rapidly for most temperatures until a plateau is reached, at 15° C it increases during the entire period, as such resulting in a denser network. In Figure 6.2(h), showing the node density for different RH values, similar trends can be observed. In this case, the densest networks are obtained at an RH of 75%.

In addition to the aforementioned measures, we also studied the morphology of the mycelium in terms of the growth angle and the average hyphal length. These measures show a significant variability over time irrespective of the temperature and RH, and no correlation with either temperature or RH was observed. The averages computed over time lead to average hyphal length values of around 200 microns and 0.75 radians for the growth angle, which agrees with the findings reported in Chapter 5, as such suggesting that these morphological features depend on the fungal species and to a much lesser extent on the environmental conditions.

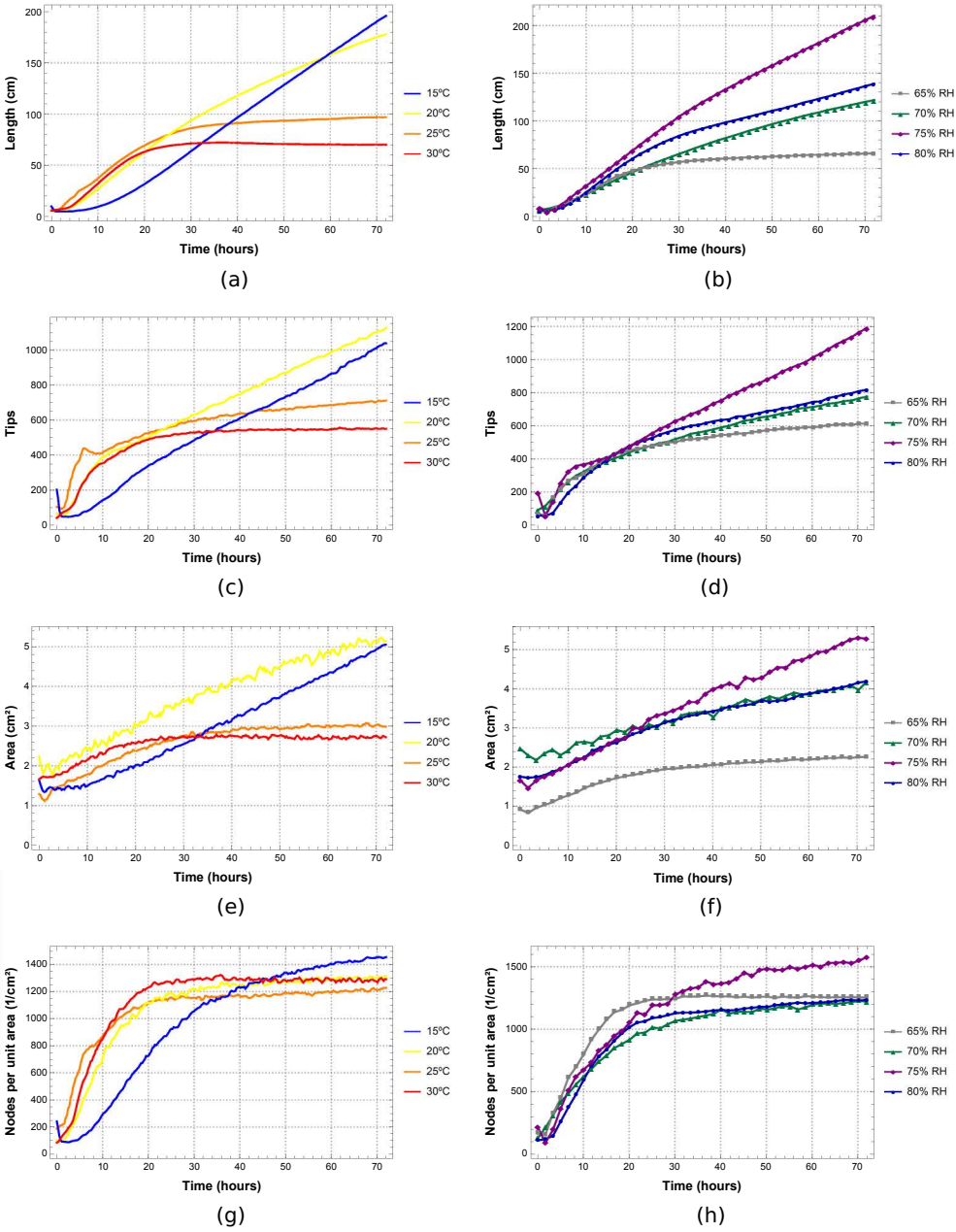

Figure 6.2: Topological measures averaged over temperature or RH. The graphs show the evolution over time of the total length (a-b), the number of tips (c-d), the area covered by the mycelium (e-f) and the node density (g-h) grouped by temperature and RH, respectively.

6.3.2 Effects of temperature and relative humidity on fungal growth

6.3.2.1 Modelling stages

In the primary modelling stage, the log of the average data over the four replicates for each studied environmental condition was used to fit the functions described in Eqs. (6.1) and (6.2), as such resulting in two sets of parameters for each condition and measure. This allows us to study the effect of the environmental conditions on the parameters of the fitted functions. Here, we focus on two growth parameters, namely the lag phase duration λ and the maximum growth rate g.

As an example, Figure 6.3 shows the fitted Gompertz and Baranyi functions for the total length for four environmental conditions together with the corresponding data. The average coefficients of determination (R^2) of the fitted functions can be found in Table 6.1 for all considered topological measures. As can be observed in this table, for most conditions both functions yield R^2 that are higher than 0.9, indicating a good fit (Saltelli et al., 2004). Therefore, we may conclude that the Gompertz and Baranyi functions properly represent the data obtained for each topological measure.

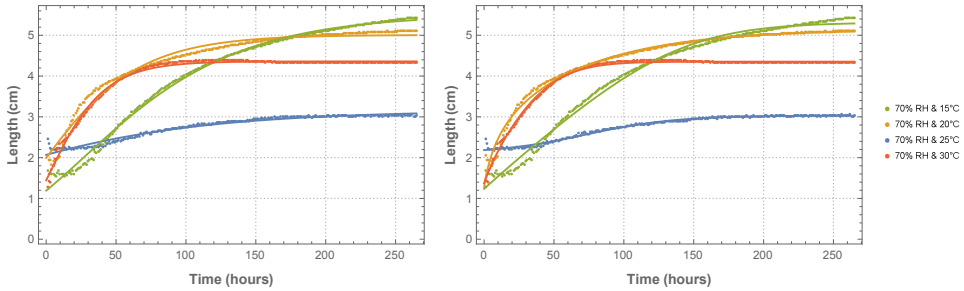

Figure 6.3: Average measured total length for four temperatures at 70% RH over time (dot) and the corresponding fitted (a) Gompertz and (b) Baranyi functions (solid lines).

Table 6.1: Average coefficient of determination (R^2) for the Gopertz and Baranyi functions fitted to the average data obtained for each topological measure.

Topological measure	Gompertz	Baranyi
Total length	0.999166	0.999426
Tips	0.997813	0.999495
Area	0.993473	0.977230
Node density	0.997999	0.891336

As a preliminary step, we conduct a correlation analysis between the growth pa-

rameters of the fitted functions (g and λ) and the environmental conditions (Table 6.2) in order to get some insight about their underlying association. Most correlation coefficients are low, indicating a lack of correlation between the fitted parameters and the environmental conditions. However, the correlation values are higher for the maximum growth rate g, especially for the parameters obtained for the Gompertz function. While temperature exhibits a positive association with most of the studied topological measures indicating that most measures increase as a function of temperature, the linear association between the RH and the topological measures varies significantly and therefore it is not possible to depict a general trend. This correlation analysis suggests that a linear association is not able to capture the existent relation between the primary modelling parameters and the environmental conditions and therefore other types of association should be studied.

Table 6.2: Correlation coefficients between the fitted parameters, maximum growth rate g and lag phase duration λ, and the environmental conditions, temperature and RH.

Measure	Total length		Number of tips		Area		Node density	
Function	Gompertz	Baranyi	Gompertz	Baranyi	Gompertz	Baranyi	Gompertz	Baranyi
Temperature and g	0.6516	0.5979	-0.3460	0.2117	0.1225	0.1202	0.4572	0.1407
Temperature and λ	0.0753	0.0778	0.2487	0.1672	0.1071	-0.2461	-0.3015	0.1017
RH and g	-0.1014	-0.0769	0.1152	-0.3751	-0.1144	0.3294	-0.1360	-0.0228
RH and λ	0.0747	-0.0089	0.0245	-0.0002	-0.1122	0.3206	0.1673	-0.0115

In the secondary modelling stage, the dependency of the growth parameters on temperature and RH is further investigated. These parameters are used to fit one of Eqs. (6.4), (6.5) and (6.6). In order to better represent the effects of the environmental conditions and to be consistent with previous studies, we use transformed values $\ln(g)$ and $1/\lambda$ of the growth parameters to fit the aforementioned models, a common practice in similar studies (Samapundo et al., 2005, 2007; Zhou et al., 2012; Mousa et al., 2016).

6.3.2.2 Temperature and fungal growth

In order to study the individual effect of temperature on the selected topological measures, we fit Eq. (6.4) to model parameters g and λ obtained during the primary modelling stage. The coefficients of Eq. (6.4) fitted to $\ln(g)$ and $1/\lambda$ are shown in Tables 6.3 and 6.4, respectively. For what concerns the total length, the polynomial shows a good fit for the maximum growth rate (see Table 6.3). Even though the coefficients of the two fitted polynomials have opposite signs within the range of interest, the maximum growth rate increases as a function of temperature for both the Gompertz and the Baranyi functions (see Figure 6.4). This behaviour has been observed by others (Fuhr et al., 2012; Ekesi et al., 1999). As can be observed in this figure, the values obtained for the parameters of the Gompertz and the Baranyi functions differ somewhat, which could be due to their

dependence on the specific functional form (Baty and Delignette-Muller, 2004). In addition, a few of the values lie further from the rest of the data-set. This could be caused by the differences in growth behaviour shown in Figure 6.1. The maximum growth rate of the number of tips obtained using the Gompertz function cannot be properly expressed as a polynomial depending only on temperature given the low R^2 (0.4894). On the other hand, the maximum growth rates obtained using the Baranyi function increase as a function of temperature. The maximum growth rate of the area and the node density obtained with the Baranyi function cannot be fitted by a polynomial, as opposed to those obtained with the Gompertz function. The maximum growth rate of the mycelium area shows an increase until a maximum after which it decreases, a similar behaviour to that reported for the colony radius for other fungal species (Ekesi et al., 1999; Boddy, 1983; Kim et al., 2005). While the maximum growth rate of the node density shows a similar trend as the one observed for the total length and the number of tips,

Table 6.3: Fitted parameters of $\ln(g) = C_0 + C_1 T + C_2 T^2$ using the maximum growth rates g obtained from the primary modelling stage.

Measure	Total length		Number of tips		Area		Node density	
Function	Gompertz	Baranyi	Gompertz	Baranyi	Gompertz	Baranyi	Gompertz	Baranyi
C_0	-4.8614	-2.0012	8.3317	-3.9469	-12.5767	N/A	-2.5049	N/A
C_1	0.1191	-0.1641	-0.8936	-0.0563	0.7019	N/A	0.1143	N/A
C_2	-0.0015	0.0049	0.0184	0.0037	-0.0138	N/A	-0.0018	NA
R^2	0.9784	0.9821	0.4894	0.8129	0.9272	N/A	0.7048	N/A
MSE	0.3196	0.2762	6.3182	3.9369	2.2572	N/A	0.6038	N/A

For the lag phase duration λ, only the one for the total length with the Gompertz function could be fitted by the polynomial (Table 6.4). Apparently the lag phase duration increases as a function of temperature (Figure 6.4) in contrast to the dynamics observed in previous studies (Samapundo et al., 2005, 2007; Boddy, 1983). We should note that even though the effects of the environmental conditions are discussed on the lag phase duration directly, the graphs and tables in the remainder of this chapter show its reciprocal. Therefore, an increase of the lag phase duration is reflected as a decrease of its reciprocal and vice versa. For the other parameters we cannot draw any conclusions due to the lack of correlation between the data and the fitted curves.

Table 6.4: Fitted parameters of $\frac{1}{\lambda} = C_0 + C_1 T + C_2 T^2$ using the lag phase duration values λ obtained from the primary modelling stage.

Measure	Total length		Number of tips		Area		Node density	
Function	Gompertz	Baranyi	Gompertz	Baranyi	Gompertz	Baranyi	Gompertz	Baranyi
C_0	-0.0231	-0.4817	1.4725	0.0464	1.4942	-0.1444	1.4725	0.0464
C_1	0.004	0.0415	-0.1262	-0.0040	-0.1504	0.0115	-0.1262	-0.0040
C_2	-0.00006	-0.0008	0.0027	0.00008	0.0035	-0.0001	0.0027	0.00008
R^2	0.8174	0.1159	0.2071	0.2190	0.1851	0.2281	0.2071	0.2190
MSE	0.0009	0.0139	0.1202	0.00004	0.0862	0.0028	0.1202	0.00004

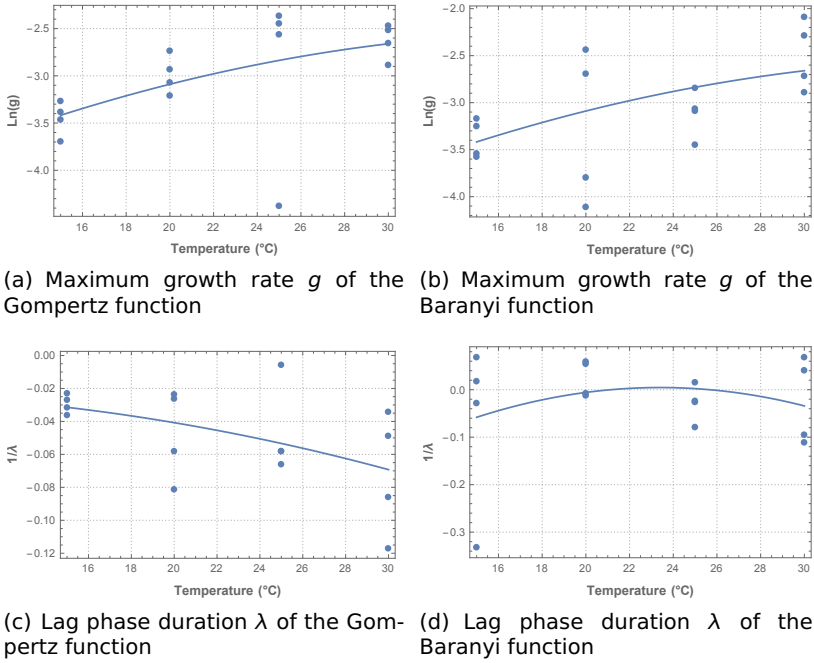

(a) Maximum growth rate g of the Gompertz function

(b) Maximum growth rate g of the Baranyi function

(c) Lag phase duration λ of the Gompertz function

(d) Lag phase duration λ of the Baranyi function

Figure 6.4: Plot of the maximum growth rate (a-b) and the lag phase duration (c-d) obtained for the total length given by Eq. (6.4). The dots represent the model parameters of the Gompertz and the Baranyi functions determined in the primary modelling stage.

6.3.2.3 RH and fungal growth

A similar analysis was performed for the RH using Eq. (6.5) in order to assess the effect of RH on the growth parameters of the Gompertz and Baranyi functions. The fitted parameters are shown in Tables 6.5 and 6.6 for g and λ, respectively. Both the Gompertz and Baranyi parameters obtained for the total length behave similarly: the maximum growth decreases, reaches a minimum around 70% RH and then increases again (see Figure 6.5). In order to study the impact of the RH on the maximum growth rate of the number of tips, we must turn to the Baranyi function since the Gompertz shows a suboptimal fit with a R^2 below 0.70. The maximum growth rate of this measure reaches a minimum between 70 and 75% RH and then grows again. The parameters obtained for the maximum growth rate of the area and the node density take significantly low values, as such suggesting that these measures are not strongly influenced by RH. Even though growth rates have been widely studied using the water potential and the moisture content (Gock et al., 2003; Samapundo et al., 2007; Boddy, 1983; Pardo et al., 2004), the values studied cover a different range than our study and therefore are difficult to relate to our data as such hindering an accurate validation of the maximum growth rates obtained. For instance, one of the few studies investigating the effect of RH on

fungal growth in a similar range of interest (Pasanen et al., 1991) shows very similar growth rates of the colony diameter for RH between 75 and 92% as such agreeing with our findings.

Table 6.5: Fitted parameters of $\ln(g) = C_0 + C_1 H + C_2 H^2$ using the maximum growth rates g obtained from the primary modelling stage.

Measure	Total length		Number of tips		Area		Node density	
Function	Gompertz	Baranyi	Gompertz	Baranyi	Gompertz	Baranyi	Gompertz	Baranyi
C_0	34.2995	55.3757	-96.3801	152.568	-35.8295	N/A	37.9888	N/A
C_1	-1.0332	-1.6195	2.5975	-4.2456	0.8931	N/A	-1.0727	N/A
C_2	0.0071	0.0111	-0.0177	0.0287	-0.0062	N/A	0.0073	NA
R^2	0.9731	0.9783	0.4737	0.8358	0.9122	N/A	0.7080	N/A
MSE	0.3986	0.3345	6.5120	3.455	2.7226	N/A	0.5973	N/A

As in the case of temperature, the dependence between λ and RH cannot be described adequately using Eq. (6.5). The only valid fit is obtained for the maximum growth rate computed from the Gompertz function, which suggests that the lag phase duration decreases as the RH increases (see Figure 6.5) agreeing with the behaviour observed in similar studies (Samapundo et al., 2007; Boddy, 1983). However, this growth parameter shows low curvature and slope, indicating a weak effect of RH.

Table 6.6: Fitted parameters of $\frac{1}{\lambda} = C_0 + C_1 H + C_2 H^2$ using the lag phase duration values λ obtained from the primary modelling stage.

Measure	Total length		Number of tips		Area		Node density	
Function	Gompertz	Baranyi	Gompertz	Baranyi	Gompertz	Baranyi	Gompertz	Baranyi
C_0	-2.3161	9.2678	4.4818	16.2212	-3.0474	-0.6150	23.5676	-0.1969
C_1	0.0618	-0.2565	-0.1247	-0.4541	0.0909	0.0188	-0.6591	0.0052
C_2	-0.0004	0.0017	0.0008	0.0031	-0.0006	-0.0001	0.0046	-0.00003
R^2	0.7991	0.2593	0.3145	0.3479	0.0321	0.1191	0.3188	0.1361
MSE	0.0010	0.0116	0.0120	0.0533	0.1024	0.0032	0.1033	0.00004

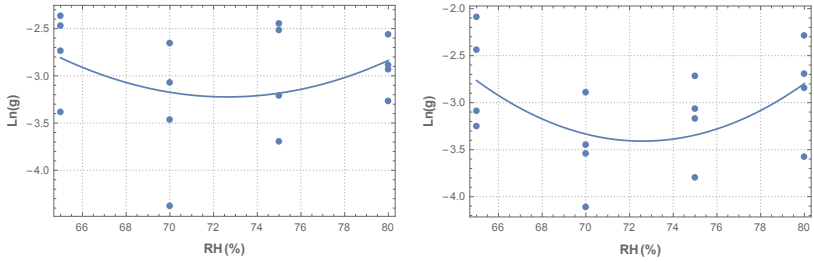

(a) Maximum growth rate g of the Gompertz function

(b) Maximum growth rate g of the Baranyi function

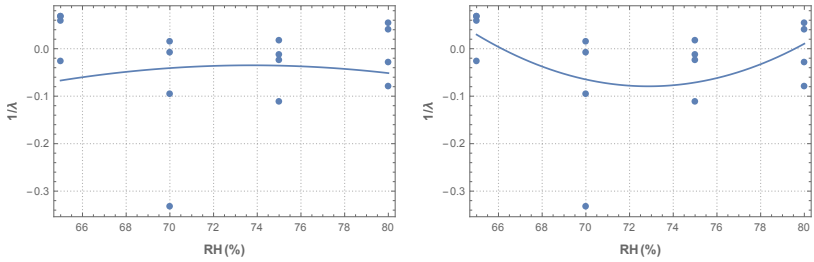

(c) Lag phase duration λ of the Gompertz function

(d) Lag phase duration λ of the Baranyi function

Figure 6.5: Plot of the maximum growth rate (a-b) and the lag phase duration (c-d) obtained for the total length given by Eq. (6.5). The dots represent the model parameters of the Gompertz and the Baranyi functions determined in the primary modelling stage.

6.3.2.4 Combined effect of temperature and RH on fungal growth

In order to assess the interactive effect of temperature and RH on the topological measures, we fit Eq. (6.6) to the model parameters obtained in the primary modelling stage. Tables 6.7 and 6.8 show the coefficients of Eq. (6.6) for g and λ, respectively. It can be observed that the R^2 are not substantially higher and the mean squared errors are only slightly lower with the incorporation of the combined effects. In addition, the order of magnitude of the combined effect coefficient, C_5, is much lower than those of the others. This suggests a weak interaction between the two environmental factors.

In order to further compare the models constructed in this section we use the Akaike information criterion (AIC) (Posada and Buckley, 2004). Consequently, we compute the AIC value of each of the models as listed in Table 6.9. The minimum AIC value is always obtained with the polynomial of Eq. (6.6), as such indicating that this is the best model to represent the parameters of the primary modelling functions. For most measures and parameters, there is a significant difference between the AIC values obtained with Eq. (6.4) and (6.5) and the minimum AIC value obtained with Eq. (6.6) which implies an improvement by the addition of the interactive effect of both environmental conditions. However, for some measures

Table 6.7: Fitted parameters of $\ln(g) = C_0 + C_1 H + C_2 H^2 + C_3 T + C_4 T^2 + C_5 T H$ using the maximum growth rates g obtained from the primary modelling stage.

Measure	Total length		Number of tips		Area		Node density	
Function	Gompertz	Baranyi	Gompertz	Baranyi	Gompertz	Baranyi	Gompertz	Baranyi
C_0	31.3395	57.8492	-105.961	146.958	-50.555	N/A	29.5582	N/A
C_1	-1.0180	-1.6390	2.8702	-4.1784	0.9807	N/A	-0.9781	N/A
C_2	0.0071	0.0111	-0.0177	0.0287	-0.0062	N/A	0.0073	N/A
C_3	0.1680	-0.2270	-0.0150	0.1601	0.9842	N/A	0.4191	N/A
C_4	-0.0015	0.0049	0.0184	0.0037	-0.0138	N/A	-0.0018	N/A
C_5	-0.0006	0.0008	-0.0121	-0.0029	-0.0038	N/A	-0.0042	N/A
R^2	0.9819	0.9902	0.535966	0.8667	0.9296	N/A	0.7460	N/A
MSE	0.2682	0.1504	5.7421	2.8044	2.1826	N/A	0.5195	N/A

Table 6.8: Fitted parameters of $\frac{1}{\lambda} = C_0 + C_1 H + C_2 H^2 + C_3 T + C_4 T^2 + C_5 T H$ using the lag phase duration values λ obtained from the primary modelling stage.

Measure	Total length		Number of tips		Area		Node density	
Function	Gompertz	Baranyi	Gompertz	Baranyi	Gompertz	Baranyi	Gompertz	Baranyi
C_0	-1.9394	8.3847	4.86722	15.5051	-1.5355	0.3217	30.6773	-0.1114
C_1	0.0570	-0.2507	-0.1364	-0.4553	0.0902	0.0037	-0.7386	0.0046
C_2	-0.0004	0.0017	0.0008	0.0031	-0.0006	-0.0001	0.0046	-0.00003
C_3	-0.0151	0.0604	0.0022	0.0776	-0.1525	-0.0371	-0.3822	-0.0058
C_4	-0.00006	-0.0008	-0.0008	-0.0019	0.0035	-0.0001	0.0027	0.00008
C_5	0.0002	-0.0002	0.0005	0.00005	0.00002	0.0006	0.0035	0.00002
R^2	0.8774	0.3240	0.4137	0.4071	0.2034	0.4517	0.4986	0.3102
MSE	0.0006	0.0106	0.0102	0.0484	0.0843	0.0020	0.0760	0.00003

and parameters (e.g. the maximum growth rate and the lag phase of the mycelium area) the AIC values are very close to each other, denoting poor improvement, as such it is impossible to decide which model is better to represent them.

Table 6.9: Akaike information criterion (AIC) value obtained for the fit of Eq.(6.4), 6.5 and 6.6 to the parameters of the Baranyi and the Gompertz function.

Measure	Total length		Number of tips		Area		Node density	
Function	Gompertz	Baranyi	Gompertz	Baranyi	Gompertz	Baranyi	Gompertz	Baranyi
$\ln(g) = C_0 + C_1 T + C_2 T^2$	33.6389	31.3052	81.381	73.8124	64.9125	N/A	43.8144	N/A
$\ln(g) = C_0 + C_1 H + C_2 H^2$	37.1692	34.3686	81.8645	71.7231	67.9115	N/A	43.6424	N/A
$\ln(g) = C_0 + C_1 H + C_2 H^2 + C_3 T + C_4 T^2 + C_5 T H$	30.8296	21.5821	79.8513	68.3854	64.3748	N/A	41.4096	N/A
$\frac{1}{\lambda} = C_0 + C_1 T + C_2 T^2$	-59.981	-16.454	-19.568	7.09022	12.6858	-41.954	17.9947	-108.31
$\frac{1}{\lambda} = C_0 + C_1 H + C_2 H^2$	-58.456	-19.285	-18.861	4.98271	15.4384	-39.841	15.566	-106.69
$\frac{1}{\lambda} = C_0 + C_1 H + C_2 H^2 + C_3 T + C_4 T^2 + C_5 T H$	-66.362	-20.749	-21.362	3.46084	12.3216	-47.429	10.6616	-110.30

As an example, the growth parameters obtained in the primary modelling stage and the response surface obtained with Eq. (6.6) are shown in Figure 6.6 for the total length. The graphs suggest that the effect of RH is slightly stronger than the effect of temperature, in agreement with other studies (Samapundo et al., 2007, 2005). Even though the synergistic interaction between the two environmental factors can be observed, it is much less pronounced than reported for other fungal species and growth scenarios (Samapundo et al., 2007; Zhou et al., 2012). As can be observed in Figure 6.6, the effects of the environmental conditions are more pronounced for the Baranyi function than for the Gompertz function. As was already observed in Section 6.3.2.2, the maximum growth increases with temper-

ature. In contrast, it decreases until it reaches a minimum and then grows again as RH increases. The effect of the environmental conditions is even more evident for the lag phase. However, only the polynomial fitted to the parameters of the Gompertz function showed a sufficiently good fit. The lag phase duration λ of the total length for the Gompertz parameters increases as a function of temperature and decreases as a function of RH. The surface plots of the other measures show a similar behaviour, i.e. mainly the combination of the effects obtained from the individual effects without much interaction and therefore will not be further discussed.

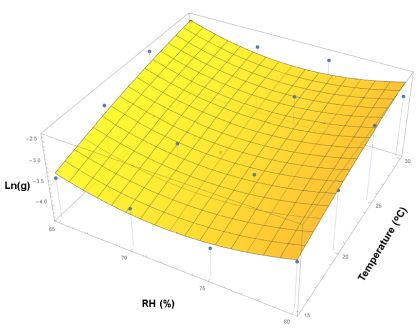

(a) Maximum growth rate g of the Gompertz function

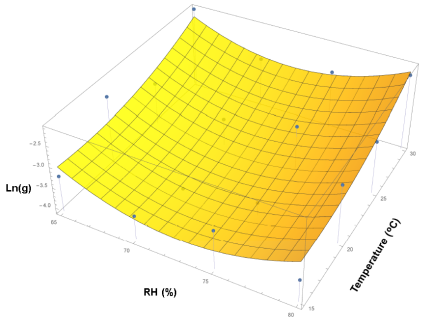

(b) Maximum growth rate g of the Baranyi function

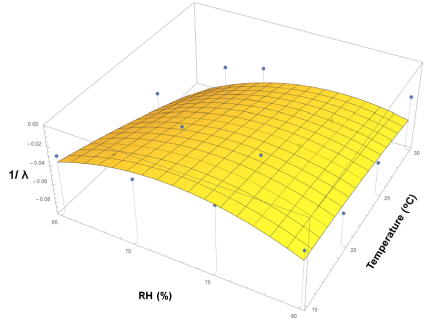

(c) Lag phase duration λ of the Gompertz function

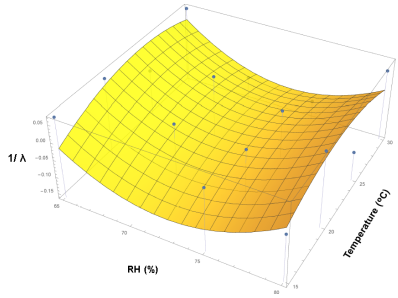

(d) Lag phase duration λ of the Baranyi function

Figure 6.6: Response surfaces of the maximum growth rate (a-b) and the lag phase duration (c-d) given by Eq. (6.6). The dots represent the model parameters of the Gompertz and the Baranyi functions determined in the primary modelling stage.

6.4 Discussion

The experimental set-up presented in Chapter 5 was adjusted in this chapter in order to assess the effect of temperature and RH on fungal growth by using agar

disks, allowing us to capture better images and to build masks automatically. The images were acquired in a climate cabinet with control of the environmental conditions could be changed.

Images were used here to compute different topological measures accounting for different aspects of fungal growth, instead of focussing on a single measure as in most studies (Samapundo et al., 2007; Pardo et al., 2004; Boddy, 1983; Kim et al., 2005; Zhou et al., 2012). Topological measures such as the total length provide more accurate information on the development of fungi since they track all hyphae of the mycelium instead of relying on macroscopic measures such as the colony radius (Samapundo et al., 2007; Boddy, 1983) or limiting to a few hyphae (Ramakrishna et al., 1993; Laarhoven et al., 2015; Siripatrawan and Makino, 2015; Gougouli and Koutsoumanis, 2013). Also the morphology and the compactness of the fungus can be followed over time, as well as the impact of temperature and RH thereon. In addition, these measures can be obtained from the same sample over time since image analysis is non destructive. Essentially, our method provides an alternative to destructive techniques often use to study the effect of the environment on fungi (Meyer and Brischke, 2015; Brischke and Rapp, 2008; Osono, 2015). Furthermore, the image acquisition and the computation of the topological measures is done automatically, as such avoiding the use of manual techniques. Even though our technique presents a valid alternative to established techniques, there is still room for improvement in both the experimental set-up and the image processing as discussed in Chapter 5.

The main results presented in this chapter agree with those obtained in different studies, as such demonstrating the validity of our method to assess the effects of temperature and RH on fungal growth. For instance, two distinct types of growth behaviour were observed: uniform growth (Indermitte et al., 1994) and exponential growth (Trinci, 1974; Prosser and Trinci, 1979; Pasanen et al., 1991). The optimal growth conditions of *Coniophora puteana* observed at 70% RH and 25° C also agree with those reported in other studies (Adan and Samson, 2011; Etheridge, 1957). The data obtained from the time series of images allows for fitting a Gompertz and Baranyi functions to the extracted topological measures. The involved model parameters can subsequently be studied as functions of temperature and RH. We note here that the value of these parameters are dependent on the form of the fitted function (Baty and Delignette-Muller, 2004) and are thus different for the Gompertz compared to the Baranyi, as can be observed in Figures 6.4, 6.5 and 6.6.

These growth parameters can be compared with those obtained in similar studies (Samapundo et al., 2007; Pardo et al., 2004; Zhou et al., 2012). The effect of temperature on the maximum growth rate seems to agree with previous findings irrespective of the topological measures considered. However, the relation of λ and the temperature and RH cannot be properly considered using this approach since the values obtained for λ yielded poor fits for most measures. This might

be a consequence of the experimental design, as in our experiments growth starts almost immediately since an active mycelium is present from the beginning of the experiment, so that a lag phase is not captured. One of the most striking observations from this analysis is the effect of temperature on the maximum growth rate of the total length. The maximum growth rate increases as a function of temperature for this measure even though the maximum total length values are observed at lower temperatures. This actually suggests that growth occurs in an exponential way at high temperatures, after which a plateau is reached, while lower temperatures lead to mycelium that grows continuously during the entire period and as such results in a much higher total hyphal length. A similar behaviour can be observed for the number of tips, which is strongly correlated with the latter measure, a correlation that seems to persist even under changing environmental conditions. When studying the effect of the RH, we also observed that higher growth rates result in smaller mycelia. However, in this case the correlation is not that clear since the growth rate as a function of RH shows a change of behaviour after a minimum is reached. Even though the interactive effect of both environmental factors plays a role in fungal growth, it is not significant for any of the topological measures within the range studied.

Even though similar results have already been observed for different fungal species and conditions, this work presents the first characterization relying on images of growing fungi. In addition, we were able to study measures by considering the entire mycelium, resulting in a comprehensive characterization of fungal dynamics under different environmental conditions, as opposed to other studies. For instance, this method could be used in the assessment of decay, as an alternative to the visual inspection of the samples, thereby yielding more objective results and avoiding manual work (Pasanen et al., 2000; Nielsen et al., 2004). In addition, models such as the ones introduced in Chapter 3 often neglect the effects of the environmental conditions but using the methods described in this chapter some of the model parameters could be replaced by a relationship characterising their dependence on temperature and RH.

6.5 Conclusions

In this chapter an automated method based on image analysis was used to measure the effects of two environmental conditions on fungal growth. For this purpose, we employed an adapted version of the method presented in Chapter 5, allowing us to study fungal images captured under different temperatures and RH. This method overcomes some of the problems of most currently used approaches, yielding a complete characterization of the effects of temperature and RH on fungal growth. The main results of this study are in line with similar studies found in literature as such suggesting that our approach is suitable for studying these

factors. Finally, due to the simplicity of the techniques used in this work, similar characterizations could be easily achieved for several growth species and environmental conditions, as such allowing researches to address further open questions regarding the effect of environmental conditions on fungal growth.

PART III

MATHEMATICAL MODELLING FOR FUNGAL GROWTH

7

Modelling three-dimensional fungal growth in response to environmental stimuli

7.1 Introduction

Fungi develop complex networks that function as efficient transport structures along which nutrients can be translocated over large distances, as such covering local needs (Boddy et al., 1999; Dickson and Kolesik, 1999). Thanks to these structures, fungi are able to grow and survive even in the most extreme conditions (Magan, 2007), which explains why these organisms are present in most natural and man-made ecosystems. Fungi are decomposers of organic material,

This chapter has been published as: Vidal-Diez de Ulzurrun, J.M. Baetens, J. Van den Bulcke, B. De Baets (2017). Modelling three-dimensional fungal growth in response to environmental stimuli. Journal of Theoretical Biology 414, 35-49.

making them essential for the proper functioning of nutrient cycles in natural ecosystems (Krivtsov et al., 2006). In human ecosystems, fungi cause damage and economic losses since building materials (Adan and Samson, 2011), food products (Panagou et al., 2007) and plants (Henkel et al., 2012) are prone to their attack. Fungi are also used to produce food products and medicines (Grimm et al., 2005), and some are used as biological agents against nematodes or insects (Weinzierl and Henn, 1991; Alvindia and Natsuaki, 2008).

For all of these reasons, fungi have been extensively studied, especially through laboratory experiments. The latter are generally expensive, tedious or of a limited scope (Fricker et al., 2009), thus comprehensive studies of fungal dynamics *in vitro* or *in situ* are rare. Moreover, fungi grow in environments and under environmental circumstances that cannot always be mimicked easily in laboratories (Boswell et al., 2007). Finally, even though it might be possible to mimic certain environmental conditions, it is practically impossible to account for intra species variability. *In silico*, however, there are no such limitations.

Different disciplines benefit from mathematical models to complement laboratory experiments and verify theoretical hypotheses (Edelstein-Keshet, 1988; Larsen et al., 2012; Davidson, 2007), as is the case in mycology. Such models allow researchers to study fungal growth across larger areas and in more diverse environmental conditions than ever possible in the laboratory, and in more detail than most experimental devices are able to capture. Additionally, *in silico* simulations are inexpensive and can be repeated several times, as such making it possible to capture the natural variability in fungal growth dynamics.

Several mathematical models have been proposed to mimic fungal growth by relying on different hypotheses, methods and modelling paradigms (Davidson, 2007; Boswell and Hopkins, 2008). Fungal growth models can be classified according to the scale they are operating at. Microscopic models study the evolution of fungal cells (Regalado and Sleeman, 1999), mesoscopic models aim at studying the extension of hyphae (Boswell, 2008; Carver and Boswell, 2008; Hopkins and Boswell, 2012; Meškauskas et al., 2004a), while macroscopic models focus on biomass change (Edelstein, 1982; Davidson, 1998; Falconer et al., 2005). Some of these models acknowledge the three-dimensional structure of the mycelium (Fuhr et al., 2011; Meškauskas et al., 2004a; Boswell, 2008), whereas others restrict growth to two dimensions (Carver and Boswell, 2008; Hopkins and Boswell, 2012; Edelstein, 1982; Davidson, 1998; Falconer et al., 2005). While some modellers use differential equations to formalize the governing physical and biological processes (Edelstein, 1982; Davidson, 1998; Falconer et al., 2008; Boswell et al., 2002), others shift from the continuum to spatially explicit models (SEM) that allow for tracking the fungal structure over time in detail (Boswell, 2008; Carver and Boswell, 2008; Hopkins and Boswell, 2012). Such models typically mimic biological processes using sets of simple rules rather than forcing biological processes into the mold of differential equations. Spatially explicit models have proven their usefulness in

different disciplines (see Grimm (1999)) and are increasingly acknowledged as a powerful alternative to classical models. There are two possible approaches for the representation of physical space in such models: either space is discretized by using a lattice or grid, as such restricting the degrees of freedom tied up with the fungal growth processes (Boswell, 2008; Fuhr et al., 2011; Boswell et al., 2002), or alternatively, no discretization is imposed at all and the *in silico* fungus can grow freely. The latter lattice-free models can capture the complex nature of mycelia (Carver and Boswell, 2008; Hopkins and Boswell, 2012; Meškauskas et al., 2004a).

Although macroscopic models are able to represent fungal expansion, they cannot offer a complete understanding of the processes leading to the complex structure of typical mycelia (Edelstein, 1982; Davidson, 1998; Falconer et al., 2005). On the other hand, microscopic models are difficult to upscale, so they are not able to provide information about the overall evolution of the fungal colony. In contrast, mesoscopic models capture both the complexity of the network and the biomass evolution. Moreover, imaging devices nowadays enable the collection of data needed for the calibration of mesoscopic models (e.g. Falconer et al. (2010)). Unfortunately, most of these models study fungal growth in only two dimensions (Boswell et al., 2007; Carver and Boswell, 2008; Hopkins and Boswell, 2012), which is a simplification as fungal growth is known to occur in three dimensions, and many phenomena can only become fully appreciated in the three-dimensional space. Even though some mesoscopic studies investigate hyphal growth in three dimensions, most of them confine the growth to a lattice resulting in unrealistic *in silico* mycelia (Boswell, 2008; Fuhr et al., 2011). Finally, only a few models are lattice free, thus leading to more realistic *in silico* results, but they still neglect the interactions between the *in silico* fungi and their environment (Carver and Boswell, 2008; Meškauskas et al., 2004a).

In response to the shortcomings of current fungal growth models, this chapter presents a lattice-free three-dimensional fungal growth model that accounts for the interactions between the *in silico* fungus and its environment. The model simulates both the biological processes driving fungal growth and the hyphal response to external stimuli. It is discrete in both time and space and it tracks the structure of the entire mycelium as it evolves over time. This model is highly versatile since it is able to represent the reaction of fungi to different materials. The outcome of the model comprises all details on the shape and position of the individual hyphae in the *in silico* mycelium, the evolution over time of substrate both inside and outside the fungus and the connections emerging between hyphae within the mycelium. On the basis of these outputs, it is possible to track the evolution of different growth features that can then be compared to those obtained *in vitro* or *in situ* (Chapter 5).

7.2 Materials and methods

The model described here is a SEM that tracks the hyphae individually as they evolve in discrete time steps. It is biologically based, since *in silico* hyphal growth is mimicked by relying on sound mathematical representations of the governing processes, namely uptake and translocation of nutrients, apical growth, branching, and anastomosis (see Section 7.2.1). The model is implemented in Mathematica (Version 10.0, Wolfram Research Inc., USA) and it can simulate growth in three dimensions without imposing any kind of lattice, therefore allowing hyphae to grow freely in the environment. In addition, the *in silico* fungus is able to interact with different compounds and stimuli in its environment, such as substrate, inert materials or physical forces, which allows to simulate fungal growth in a variety of scenarios.

7.2.1 Model assumptions

In nature, fungal growth occurs as the combined result of various biological processes. Therefore, in order to obtain realistic *in silico* simulations of fungal growth, each of these processes is incorporated in our model. In this subsection, the key processes steering fungal growth are discussed in detail to motivate the model formulation described in Section 7.2.2.

Fungi can be divided into two main categories according to the structure of their vegetative body, namely yeast-like and filamentous fungi (Wendland, 2001). While the former typically give rise to unicellular bodies, the latter develop multicellular filaments, called hyphae. The ensemble of hyphae makes up a complex connected network that is considered to be a single organism, and is referred to as a fungal colony or mycelium. Nutrients are taken up by the filamentous network and are subsequently transformed into internal substrate. Usually, the nutritional requirements of fungi are minimal and can be met by most materials (Adan and Samson, 2011). Substrate is translocated in the mycelium in order to cover its local needs. Translocation of nutrients is extremely effective (Tlalka et al., 2007; Fricker et al., 2008), which is one of the reasons why fungi succeed in surviving and expanding even in harsh environmental conditions, radiation or extreme temperatures (Magan, 2007). For the same reason, infections spread rapidly within the mycelium, even when they are initially very localized, which demonstrates that different parts of a fungal colony are able to communicate with one another (Dijksterhuis, 2011).

The shape of the mycelium results from two main processes, being apical growth and branching (Edelstein, 1982). The former occurs when a hyphal tip or apex generates new biomass by extending. Hyphal tips represent the most dynamic areas of the mycelium, where different cell organelles, e.g. Spitzenkörper, cooperate in

order to ensure extension (Riquelme et al., 1998). The position of the Spitzenkörper in the hyphal tip determines the growth direction, i.e. the direction along which a filament extends and creates new biomass (Riquelme et al., 1998; Reynaga-Peña et al., 1997). Even though this direction usually does not change dramatically, it has been proven that small changes occur during the growth process (Riquelme et al., 1998). New biomass can also be created when new hyphae emerge from the existing filamentous mycelium, just like branches on a tree. There are two different types of branching, called lateral and dichotomous branching (Edelstein, 1982), with the latter one being the most common (Reynaga-Peña et al., 1997; Mouriño Pérez et al., 2006). While lateral branching can occur in any part of the mycelium, apical branching is restricted to the hyphal tips. The angle at which a new hypha branches relative to the existing one depends on the species, as such constituting a characteristic feature to recognize fungal species (Kamel et al., 2009).

While growing and exploring, a hypha can encounter another hypha and fuse with it (anastomosis), as such changing the shape of the hyphal network and increasing the efficiency of the nutrient cycle (Simonin et al., 2012). Some researchers hypothesize that hyphae can sense and avoid each other, a behaviour referred to as negative autotropism (Hickey et al., 2002), which would result from an aerotropism towards oxygen, (away from oxygen-depleted zones) or a negative chemotropism (away from depleted products). Yet, proof of either mechanism remains elusive (Brand and Gow, 2009). Similarly, it has been hypothesized that hyphae sense the environmental conditions in their surroundings, and can adapt their dynamics depending on the local conditions, ultimately leading to changes in the shape of the mycelium (Papagianni, 2004; Fomina et al., 2000; Watts et al., 1998). For example, it has been reported that fungi can sense and adapt to the presence of toxic metals (Fomina et al., 2000) or surface contours (Watts et al., 1998). The clearest example of how fungal growth is influenced by the environmental conditions is the effect of gravity on aerial hyphae (hyphae growing in the air), i.e. a gravitropic tropism (Moore, 1991).

Many fungi can penetrate plant, animal or human tissue, but there are man-made materials, such as plastic or glass, that are practically impenetrable, as such restricting fungal growth (Samson, 2011). When encountering such inert materials, the fungal organisms adapt their dynamics, which typically results in filaments crawling over the surface of these materials. In addition, fungicides and fungal growth inhibitors are usually present in natural and human environments limiting the growth of fungal organisms (Mauch et al., 1988), thus altering the shape of the mycelium.

7.2.2 Modelling the growing fungus

In order to mimic the evolution of the mycelium over time, the *in silico* fungus at time step t is encoded as an array F^t containing the description of all hyphae present in the mycelium at that time step. Each row i of the array represents an *in silico* hypha. The hyphae are divided into connected hyphal segments and the description $S^t_{i,j}$ of a segment $S_{i,j}$ at time step t is located in the row of the hypha to which it belongs (i) and the column corresponding to the time step when it emerged (j). Hence, we have $F^t_{i,j}{=}S^t_{i,j}$ for any $t \geqslant j$, and the convention $F^t_{i,j}{=}\varnothing$ for any $t < j$. In turn, any hyphal segment $S_{i,j}$ is encoded as an array containing data on its individual features at time step t, such as its location, growth direction, amount of internal substrate and its current state. The hyphal segment is the fundamental entity of our SEM, as such allowing to mimic the spatio-temporal dynamics of an individual hypha from the evolution of its hyphal segments (Boswell, 2008; Carver and Boswell, 2008; Hopkins and Boswell, 2012).

Every segment $S_{i,j}$ is assigned a certain state that may change over time, denoted as $T^t_{i,j}$. In line with an established classification of hyphal segments (Boswell and Hopkins, 2008), we distinguish four states: active (s_1), passive (s_2), branched (s_3), or involved in anastomosis (s_4). The state of a segment is used to determine its role in the mycelium, and whether or not it is able to grow, i.e. generate new hyphal segments.

Each hyphal segment has two endpoints. Since segments from the same hypha are connected, two adjacent segments always share an endpoint. Therefore the location in space of segment $S_{i,j}$ is determined by the Cartesian coordinates of its two endpoints, i.e. $X_{i,k} = (x_{i,k}, y_{i,k}, z_{i,k})$ and $X_{i,j} = (x_{i,j}, y_{i,j}, z_{i,j})$, with $k < j$. The endpoint $X_{i,k}$ is shared with the preceding segment $S_{i,k}$, therefore only the coordinates of the endpoint $X_{i,j}$ and the position (i, k) of the preceding segment are stored for each segment $S_{i,j}$. In this way, the length of segment $S_{i,j}$ is conveniently given by

$$h(S_{i,j}) = d(X_{i,k}, X_{i,j}), \tag{7.1}$$

where d is the Euclidean distance.

All the nutrients within the fungus are grouped into an imaginary substrate referred to as internal substrate. Consequently, the translocation of nutrients within the network is mimicked as the flow of the internal substrate. The internal substrate can be absorbed by the hyphal segments and subsequently used by the fungus to generate new biomass. This substrate can also be retained by segments, irrespective of their state and the amount of substrate in segment $S_{i,j}$ at time step t is denoted by $I^t_{i,j}$ [mol]. Each segment can retain substrate up to a maximum determined by the segment length and a maximum concentration M_{cap} [mol mm^{-1}] (Hopkins and Boswell, 2012). Consequently, the maximum capacity

of segment $S_{i,j}$ is given by $h(S_{i,j})M_{cap}$ mol. Substrate is displaced through connected segments (also known as neighbouring segments) through translocation, as such covering the needs of the whole mycelium (see Section 7.2.1). A segment is not only connected to its adjacent segments, i.e. predecessor and successor segments, but it can also be connected to other segments as the result of anastomosis or branching. Translocation is often described as the consequence of an active and a passive term (see the review of Boswell and Hopkins (2008)). While the passive term is defined as substrate diffusion, the active term is described as metabolically driven, i.e. it depends on the local demands of the fungus. For the sake of simplicity, our SEM mimics translocation using a single term, similar to the principle described in Boswell (2008), Carver and Boswell (2008) and Davidson (1998). Computing the change of substrate in this way, it is possible to mimic the internal substrate translocation from those parts of the mycelium with a relatively high substrate concentration to those parts with a relatively low substrate concentration (Carver and Boswell, 2008), as such accounting for both diffusion and active translocation. Firstly, the amount of substrate to be transferred is calculated and secondly the transferred substrate is corrected if the governing biological constraints happen to be violated.

Explicitly, the amount of internal substrate transferred between two neighbouring segments $S_{k,l}$ and $S_{i,j}$, where $k \leqslant i$, $l \leqslant j$ and $\{i,j\} \neq \{k,l\}$, at time step $t+1$, is computed as follows. First, the maximal amount of internal substrate that can be physically transferred between $S_{k,l}$ and $S_{i,j}$ is calculated as:

$$\delta_{i,j}^{k,l} = \Delta t\, D\, \frac{I_{k,l}^{t} - I_{i,j}^{t}}{\big(h(S_{k,l}) + h(S_{i,j})\big)/2}, \tag{7.2}$$

where D [mm d^{-1}] is the internal substrate diffusion coefficient, Δt [d] is the time step duration and the denominator is the average length of the involved segments. Second, we have to account for the fact that the amount of internal substrate in any segment must always be non-negative and must not exceed its capacity, i.e. $0 \leqslant I_{i,j}^{t} \leqslant h(S_{i,j})M_{cap}$, and similarly for $S_{k,l}$. Therefore, the amount of substrate obtained from Eq. (7.2), which can be either positive or negative, is added to $I_{i,j}^{t}$ and subtracted from $I_{k,l}^{t}$ at time step $t+1$, only if the resulting amounts of internal substrate of the involved segments lie inside their permitted ranges. More specifically, this condition is given by:

$$\delta_{i,j}^{k,l} \in \Big[\max(-I_{i,j}^{t}, I_{k,l}^{t} - h(S_{k,l})M_{cap}), \min(I_{k,l}^{t}, h(S_{i,j})M_{cap} - I_{i,j}^{t})\Big]. \tag{7.3}$$

If this condition is not met, then $\delta_{i,j}^{k,l}$ is changed into the nearest endpoint of this interval, resulting in $\tilde{\delta}_{i,j}^{k,l}$. Finally, $\tilde{\delta}_{i,j}^{k,l}$ is added to $I_{i,j}^{t}$ and subtracted from $I_{k,l}^{t}$, as such overwriting their original values. At every time step, an exchange of substrate is simulated between every pair of neighbouring segments, according to the proce-

dure above. Even though the *in vivo* substrate updates may occur in parallel for all segments, the exchange of substrate between a segment $S_{i,j}$ and its neighbours is executed following the order imposed by their position in the array F, i.e. first by column and then by row. In this way, we ensure the stability of the translocation algorithm. Moreover, each segment exchanges substrate only with its preceding segments, as such making sure every connection is taken into account only once. The total amount of substrate that is exchanged between segment $S_{i,j}$ and its n neighbouring segments is calculated in iterative steps. Each step represents the exchange of substrate between segment $S_{i,j}$ and a single neighbour S_{k_τ,l_τ}. The total substrate in $S_{i,j}$ after a single exchange with S_{k_τ,l_τ} is denoted by ${}^{\tau}I^t_{i,j}$ and is computed as follows:

$$ {}^{\tau}I^t_{i,j} = {}^{\tau-1}I^t_{i,j} + {}^{\tau-1}\tilde{\delta}^{k_\tau,l_\tau}_{i,j}, \tag{7.4} $$

where

$$ {}^{\tau-1}\tilde{\delta}^{k_\tau,l_\tau}_{i,j} = \begin{cases} \tilde{\delta}^{k_\tau,l_\tau}_{i,j} & \text{, if } S_{k_\tau,l_\tau} \text{ is a predecessor of } S_{i,j}, \text{ so } k_\tau \leq i \text{ and } l_\tau < j, \\ -\tilde{\delta}^{i,j}_{k_\tau,l_\tau} & \text{, else,} \end{cases} \tag{7.5} $$

with $\tau \in \{1, \ldots, n\}$ referring to the neighbour S_{k_τ,l_τ}, following the order imposed by the array F. Furthermore, ${}^{0}I^t_{i,j} = I^t_{i,j}$, and ${}^{\tau-1}I^t_{i,j}$ is used when evaluating the right-hand side of Eq. (7.5). Finally, $I^t_{i,j}$ is assigned a new value, namely ${}^{n}I^t_{i,j}$ which therefore represents the total amount of substrate in $S_{i,j}$ after translocation with its n neighbours, i.e. $I^t_{i,j} = {}^{n}I^t_{i,j}$.

In order to grow, active segments can generate new biomass and the amount of internal substrate needed to generate this biomass is given by c_g [mol mm^{-1}]. The new biomass comes in the form of new hyphal segments that are appended at the end of the growing segment as the result of one of two growth processes, apical growth and branching. While the former results in the generation of an additional hyphal segment, the latter generates two additional hyphal segments. The new segments have a length denoted by h_0 [mm], hence the amount of substrate needed to create a new segment is given by $c_g\, h_0$ [mol]. Still, it should be pointed out that new segments can be shortened, i.e. $h(S_{i,j}) \leqslant h_0$, due to anastomosis or interactions with the environment.

Apical growth is modelled as follows. An *in silico* tip can extend apically as long as its substrate content is sufficiently high to cover this cost. The segment emerging from $S_{i,j}$ at time step j^* as a consequence of apical growth is appended to the i-th row of the array F in the column j^* (Table 7.1). It should be noted that apical growth does not necessarily occur at each time step and therefore there may be a delay of several time steps before a new segment emerges from its predecessor. The new segment S_{i,j^*} grows according to the growth direction imposed at the endpoint of its predecessor $S_{i,j}$ and its state is initialized as active, i.e. $T^{j^*}_{i,j^*} = s_1$. This growth direction is denoted by $\Theta_{i,j} = (\theta_{i,j}, \varphi_{i,j})$, where $\theta_{i,j}$ [−] refers to the polar

angle of a unitary vector aligned with the growth direction, and $\varphi_{i,j}$ [−] refers to its azimuthal angle (Figure 7.1(a)). This definition constitutes an extension to three dimensions of the angular representation defined in Carver and Boswell (2008). Then, the position of segment S_{i,j^*} is computed from this growth direction and the coordinates of the endpoint of its predecessor $S_{i,j}$ as follows:

$$X_{i,j^*} = (x_{i,j} + h_0 \sin(\theta_{i,j}) \cos(\varphi_{i,j}),\ y_{i,j} + h_0 \sin(\theta_{i,j}) \sin(\varphi_{i,j}),\ z_{i,j} + h_0 \cos(\theta_{i,j})). \tag{7.6}$$

The growth direction at the endpoint of the new segment S_{i,j^*} is then determined as the one of its predecessor plus a vector of noise terms $\zeta = (\zeta_1, \zeta_2)$, drawn uniformly from $[-\omega/2, \omega/2]^2$ (Figure 7.1), where ω [−] is the maximum variation in radians of the polar and azimuthal angles. This approach is similar to the one outlined in Carver and Boswell (2008) for a two-dimensional model.

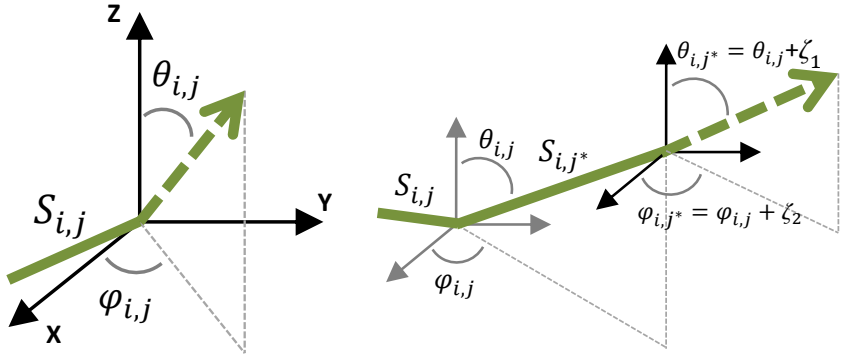

(a) Growth direction angles (b) Update of the growth direction

Figure 7.1: Definition of the polar (θ) and azimuthal (φ) angles defining the growth direction at the endpoint of segment $S_{i,j}$ (a) and growth direction of new segments after extension (b), where ζ is drawn uniformly from $[-\omega/2, \omega/2]^2$.

Once a new segment S_{i,j^*} emerges, the preceding segment $S_{i,j}$ cannot extend any further apically but it is still able to translocate nutrients and therefore its state is updated to passive. In the last step of an *in silico* apical growth event, the internal substrate of the preceding segment $S_{i,j}$ is reduced by the cost $c_g\, h_0$ of growing one new segment, while the internal substrate of the new segment S_{i,j^*} is initially considered to be zero, i.e. $I^{j^*}_{i,j^*} = 0$. It is worth mentioning that hyphal death is not reflected in the model since the time frame we aim to capture is shorter than the natural life span of the hyphae.

The branching process resulting in two additional segments is simulated in this model in the following way. In order to branch at time step t, a segment $S_{i,j}$ must contain at least the amount of substrate that is needed to cover the cost of growing two new segments (Boswell, 2008; Carver and Boswell, 2008; Hopkins

and Boswell, 2012). However, even when a segment contains enough substrate, it does not automatically branch, as apical growth is still the dominant growing process (Riquelme et al., 1998). Therefore, a branching probability P [−] is introduced (Boswell, 2008). The result of a branching event is equivalent to two apical extensions, where one of the new segments $S_{i,j*}$ actually extends the parent hypha, while the other is the first element of a new hypha k, i.e. $S_{k,j*}$. The latter is encoded in the array F by extending it with a new row k that has as its first non-empty element $S_{k,j*}$ (see Table 7.1). Both the coordinates of the endpoint of $S_{k,j*}$ and its growth direction are computed using the growth direction of the parent segment $S_{i,j}$ plus a noise vector ζ drawn uniformly from $[-\omega/2, \omega/2]^2$. This new segment is connected to the parent segment $S_{i,j}$ and this connection is taken into account when translocating internal substrate. The presence of branches in the network is tracked by means of a branching matrix R^t. The former matrix is an adjacency matrix, where every element $R^t_{i,j}$ corresponds to the row number k in the array F^t of the new hypha that emerged from segment $S_{i,j}$.

Table 7.1: Evolution of an *in silico* fungus and the corresponding array F^t.

Time	*In silico* mycelium	Array F^t
$t = 0$		$\mathrm{F}^0 = (S^0_{1,0})$
$t = 1$	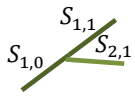	$\mathrm{F}^1 = \begin{pmatrix} S^1_{1,0} & S^1_{1,1} \\ - & S^1_{2,1} \end{pmatrix}$
$t = 2$	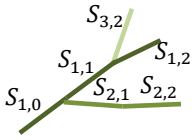	$\mathrm{F}^2 = \begin{pmatrix} S^2_{1,0} & S^2_{1,1} & S^2_{1,2} \\ - & S^2_{2,1} & S^2_{2,2} \\ - & - & S^2_{3,2} \end{pmatrix}$
$t = 3$	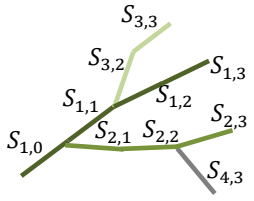	$\mathrm{F}^3 = \begin{pmatrix} S^3_{1,0} & S^3_{1,1} & S^3_{1,2} & S^3_{1,3} \\ - & S^3_{2,1} & S^3_{2,2} & S^3_{2,3} \\ - & - & S^3_{3,2} & S^3_{3,3} \\ - & - & - & S^3_{4,3} \end{pmatrix}$

In vivo, intersecting hyphae might fuse and give rise to an anastomosis event, a process simulated *in silico* as follows. As the segments extend either by apical growth or branching, they may encounter other hyphae (see Section 7.2.1), lead-

ing to anastomosis. Intersections between new and existing hyphal segments are identified at every consecutive time step t. In the case of an intersection between two segments, the endpoint coordinates of the intersecting segment (the newest) are replaced by those of the intersection point and its state is updated to anastomosis (Table 7.2). Segments in this state cannot grow any further, but are able to translocate substrate to their neighbours, including the intersected hyphal segment. In order to model translocation between neighbouring segments that are linked as the consequence of an anastomosis event, the intersections of segments are recorded in an auxiliary anastomosis matrix A^t (Table 7.2). The element A^t_{k,j^*} in this matrix is the position (i, j) in F of the segment $S_{i,j}$ that has been intersected by segment S_{k,j^*} at time step j^*. Therefore, $A^t_{k,j^*} = (i, j)$ for any $t \geq j^*$, and $A^t_{k,j^*} = \emptyset$ for any $t < j^*$.

Table 7.2: Possible intersections between *in silico* hyphal segments. Dark green segments represent existing segments and light green segments represent segments that emerged during time step $j^* > j$.

Anastomosis type	Before anastomosis	After anastomosis	Changes in A^t
New segment with existing segment	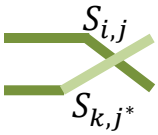	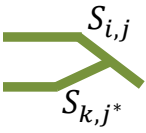	$A^{j^*}_{k,j^*} = (i, j)$
New segment with new segment ($i < k$)	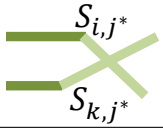	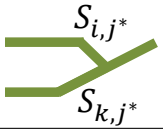	$A^{j^*}_{k,j^*} = (i, j^*)$
New segment with two existing segments	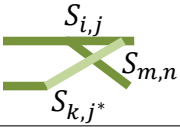	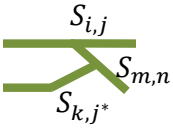	$A^{j^*}_{k,j^*} = (m, n)$

7.2.3 Interaction between the *in silico* fungus and its environment

The environment of the *in silico* mycelium is represented by means of a collection of cuboids C_k whose properties evolve over time. Essentially, these cuboids embody boundary conditions that are tied up with the governing environmental constraints. Fungal growth often occurs in heterogeneous environments where different materials and substances are present, which can be easily represented by such

cuboids. This kind of representation has been used by others, but most of them restricting to a single type of environment, such as substrate (Boswell et al., 2007; Boswell, 2008; Hopkins and Boswell, 2012; Davidson, 1998), inert material (Fuhr et al., 2012) or tropisms (Meškauskas et al., 2004a), and rarely allowing to combine different types, consequently hindering a realistic representation of a natural environment. The cuboids can be located anywhere in the three-dimensional space and their size and position can be chosen in order to represent the environmental constraints in question. The array C_k^t representing the k-th cuboid contains its position, given by the Cartesian coordinates of its centre $X_k = (x_k, y_k, z_k)$, and its dimensions $L_k = (l_k, w_k, h_k)$, where l_k [mm], w_k [mm] and h_k [mm] denote its side length, width and height, at time step t, respectively. In this chapter, we consider penetrable, impenetrable, inhibiting, repelling and attracting boundary conditions.

The penetrable boundary condition might reflect porous materials that can be penetrated by growing fungi, such as solid agar or oatmeal, and subsequently serve as a source of substrate (see Figure 7.2(a)). The external substrate that these materials contain, can be absorbed by penetrating hyphae, after which it gets redistributed across the entire mycelium through translocation (Eq. (7.4)). *In silico*, the penetrable cuboids contain a certain amount of external substrate at time step t, denoted E_k^t [mol], that can be absorbed by the fungus and transformed into internal substrate. This uptake process is simulated as a flow of substrate from the cuboid to the hyphal segments intersecting it. This process has proven to be autocatalytic and it is usually modelled using the Michaelis-Menten formula (Hopkins and Boswell, 2012; Davidson, 1998). For the sake of simplicity, we use a linearization of the Michaelis-Menten equation (Boswell et al., 2003; Boswell, 2008), which states that the amount of substrate taken up is proportional to the external substrate in the nutrient source, in our case a cuboid C_k, and the internal substrate of segment $S_{i,j}$. As in the case of translocation of internal substrate, the flow of substrate must fall within a biologically meaningful range, assuring that the amount of substrate in the intersecting segment $S_{i,j}$ after uptake is positive and not greater than its maximum capacity $h(S_{i,j})M_{cap}$, while the amount of substrate in the cuboid should only take non-negative values. Therefore, the amount of external substrate flowing from the cube to the intersecting segment is calculated in a similar way as in Eq. (7.2). The maximal amount of external substrate that can be physically exchanged between cuboid C_k and an intersecting segment $S_{i,j}$ is given by:

$$\vartheta_{i,j}^k = \Delta t \, \mu_k \, E_k^t \, I_{i,j}^t, \tag{7.7}$$

where μ_k [mol^{-1} d^{-1}] denotes the uptake coefficient of cuboid C_k, a parameter reflecting how easily the external substrate can be extracted from the cuboid by the fungus. The corrected value of $\vartheta_{i,j}^k$ in light of the biologically meaningful range

$\left[0, \min(E_k^t, h(S_{i,j})\, M_{cap} - I_{i,j}^t)\right]$ is then given by:

$$\tilde{\vartheta}_{i,j}^k = \min(\vartheta_{i,j}^k, E_k^t, h(S_{i,j})\, M_{cap} - I_{i,j}^t). \tag{7.8}$$

This amount of substrate $\tilde{\vartheta}_{i,j}^k$ is subtracted from the external substrate of cuboid C_k and added to the internal substrate of the intersecting segment $S_{i,j}$. Analogously to Eqs. (7.4) and (7.5), the total amount of substrate subtracted from C_k is calculated iteratively. Let ${}^{\nu}E_k^t$ represent the amount of substrate left in C_k after uptake by a single intersecting segment S_{i_ν,j_ν}, then:

$${}^{\nu}E_k^t = {}^{\nu-1}E_k^t - {}^{\nu-1}\,\tilde{\vartheta}_{i_\nu,j_\nu}^k, \tag{7.9}$$

where

$${}^{\nu-1}\tilde{\vartheta}_{i_\nu,j_\nu}^k = \tilde{\vartheta}_{i_\nu,j_\nu}^k, \tag{7.10}$$

for $\nu \in \{1, \ldots, n\}$, following the order imposed by the array F, and ${}^0E_k^t = E_k^t$. Furthermore, the right-hand side of Eq. (7.10) is computed using the values of E_k^t and I_{i_ν,j_ν}^t at the ν-th interaction. The amount of substrate E_k^t left in C_k after uptake with its n intersecting segments is then given by ${}^nE_k^t$, i.e. $E_k^t = {}^nE_k^t$. Consequently, the amount of substrate in each of the intersecting segments I_{i_ν,j_ν}^t is also updated to account for the effect of the uptake from cuboid C_k.

Impenetrable cuboids represent inert materials, such as glass or plastic, which cannot be penetrated by the fungus such that it is forced to grow along their surface (Samson, 2011) (see Figure 7.2(b)). A preliminary approach to model this kind of behaviour can be found in several papers (Boswell et al., 2007; Boswell, 2008; Fuhr et al., 2011), where the growth of an *in silico* fungus is restricted to the water surface, the pores of a soil sample or the pits of a wooden block, respectively. These approaches mimic the corresponding behaviour by not allowing fungal growth in certain regions, rather than updating the fungal growth dynamics. When a hyphal segment $S_{i,j}$ intersects such an impenetrable cuboid C_k in our model, the coordinates of the endpoint of this segment are set to those of the intersection point between the cuboid's surface and the segment $S_{i,j}$. Furthermore, the growth direction of this segment is updated to be consistent with its new location. In nature some materials are initially impenetrable, yet prolonged exposure results in damage to the material, which can then be penetrated by the fungus (Adan and Samson, 2011). In order to simulate this kind of erosion, in our model the cuboid remains impenetrable for a certain number of interaction events with the *in silico* fungus, during which period the fungus can only grow along the cuboid's surface. After reaching this interaction limit, which is characterized by the resistance τ_k [−] of cuboid C_k, the hyphal segments are able to penetrate the material. This parameter is defined as the maximum number of interactions between the cuboid and the fungus, i.e. the maximum number of segments capable

of intersecting the cube, beyond which the cuboid becomes penetrable.

The effect of fungicides and other fungal growth inhibitors on fungal dynamics can also be mimicked by our model (Figure 7.2(c)). The inhibitory effects of the corresponding cuboids might be limited in time, denoted by the durability δ_k [d]. When an *in silico* tip intersects one of these cuboids, the segment becomes passive, i.e. $T^t_{i,j} = s_2$, so that it can no longer grow, but it can still translocate or absorb substrate.

The last type of boundary condition mimics different tropisms, i.e. responses to external stimuli, which can have either negative (repulsion, Figure 7.2(d)) or positive (attraction, shown in Figure 7.2(e)) effects on the hyphal growth. Different modelling approaches have been proposed for such tropisms (Hopkins and Boswell, 2012; Meškauskas et al., 2004a). As proposed in Meškauskas et al. (2004a), the tropisms in our model have a certain area of influence beyond which their effect becomes negligible; this area is represented by the corresponding cuboid's volume. Once a hyphal segment enters the area of influence of the tropism, i.e. once it intersects the cuboid C_k, it is repelled from or attracted towards its centre X_k. The effect of the tropisms is mimicked by changing the growth direction of the intersecting hyphal segments in such a way that the closer a segment is located to the cuboid's centre, the stronger the tropism affects its growth direction. In order to mimic both repulsion and attraction, tropisms have a certain strength γ_k [−] and durability δ_k [d]. The sign of the former determines the nature of the tropism, while its magnitude, taking a value in the range of $[-1, 1]$, determines its strength. A tropism alters the growth direction of the *in silico* hyphal segments within its area of influence, as follows:

$$\tilde{\Theta}_{i,j} = \alpha_{ijk} \Psi^{-1}\left(\hat{\mathbf{u}}_{ijk}\right) + \left(1 - \alpha_{ijk}\right) \Theta_{i,j}\,, \tag{7.11}$$

where $\hat{\mathbf{u}}_{ijk} = \frac{\mathbf{u}_{ijk}}{\|\mathbf{u}_{ijk}\|}$, with $\mathbf{u}_{ijk}$ the vector connecting the endpoint of segment $S_{i,j}$ and the centre of cuboid C_k, and Ψ^{-1} indicating a transformation from Cartesian to spherical coordinates. As such, the final growth direction $\tilde{\Theta}_{i,j}$ is a weighted average of the original direction and the direction defined by $\mathbf{u}_{ijk}$. The vector $\mathbf{u}_{ijk}$ points towards the centre of the cuboid C_k in the case of a positive tropism, whereas it is pointing outwards otherwise, i.e.

$$\mathbf{u}_{ijk} = \begin{cases} \overrightarrow{X_{i,j}X_k} & \text{, if } \gamma_k > 0, \\ \overrightarrow{X_k X_{i,j}} & \text{, if } \gamma_k \leq 0. \end{cases} \tag{7.12}$$

The coefficient α_{ijk} in Eq. (7.11) is given by:

$$\alpha_{ijk} = |\gamma_k| \, \frac{M_{dist} - \left\|\mathbf{u}_{ijk}\right\|}{M_{dist}}\,, \tag{7.13}$$

where M_{dist} denotes the maximum distance between the centre of C_k and any of the points it encloses. In this way, the effect of the tropism is maximal at the centre and zero at the cuboid's vertices, i.e. the points of the cuboid farthest from the centre. The effect of the different boundary conditions on the dynamics of the *in silico* fungus is summarized in Figure 7.2.

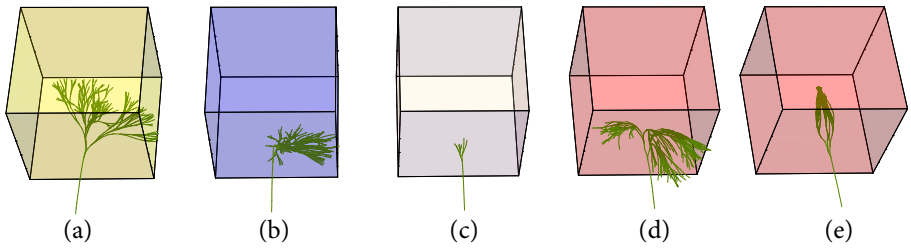

Figure 7.2: Possible interactions between *in silico* hyphae and their environment: substrate (a), inert material (b), inhibitor (c), negative tropism (d) and positive tropism (e).

The list of model parameters together with their dimensions is given in Table 7.3.

Table 7.3: Model parameters, corresponding notation, descriptions and units.

Parameter	Notation	Description	Dimensions
Number of steps	T	Number of time steps in the simulation	–
Hyphal segment length	h_0	Length of a hyphal segment	mm
Time step	Δt	Time step duration	d
Variation of growth direction	ω	Maximum deviation of the growth direction	rad
Branching probability	P	Probability of branching	–
Cost of growth	c_g	Cost of growing a hyphal segment	$\mathrm{mol\,mm^{-1}}$
Diffusion coefficient	D	Coefficient of internal substrate diffusion	$\mathrm{mm\,d^{-1}}$
Maximum concentration	M_{cap}	Maximum concentration of internal substrate	$\mathrm{mol\,mm^{-1}}$
Uptake coefficient	μ_k	Uptake coefficient for C_k	$\mathrm{mol^{-1}\,d^{-1}}$
Tropism strength	γ_k	Strength of the tropisms represented by C_k	–
Resistance	τ_k	Resistance of the inert material imposed by C_k	–
Durability	δ_k	Durability of the tropism imposed by C_k	d

7.2.4 Initialization and update procedure

At the beginning of an *in silico* experiment, the number of initial segments H_0 [−] and the initial amount of internal substrate in the *in silico* segments Ω_0 [mol] have to be specified. The initial array F^0 contains as many rows as there are initially segments in the *in silico* inoculum. The initial segments are in state active and located at the origin, i.e. $X_{i,0} = (0, 0, 0)$, for $i = 1, \ldots, H_0$. The amount of internal substrate in the *in silico* mycelium is equally distributed among the initial segments, which means that each of them initially contains exactly $\frac{\Omega_0}{H_0}$ mol of internal substrate at the beginning of an *in silico* experiment. Finally, the initial growth direction of these segments, $\Theta_{i,0} = (\theta_{i,0}, \phi_{i,0})$, $i = 1, \ldots, H_0$, is drawn uniformly from $[0, 2\pi]^2$. In summary, an initial segment $S_{i,0}$ is encoded as follows:

$$S^0_{i,0} = (0, 0, 0, \theta_{i,0}, \phi_{i,0}, \frac{\Omega_0}{H_0}, \text{Active}, 0), \tag{7.14}$$

where the last entry refers to the age of the segment, which is defined as the time step at which the segment was created.

In addition to the initial inoculum, also the growth environment needs to be defined at the beginning of an *in silico* experiment by constructing a matrix Σ^0 that encodes the cuboids imposing the governing boundary conditions (Section 7.2.3):

$$\Sigma^0 = (C^0_1, C^0_2, \ldots, C^0_{n-1}, C^0_n),$$

where

$$C^0_k = (X_k, L_k, E^0_k, T_k, A^0_k).$$

Here, T_k represents the type of boundary condition (penetrable, impenetrable, inhibiting or tropism) and A^0_k represents the specific attributes (resistance τ_k, durability δ_k and γ_k) that come along with the boundary condition defined by cuboid C_k.

Once the inoculum and environment have been initialized, the *in silico* mycelium is evolved in discrete time steps. In one simulation step all the fungal processes are mimicked in the order shown in Figure 7.3. Even though these fungal processes occur simultaneously in nature, such an order needs to be imposed to model *in silico* fungal growth. This order was chosen taking into account the relationships between the different fungal processes. The internal substrate values are computed and updated after each fungal process, i.e. the internal substrate values obtained after translocation are used to determine and calculate growth, which are then used to compute uptake values, and so on. Therefore $I^{t+1}_{i,j}$, the value of the internal substrate in segment $S_{i,j}$ after time step t, is given by the amount of substrate after all fungal processes have been carried out.

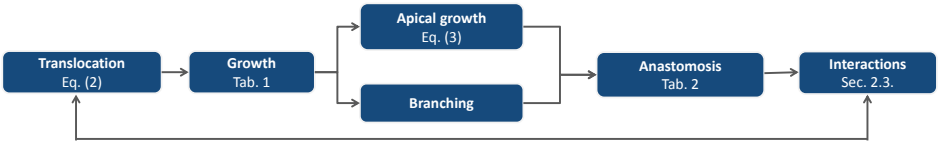

Figure 7.3: Fungal growth processes mimicked in one simulation step.

The result of multiple time steps is an array containing all the information about the shape and evolution of the mycelium over time. This array can then be used to compute different growth features or visual representations of growing *in silico* fungi (Figure 7.4).

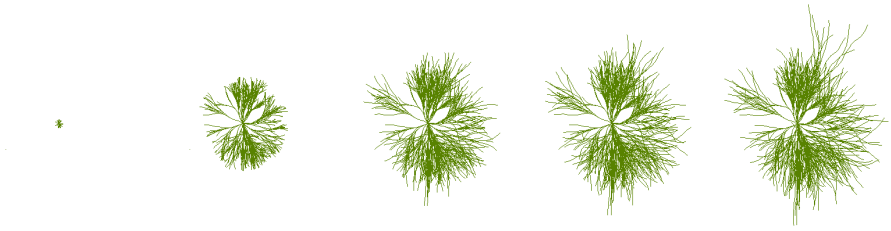

(a) $t = 1$ (b) $t = 5$ (c) $t = 10$ (d) $t = 15$ (e) $t = 20$

Figure 7.4: *In silico* fungus at time step 1 to 20 (0.01 to 0.2 days), obtained using the parameters and initial conditions given in Table 7.5 and without environmental constraints.

7.3 Results and discussion

7.3.1 Model Analysis

7.3.1.1 Topological measures

In order to summarize and compare the simulation results across several *in silico* experiments, we extract topological measures of the *in silico* network as it evolves. This is done by computing measures reflecting the growth and compactness of the *in silico* mycelium, and the internal and external substrate depletion. These measures can also be computed from fungal images (see Chapters 5 and 6), enabling a future model calibration. Essentially, a mycelium may be conceived as a set of nodes (intersections and apices) and edges (hyphal segments) (Obara et al., 2012), which eases the analysis of the mycelium.

To track the evolution of the *in silico* mycelium we calculate the amount of internal substrate in the network, the extent of the mycelium, the total number of tips and the total hyphal length. The extent of the mycelium is given by the Euclidean distance from the centre of the inoculum to the tip at the largest distance from this centre, and it allows to study the expansion of the *in silico* fungus. The number of tips gives an insight into the compactness of the mycelium and is computed as the number of nodes with degree 1. Finally, the total hyphal length is given by the sum of the lengths of all hyphal segments in the mycelium (Trinci, 1974).

7.3.1.2 Sensitivity analysis

A global sensitivity analysis (SA) was carried out to assess the impact of the model parameters (Section 7.2.2) on the topological measures described above, and to gain insight in their order of importance. More precisely, Sobol indices (Lilburne and Tarantola, 2009) were used. Sobol indices decompose the total variance of the model output, as such indicating what proportion of the variance is related to each parameter. In our case, the studied parameters are the variation of the growth direction ω, branching probability P, cost of growth c_g, diffusion coefficient of internal substrate D and maximum concentration M_{cap}. Their values were selected using Latin Hypercube Sampling from the ranges shown in Table 7.4, and the remaining parameters were fixed as shown in the same table. The range of each parameter was determined by the minimum and the maximum values assuring fungal growth and stability of the solutions of each equation in Section 7.2.2. For some but not all parameters, these meaningful ranges are sensitive to changes in the initial conditions. For instance, the maximum value for the cost of growth and maximum concentration ranges are computed as a function of the initial amount of substrate in order to ensure fungal growth. In order to minimize the effect of the environment on the outcome of the SA, the simulations were performed in a scenario without sources of external substrate or cuboids imposing boundary conditions.

In order to decompose the variance, we define two matrices Q and R, whose columns are random samples of the studied parameters (Sobol, 2001). These two matrices have dimensions $N \times M$, where N is the total number of model runs and M the number of parameters. Then, an auxiliary matrix Q_i is created by taking the i-th column of Q and all other columns of R. The model is initiated using the parameter values specified in the matrices Q, R and Q_i resulting in several *in silico* fungi. These *in silico* fungi are then used to compute each of the topological measures presented in Section 7.3.1.1, as such yielding for each topological measure f three output vectors:

$$\mathbf{y}_Q = f(Q), \quad \mathbf{y}_R = f(R), \quad \mathbf{y}_{Q_i} = f(Q_i).$$

Table 7.4: Parameter values and ranges used to perform a global SA of the SEM presented in Section 7.2.

Parameter	Notation	Value	Dimensions
Number of steps	T	150	–
Hyphal segment length	h_0	0.05	mm
Time step	Δt	0.01	d
Initial tips	H_0	25	–
Initial substrate	Ω_0	5×10^{-6}	mol
Variation of growth direction	ω	$[0, \pi]$	rad
Branching probability	P	$[0, 1]$	–
Cost of growth	c_g	$\left[0, \frac{\Omega_0}{H_0}\right]$	$\mathrm{mol\,mm^{-1}}$
Diffusion coefficient	D	$[0, 5]$	$\mathrm{mm\,d^{-1}}$
Maximum concentration	M_{cap}	$\left[0, \frac{\Omega_0 \cdot h}{H_0}\right]$	$\mathrm{mol\,mm^{-1}}$

The Sobol index $\widehat{S}_i$ for each parameter i is estimated from these outputs using the following formula (Lilburne and Tarantola, 2009):

$$\widehat{S}_i = \frac{\frac{1}{N}\sum_{j=1}^{N} y_Q^{(j)} y_{Q_i}^{(j)} - \left(\frac{1}{N}\sum_{j=1}^{N} y_Q^{(j)}\right)^2}{\frac{1}{N}\sum_{j=1}^{N} \left(y_Q^{(j)}\right)^2 - \left(\frac{1}{N}\sum_{j=1}^{N} y_Q^{(j)}\right)^2},$$

where $y_Q^{(j)}$ is the j-th element of the vector $\mathbf{y}_Q$.

The benchmark scenario we used to perform the SA was a survival growth scenario, where none of the boundary conditions described in Section 7.2.3 were imposed, as a means to study the *in silico* fungus independently from its environment. Therefore, all available substrate, $\Omega_0 = 5 \times 10^{-6}$ mol, is placed inside the inoculum at the beginning of the simulation after which it was gradually depleted. This results in a high concentration of substrate in the segments near the inoculum, particularly at the beginning of the simulation. The number of runs N used to compute the matrices Q, R and Q_i was 500 and each simulation was run for 150 time steps (1.5 days). The resulting Sobol indices over time for the considered topological measures can be found in Figure 7.5.

As can be seen in Figure 7.5(a), the main factors influencing the total amount of internal substrate are the branching probability P and the internal substrate diffusion coefficient D. We can distinguish two different phases. Firstly, an exponential growth phase when most of the growth occurs, which is possible through the high

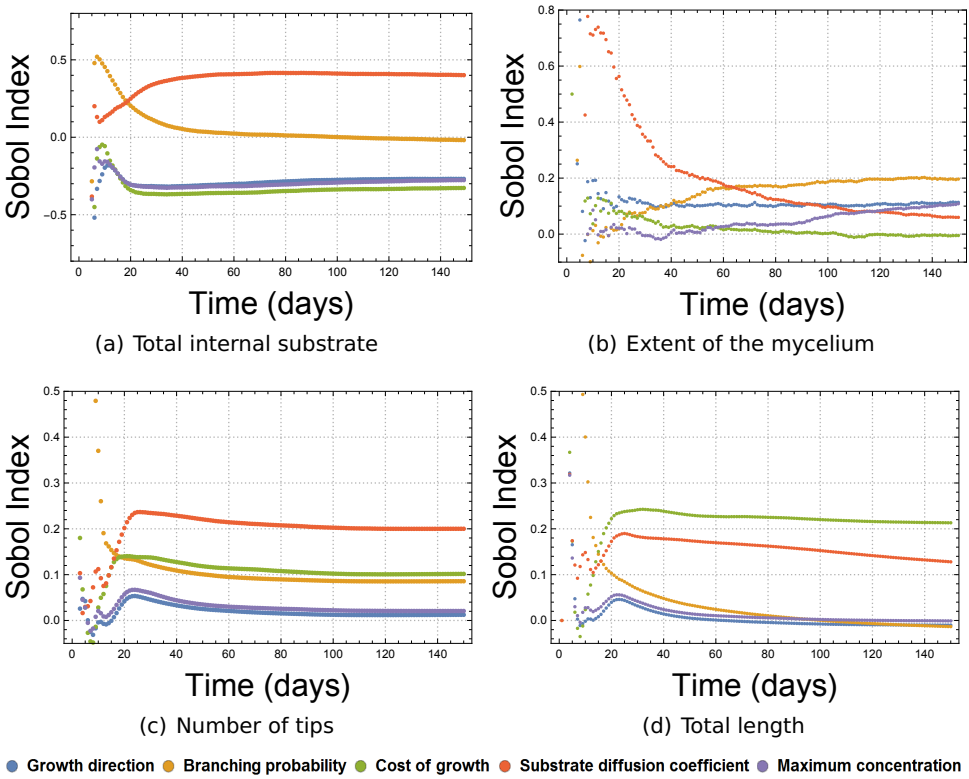

Figure 7.5: Sobol indices of the topological measures over time, computed from 500 simulations covering 150 time steps (1.5 days).

initial concentration of internal substrate in the inoculum, and secondly, a steady state phase were the amount of internal substrate at the tips is lower, a behaviour already reported for different fungal species (Trinci, 1974; Prosser and Trinci, 1979). During the exponential phase, the branching probability P is the main parameter driving the depletion of internal substrate. Once the growth stabilizes, the substrate diffusion coefficient D starts driving the internal substrate depletion. This finding can be explained by the fact that growth happens only at the tips, so that the substrate needs to reach the tips before it can be used to create new biomass. Hence, the faster the substrate diffuses, the sooner it will be depleted. The Sobol indices of the other three parameters are negligibly small, which indicates that they do not play an important role in the evolution of the internal substrate, compared to the substrate diffusion coefficient D and branching probability P.

The Sobol indices for the extent of the mycelium (Figure 7.5(b)) indicate that this measure is governed also by the internal substrate diffusion coefficient D and the branching probability P. The internal substrate diffusion coefficient D is the most relevant parameter at the beginning of the simulations due to the concentration of substrate in the inoculum. In a mycelium full of substrate, an efficient

internal substrate diffusion ensures fast growth, resulting in a faster expansion of the mycelium (Cunniffe and Gilligan, 2008). Once the substrate starts to be depleted the branching probability P takes the lead. The length of a hypha is maximized when its growth is predominantly apical, therefore networks having a limited branching probability P result in mycelia with a larger extent (Molin et al., 1992). The variation of the growth direction ω is also significant for the extent of the mycelium since fungi with a low growth angle variation are able to extent farther than those presenting high variation of their growth angle. Finally, the cost of growth c_g and the maximum concentration M_{cap} also influence the extent of the colony, but to a much lesser extent than the other parameters.

Figure 7.5(c), showing the Sobol indices for the number of tips, also reflects the exponential growth phase. The branching probability P is the most relevant parameter during this initial phase, while its Sobol index decreases once the growth stabilizes. After the exponential growth phase, the substrate diffusion coefficient D is the dominating factor followed by the cost of growth c_g. The Sobol indices of the maximum concentration M_{cap} and the growth direction variation ω are negligible throughout almost the entire simulation.

Figure 7.5(d) summarizes the Sobol indices of the different parameters over time for the total length of the mycelium. Once again, the branching probability P proves to be the most influential during the exponential growth phase, after which the cost of growth c_g and the substrate diffusion coefficient D take over. In the case of the latter, it is clear that the growth of the network is related to the amount of substrate in the tips and therefore the substrate diffusion coefficient D. On the other hand, the cost of growth c_g determines how many fungal segments can be generated from one unit of substrate, and therefore governs the total number of segments of the network.

In summary, the *in silico* growth process is characterized by two phases. Firstly, an exponential growth phase, when the network is saturated with substrate and therefore able to rapidly generate new hyphae, and secondly a stable growth phase, during which the initial substrate is slowly depleted, as such decreasing the frequency of growth events (Trinci, 1974; Prosser and Trinci, 1979). During the former phase, the most important parameter is the branching probability P. The second growth phase is influenced by several parameters and their relative importance depends on the topological measure in question, but the substrate diffusion coefficient D appears influential for all of them. The reasoning is clear, the substrate diffusion coefficient D determines how fast the substrate can move to the tips, where growth takes place. The number of tips and the total length are also influenced by the cost of growth c_g, which determines the number of segments that can be created from one unit of substrate. The growth direction variation ω is only relevant for the extent of the mycelium. Still, it is of particular interest from a morphological point of view since it is often used to characterize fungal species (Kamel et al., 2009). Since the entire meaningful parameter range was

used in this sensitivity analysis, these results provide useful information for future model calibration. Finally, when it comes to experimental design guidelines for achieving this, we can conclude that most efforts should focus on an accurate assessment of the substrate diffusion coefficient D, the branching probability P and the cost of growth c_g.

7.3.2 Scenario analysis

In this section, we study some of the most common scenarios described in literature. In order to mimic the different growth scenarios, we use the cuboids introduced in Section 7.2. Every *in silico* experiment covers 1.5 days (i.e. 150 time steps), and is repeated 200 times in order to account for the involved stochasticity. *In silico* fungal growth is quantified using the measures introduced in Section 7.3.1.1. For the sake of comparability, the model parameters are the same across the scenarios and their values are given in Table 7.5.

Table 7.5: Parameters, corresponding notation, values and references used for the scenario analysis.

Parameter	Notation	hline Value	Source
Number of steps	T	150 time steps	—
Hyphal segment length	h_0	0.05 mm	Hopkins and Boswell (2012)
Time step	Δt	0.01 d	Hopkins and Boswell (2012)
Initial tips	H_0	25 tips	—
Initial substrate	Ω_0	5×10^{-6} mol	Computed from Boswell (2008)
Variation of growth direction	ω	$\frac{\Pi}{6}$ rad	Hopkins and Boswell (2012)
Branching probability	P	0.5	Carver and Boswell (2008)
Cost of growth	c_g	10^{-7} mol mm^{-1}	Boswell (2008)
Diffusion coefficient	D	3.456 mm d^{-1}	Boswell (2008) and Carver and Boswell (2008)
Maximum concentration	M_{cap}	2×10^{-6} mol mm^{-1}	Assumed

7.3.2.1 Description of scenarios

In order to have a reference for the effect of the different boundary conditions on the simulated fungal growth, we first considered a benchmark scenario (see Table 7.6). This benchmark scenario is similar to the one used in Section 7.3.1.1 to perform the SA, where the fungus grows freely in the three-dimensional space.

Fungal growth experiments are typically conducted to test the durability of materials (Adan, 2011), study the network of hyphae (Papagianni, 2004) or compare features across different fungal species (Fricker et al., 2007). In these experiments, the environmental conditions (temperature and relative humidity) are usually fixed and the samples are grown in Petri dishes to confine and control the accessible growth area. To conduct these experiments, only a substrate source and an inoculum are needed. Scenario 1 (see Table 7.6) mimics fungal growth in such a Petri dish, represented by two parallel impenetrable cuboids of size $10 \times 10 \times 0.1$ mm^3 that are separated by 0.2 mm with permanent resistance, and 12 droplets of solid substrate, on the bottom lid. *In silico*, we restrict to solid substrate (such as malt extract agar) in order to avoid external substrate diffusion. The substrate droplets are represented as cuboids of size 8×10^{-3} mm^3 and are positioned equidistantly on a circle with radius 0.5 mm centred at the centre of the Petri dish. Each cuboid contains enough substrate to generate 150 new hyphal segments, i.e. 10^{-7}mol. The uptake coefficient μ_k is set to 10^8 $mol^{-1}\,d^{-1}$, based on the value given in Boswell (2008).

Scenario 2 (see Table 7.6) is similar to the first one, since it also mimics fungal growth within a Petri dish, yet more droplets are added. It includes 36 substrate cuboids of 8×10^{-3} mm^3 with different external substrate concentrations that are positioned equidistantly on three concentric circles with radii of 0.5 mm (6 cuboids with 10^{-7} mol), 1 mm (12 cuboids with $\frac{10^{-7}}{2}$ mol) and 1.5 mm (18 cuboids with $\frac{10^{-7}}{4}$ mol), respectively. A similar *in vitro* configuration is reported in Davidson (1998) and Jacobs et al. (2002).

In Scenario 3 (Figure 7.8 and Table 7.6), the substrate is arranged according to the scaled coordinates of the main cities in Belgium (Brussels, Ghent, Antwerp, Ostend, Kortrijk, Leuven, Mons, Charleroi, Namur, Liège and Bastogne). This kind of experiment is common in literature, using oatmeal or agar as nutrient source, in order to test the ability of the fungi to find the shortest or most efficient path between different points in space (Adamatzky et al., 2012). The substrate cuboids have the same size and characteristics as in Scenario 1.

The following two scenarios (Scenarios 4 and 5) involve tropisms, since many researchers reported the ability of fungi to sense and react to external stimuli (see Section 7.2.3). Scenario 4 (see Table 7.6) comprises two forces repelling the fungus and no additional external substrate. Both of them have a negative effect with relative strength $\gamma_k = -1$, and it is assumed that their effect lasts throughout the entire simulation. The two forces are represented by cuboids of size 27 mm^3 with their centre located 1.6 mm apart from either side of the inoculum. Motivated by Meškauskas et al. (2004a), Scenario 5 (see Table 7.6) includes both positive and negative tropisms, such that the fungus gets attracted and repelled by different forces at the same time. This scenario consists of ten positive tropisms with strength $\gamma_k = 0.8$ and duration $\delta_k = 0.2$ d, and two negative tropisms with strength $\gamma_k = -1$ that are affecting the fungus for the entire simulation period. The positive

forces are placed on a circle of radius 0.5 mm and have a size of 8×10^{-3} mm^3. The two negative tropisms have a size of 27 mm^3 and are separated by 0.6 mm, with the positive forces in between them.

Scenario 6 (see Table 7.6) involves a wood block using a similar approach as Fuhr et al. (2011) for Norway spruce (*Picea abies*). Fungi are able to degrade lignin (Krivtsov et al., 2006; Schwarze, 2007), a substance present in plants. Consequently, they are essential for maintaining nutrient cycles in forests, while their effects can be adverse in human environments. For the latter issue, it is important to be able to simulate fungal growth within woody structures (Henkel et al., 2012; Wadsö et al., 2013). The wood structure is simplified as a bundle of tracheids with 95% of their cell walls consisting of solid material and 5% consisting of pits, penetrable and full of substrate. The dimensions of the wood block are 0.4 mm^3 and the wood cells are arranged in a cuboid grid, a grid consisting of cuboids with unit length 0.04 mm, height 0.04 mm and width 1 mm. Fungi are not able to grow through these walls, but they can penetrate them through the pits, which are randomly distributed along the centreline of the walls. In total, there are 237 pits, represented by cuboids of length 0.01 mm containing enough substrate to generate 150 new hyphal segments each (i.e. 10^{-7} mol).

7.3.2.2 Scenario analysis results

The dynamics of the *in silico* fungus under the different scenarios is studied by considering the following topological measures: total amount of internal substrate, extent, total number of tips and total length (Section 7.3.1.1). As an example, the variability of the scenarios is illustrated in Figure 7.6 showing the total length obtained for 200 runs per scenario over a period of 150 time steps (1.5 d). The scenarios without additional external substrate sources and without spatial restrictions (Scenarios 0, 4 and 5) result in values of total length that are very similar for all simulations. In contrast, the other scenarios (Scenarios 1, 2, 3 and 6) show more variability, as such illustrating the importance of external stimuli on fungal growth. Per scenario, mean curves for every topological measure were obtained from 200 simulations (Figure 7.7).

Figure 7.7(a) shows how the internal substrate within the mycelium evolves over time. The three scenarios without additional external substrate (Scenarios 0, 4 and 5) result in a depletion of internal substrate until a minimum amount is reached, beyond which growth and branching are not longer possible. In contrast, in the scenarios with additional substrate this can be used during the course of the simulation. The replenishment of substrate in these scenarios allows more internal substrate to reach the tips where it is consumed to create new biomass, as such resulting in lower final values of the total amount of internal substrate despite this replenishment. Scenario 2 evolves in a similar manner as the other scenarios with additional substrate, but in this scenario the impact of the substrate replenishment

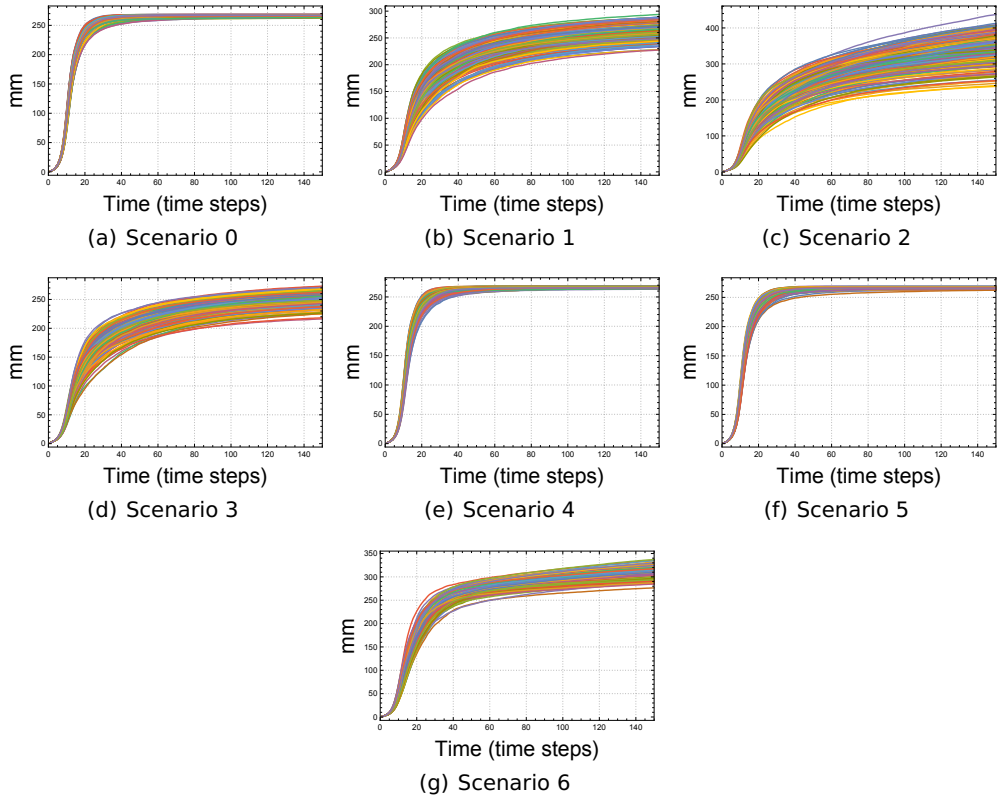

Figure 7.6: For each scenario in Section 7.3.2, the evolution of the total length during 1.5 days of growth for 200 simulations is given.

is even more pronounced. The position of the substrate cuboids in this scenario enables the mycelium to reach most of them and, therefore, to absorb more external substrate than in the other scenarios resulting in higher values of internal substrate.

The evolution of the extent of the mycelium under the different scenarios is shown in Figure 7.7(b). In Scenario 2, the mycelium becomes the largest. Again, this might be explained by the relatively high concentration of internal substrate during the entire simulation, which ultimately results in more branches and apical growth events. Scenarios 4 and 5 result in *in silico* fungi with a limited spatial extent, which is caused by the fact that the position of the hyphae is governed by the tropisms. The remaining scenarios present similar values for this measure, proving that the lack of internal substrate is as significant as the spatial confinement when it comes to the extent of the mycelium. Even in Scenario 6, where the fungus is confined to the long cavities of a wood block, which makes the fungus follow an almost straight line, its extent is close to the ones observed for the other scenarios.

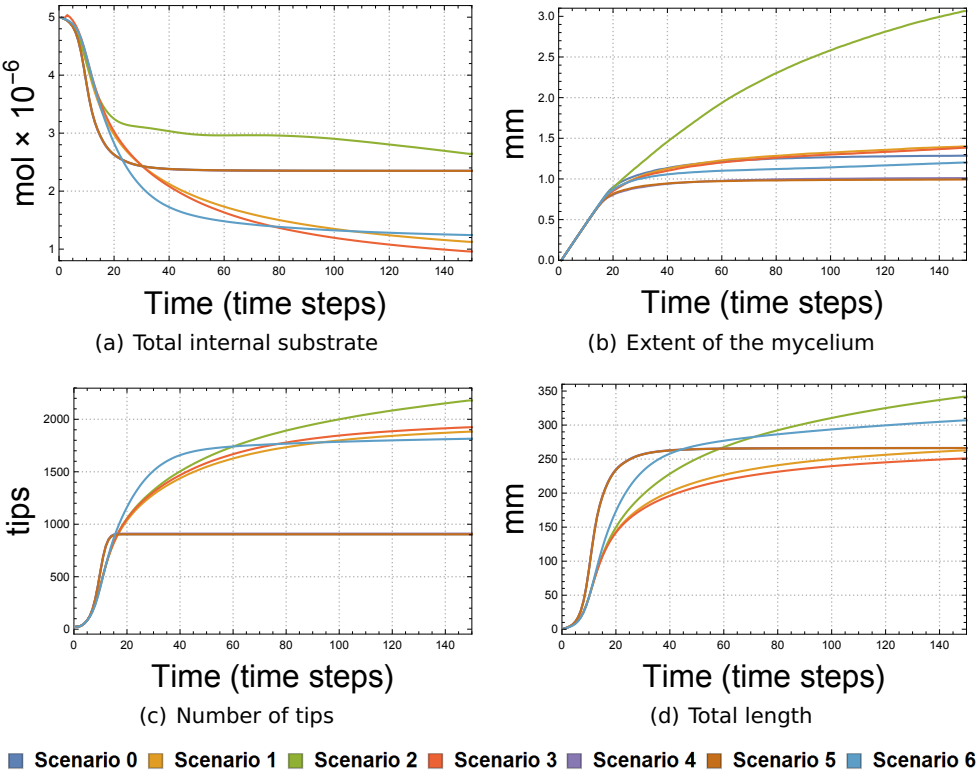

Figure 7.7: Mean curves of the topological measures for the different scenarios outlined in Section 7.3.2, computed from 200 simulations covering 1.5 days of growth.

Two different phenomena can be observed for what concerns the evolution of the number of tips over time (Figure 7.7(c)). In Scenarios 0, 4 and 5 the number of tips increases rapidly until it reaches a maximum. This behaviour is similar to the one observed for the internal substrate (Figure 7.7(a)) and it is related to the limited amount of substrate in these scenarios. The initial rapid generation of biomass implies an equally rapid depletion of internal substrate, after which the substrate availability within the fungus is no longer sufficient to create new branches. In the other scenarios (Scenarios 1, 2, 3 and 6) the number of tips increases during the entire simulation, though two phases can be distinguished: an exponential growth phase where the number of tips increases rapidly followed by a linear growth phase where the number of tips increases much slower. During the former, the *in silico* fungus generates new tips rapidly and consumes substrate faster than it is replenished, resulting in a mycelium full of segments with a limited amount of internal substrate left. Hence, the amount of substrate per segment at the linear growth phase is not enough to continue with this exponential branching and new tips are slowly generated as a consequence of the replenishment of substrate.

The mean curves obtained for the total length (Figure 7.7(d)) prove that the con-

finement of the area available for growth limits fungal growth. As can be observed in this graph, the scenarios without inert boundary conditions (Scenarios 0, 4 and 5) lead to a faster growth during the exponential growth phase, resulting in a higher total length than some of those confined by such conditions. We note a clear difference between Scenario 2 and the other scenarios representing growth in a Petri dish (Scenarios 1 and 3), which can only be explained by the available amount of external substrate. In Scenario 6, an in silico fungus grows inside a wood block full of substrate cubes placed in the wood walls where they can be reached but not as easily as in the other scenarios. In addition, the dimensions of the wood block allow the fungus to grow beyond the limits of the wood block in most simulations, and to grow without further restrictions from boundary conditions. The high substrate concentration together with the confined and free growth phases result in the high values of total length observed in Figure 7.7(d).

Even though the results of the scenario analysis are of a qualitative nature, some of the most striking characteristics of fungal growth can already be observed. For instance, the benchmark scenario produces similar growth patterns (Figure 7.4) as those obtained with other models that mimic survival scenarios (Boswell, 2008; Carver and Boswell, 2008). Scenario 1 can be compared with experimental set-ups, where most substrate is placed close to the mycelium (Vidal-Diez de Ulzurrun et al., 2015). The topological measures quantifying the *in silico* dynamics of this scenario resemble those observed for *Rhizoctonia Solani*, but on a different scale due to the initial conditions of the experimental set-up, where the initial shape of the mycelium is not known. The amount of external substrate and its spatial distribution are key when modelling fungal growth, as should be clear from Scenario 2. The topological measures for this scenario take values significantly different from those obtained for the other scenarios. The main reason for this is the replenishment of substrate in Scenario 2, which has been also observed in similar growth scenarios (Jacobs et al., 2002) and further investigated in Boswell et al. (2003). Unfortunately, our *in silico* results for Scenario 3 (Figure 7.8) are not easy to compare to those of similar experimental set-ups (Adamatzky et al., 2012), especially without a proper calibration.

In contrast, the effects of single droplets of agar on the shape of the *in silico* mycelium agree with the ones presented in Hopkins and Boswell (2012) for a growth scenario where nutrient sources are placed randomly in space. The scenarios involving tropisms (Scenarios 4 and 5) lead to *in silico* mycelial structures that are similar to those shown in Meškauskas et al. (2004a), in particular those obtained for the scenarios including attracting substrate forces and horizontal plane tropisms (Figure 7.9).

Our last scenario was designed according to the set-up of Fuhr et al. (2011). The latter considers fungal growth from a substrate point of view, while the model presented in this manuscript is based on the biological processes of the fungi, which makes the output of the models fundamentally different. Still, growth patterns pro-

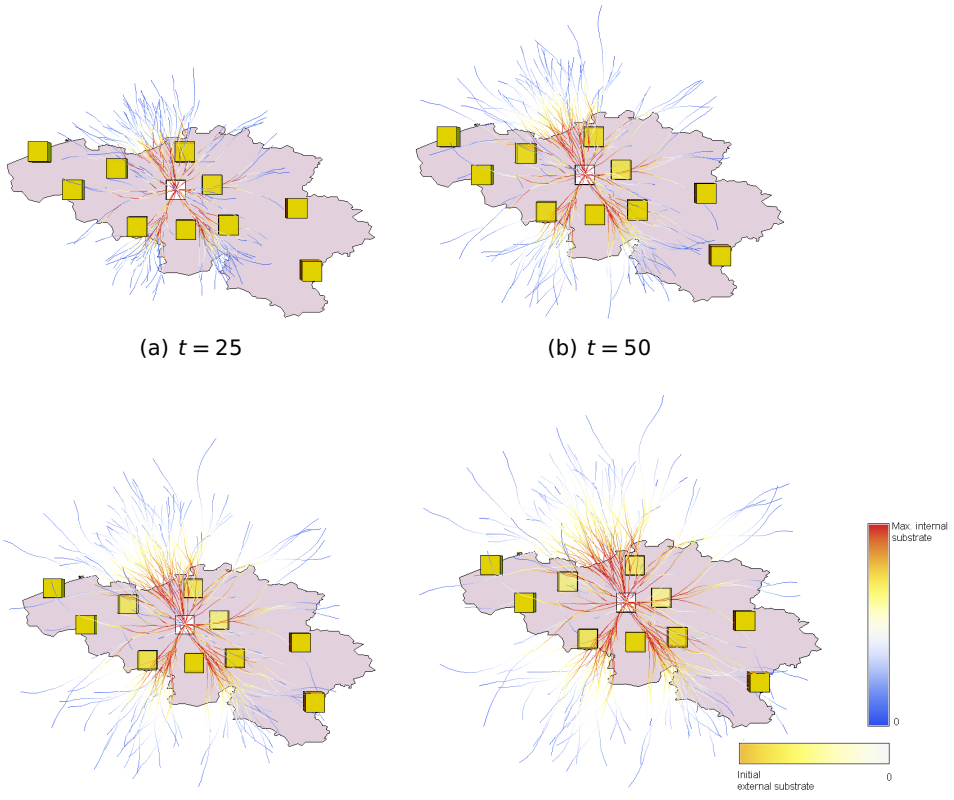

(a) $t = 25$ (b) $t = 50$

(c) $t = 75$ (d) $t = 100$

Figure 7.8: *In silico* mycelium at 25 to 100 time steps (0.25 to 1 day) with indication of the internal substrate concentration, using $h_0 = 0.1$ mm, $c_{gr} = 5 \times 10^{-8}$ mol mm^{-1} and the other parameters as shown in Table 7.5.

duced by both models show some similarities, which once more proves the ability of our model to replicate growth behaviour driven by different environmental conditions.

Overall, the model presented in this chapter is able to reproduce different types of fungal behaviour that have been previously presented in literature. The studied topological measures show that the amount of substrate, as well as the confinement of space, are two key factors determining the overall growth and shape of the *in silico* mycelium.

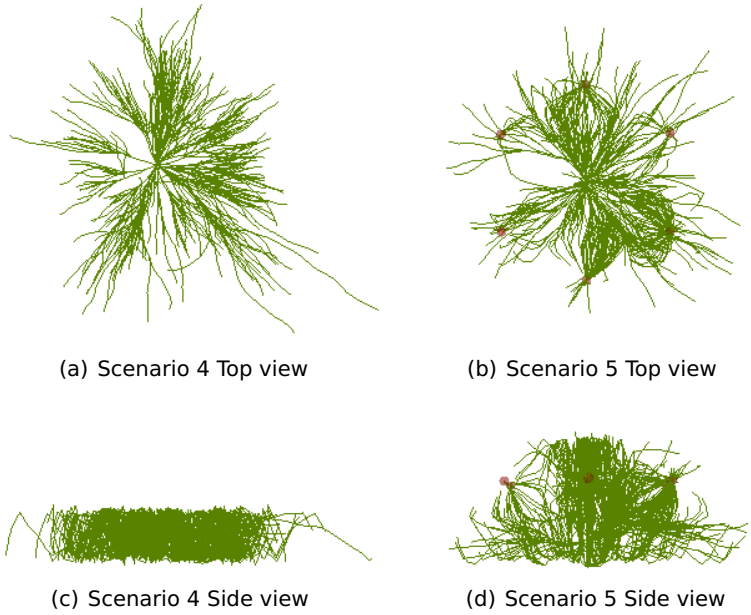

(a) Scenario 4 Top view (b) Scenario 5 Top view

(c) Scenario 4 Side view (d) Scenario 5 Side view

Figure 7.9: Example of different tropisms on the *in silico* fungus shape, top and side view. These *in silico* mycelia correspond to the visual representations of Scenario 4 (7.9(a) and 7.9(c)) and Scenario 5 (7.9(b) and 7.9(d)) using the parameters given in Table 7.5 after 150 time steps.

7.3.3 Discussion

In this chapter we have presented a new SEM able to mimic fungal growth in three dimensions. It focuses on the evolution of the hyphae as the result of biological processes and effects of different external stimuli. The *in silico* mycelium and the environment are designed as independent entities that interact with each other. Our model is based on established fungal growth models (Boswell, 2008; Carver and Boswell, 2008; Hopkins and Boswell, 2012; Meškauskas et al., 2004a). However, fungal growth is here not confined to a lattice and growth is replicated in three dimensions, as such leading to more realistic representations of the mycelium. Since most of the underlying assumptions have been advocated by other studies, we believe it is capable of mimicking fungal growth in a realistic way. However, processes like hyphal degradation (Gadd et al., 2007) or lateral branching (Edelstein, 1982; Mouriño Pérez et al., 2006) are still to be incorporated. In addition, some processes already incorporated in the model, such as translocation and uptake, are not yet well understood and even less so in the three-dimensional space. On the other hand, even though the values of most model parameters can be found in literature (see Table 7.5), these data originate from a few species and environmental conditions, hindering a more detailed study of specific fungal species

and conditions. Furthermore, current experimental set-ups and techniques are usually narrow in scope (Fricker et al., 2009), not allowing for the calibration of the parameters involved in most fungal growth models. In response, several techniques based on image analysis (Obara et al., 2012; Lopez-Molina et al., 2015; Vidal-Diez de Ulzurrun et al., 2015) have been developed for the purpose of extracting the data needed to calibrate SEMs. Yet, parameters related to internal substrate diffusion or maximum concentration have to be identified using different techniques, since they cannot be visually assessed. For instance, X-ray computed tomography (Van den Bulcke et al., 2009) and confocal microscopy (Dickson and Kolesik, 1999; Bago et al., 2002; Fricker et al., 2008) could offer a way out. The substrate diffusion has turned out to be the most important parameter (see Section 7.3.1.1), and therefore efforts should be made in order to carefully determine this parameter.

In our model, the environment is discretized using cuboids representing different boundary conditions (see Section 7.3.2). Even though some of these conditions have been studied before (Boswell et al., 2007; Boswell, 2008; Hopkins and Boswell, 2012; Fuhr et al., 2012; Meškauskas et al., 2004a), this chapter reports on the first attempt to mimic so many of them and combinations thereof. The boundary conditions presented in this chapter allow to mimic most real-world situations, and combining them makes it possible to design complex and realistic scenarios. The scenarios presented in Section 7.3.2 illustrate the scope of our model. It is able to replicate the environments and conditions of some of the most common experiments found in literature. Moreover, complex scenarios such as growth in soils (Morgan et al., 1993; Boddy et al., 1999; Pajor et al., 2010) could be studied with this approach by discretizing the soil according to its actual structure. Another possible extension would be to study the resistance of different materials to fungi (Gobakken and Westin, 2008), where each of these materials could be encoded easily using appropriate boundary conditions. The boundary conditions mainly affect the direction and the internal substrate of the hyphae, while parameters like the cost of growth or the hyphal length are not affected. Nevertheless, the values of the latter parameters may depend on other environmental conditions not yet included in our model, such as relative humidity and temperature, since these have proven to affect the growth dynamics independently from the growth scenarios (Ayerst, 1969; Magan and Lacey, 1984) and therefore should be taken into account in further work.

The interactions between fungi and their environment are not yet completely understood and the available knowledge is often based upon hypotheses and assumptions (Gadd et al., 2007). Even though fungal growth models can help to clarify the nature of such interactions, they need to be properly calibrated in order to provide valid results. Therefore, further experimental studies of the interactions between the fungus and its environment are needed for the calibration of fungal growth models incorporating both fungi and environment. Furthermore, these ex-

periments should be designed to complement the theoretical models that they aim to calibrate. For these reasons, future extensions of this research must include the generation of experimental data which can be incorporated into the current model, as such increasing its reliability and applicability.

In summary, we have developed the first three-dimensional lattice-free model able to replicate fungal growth in different environments. The model is based on biological processes and theories, as such ensuring a realistic representation of the fungal dynamics. In addition, the growth environment is reduced to a set of cuboids, representing different boundary conditions, allowing for the representation of a vast number of *in silico* growth scenarios. A global SA was performed in order to study the impact of the different parameters on a set of topological measures commonly used to track fungal growth. The SA has shown that the internal substrate coefficient, the branching probability and the cost of growth are crucial to our model. A scenario analysis was conducted to study the effect on the overall fungal growth of different growth scenarios. These scenarios included some of the most studied experimental set-ups described in literature, as such illustrating the capability of the model to replicate *in situ* growth scenarios.

Table 7.6: Summary of different *in silico* fungal growth scenarios: description and visual representation.

Scenario	Description	Representation
Benchmark	Three-dimensional space without spatial restrictions.	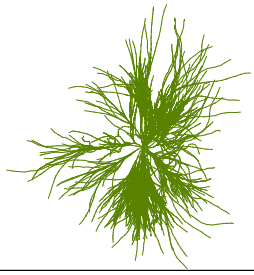
Scenario 1	Petri dish inoculated with substrate droplets 2 x Impenetrable cuboids 12 x Substrate cuboids	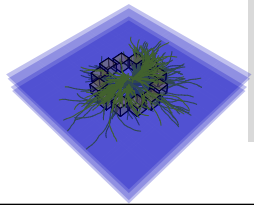

Continued on next page

Table 7.6 – *Continued from previous page*

Scenario	Description	Representation
Scenario 2	Petri dish inoculated with substrate droplets of different concentrations. 2 x Impenetrable cuboids 36 x Substrate cuboids	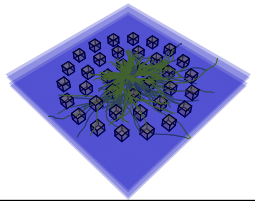
Scenario 3	Petri dish inoculated with substrate droplets placed on a scaled map of Belgium. 2 x Impenetrable cuboids 11 x Substrate cuboids	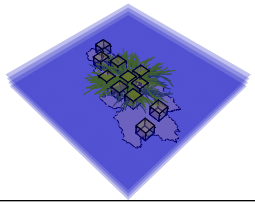
Scenario 4	Two parallel negative tropisms (repulsion). 2 x Tropism cuboids	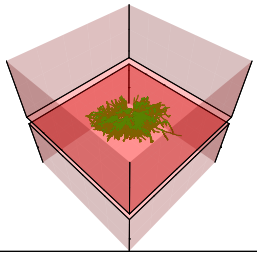
Scenario 5	Two parallel negative tropisms and six temporal positive tropisms (repulsion and attraction) 8 x Tropism cuboids	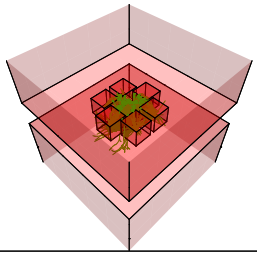

Continued on next page

Table 7.6 – *Continued from previous page*

Scenario	Description	Representation
Scenario 6	Wood block. 10 x Impenetrable cuboids 237 x Substrate cuboids	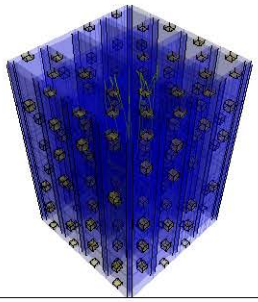

PART IV

CONCLUSIONS AND PERSPECTIVES

8

Conclusions

Fungi have been widely studied to gain a better understanding of their unique characteristics, to improve production processes and develop new products, and to limit their growth in order to protect organic materials (Chapter 2). Their growth is their most remarkable characteristic. For instance, most fungi are able to gain biomass only by extending and branching existing hyphae, resulting in complex networks that allow them to colonize and survive in different habitats. Different processes are involved in the generation of new fungal biomass, some of which occur in distant regions of the fungal network. Even though fungal growth has been the subject of many studies, some of the underlying processes driving it are still unknown. In addition, external factors also play an important role in the development of fungal networks, since each fungal species grows only under certain environmental and nutritional conditions that differ significantly among different species. Therefore, fungal growth is a challenging topic that is not yet fully understood.

One of the main factors hindering the study of fungal growth is the nature of the established experimental techniques that are not able to produce quality data. Experiments have to be performed repeatedly to account for the natural variability of

fungi, even when considering the same fungal species, and to account for the wide range of possible substrate sources, habitats and environmental conditions. Unfortunately, most of the current techniques involve manual steps, and in some cases even the destruction of the sample, which makes it impossible to track growth over time on a single individual fungus. In addition, other techniques focus on extremely small regions of the network, so that the corresponding findings do not explain the behaviour of the whole fungal network. For these reasons, techniques able to produce large high-quality data sets in an efficient way are needed in order to advance the study of fungal growth.

The increase in computing power and the rise of new data acquisition techniques open new avenues of study which can help to overcome these limitations. For instance, the automated processing of biological imagery has gained momentum in the past years due to the availability of cheap imaging and processing equipment, and the development of dedicated image analysis algorithms. The scale at which fungi grow allows for the extraction of numerous images using basic machinery, making them the perfect subjects to study with such techniques. Furthermore, images can be captured in an automated and non-destructive way, as such overcoming the limitations of some existing techniques. Consequently, we investigated the possibilities that image analysis has to offer to the study of fungi in Chapter 4. For this purpose, we built an image analysis algorithm able to extract ridges from raw images of different fungi taken at different scales. This algorithm is based on anisotropic multiscale kernels for second order image differentiation, as such allowing for the use of multiple scales and anisotropy indices. In addition, the algorithm was tested on a new data set of images featuring different fungal species, thereby proving that it produces better results than those obtained with other ridge extraction algorithms.

Motivated by the results obtained with the ridge detection algorithm, we developed a new method able to automatically capture images of growing fungi. On the basis of the resulting binary ridge maps, we were able to compute different topological measures for the studied fungi, as such synthesizing their growth dynamics (Chapter 5). For this purpose, we designed an innovative experimental set-up that does not require expensive or complex equipment, as such permitting its reproducibility in most laboratories. The resulting time series of images are processed using the ridge extraction algorithm and subsequently transformed into graphs, from which several topological measures accounting for different aspects of the fungal dynamics can be computed. In addition, this method can be used to study the growth kinetics of various fungal species. In order to illustrate and test the versatility of this method, the dynamics of five fungal species were mutually compared. The results of this comparison concurs with key fungal growth assumptions and studies, as such supporting the efficiency and applicability of our method.

Assessing the effect of the prevailing environmental conditions on fungal growth is still an important topic for the research community. New materials and preser-

vative products used in construction to protect buildings from fungal decay need to be tested under different environmental conditions. Unfortunately, not all of the tests used are able to efficiently assess their effect in sufficient detail. In addition, climate change has altered the habitats of fungi, thereby affecting their growth dynamics and having a strong impact on their ecosystems. For these reasons we decided to quantify the effects of the environmental conditions on fungal growth using the aforementioned method in Chapter 6.

The original experimental set-up was adjusted to assess the effect of different temperatures and relative humidities on the growth of *Coniophora puteana*. Besides, the preparation of samples was slightly improved, as such resulting in images of higher quality. These images were used to perform a detailed analysis of 16 environmental conditions by studying their effects on several topological measures. The obtained results are in line with similar studies found in literature, as such suggesting that our approach is suitable for studying the effect of these factors. Essentially, our method constitutes an alternative to overcome some of the problems of other approaches studying the effects of environmental conditions on fungal growth.

However, the method presented in Part II also has some limitations since processes occurring inside the fungal network cannot be studied by means of images. Still, these processes have proven to be crucial for the development of fungi. In addition, growth scenarios involving opaque structures cannot be studied easily by our method since simple imaging devices are not able to capture fungal growth occurring inside these structures. Finally, even though the method here proposed is able to produce accurate data faster and more efficiently than most experimental techniques, it is subject to the space and time restrictions of laboratories. In order to overcome the aforementioned limitations and to better understand the processes driving fungal growth, we turned to mathematical modelling.

Several mathematical models have already been proposed to mimic fungal growth by relying on different hypotheses, methods, scales and modelling paradigms. The most relevant fungal growth models were reviewed and compared in Chapter 3. In the light of this review, we formulated a spatially explicit model representing fungal growth at mesoscopic scale (Chapter 7). It takes biological processes into account and relies on established theories, as such ensuring a realistic representation of the fungal dynamics. In addition, this model mimics growth in three dimensions without any restriction on the spatial degrees of freedom and takes into account the effects of different external stimuli that are often neglected by modellers.

This three-dimensional lattice-free approach allows us to simulate fungal growth in a more realistic way than most models working at the same scale. Furthermore, the external stimuli interacting with the *in silico* fungus can be combined to represent various boundary conditions, allowing for the representation of a vast number of *in silico* growth scenarios, including some of the most commonly used experimental set-ups and even wood degradation scenarios. Therefore, a scenario

analysis was conducted illustrating the capability of the model to replicate *in situ* growth scenarios. In addition, a sensitivity analysis was conducted in order to determine the model parameters that should be further investigated. Even though further calibration of the model parameters is still needed on the basis of more extended data sets, this model is already able to mimic different observed growth behaviours.

In conclusion, the methods presented in this thesis offer an updated and broader alternative to classical and narrowly focused studies, thus opening new avenues of investigation in the field of fungal growth research. This dissertation therefore provides powerful instruments useful for the advancement of the study of fungal growth.

9

Future perspectives

The methods and results described in this dissertation are a significant progress for the assessment and modelling of fungal growth. First, an image analysis technique was described in Part II. This technique is able to generate detailed data on the development and growth of different filamentous fungal species, and this under different environmental and nutritional conditions, as such allowing for a better understanding of fungal growth. In addition, a mathematical model was formulated in Part III. This model combines different models and includes the interactions between fungi and different external stimuli occurring in three dimensions. Still, both the image analysis technique and the mathematical modelling can be further extended and employed, targeting at several different applications and studies. In the remainder of this chapter, we will discuss different growth scenarios that could benefit from the use of the image analysis technique here presented and how to improve and adapt this technique to other scales and features. Possible extensions of the current mathematical model, including necessary adaptations to model more complex and diverse growth scenarios and to simulate the growth of other filamentous organisms will be examined as well.

9 9.1 Extending our image analysis technique

The image analysis technique described in Section 5 comprises three consecutive stages: sample preparation and image extraction, image processing and extraction of fungal growth features. The results obtained using the aforementioned technique represent a significant advance compared to most traditional methods used for the same purposes. However, there is still room for improvement; therefore, we will discuss some limitations and possible extensions of our image analysis technique in this section.

9.1.1 Sample preparation and image extraction

Fungi are able to grow on many different substrates, even those containing a limited amount of nutrients only (Pasanen et al., 1991) and therefore almost any material is prone to their attack. For example, new designs and treatments are being developed to protect building materials against the action of fungi. Each material and treatment have to be tested under different environmental conditions and against different fungal species in order to study its efficiency. However, most standard tests are subjective and do not take growth patterns into account (Adan, 2011). For these reasons, alternative testing methods able to assess fungal growth in a more objective and detailed manner are needed. We believe the image analysis approach discussed in this dissertation could be adapted to test fungal resistance of different materials under different environmental conditions. However, this image analysis approach requires certain quality criteria that could impose a problem when studying the growth of fungi on different materials.

In order to use our technique, images need to present certain contrast levels ensuring that hyphal material can be distinguished from the background. In scenarios involving limited substrate sources, i.e. fungal growth in the empty space, the contrast level required can be easily obtained. Fungal growth on agar, on wood or wall paper could have limited contrast and require further analysis. These scenarios are crucial when studying the aesthetic performance of materials and to test the efficiency of fungicides and therefore need to be tackled. A possible solution is the use of dyes (Card et al., 2013), radioactive labelling (Riquelme et al., 2011) or immunofluorescence labelling (Xiao et al., 1999) in order to achieve a higher contrast. However, the effect of these treatments on fungal growth needs to be taken into account.

Another criterion of the image analysis technique is that vertical growth needs to be limited to a few millimetres. This limitation is not a problem when studying growth scenarios involving agar, however, other materials cannot be constrained to these dimensions. For instance, some engineered wood materials are composed

of several different materials and therefore a small sample would not be able to represent their overall characteristics. A possible solution for this problem would be to reduce the studied material to a basic physical state by removing its spatial structure, for example, by grinding. Even though further analysis has to be conducted, we believe this small change would be sufficient to assess fungal growth on different materials objectively and in extensive detail.

Internal processes and mainly translocation of nutrients are crucial to understand fungal growth, unfortunately, processes occurring within the mycelium cannot yet be tracked using our current experimental set-up. These processes can be followed using techniques relying on fluorescent labels or chemical markers, such as confocal microscopy (Bartnicki-García, 2002) and multiphoton microscopy (Bago et al., 2002). Our image analysis technique should be easily adaptable to study images obtained using the aforementioned techniques. In addition, a better understanding of nutrient translocation and uptake is needed in order to improve mathematical models such as the one presented in Part III of this dissertation. Since the parameters driving translocation in *Coniophora puteana* have not yet been calibrated, the adaptation of the current image analysis technique to study the processes occurring within the mycelium constitutes a priority in order to fully calibrate our model.

In addition, the experimental set-up here discussed does not allow for the tracking of hyphal growth inside opaque substrates. Such scenarios are important since processes such as material degradation or food spoilage mainly occur within host organisms. Current imaging techniques, including scanning electron microscopy (Sherif et al., 2016), X-ray computed tomography (Van den Bulcke et al., 2009) and optical fluorescence microscopy (OFM) (Romão-Dumaresq et al., 2016), are able to track hyphae in the interior of opaque structures (see Figure 9.1). Even though the use of such imaging devices defeats the purpose of our image analysis technique, i.e. providing an easy and cheap alternative to current experimental methods, images obtained with such devices could also be studied using an adapted version of our image analysis technique.

The image analysis technique presented in Part II of this dissertation is only able to study two-dimensional images of fungi. However, different devices are able to capture three-dimensional images of fungi, such as laser scanning confocal microscopes (CLSM) (Du et al., 2016) and X-ray computed tomography (CT) scanners (Van den Bulcke et al., 2009). For instance, CLSM constructs three-dimensional images by assembling several two-dimensional images representing different sections of the studied entity. In addition, several images can be captured over time, as such allowing to track the evolution of fungi in three dimensions. Even though time series of fungi growing in 3D can be obtained, classical image analysis techniques, including the one described here, are not yet able to deal with these kind of data. Therefore, in order to deal with three-dimensional images, all the techniques here described should be revisited. This poses a significant challenge, but

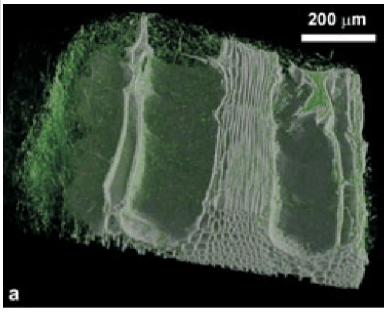

(a) X-ray computed tomography

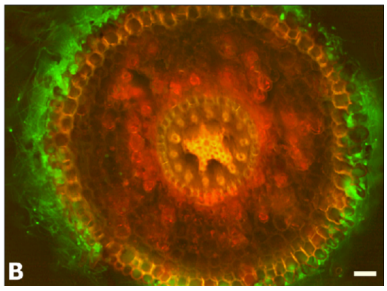

(b) Optical fluorescence microscopy

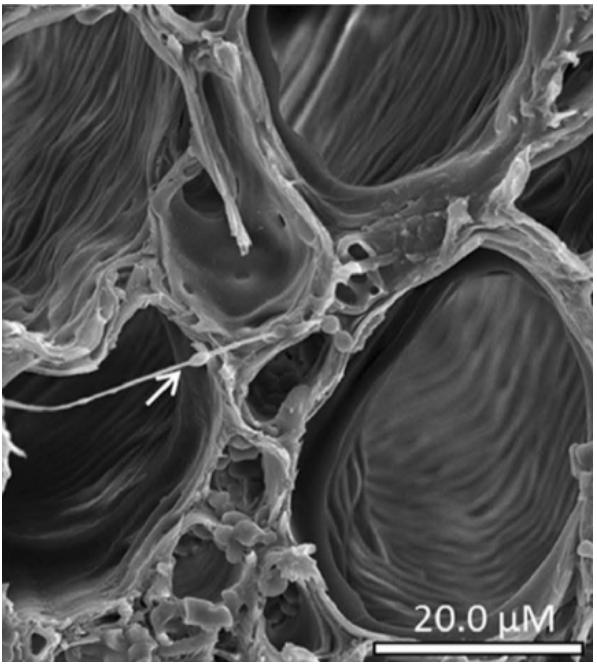

(c) Scanning electron microscopy

Figure 9.1: Images of growing hyphae in the interior of wood obtained with: (a) X-ray computed tomography, (b) optical fluorescence microscopy and (c) scanning electron microscopy. (Sources: (a) Van den Bulcke et al. (2009), (b) Romão-Dumaresq et al. (2016) and (c) (Sherif et al., 2016))

the possible results are worth the effort and therefore we plan to work further in this direction.

9.1.2 Image processing

The image analysis algorithm used to extract ridge maps from fungal images was presented in Chapter 4. This algorithm is able to simplify the information contained in raw images representing mycelia. This is achieved by relying on the individual characteristics of each image. For instance, the binarization thresholds are computed using only the image histogram. Consequently, we can conclude that the current technique does not take into account correlation between consecutive images. In contrast, the output of our experimental set-up consists of time series of correlated images representing the evolution of the mycelium instead of individual unrelated images. In addition, small variations in a single image have a high impact on the results of the whole series. For example, dust particles or slight light changes may change the image histogram and subsequently the binarization thresholds affecting the amount of hyphal material detected by the algorithm

contrasting with those detected in previous or subsequent images. Unfortunately, this contamination during the image capturing stage is almost impossible to avoid. Therefore, the incorporation of time into the image analysis algorithm could be beneficial for the overall results.

The time series of images could be studied as a whole instead of as a collection of individual images. For instance, computing binarization thresholds using a global histogram (composed of the histograms of all images in the time series) should significantly minimize the impact of small perturbations. In addition, some important features, such as branching and anastomosis of fungi, cannot be explicitly assessed using the current technique due to their time dependency. For this purpose, nodes and edges should be explicitly tracked over time, which requires a significant amount of computing power and a proper characterization of all graph elements. Even though this adaptation is quite challenging, the adapted techniques would rely on graphs similar to those obtained with our current experimental set-up. We believe the inclusion of time would result in relevant improvements.

9.2 Model calibration and validation: combining image analysis and mathematical modelling

Mathematical models can be used to describe many natural phenomena. However, this can only be achieved by calibrating the models and validating their results using experimental data. During the calibration stage, the model parameters are determined using experimental data in such a way that the agreement between the model outputs and the data is maximized. Then, the accuracy of the model results needs to be tested to determine if the model is able to realistically describe the modelled phenomena. The validation needs to be objective and therefore it needs to be performed using an independent data-set. In the remainder of this section we will discuss how the techniques described in Part II could be used in order to calibrate and validate the model proposed in Part III.

The image analysis technique captures images of the whole mycelium growing at a centimetre scale, hence producing data at mesoscopic scale, the same scale the model works at. Additionally, the model is able to simulate different growth scenarios including *in silico* counterparts of the elements employed in the experimental set-up, such as Petri dishes and agar droplets. Therefore, the model and the image analysis technique can be combined in order to both determine the values of the model parameters and to assess the accuracy of the model results.

For instance, several model parameters can be computed directly from topological measures obtained using the image analysis technique. For example, the hyphal

length h_0 and the growth angle ω can be computed directly using the mean observed hyphal length and the growth angle, respectively, or even their corresponding experimental distributions. Even the initial number of tips or the distribution of additional nutrients sources can be incorporated into the model using the imagery data obtained.

In contrast, the calibration of other parameters requires more consideration. For instance, the cost of growth, c_g, cannot be computed using a single growth scenario since different substrate concentrations need to be compared in order to determine their value. Actually, the set-up described in Chapters 5 and 6 should be repeated several times starting from different substrate concentrations. Consequently, the total hyphal length obtained for each of these experiments could be used to determine the amount of substrate that is needed to growth a single hyphal segment. Such growth scenarios would also give an insight in how the nutrients concentration and distribution affect other parameters, namely the branching probability P which is strongly correlated in the model to the internal substrate. However, further investigation is needed to determine the latter parameter since the current image analysis technique does not allow to track branching and anastomosis explicitly (see Section 9.1.2).

Unfortunately, a third group of parameters cannot be determined by means of the techniques described in Part II of this dissertation since they occur inside the mycelium and cannot be captured by the imaging devices employed. Therefore, parameters accounting for the substrate translocation, such as the diffusion coefficient D and the maximum hyphal capacity $Mcap$ would require a different kind of experiments. A possibility to study the latter parameters resides in the use of fluorescent and chemical markers as discussed in Section 9.1.1.

Once the model is properly calibrated a new growth scenario needs to be implemented, both *in silico* and *in vivo* in order to quantify the accuracy of the model. Then, some distance measure, such as the bias or the accuracy factor can be used to assess the agreement between the experiments and the model results (Zhou et al., 2012; Samapundo et al., 2005). The main advantage of our image analysis technique in this stage is that it leads to several topological measures over time. This allows to test how accurate the model represents different aspects of the growing fungus, including its morphology, compactness and its overall growth dynamics.

Due to the versatility of the image analysis technique we argue that it would be of use also for the calibration and validation of other mathematical models. Even though the nature of the model parameters varies widely depending on the scale and modelling approach, the image analysis technique can be tuned in order to determine different parameters. In addition, the results of most models consist of *in silico*representations of the mycelium (see Chapter 3), which can be characterized by the topological measures introduce in Chapters 4 and 6, as such allowing for

their comparison with those extracted from the *in vivo* fungal images and therefore, for the validation of the models.

9.3 Model extensions

In Part III a new mathematical model representing fungal growth was described. This model represents the hyphae of an *in silico* fungus growing and interacting in three dimensions. This model opens new avenues of investigation due to its versatility. However, it constitutes only a first version on the basis of which we plan to build several improved models yet to come. Consequently, some of the possible model extensions will be discussed here.

9.3.1 Dynamical fungal growth parameters

One of the main assumptions of most fungal growth models is that growth parameters are constant through time. Hence, concepts such as hyphal segment length, substrate diffusion coefficient, cost of growth or branching probability are vastly used by the fungal growth modelling community. The use of these constants results in simple and robust models. In addition, these constants have been studied in literature for several fungal species and can be derived from direct observations of *in vivo* fungi. However, even basic experiments show that most fungal growth parameters depend on different factors including environmental conditions (Pasanen et al., 1991), time (Gadd et al., 2007) and the position of a hypha within the fungal colony (de Bekker et al., 2011; Hickey et al., 2002).

The impact of temperature and relative humidity was studied in Chapter 6. As reported by other researchers, these two environmental factors play an important role in the development of mycelia. This means that for each fixed environmental condition the model aims at mimicking, recalibration of its parameters is required. Furthermore, *in vivo*, environmental conditions change over time and space and therefore the restriction of fixed environmental conditions is a significant constraint. Therefore, we believe that growth parameters could be better represented as functions of, for example, temperature and relative humidity than as simple constants. Even though this extension may seem easy to implement, recognizing which fungal growth parameters are affected and the exact effect of the external conditions requires further investigation. However, a model able to predict fungal growth under changing environmental conditions would be of relevance for several sectors and industries, principally for the building sector.

On the other hand, other factors such as the position of a hyphal tip further or closer to the center of the colony has also an impact on its growth features. For

instance, lateral branching occurs mainly at the center of the colony, while apical branching is mainly observed at the periphery (Hickey et al., 2002). Therefore, in our model, the distance of a hyphal segment to the center of the colony could be used to compute its branching probability or its growth angle. By using dynamic parameters, other fungal processes such as fungal autolysis could be included in the model. Hyphae become inactive over time and during this inactivation process their ability to take up and translocate substrate decreases gradually (Boswell et al., 2003). Therefore, the age of a hyphal segment could be used to determine the amount and velocity of the substrate diffused through it. All these extensions would result in a more realistic model, yet substantial work has to be done in order to achieve this.

9.3.2 Revision of substrate uptake and translocation

Substrate plays a central role in our fungal growth model. As suggested in previous studies (Boswell et al., 2003; Carver and Boswell, 2008), substrate is not only used to create new biomass, but also to determine whether or not a branching event occurs or to determine the amount of substrate that can be incorporated into the mycelium. In our model, substrate reaches hyphal segments through one of two processes: uptake of external substrate, where external substrate is absorbed, converted into internal substrate and incorporated into the hyphal segment, or by translocation of internal substrate, where internal substrate is provided by neighbouring hyphal segments. Different theories have been formulated over the years about these two processes (Fricker et al., 2008; Tlalka et al., 2007) and due to the difficulties to study them at larger scale, they are not yet completely understood (Fricker et al., 2008). Due to the importance of these processes in the model, we believe further effort has to be made in this direction.

For example, our model mimics translocation as the effect of diffusion. Even though a similar approach has been used by several modellers (Boswell, 2008; Carver and Boswell, 2008; Davidson, 1998), most theories suggest that translocation may be the result of an active and a diffusive process (Boswell and Hopkins, 2008). For instance the diffusion of external substrate in the environment is not taken into account and the conversion of external substrate happens immediately and without the use of an explicit conversion rate. Although these assumptions do not interfere with the purpose of the current model, further versions of the model would need a revisited version of these substrate-related processes.

9.3.3 A realistic wood decay scenario

Fungi are the main organisms degrading wood and wood-based materials (Schwarze, 2007) and the building sector is especially affected by their degrading action (Adan

and Samson, 2011). Therefore, Chapter 7 includes a growth scenario representing a simplified version of a wood block within which an *in silico* fungus is growing. The wood block is represented as a collection of wood tracheids arranged in a square lattice in three dimensions. It is composed of two different materials: impenetrable and substrate cubes representing wood walls and pits, respectively. Even though this basic representation allows to simulate the physical restrictions imposed by the wood structure on the growing fungus, it cannot fully grasp the complexity of the wood degradation process.

In order to develop a more realistic wood degradation scenario, several additional features should be incorporated into the model. For instance, fungi degrade wood by releasing enzymes targeting different chemical wood components, resulting in different types of wood degradation, which are referred to as brown rot, white rot and soft rot (Schwarze, 2007). Hence, the secretion of enzymes needs to be included in the model in order to represent any of the aforementioned rotting processes. Secretion of enzymes by *in silico* hyphae has been successfully modelled for different purposes (Hopkins and Boswell, 2012). Therefore, we believe that the incorporation of the secretion of enzymes in the current model, in a similar manner, should be feasible. However, the effect of the *in silico* enzymes would require further analysis.

Additionally, the representation of the wood block structure could be better represented using real three-dimensional images such as the ones obtained using X-ray computed tomography (Van den Bulcke et al., 2009) (see Figure 9.2). Such three dimensional images could serve as templates to develop *in silico* growth scenarios, where the structure of the wood block would be represented by using different cubes. Furthermore, the evolution of the mycelium and the structural changes of wood could be tracked in three-dimensions using the image-based technique suggested in Section 9.1.1, enabling a 3D calibration of the model.

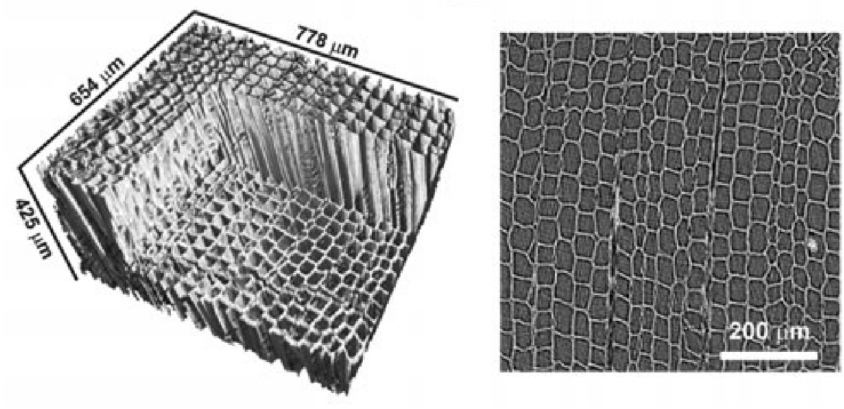

Figure 9.2: Three-dimensional reconstructions of a pine wood block and cross-sectional view obtained using X-ray computed tomography. (Source: Van den Bulcke et al. (2009))

9

9.3.4 Modelling other filamentous organisms

The most interesting characteristic of filamentous fungi is their growth as structured networks. However, fungi are not the only organisms presenting this kind of growth. For instance, neurons (Osório et al., 2013) or arteries (Burrowes and Tawhai, 2006) extend in a similar manner to that observed for fungi. The roots of plants are another example of apical growth and branching (Dupuy et al., 2010). Physical phenomena such as rock cracking (Ghazvinian et al., 2014) or lightning (Reed and Wyvill, 1994) can also be envisioned as a collection of segments extending and branching.

In the framework of this research we had the opportunity to collaborate with the Earth and Life Institute of the Université Catholique de Louvain (Belgium) in order to study the growth of the red seaweed *Agardhiella subulata*. This organism presents a similar growth behaviour and physical structure as fungi (see Figure 9.3(a)). This seaweed inhabits the coastal regions of ocean waters and it possesses potential pharmaceutical properties (Rorrer and Cheney, 2004). *Agardhiella subulata* consists of branched shoots and grows by dichotomous branching and elongation occurring at the end of these branches, i.e. at the tips. The growth of this seaweed is symmetrical throughout the colony, thereby resulting in ball-like shapes reaching maximally about 10 mm in diameter. During the growth process, small fragments often detach from the mother seaweed and become subcultures able to grow independently. In contrast with fungi, these seaweeds are photolithotropic and therefore they need light in order to produce new biomass. Finally, the growth environment of the seaweeds differs from that of most fungi. Seaweeds are submerged in water where they are exposed to currents with a direct impact on their growth and development.

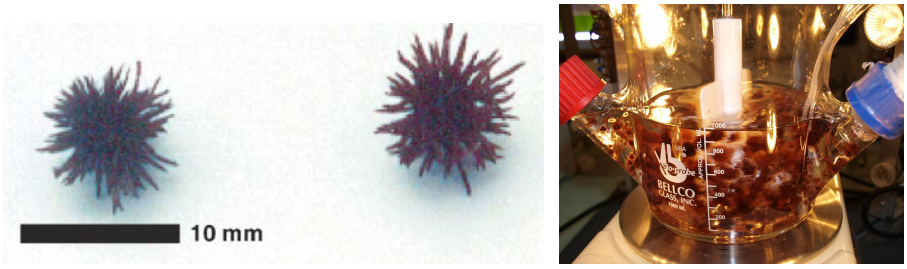

(a) *Agardhiella subulata* (b) Laboratory culture of algae

Figure 9.3: Individuals of *Agardhiella subulata* outside (a) and inside (b) a spinner flask containing all the nutrients needed for biomass production and surrounded by artificial light sources.

Replicating the growth conditions of seaweeds in the laboratory is not straightforward. For this purpose, seaweeds are cultivated in cultures with nutrients and surrounded by artificial light sources (see Figure 9.3(a)). Water currents are sim-

ulated using shakers which make the seaweeds revolve as such assuring that the entire surface of the algae gets sufficient light. Therefore, these laboratory conditions allow to control the different factors affecting the growth of this red seaweed accurately. For instance, the number of photons impacting on the surface of the seaweeds or the speed at which seaweeds revolve in the media can be tuned in order to mimic different growth conditions. Since nutrients are sufficiently available in the culture, light becomes the main limiting factor of growth.

The original fungal growth model was modified in order to simulate the growth of *Agardhiella subulata*. The seaweed can be seen as a collection of branches divided in segments similar to hyphal segments. Contrary to hyphal segments these branches are cylindrical and have a constant diameter. While for fungal growth substrate was the limiting factor, in the case of seaweeds the limiting factor is light. Therefore, each branch segment stores photons that are used to produce new biomass, either by apical branching or apical growth. Only active tips can produce new biomass and tips inactivate once their photon concentrations reach a minimum value. As external substrate can be taken up by the hyphal segments, the seaweed branches are capable of capturing light. However, this uptake process is modelled in a significantly different way. The number of photons a branch segment can absorb is determined using the Lambert-Beer law. In addition, this number depends on the distance between the segment and the center of the seaweed. Segments further from the center receive more photons than segments closer to the center since the latter are closer to the light source. In order to account for a more realistic uptake of photons, the area of the branches is also taken into account when simulating this process. Finally, photons are transformed into energy that travels within the seaweed branches in a process similar to nutrient translocation in fungi.

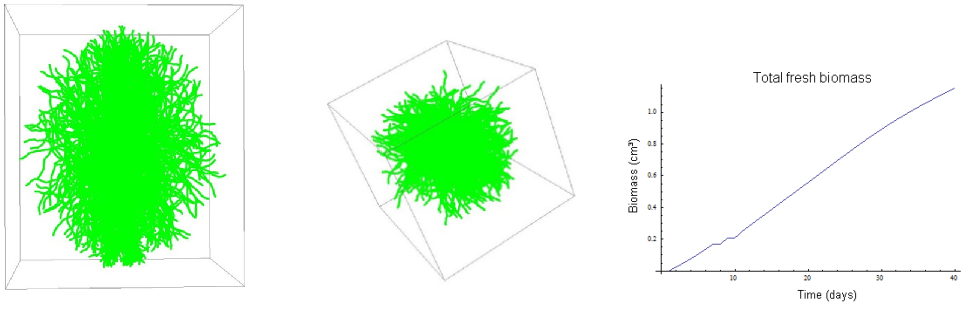

(a) Front view (b) Top view (c) Fresh biomass evolution

Figure 9.4: (a) Front and (b) top view of the final configuration of an *in silico* seaweed and (c) its biomass evolution over time. This simulation was performed using the following parameter values: Light intensity = 100 μphotons $s^{-1}\,m^{-2}$, initial inoculum density = 0.21cm^3, initial tips= 500, minimum amount of light at an active tip= 0.8 cost of growth, growth angle = $\pi/4$ radians, branching probability= 0.05 and cost of growth obtained from the relation given by 2.6 mol photons generates 5 cm^3 of fresh biomass.

The aforementioned assumptions were used to build upon our fungal growth model in order to develop a seaweed growth model. Consequently, all parameters were changed in order to account for seaweed growth processes. Growth scale and time step were also adapted to simulate the growth of the new organism. In addition, different growth scenarios and parameters were studied yielding different biomass densities and shapes consistent with experiments (see Figure 9.4). Unfortunately, the lack of data and techniques able to track the dynamics of individual seaweeds makes it impossible to further calibrate this model. Despite the simplicity and basic assumptions of this model, the versatility of the modelling approach employed for fungi illustrated. Therefore we believe that small changes in our current model, such as the ones here discussed, could result in the simulation of diverse phenomena. In conclusion, the results presented in this section demonstrates the versatility of our model that could be used not only to advance the research in the field of mycology but also in several different fields of study.

10

Nederlandstalige samenvatting

Schimmels ontwikkelen complexe netwerken van hyfen die fungeren als snelwegen waarover nutriënten over grote afstanden worden getransporteerd. Dankzij deze structuren zijn schimmels in staat om zich voort te planten en te overleven in de meeste extreme omstandigheden. Vandaar dat zij aanwezig zijn in de meeste natuurlijke en door de mens gecreëerde ecosystemen. Zij kunnen op talrijke substraten groeien, zelfs nutriëntarme, en zij veroorzaken schade aan bouwmaterialen, voedsel, planten en dieren.

Schimmels bieden evenwel ook voordelen. Zo zijn ze de voornaamste ontbinders van organisch materiaal in bossen, waar ze aggregaties vormen met boomwortels en hierdoor een efficiënte nutriëntenopname en -verdeling mogelijk maken in bosecosystemen. Daarenboven gebruiken de farmaceutische en voedingssector schimmels voor de productie van onder meer alcohol, brood, industriële enzymen en antibiotica. Ten slotte worden schimmels gebruikt voor bioremediatie.

Bovenstaande redenen verklaren waarom schimmels vaak onderzocht worden, voornamelijk aan de hand van laboratoriumexperimenten.

Zulke experimenten zijn meestal duur, tijdrovend en van beperkte omvang; uitgebreide studies van *in vitro* of *in situ* schimmeldynamiek zijn bijgevolg zeldzaam. De meeste technieken bieden niet de mogelijkheid om de evolutie van het volledige schimmelnetwerk doorheen de tijd te volgen. Bovendien groeien schimmels in milieuomstandigheden die moeilijk nagebootst kunnen worden in laboratoria. Geautomatiseerde niet-destructieve technieken zijn derhalve nodig om een beter inzicht te verkrijgen in de groei van schimmels.

Om de tekortkomingen van de bestaande technieken te overwinnen, worden in dit werk innovatieve technieken en methodes ontwikkeld waarmee bijvoorbeeld de spatio-temporele dynamiek van een zich ontwikkelend mycelium kan gevolgd worden. Deel I geeft de biologische en wiskundige context die nodig is voor een goed begrip van dit werk.

Hoofdstuk 2 geeft naast de biologische achtergrond van schimmels tevens een overzicht van hun industriële waarde, hun belang voor natuurlijke ecosystemen en hun invloed op de mens en andere levende wezens. De morfologie en diversiteit van schimmels wordt eveneens in dit hoofdstuk besproken, alsook wordt er een gedetailleerd overzicht gegeven van de processen die schimmelgroei drijven.

Hoofdstuk 3 bevat een gedetailleerde analyse en vergelijking van de bestaande wiskundige schimmelgroeimodellen. Enkele van de meest gebruikte wiskundige modelleerparadigma's worden in dit hoofdstuk besproken volgens de schaal waarop ze werken.

In Deel II leggen we ons toe op de ontwikkeling van nieuwe technieken die het mogelijk maken om schimmelgroeikenmerken af te leiden uit beeldmateriaal. Een beeldverwerkingsalgoritme dat ruwe beelden van schimmelnetwerken omzet in beelden die slechts de informatie bevatten over de structuur van het mycelium wordt in Hoofdstuk 4 voorgesteld en uitgetest.

In Hoofdstuk 5 beschrijven we een innovatieve experimentele opstelling die toelaat om schimmelgroei te volgen doorheen tijd en ruimte dankzij eenvoudige beeldapparatuur en het in Hoofdstuk 4 voorgestelde algoritme. Tevens wordt het groeigedrag van meerdere soorten vergeleken.

Hoofdstuk 6 gebruikt dezelfde technieken om de effecten van temperatuur en relatieve luchtvochtigheid op schimmelgroei te kwantificeren.

Niet enkel kunnen de technieken beschreven in Deel II gebruikt worden voor een analyse van de schimmelgroeidynamiek, tevens kunnen ze de ontwikkeling van schimmelgroeimodellen ondersteunen. Immers, toenemende rekenkracht en afnemende kosten hebben ervoor gezorgd dat zulke modellen meer en meer hun ingang vinden. Zij worden gebruikt als aanvulling op laboratoriumexperimenten of om bepaalde hypotheses te bevestigen of ontkrachten.

In die optiek stelt Deel III een ruimtelijk expliciet model voor waarmee schimmelgroei in drie dimensies en onder verschillende groeiscenario's kan gesimuleerd

worden.

In Hoofdstuk 7 wordt de ontwikkeling van het model voorgesteld, alsook de daaraan gekoppelde gevoeligheidsanalyse. Om het belang van de omgeving op de schimmelgroei te benadrukken worden er tot slot verscheidene scenario's nagebootst.

De belangrijkste conclusies van dit werk worden in Hoofdstuk 8 samengevat, terwijl Hoofdstuk 9 suggesties voor verder onderzoek aanreikt.

De voornaamste resultaten van dit werk zijn 1) een veelzijdige beeldverwerkingstechniek die toelaat om schimmelgroei op te volgen doorheen tijd en ruimte en dit voor verschillende soorten onder een brede waaier aan milieuomstandigheden, en 2) een driedimensionaal ruimtelijk expliciet schimmelgroeimodel. Deze resultaten vormen een substantiële bijdrage tot de mycologie en dragen bij tot een beter begrip van schimmels, in het bijzonder hun groeiprocessen.

11

English summary

Fungi develop complex networks that function as efficient transport structures along which nutrients can be translocated over large distances, as such covering local needs. Thanks to these structures, fungi are able to grow and survive even in the most extreme conditions, as such being present in most natural and man-made ecosystems. In addition, fungi are able to grow on many different substrates, even those containing a limited amount of nutrients. This ultimately results in damage of building materials, food products, plants and animals. On the other hand, the action of fungi can be beneficial. In forests, fungi are the primary decomposers of organic matter, where they also form mycorrhizal associations with tree roots allowing for an effective distribution of nutrients within the whole forest. In addition, pharmaceutical and food industries benefit from fungi considerably, as they are used to create products ranging from alcohol and bread to industrial enzymes and antibiotics. Furthermore, fungi are used in biocontrol to fight plant pathogens affecting crops, such as insects and other fungi.

For all of these reasons, fungi have been extensively studied, more in particular through laboratory experiments. Laboratory experiments are generally expensive, tedious or of a limited scope, which explains why comprehensive studies of fungal dynamics *in vitro* or *in situ* are scarce. Moreover, most of the employed techniques

do not allow for tracking the entire mycelium through time. In addition, fungi grow in environments and under environmental circumstances that cannot always be mimicked easily in laboratories. Therefore, automated non-destructive techniques are needed to generate updated data on fungi and fungal growth.

In order to overcome these limitations, this dissertation investigates the possibilities that mathematics has to offer to the study of fungi. For this purposes, Part I of this dissertation introduces the biological and mathematical context in which our research has been developed.

Chapter 2 gives the biological background on fungi and summarizes their most relevant uses in industry, their importance in natural ecosystems and their impact on human and other living organisms. In addition, the morphology and diversity of fungi is briefly discussed, followed by a detailed overview of the processes driving the growth of filamentous fungi.

Chapter 3 consists of a detailed discussion and comparison of different mathematical models encoding fungal growth. Some of the most common mathematical paradigms and different modelling approaches are explained in this chapter. In addition, the most relevant fungal growth models are presented according to the scale they work at.

Part II focuses on new techniques able to extract fugal growth features from images. For this purpose, an image analysis algorithm able to transform fungal images into simplified binary images is introduced and tested in Chapter 4. In addition, it is able to remove redundant information from the original images, as such allowing for a better analysis of the fungal images.

In Chapter 5, an innovative experimental set-up to track fungal growth using basic imaging devices and the mathematical techniques used to extract fungal growth features from the binary images obtained using the algorithm introduced in Chapter 4, are described. Several fungal growth features are then extracted for different fungal species allowing for a mutual comparison of their growth behaviour and a detailed study of their evolution. Chapter 6 uses similar techniques to assess the effect of temperature and relative humidity on fungal growth.

The techniques presented in Part II can also be used to support the development of fungal growth models. The increase of computing power and the decrease of computing cost have led to advances in the mathematical modelling of different biological phenomena, including fungal growth. Models are used to complement laboratory experiments and verify different theoretical hypotheses, as such arising as an alternative to classical experiments.

Therefore, Part III presents an innovative spatially explicit model able to simulate fungal growth in three dimensions occurring under a variety of growth scenarios. Chapter 7 explains the development of the model after which a sensitivity analysis is preferred. In addition, different scenarios are simulated showing the importance of the environment on the growth of fungi.

In Chapter 8 the most important conclusions of this dissertation are summarized, while Chapter 9 presents avenues for future research.

The main findings of this research include a versatile and innovative image analysis technique able to track fungal growth of different species under varying growth conditions, and a three-dimensional spatially explicit model simulating fungal growth as the result of the interactions between the fungus and different elements in its environment. These findings represent significant contributions to mycology that helped to move forward the study of fungi, and particularly provide a better understanding of fungal growth and its underlying processes.

Bibliography

Adamatzky, A., De Baets, B., Van Dessel, W., 2012. Slime mould imitation of belgian transport networks: redundancy, bio-essential motorways, and dissolution. International Journal of Unconventional Computing 8, 235–261.

Adams, D. J., 2004. Fungal cell wall chitinases and glucanases. Microbiology 150 (7), 2029–2035.

Adan, O. C., 2011. The fungal resistance of interior finishing materials. In: Adan, O. C., Samson, R. A. (Eds.), Fundamentals of Mold Growth in Indoor Environments and Strategies for Healthy Living. Wageningen Academic, Wageningen, The Netherlands, Ch. 12, pp. 335–352.

Adan, O. C., Samson, R. A., 2011. Fundamentals of Mold Growth in Indoor Environments and Strategies for Healthy Living. Wageningen Academic, Wageningen, The Netherlands.

Adl, S. M., Simpson, A. G., Farmer, M. A., Andersen, R. A., Anderson, O. R., Barta, J. R., Bowser, S. S., Brugerolle, G., Fensome, R. A., Fredericq, S., et al., 2005. The new higher level classification of eukaryotes with emphasis on the taxonomy of protists. Journal of Eukaryotic Microbiology 52 (5), 399–451.

Agarwal, S., Manchanda, V., Verma, N., Bhalla, P., et al., 2011. Yeast identification in routine clinical microbiology laboratory and its clinical relevance. Indian Journal of Medical Microbiology 29 (2), 172.

Akiyama, K., Matsuzaki, K.-i., Hayashi, H., 2005. Plant sesquiterpenes induce hyphal branching in arbuscular mycorrhizal fungi. Nature 435 (7043), 824–827.

Alexopoulos, C. J., Mims, C. W., Blackwell, M., et al., 1996. Introductory mycology. No. Ed. 4. John Wiley and Sons, New York, USA.

Alvindia, D. G., Natsuaki, K. T., 2008. Evaluation of fungal epiphytes isolated from banana fruit surfaces for biocontrol of banana crown rot disease. Crop Protection 27 (8), 1200–1207.

Anderson, J. B., 1992. The fungus *Armillaria bulbosa* is among the largest and oldest living organisms. Nature 356, 428–431.

Arbelaez, P., Maire, M., Fowlkes, C., Malik, J., 2011. Contour detection and hierarchical image segmentation. IEEE Trans. on Pattern Analysis and Machine Intelligence 33, 898–916.

Ayerst, G., 1969. The effects of moisture and temperature on growth and spore germination in some fungi. Journal of Stored Products Research 5 (2), 127–141.

Babaud, J., Witkin, A. P., Baudin, M., Duda, R. O., 1986. Uniqueness of the Gaussian kernel for scale-space filtering. IEEE Trans. on Pattern Analysis and Machine Intelligence 8 (1), 26–33.

Bago, B., Zipfel, W., Williams, R. M., Jun, J., Arreola, R., Lammers, P. J., Pfeffer, P. E., Shachar-Hill, Y., 2002. Translocation and utilization of fungal storage lipid in the arbuscular mycorrhizal symbiosis. Plant Physiology 128 (1), 108–124.

Bailey, D., Otten, W., Gilligan, C. A., 2000. Saprotrophic invasion by the soil-borne fungal plant pathogen *Rhizoctonia solani* and percolation thresholds. New Phytologist 146 (3), 535–544.

Balasubramanian, M. K., Bi, E., Glotzer, M., 2004. Comparative analysis of cytokinesis in budding yeast, fission yeast and animal cells. Current Biology 14 (18), R806–R818.

Baranyi, J., Roberts, T. A., 1994. A dynamic approach to predicting bacterial growth in food. International Journal of Food Microbiology 23 (3-4), 277–294.

Barnett, H. L., Hunter, B. B., 1972. Illustrated genera of imperfect fungi.

Barry, D., McGee, S., Ifeyinwa, O., Ryan, R., Williams, G., Blackledge, J., 2009a. Relating fractal dimension to branching behaviour in filamentous microorganisms. ISAST Transactions on Electronics and Signal Processing 4 (1), 71–76.

Barry, D., Williams, G., 2011. Microscopic characterisation of filamentous microbes: towards fully automated morphological quantification through image analysis. Journal of Microscopy 244 (1), 1–20.

Barry, D. J., Chan, C., Williams, G. A., 2009b. Morphological quantification of filamentous fungal development using membrane immobilization and automatic image analysis. Journal of Industrial Microbiology and Biotechnology 36 (6), 787–800.

Bartnicki-García, S., 2002. Hyphal tip growth: outstanding questions. Mycology Series 15, 29–58.

Bartnicki-Garcia, S., Bartnicki, D. D., Gierz, G., López-Franco, R., Bracker, C. E., 1995. Evidence that spitzenkörper behavior determines the shape of a fungal hypha: a test of the hyphoid model. Experimental Mycology 19 (2), 153–159.

Bartnicki-Garcia, S., Hergert, F., Gierz, G., 1989. Computer simulation of fungal morphogenesis and the mathematical basis for hyphal (tip) growth. Protoplasma 153 (1-2), 46–57.

Basu, M., 2002. Gaussian-based edge-detection methods- A survey. IEEE Trans. on Systems, Man, and Cybernetics, Part C: Applications and Reviews 32 (3), 252–260.

Baty, F., Delignette-Muller, M.-L., 2004. Estimating the bacterial lag time: which model, which precision? International journal of food microbiology 91 (3), 261–277.

Bayram, O., Krappmann, S., Ni, M., Bok, J. W., Helmstaedt, K., Valerius, O., Braus-Stromeyer, S., Kwon, N.-J., Keller, N. P., Yu, J.-H., et al., 2008. VelB/veA/laeA complex coordinates light signal with fungal development and secondary metabolism. Science 320 (5882), 1504–1506.

Benmansour, F., Cohen, L. D., 2011. Tubular structure segmentation based on minimal path method and anisotropic enhancement. International Journal of Computer Vision 92 (2), 192–210.

Berdy, J., 2005. Bioactive microbial metabolites. Journal of Antibiotics 58 (1), 1–26.

Berec, L., 2002. Techniques of spatially explicit individual-based models: construction, simulation, and mean-field analysis. Ecological Modelling 150 (1), 55–81.

Bergholm, F., 1987. Edge focusing. IEEE Trans. on Pattern Analysis and Machine Intelligence 9 (6), 726–741.

Bistis, G. N., Perkins, D. D., Read, N. D., 2003. Different cell types in *Neurospora crassa*. Fungal Genetics Newsletter 50, 17–19.

Bjurman, J., Wadsö, L., 2000. Microcalorimetric measurements of metabolic activity of six decay fungi on spruce wood as a function of temperature. Mycologia 92 (1), 23–28.

Blackledge, J., Barry, D., 2011. Morphological analysis from images of hyphal growth using a fractional dynamic model. In: Hamish Carr, I. G. (Ed.), Theory and Practice of Computer Graphics, University of Warwick. Dublin, Ireland, pp. 17–24.

Blackwell, M., 2011. The fungi: 1, 2, 3 . . . 5.1 million species? American Journal of Botany 98 (3), 426–438.

Boddy, L., 1983. Effect of temperature and water potential on growth rate of wood-rotting basidiomycetes. Transactions of the British Mycological Society 80 (1), 141–149.

Boddy, L., 1999. Saprotrophic cord-forming fungi: meeting the challenge of heterogeneous environments. Mycologia 91 (1), 13–32.

Boddy, L., Büntgen, U., Egli, S., Gange, A. C., Heegaard, E., Kirk, P. M., Mohammad, A., Kauserud, H., 2014. Climate variation effects on fungal fruiting. Fungal Ecology 10, 20–33.

Boddy, L., Wells, J. M., Culshaw, C., Donnelly, D. P., 1999. Fractal analysis in studies of mycelium in soil. Geoderma 88 (3), 301–328.

Boddy, L., Wood, J., Redman, E., Hynes, J., Fricker, M. D., 2010. Fungal network responses to grazing. Fungal Genetics and Biology 47 (6), 522–530.

Bolton, M. D., Kolmer, J. A., Garvin, D. F., 2008. Wheat leaf rust caused by puccinia triticina. Molecular Plant Pathology 9 (5), 563–575.

Bolton, R. G., Boddy, L., 1993. Characterization of the spatial aspects of foraging mycelial cord systems using fractal geometry. Mycological Research 97 (6), 762–768.

Bonner, J. T., 1948. A study of the temperature and humidity requirements of *Aspergillus niger*. Mycologia 40 (6), 728–738.

Bonner, R. D., Fergus, C. L., 1960. The influence of temperature and relative humidity on growth and survival of silage fungi. Mycologia 52 (4), 642–647.

Boswell, G. P., 2008. Modelling mycelial networks in structured environments. Mycological Research 112 (9), 1015–1025.

Boswell, G. P., 2012. Modelling combat strategies in fungal mycelia. Journal of Theoretical Biology 304, 226–234.

Boswell, G. P., Hopkins, S., 2008. Linking hyphal growth to colony dynamics: spatially explicit models of mycelia. Fungal Ecology 1 (4), 143–154.

Boswell, G. P., Jacobs, H., Davidson, F. A., Gadd, G. M., Ritz, K., 2002. Functional consequences of nutrient translocation in mycelial fungi. Journal of Theoretical Biology 217 (4), 459–477.

Boswell, G. P., Jacobs, H., Davidson, F. A., Gadd, G. M., Ritz, K., 2003. Growth and function of fungal mycelia in heterogeneous environments. Bulletin of Mathematical Biology 65 (3), 447–477.

Boswell, G. P., Jacobs, H., Ritz, K., Gadd, G. M., Davidson, F. A., 2007. The development of fungal networks in complex environments. Bulletin of Mathematical Biology 69 (2), 605–634.

Bowman, S. M., Free, S. J., 2006. The structure and synthesis of the fungal cell wall. Bioessays 28 (8), 799–808.

Bowyer, K., Kranenburg, C., Dougherty, S., 2001. Edge detector evaluation using empirical ROC curves. Computer Vision and Image Understanding 84 (1), 77–103.

Brand, A., Gow, N. A., 2009. Mechanisms of hypha orientation of fungi. Current Opinion in Microbiology 12 (4), 350–357.

Brimner, T. A., Boland, G. J., 2003. A review of the non-target effects of fungi used to biologically control plant diseases. Agriculture, Ecosystems and Environment 100 (1), 3–16.

Brischke, C., Lampen, S. C., 2014. Resistance based moisture content measurements on native, modified and preservative treated wood. European Journal of Wood and Wood Products 72 (2), 289–292.

Brischke, C., Meyer, L., Bornemann, T., 2013. The potential of moisture content measurements for testing the durability of timber products. Wood Science and Technology 47 (4), 869–886.

Brischke, C., Rapp, A. O., 2008. Influence of wood moisture content and wood temperature on fungal decay in the field: observations in different micro-climates. Wood Science and Technology 42 (8), 663–677.

Brischke, C., Thelandersson, S., 2014. Modelling the outdoor performance of wood products–a review on existing approaches. Construction and Building Materials 66, 384–397.

Burrowes, K. S., Tawhai, M. H., 2006. Computational predictions of pulmonary blood flow gradients: gravity versus structure. Respiratory Physiology and Neurobiology 154 (3), 515–523.

Canny, J., 1986. A computational approach to edge detection. IEEE Transactions on Pattern Analysis and Machine Intelligence 8 (6), 679–698.

Card, S. D., Tapper, B. A., Lloyd-West, C., Wright, K. M., 2013. Assessment of fluorescein-based fluorescent dyes for tracing neotyphodium endophytes in planta. Mycologia 105 (1), 221–229.

Carver, I., Boswell, G. P., 2008. A lattice-free model of translocation-induced outgrowth in fungal mycelia. International Journal of Applied Mathematics 38 (4), 173–179.

Chaudhuri, S., Chatterjee, S., Katz, N., Nelson, M., Goldbaum, M., 1989. Detection of blood vessels in retinal images using two-dimensional matched filters. IEEE Trans. on Medical Imaging 8 (3), 263–269.

Cooley, J. D., Wong, W. C., Jumper, C. A., Straus, D. C., 1998. Correlation between the prevalence of certain fungi and sick building syndrome. Occupational and Environmental Medicine 55 (9), 579–584.

Coppin, E., Debuchy, R., Arnaise, S., Picard, M., 1997. Mating types and sexual development in filamentous ascomycetes. Microbiology and Molecular Biology Reviews 61 (4), 411–428.

Cornelis, B., Ruzić, T., Gezels, E., Dooms, A., Pizurica, A., Platisa, L., Cornelis, J., Martens, M., De Mey, M., Daubechies, I., 2013. Crack detection and inpainting for virtual restoration of paintings: The case of the Ghent altarpiece. Signal Processing 93 (3), 605–619.

Couch, B. C., Fudal, I., Lebrun, M.-H., Tharreau, D., Valent, B., van Kim, P., Nottéghem, J.-L., Kohn, L. M., 2005. Origins of host-specific populations of the blast pathogen *Magnaporthe oryzae* in crop domestication with subsequent expansion of pandemic clones on rice and weeds of rice. Genetics 170 (2), 613–630.

Crawford, J. W., Ritz, K., Young, I. M., 1993. Quantification of fungal morphology, gaseous transport and microbial dynamics in soil: an integrated framework utilising fractal geometry. Geoderma 56 (1), 157–172.

Cunniffe, N. J., Gilligan, C. A., 2008. Scaling from mycelial growth to infection dynamics: a reaction diffusion approach. Fungal Ecology 1 (4), 133–142.

Czerwinski, R., Jones, D., O'Brien, W., 1999. Detection of lines and boundaries in speckle images- Application to medical ultrasound. IEEE Trans. on Medical Imaging 18 (2), 126–136.

Dantigny, P., Guilmart, A., Bensoussan, M., 2005. Basis of predictive mycology. International Journal of Food Microbiology 100 (1), 187–196.

Dashtban, M., Schraft, H., Syed, T. A., Qin, W., 2010. Fungal biodegradation and enzymatic modification of lignin. International Journal of Biochemistry and Molecular Biology 1 (1), 36–50.

Davidson, F., 1998. Modelling the qualitative response of fungal mycelia to heterogeneous environments. Journal of Theoretical Biology 195 (3), 281–292.

Davidson, F., Sleeman, B., Rayner, A., Crawford, J., Ritz, K., 1997. Travelling waves and pattern formation in a model for fungal development. Journal of Mathematical Biology 35 (5), 589–608.

Davidson, F. A., 2007. Mathematical modelling of mycelia: a question of scale. Fungal Biology Reviews 21 (1), 30–41.

de Bekker, C., van Veluw, G. J., Vinck, A., Wiebenga, L. A., Wösten, H. A., 2011. Heterogeneity of *Aspergillus niger* microcolonies in liquid shaken cultures. Applied and Environmental Microbiology 77 (4), 1263–1267.

Dean, R., Van Kan, J. A., Pretorius, Z. A., Hammond-Kosack, K. E., Di Pietro, A., Spanu, P. D., Rudd, J. J., Dickman, M., Kahmann, R., Ellis, J., et al., 2012. The top 10 fungal pathogens in molecular plant pathology. Molecular Plant Pathology 13 (4), 414–430.

Declerck, S., D'or, D., Cranenbrouck, S., Le Boulengé, E., 2001. Modelling the sporulation dynamics of arbuscular mycorrhizal fungi in monoxenic culture. Mycorrhiza 11 (5), 225–230.

Denet, B., 1996. Numerical simulation of cellular tip growth. Physical Review E 53 (1), 986.

Denning, D., O'driscoll, B., Hogaboam, C., Bowyer, P., Niven, R., 2006. The link between fungi and severe asthma: a summary of the evidence. European Respiratory Journal 27 (3), 615–626.

Dickson, S., Kolesik, P., 1999. Visualisation of mycorrhizal fungal structures and quantification of their surface area and volume using laser scanning confocal microscopy. Mycorrhiza 9 (4), 205–213.

Diéguez-Uribeondo, J., Gierz, G., Bartnicki-Garcia, S., 2004. Image analysis of hyphal morphogenesis in *Saprolegniaceae (Oomycetes)*. Fungal Genetics and Biology 41 (3), 293–307.

Dijksterhuis, J., 2011. The fungal cell. In: Fundamentals of Mold Growth in Indoor Environments and Strategies for Healthy Living. Springer, Ch. 4, pp. 83–100.

Du, H., Lv, P., Ayouz, M., Besserer, A., Perré, P., 2016. Morphological characterization and quantification of the mycelial growth of the brown-rot fungus postia placenta for modeling purposes. PloS one 11 (9), 1–16.

Dupuy, L., Gregory, P. J., Bengough, A. G., 2010. Root growth models: towards a new generation of continuous approaches. Journal of Experimental Botany, 389–401.

Eberly, D., Gardner, R., Morse, B., Pizer, S., Scharlach, C., 1994. Ridges for image analysis. Journal of Mathematical Imaging and Vision 4 (4), 353–373.

Edelstein, L., 1982. The propagation of fungal colonies: a model for tissue growth. Journal of Theoretical Biology 98 (4), 679–701.

Edelstein-Keshet, L., 1988. Mathematical Models in Biology. Vol. 46. Society for Industrial and Applied Mathematics (SIAM), Philadelphia, PA, US.

Eggen, E., de Keijzer, M. N., Mulder, B. M., 2011. Self-regulation in tip-growth: The role of cell wall ageing. Journal of Theoretical Biology 283 (1), 113–121.

Ekesi, S., Maniania, N., Ampong-Nyarko, K., 1999. Effect of temperature on germination, radial growth and virulence of metarhizium anisopliae and beauveria bassiana on megalurothrips sjostedti. Biocontrol Science and Technology 9 (2), 177–185.

EN252, 1989. Field test method for determining the relative protective effectiveness of wood preservatives in ground contact.

EN350-1, 1994. Durability of wood and wood-based products-natural durability of solid wood-part 1: guide to the principles of testing and classification of the natural durability of wood.

Etheridge, D., 1957. Moisture and temperature relations of heartwood fungi in subalpine spruce. Canadian Journal of Botany 35 (6), 935–944.

Fackler, K., Gradinger, C., Hinterstoisser, B., Messner, K., Schwanninger, M., 2006. Lignin degradation by white rot fungi on spruce wood shavings during short-time solid-state fermentations monitored by near infrared spectroscopy. Enzyme and Microbial Technology 39 (7), 1476–1483.

Fackler, K., Schmutzer, M., Manoch, L., Schwanninger, M., Hinterstoisser, B., Ters, T., Messner, K., Gradinger, C., 2007. Evaluation of the selectivity of white rot isolates using near infrared spectroscopic techniques. Enzyme and Microbial Technology 41 (6), 881–887.

Faeth, S. H., Fagan, W. F., 2002. Fungal endophytes: common host plant symbionts but uncommon mutualists. Integrative and Comparative Biology 42 (2), 360–368.

Falconer, R. E., Bown, J. L., McAdam, E., Perez-Reche, P., Sampson, A. T., Van den Bulcke, J., White, N. A., 2010. Modelling fungal colonies and communities: challenges and opportunities. IMA Fungus: The Global Mycological Journal 1 (2), 155–159.

Falconer, R. E., Bown, J. L., White, N. A., Crawford, J. W., 2005. Biomass recycling and the origin of phenotype in fungal mycelia. Proceedings of the Royal Society B: Biological Sciences 272 (1573), 1727–1734.

Falconer, R. E., Bown, J. L., White, N. A., Crawford, J. W., 2008. Modelling interactions in fungi. Journal of the Royal Society Interface 5 (23), 603–615.

Fisher, M. C., Henk, D. A., Briggs, C. J., Brownstein, J. S., Madoff, L. C., McCraw, S. L., Gurr, S. J., 2012. Emerging fungal threats to animal, plant and ecosystem health. Nature 484 (7393), 186–194.

Fomina, M., Ritz, K., Gadd, G. M., 2000. Negative fungal chemotropism to toxic metals. FEMS Microbiology Letters 193 (2), 207–211.

Freeman, W., Adelson, E., 1991. The design and use of steerable filters. IEEE Trans. on Pattern Analysis and Machine Intelligence 13 (9), 891–906.

Fricker, M., Boddy, L., Bebber, D., 2007. Network organisation of mycelial fungi. In: Howard, R., Gow, N. (Eds.), Biology of the Fungal Cell. Springer, New York, USA, Ch. 13, pp. 309–330.

Fricker, M., Lee, J., Bebber, D., Tlalka, M., Hynes, J., Darrah, P., Watkinson, S., Boddy, L., 2008. Imaging complex nutrient dynamics in mycelial networks. Journal of Microscopy 231 (2), 317–331.

Fricker, M. D., Boddy, L., Nakagaki, T., Bebber, D. P., 2009. Adaptive biological networks. In: Thilo, G., Sayam, H. (Eds.), Adaptive Networks. Springer Berlin Heidelberg, Berlin, Germany, pp. 51–70.

Fu, H., Chi, Z., 2003. A two-stage approach for leaf vein extraction. In: Proceedings of the 2003 International Conference on Neural Networks and Signal Processing. Vol. 1. IEEE, pp. 208–211.

Fuhr, M., Schubert, M., Schwarze, F., Herrmann, H., 2011. Modelling the hyphal growth of the wood-decay fungus
textitphysisporinus vitreus. Fungal Biology 115 (9), 919–932.

Fuhr, M., Stührk, C., Schubert, M., Schwarze, F., Herrmann, H., 2012. Modelling the effect of environmental factors on the hyphal growth of the basidiomycete *Physisporinus vitreus*. Journal of Basic Microbiology 52 (5), 523–530.

Funk, S., Salathé, M., Jansen, V. A., 2010. Modelling the influence of human behaviour on the spread of infectious diseases: a review. Journal of the Royal Society Interface 7 (50), 1247–1256.

Gadd, G. M., Watkinson, S. C., Dyer, P. S., 2007. Fungi in the Environment. Cambridge University Press, New York, USA.

Gange, A. C., Gange, E. G., Mohammad, A. B., Boddy, L., 2011. Host shifts in fungi caused by climate change? Fungal Ecology 4 (2), 184–190.

Gauthier, G. M., 2015. Dimorphism in fungal pathogens of mammals, plants, and insects. PLoS Pathog 11 (2), e1004608.

Geng, J., Yuan, J., 2010. Cybernetic modeling based on pathway analysis for
textitPenicillium chrysogenum fed-batch fermentation. Bioprocess and Biosystems Engineering 33 (6), 665–674.

Geusebroek, J.-M., Smeulders, A. W., Van De Weijer, J., 2003. Fast anisotropic Gauss filtering. IEEE Trans. on Image Processing 12 (8), 938–943.

Ghazvinian, E., Diederichs, M., Quey, R., 2014. 3d random voronoi grain-based models for simulation of brittle rock damage and fabric-guided micro-fracturing. Journal of Rock Mechanics and Geotechnical Engineering 6 (6), 506–521.

Gibbons, A., 1985. Algorithmic Graph Theory. Cambridge University Press, Cambridge, UK.

Gibson, A. M., Hocking, A. D., 1997. Advances in the predictive modelling of fungal growth in food. Trends in Food Science and Technology 8 (11), 353–358.

Gierz, G., Bartnicki-Garcia, S., 2001. A three-dimensional model of fungal morphogenesis based on the vesicle supply center concept. Journal of Theoretical Biology 208 (2), 151–164.

Glass, N. L., Rasmussen, C., Roca, M. G., Read, N. D., 2004. Hyphal homing, fusion and mycelial interconnectedness. Trends in Microbiology 12 (3), 135–141.

Gobakken, L. R., Westin, M., 2008. Surface mould growth on five modified wood substrates coated with three different coating systems when exposed outdoors. International Biodeterioration & Biodegradation 62 (4), 397–402.

Gock, M. A., Hocking, A. D., Pitt, J. I., Poulos, P. G., 2003. Influence of temperature, water activity and ph on growth of some xerophilic fungi. International Journal of Food Microbiology 81 (1), 11–19.

Goldberg, A. V., Kennedy, R., 1995. An efficient cost scaling algorithm for the assignment problem. Mathematical Programming 71, 153–177.

Gompertz, B., 1825. On the nature of the function expressive of the law of human mortality, and on a new mode of determining the value of life contingencies. Philosophical transactions of the Royal Society of London 115, 513–583.

Goriely, A., Tabor, M., 2003. Biomechanical models of hyphal growth in actinomycetes. Journal of theoretical biology 222 (2), 211–218.

Gougouli, M., Kalantzi, K., Beletsiotis, E., Koutsoumanis, K. P., 2011. Development and application of predictive models for fungal growth as tools to improve quality control in yogurt production. Food Microbiology 28 (8), 1453–1462.

Gougouli, M., Koutsoumanis, K. P., 2013. Relation between germination and mycelium growth of individual fungal spores. International Journal of Food Microbiology 161 (3), 231–239.

Green III, F., Highley, T. L., 1997. Mechanism of brown-rot decay: paradigm or paradox. International Biodeterioration and Biodegradation 39 (2), 113–124.

Grimm, L., Kelly, S., Krull, R., Hempel, D., 2005. Morphology and productivity of filamentous fungi. Applied Microbiology and Biotechnology 69 (4), 375–384.

Grimm, V., 1999. Ten years of individual-based modelling in ecology: what have we learned and what could we learn in the future? Ecological modelling 115 (2), 129–148.

Grompone von Gioi, R., Jakubowicz, J., Morel, J.-M., Randall, G., 2008. On straight line segment detection. Journal of Mathematical Imaging and Vision 32 (3), 313–347.

Hale, M., Eaton, R., 1986. Soft rot cavity formation in five preservative-treated hardwood species. Transactions of the British Mycological Society 86 (4), 585–590.

Hansen, E. M., 2008. Alien forest pathogens: *Phytophthora* species are changing world forests. Boreal Environment Research 13, 33–41.

Haralick, R. M., 1983. Ridges and valleys on digital images. Computer Vision, Graphics, and Image Processing 22 (1), 28–38.

Harold, F., 1997. How hyphae grow: morphogenesis explained? Protoplasma 197 (3-4), 137–147.

Harris, S. D., 2008. Branching of fungal hyphae: regulation, mechanisms and comparison with other branching systems. Mycologia 100 (6), 823–832.

Hastie, T., Tibshirani, R., Friedman, J., 2009. The Elements of Statistical Learning. Vol. 2. Springer, New York, USA.

Hawksworth, D. L., 2001. The magnitude of fungal diversity: the 1.5 million species estimate revisited. Mycological research 105 (12), 1422–1432.

Heaton, L. L., López, E., Maini, P. K., Fricker, M. D., Jones, N. S., 2010. Growth-induced mass flows in fungal networks. Proceedings of the Royal Society B: Biological Sciences 277 (1698), 3265–3274.

Henkel, A., Müller, J., Pötzsche, C., 2012. Modeling the spread of *Phytophthora*. Journal of Mathematical Biology 65 (6-7), 1359–1385.

Hickey, P. C., Jacobson, D. J., Read, N. D., Glass, N. L., 2002. Live-cell imaging of vegetative hyphal fusion in *Neurospora crassa*. Fungal Genetics and Biology 37 (1), 109–119.

Hopkins, S., Boswell, G. P., 2012. Mycelial response to spatiotemporal nutrient heterogeneity: a velocity-jump mathematical model. Fungal Ecology 5 (2), 124–136.

Huang, Y., Toscano-Underwood, C., Fitt, B. D., Todd, A., West, J. S., Koopmann, B., Balesdent, M.-H., 2001. Effects of temperature on germination and hyphal growth from ascospores of a-group and b-group leptosphaeria maculans (phoma stem canker of oilseed rape). Annals of Applied Biology 139 (2), 193–207.

Hukka, A., Viitanen, H., 1999. A mathematical model of mould growth on wooden material. Wood Science and Technology 33 (6), 475–485.

Hutchinson, S., Sharma, P., Clarke, K., Macdonald, I., 1980. Control of hyphal orientation in colonies of mucor hiemalis. Transactions of the British Mycological Society 75 (2), 177–191.

Ibrahim, M., Rabah, A., Liman, B., Ibrahim, N., 2011. Effect of temperature and relative humidity on the growth of *Helminthosporium fulvum*. Nigerian Journal of Basic and Applied Sciences 19 (1), 127–129.

Indermitte, C., Liebling, T. M., Clémençon, H., 1994. Culture analysis and external interaction models of mycelial growth. Bulletin of Mathematical Biology 56 (4), 633–664.

Jacob, M., Unser, M., 2004. Design of steerable filters for feature detection using canny-like criteria. IEEE Trans. on Pattern Analysis and Machine Intelligence 26 (8), 1007–1019.

Jacobs, H., Boswell, G. P., Ritz, K., Davidson, F. A., Gadd, G. M., 2002. Solubilization of calcium phosphate as a consequence of carbon translocation by *Rhizoctonia solani*. FEMS Microbiology Ecology 40 (1), 65–71.

Jeger, M., Lamour, A., Gilligan, C., Otten, W., 2008. A fungal growth model fitted to carbon-limited dynamics of *Rhizoctonia solani*. New Phytologist 178 (3), 625–633.

Jennings, D. H., 1995. The physiology of fungal nutrition. Cambridge University Press, New York, USA.

Joshi, P., Swarup, A., Maheshwari, S., Kumar, R., Singh, N., 2011. Bioremediation of heavy metals in liquid media through fungi isolated from contaminated sources. Indian Journal of Microbiology 51 (4), 482–487.

Kaestner, A., Schneebeli, M., Graf, F., 2006. Visualizing three-dimensional root networks using computed tomography. Geoderma 136 (1), 459–469.

Kamel, A. A.-E., Mohamed, A. M., Ali, H. B., 2009. First morpho-molecular identification of *Rhizoctonia solani* ag-7 from potato tuber-borne sclerotium in saudi arabia. African Journal of Microbiology Research 3 (12), 952–956.

Kass, M., Witkin, A., 1987. Analyzing oriented patterns. Computer Vision, Graphics, and Image Processing 37 (3), 362–385.

Kauserud, H., Heegaard, E., Semenov, M. A., Boddy, L., Halvorsen, R., Stige, L. C., Sparks, T. H., Gange, A. C., Stenseth, N. C., 2010. Climate change and spring-fruiting fungi. Proceedings of the Royal Society of London B: Biological Sciences 277 (1685), 1169–1177.

Kim, Y., Xiao, C., Rogers, J., 2005. Influence of culture media and environmental factors on mycelial growth and pycnidial production of sphaeropsis pyriputrescens. Mycologia 97 (1), 25–32.

Krivtsov, V., Bezginova, T., Salmond, R., Liddell, K., Garside, A., Thompson, J., Palfreyman, J. W., Staines, H., Brendler, A., Griffiths, B., Watling, R., 2006. Ecological interactions between fungi, other biota and forest litter composition in a unique Scottish woodland. Forestry 79 (2), 201–216.

Laarhoven, K. A., Huinink, H. P., Segers, F. J., Dijksterhuis, J., Adan, O. C., 2015. Separate effects of moisture content and water activity on the hyphal extension of penicillium rubens on porous media. Environmental Microbiology 17 (12), 5089–5099.

Lam, B. S., Gao, Y., Liew, A.-C., 2010. General retinal vessel segmentation using regularization-based multiconcavity modeling. IEEE Trans. on Medical Imaging 29 (7), 1369–1381.

Laptev, I., Mayer, H., Lindeberg, T., Eckstein, W., Steger, C., Baumgartner, A., 2000. Automatic extraction of roads from aerial images based on scale space and snakes. Machine Vision and Applications 12 (1), 23–31.

Larsen, P., Hamada, Y., Gilbert, J., 2012. Modeling microbial communities: Current, developing, and future technologies for predicting microbial community interaction. Journal of Biotechnology 160 (1), 17–24.

Lauter, F.-R., Marchfelder, U., Russo, V. E., Yamashiro, C. T., Yatzkan, E., Yarden, O., 1998. Photoregulation of cot-1, a kinase-encoding gene involved in hyphal growth in *Neurospora crassa*. Fungal Genetics and Biology 23 (3), 300–310.

Le Calvez, T., Burgaud, G., Mahé, S., Barbier, G., Vandenkoornhuyse, P., 2009. Fungal diversity in deep-sea hydrothermal ecosystems. Applied and Environmental Microbiology 75 (20), 6415–6421.

Lejeune, R., Baron, G. V., 1997. Simulation of growth of a filamentous fungus in 3 dimensions. Biotechnology and Bioengineering 53 (2), 139–150.

Lew, R. R., Levina, N. N., Walker, S. K., Garrill, A., 2004. Turgor regulation in hyphal organisms. Fungal Genetics and Biology 41 (11), 1007–1015.

Li, Y., Chi, Z., Feng, D. D., 2006. Leaf vein extraction using independent component analysis. In: 2006 IEEE International Conference on Systems, Man and Cybernetics. Vol. 5. pp. 3890–3894.

Li, Y., Wadsö, L., 2013. Fungal activities of indoor moulds on wood as a function of relative humidity during desorption and adsorption processes. Engineering in Life Sciences 13 (6), 528–535.

Lilburne, L., Tarantola, S., 2009. Sensitivity analysis of spatial models. International Journal of Geographical Information Science 23 (2), 151–168.

Lindeberg, T., 1994. Scale-space theory in computer vision. Ph.D. thesis, KTH Royal Institute of Technology, Stockholm, Sweden.

Lindeberg, T., 1998. Edge detection and ridge detection with automatic scale selection. International Journal of Computer Vision 30 (2), 117–156.

Liu, G., Haralick, R. M., 2002. Optimal matching problem in detection and recognition performance evaluation. Pattern Recognition 35 (10), 2125–2139.

Liu, X., Yu, Y., Liu, B., Li, Z., 2013. Bowstring-based dual-threshold computation method for adaptive canny edge detector. In: 28th International Conference on Image and Vision Computing, New Zealand (IVCNZ). IEEE, pp. 13–18.

Lockhart, J. A., 1965. An analysis of irreversible plant cell elongation. Journal of Theoretical Biology 8 (2), 264–275.

López, A. M., Lumbreras, F., Serrat, J., Villanueva, J. J., 1999. Evaluation of methods for ridge and valley detection. IEEE Trans. on Pattern Analysis and Machine Intelligence 21 (4), 327–335.

López, J. M., Jensen, H. J., 2002. Generic model of morphological changes in growing colonies of fungi. Physical Review E 65 (2), 021903.

Lopez-Franco, R., Bartnicki-Garcia, S., Bracker, C. E., 1994. Pulsed growth of fungal hyphal tips. Proceedings of the National Academy of Sciences 91 (25), 12228–12232.

Lopez-Molina, C., De Baets, B., Bustince, H., 2013a. Quantitative error measures for edge detection. Pattern Recognition 46 (4), 1125–1139.

Lopez-Molina, C., De Baets, B., Bustince, H., Sanz, J., Barrenechea, E., 2013b. Multiscale edge detection based on Gaussian smoothing and edge tracking. Knowledge-Based Systems 44, 101–111.

Lopez-Molina, C., Galar, M., Bustince, H., De Baets, B., 2014. On the impact of anisotropic diffusion on edge detection. Pattern Recognition 47 (1), 270 – 281.

Lopez-Molina, C., Vidal-Diez de Ulzurrun, G., Baetens, J. M., Van den Bulcke, J., De Baets, B., 2015. Unsupervised ridge detection using second order anisotropic gaussian kernels. Signal Processing 116, 55–67.

Magan, N., 2007. Fungi in extreme environments. In: Environmental and Microbial Relationships, 2nd Edition The Mycota IV. Vol. 4. Springer, Ch. 6, pp. 85–100.

Magan, N., Lacey, J., 1984. Effect of temperature and ph on water relations of field and storage fungi. Transactions of the British Mycological Society 82 (1), 71–81.

Marr, D., Hildreth, E., 1980. Theory of edge detection. Proceedings of the Royal Society of London 207 (1167), 187–217.

Martin, D., Fowlkes, C., Malik, J., 2004. Learning to detect natural image boundaries using local brightness, color, and texture cues. IEEE Trans. on Pattern Analysis and Machine Intelligence 26 (5), 530–549.

Mauch, F., Mauch-Mani, B., Boller, T., 1988. Antifungal hydrolases in pea tissue. Plant Physiology 88 (3), 936–942.

Medina-Carnicer, R., Madrid-Cuevas, F., Carmona-Poyato, A., Muñoz-Salinas, R., 2009. On candidates selection for hysteresis thresholds in edge detection. Pattern Recognition 42 (7), 1284–1296.

Meškauskas, A., Fricker, M. D., Moore, D., 2004a. Simulating colonial growth of fungi with the neighbour-sensing model of hyphal growth. Mycological Research 108 (11), 1241–1256.

Meškauskas, A., McNulty, L. J., Moore, D., 2004b. Concerted regulation of all hyphal tips generates fungal fruit body structures: experiments with computer visualizations produced by a new mathematical model of hyphal growth. Mycological Research 108 (04), 341–353.

Meyer, L., Brischke, C., 2015. Fungal decay at different moisture levels of selected european-grown wood species. International Biodeterioration and Biodegradation 103, 23–29.

Milgroom, M. G., et al., 1990. A stochastic model for the initial occurrence and development of fungicide resistance in plant pathogen populations. Phytopathology 80 (4), 410–416.

Mislivec, P. B., Tuite, J., 1970. Temperature and relative humidity requirements of species of penicillium isolated from yellow dent corn kernels. Mycologia 62 (1), 75–88.

Molin, P., Gervais, P., Lemiere, J., Davet, T., 1992. Direction of hyphal growth: a relevant parameter in the development of filamentous fungi. Research in Microbiology 143 (8), 777–784.

Money, N. P., 1997. Wishful thinking of turgor revisited: the mechanics of fungal growth. Fungal Genetics and Biology 21 (2), 173–187.

Moore, D., 1991. Perception and response to gravity in higher fungi–a critical appraisal. New Phytologist 117 (1), 3–23.

Morgan, P., Lee, S. A., Lewis, S. T., Sheppard, A. N., Watkinson, R. J., 1993. Growth and biodegradation by white-rot fungi inoculated into soil. Soil Biology and Biochemistry 25 (2), 279–287.

Moss, M., 1987. Fungal biotechnology roundup. Mycologist 1 (2), 55–58.

Mouriño Pérez, R. R., Roberson, R. W., Bartnicki-Garcia, S., 2006. Microtubule dynamics and organization during hyphal growth and branching in *Neurospora crassa*. Fungal Genetics and Biology 43 (6), 389–400.

Mousa, W., Ghazali, F. M., Jinap, S., Ghazali, H. M., Radu, S., Salama, A. E.-R., 2016. Temperature, water activity and gas composition effects on the growth and aflatoxin production by *Aspergillus flavus* on paddy. Journal of Stored Products Research 67, 49–55.

Nielsen, K. F., Holm, G., Uttrup, L., Nielsen, P., 2004. Mould growth on building materials under low water activities. influence of humidity and temperature on fungal growth and secondary metabolism. International Biodeterioration and Biodegradation 54 (4), 325–336.

Obara, B., Grau, V., Fricker, M. D., 2012. A bioimage informatics approach to automatically extract complex fungal networks. Bioinformatics 28 (18), 2374–2381.

O'Brien, H. E., Parrent, J. L., Jackson, J. A., Moncalvo, J.-M., Vilgalys, R., Sep 2005. Fungal community analysis by large-scale sequencing of environmental samples. Applied and Environmental Microbiology 71 (9), 5544–50.

Oliveira, R., Bassanezi, R., Yang, H., Adami, A., 2004. A model for optimal chemical control of leaf area damaged by fungi population parameter dependence. Journal of Biological Systems 12 (01), 105–122.

Olsson, S., 1995. Mycelial density profiles of fungi on heterogeneous media and their interpretation in terms of nutrient reallocation patterns. Mycological Research 99 (2), 143–153.

Ortega, J. K., 1985. Augmented growth equation for cell wall expansion. Plant Physiology 79 (1), 318–320.

Osono, T., 2015. Effects of litter type, origin of isolate, and temperature on decomposition of leaf litter by macrofungi. Journal of Forest Research 20 (1), 77–84.

Osório, C., Chacón, P. J., Kisiswa, L., White, M., Wyatt, S., Rodríguez-Tébar, A., Davies, A. M., 2013. Growth differentiation factor 5 is a key physiological regulator of dendrite growth during development. Development 140 (23), 4751–4762.

Otsu, N., 1979. Threshold selection method for gray-level histograms. IEEE Trans. on Systems, Man and Cybernetics 9 (1), 62–66.

Pajor, R., Falconer, R., Hapca, S., Otten, W., 2010. Modelling and quantifying the effect of heterogeneity in soil physical conditions on fungal growth. Biogeosciences Discussions 7 (3), 3477–3501.

Panagou, E., Kodogiannis, V., Nychas, G.-E., 2007. Modelling fungal growth using radial basis function neural networks: The case of the ascomycetous fungus *Monascus ruber* van tieghem. International Journal of Food Microbiology 117 (3), 276–286.

Papagianni, M., 2004. Fungal morphology and metabolite production in submerged mycelial processes. Biotechnology Advances 22 (3), 189–259.

Papari, G., Petkov, N., 2011. Edge and line oriented contour detection: State of the art. Image and Vision Computing 29 (2-3), 79–103.

Pardo, E., Marín, S., Sanchis, V., Ramos, A., 2005. Impact of relative humidity and temperature on visible fungal growth and ota production of ochratoxigenic *Aspergillus ochraceus* isolates on grapes. Food microbiology 22 (5), 383–389.

Pardo, E., Marın, S., Solsona, A., Sanchis, V., Ramos, A., 2004. Modeling of germination and growth of ochratoxigenic isolates of *Aspergillus ochraceus* as affected by water activity and temperature on a barley-based medium. Food Microbiology 21 (3), 267–274.

Parnell, S., Van Den Bosch, F., Gilligan, C., 2006. Large-scale fungicide spray heterogeneity and the regional spread of resistant pathogen strains. Phytopathology 96 (5), 549–555.

Pasanen, A., Rautiala, S., Kasanen, J., Raunio, P., Rantamäki, J., Kalliokoski, P., 2000. The relationship between measured moisture conditions and fungal concentrations in water-damaged building materials. Indoor Air 10 (2), 111–120.

Pasanen, A.-L., Juutinen, T., Jantunen, M., Kalliokoski, P., 1992. Occurrence and moisture requirements of microbial growth in building materials. International Biodeterioration & Biodegradation 30 (4), 273–283.

Pasanen, A.-L., Kalliokoski, P., Pasanen, P., Jantunen, M., Nevalainen, A., 1991. Laboratory studies on the relationship between fungal growth and atmospheric temperature and humidity. Environment International 17 (4), 225–228.

Paton, K., 1979. Line detection by local methods. Computer Graphics and Image Processing 9 (4), 316–332.

Peli, T., Malah, D., 1982. A study of edge detection algorithms. Computer Graphics and Image Processing 20 (1), 1–21.

Peng, H., 2008. Bioimage informatics: a new area of engineering biology. Bioinformatics 24 (17), 1827–1836.

Perona, P., Malik, J., 1990. Detecting and localizing edges composed of steps, peaks and roofs. In: Proc. of the IEEE International Conf. on Computer Vision. pp. 52–57.

Perret, J., Al-Belushi, M., Deadman, M., 2007. Non-destructive visualization and quantification of roots using computed tomography. Soil Biology and Biochemistry 39 (2), 391–399.

Pöggeler, S., Nowrousian, M., Kück, U., 2006. Fruiting-body development in ascomycetes. In: Growth, Differentiation and sexuality. Springer, pp. 325–355.

Poggio, T., Torre, V., Koch, C., 1989. Computational vision and regularization theory. Image Understanding 3 (1-18), 111.

Poli, R., Valli, G., 1997. An algorithm for real-time vessel enhancement and detection. Computer Methods and Programs in Biomedicine 52 (1), 1–22.

Posada, D., Buckley, T. R., 2004. Model selection and model averaging in phylogenetics: advantages of akaike information criterion and bayesian approaches over likelihood ratio tests. Systematic Biology 53 (5), 793–808.

Prewitt, J. M. S., 1970. Object enhancement and extraction. Picture Processing and Psychopictorics. Academic Press, pp. 75–149.

Prosser, J., Trinci, A., 1979. A model for hyphal growth and branching. Journal of General Microbiology 111 (1), 153–164.

Prusinkiewicz, P., 2004. Modeling plant growth and development. Current Opinion in Plant Biology 7 (1), 79–83.

Ramakrishna, N., Lacey, J., Smith, J., 1993. Effects of water activity and temperature on the growth of fungi interacting on barley grain. Mycological Research 97 (11), 1393–1402.

Reed, T., Wyvill, B., 1994. Visual simulation of lightning. In: Proceedings of the 21st annual conference on Computer graphics and interactive techniques. ACM, pp. 359–364.

Regalado, C., Crawford, J., Ritz, K., Sleeman, B., 1996. The origins of spatial heterogeneity in vegetative mycelia: a reaction-diffusion model. Mycological Research 100 (12), 1473–1480.

Regalado, C. M., Sleeman, B. D., 1999. Aggregation and collapse in a mechanical model of fungal tip growth. Journal of Mathematical Biology 39 (2), 109–138.

Reynaga-Peña, C. G., Gierz, G., Bartnicki-Garcia, S., 1997. Analysis of the role of the spitzenkörper in fungal morphogenesis by computer simulation of apical branching in *Aspergillus niger*. Proceedings of the National Academy of Sciences 94 (17), 9096–9101.

Riquelme, M., Reynaga-Peña, C. G., Gierz, G., Bartnicki-Garcia, S., 1998. What determines growth direction in fungal hyphae? Fungal Genetics and Biology 24 (1), 101–109.

Riquelme, M., Yarden, O., Bartnicki-Garcia, S., Bowman, B., Castro-Longoria, E., Free, S. J., Fleißner, A., Freitag, M., Lew, R. R., Mouriño Pérez, R., et al., 2011. Architecture and development of the *Neurospora crassa* hypha–a model cell for polarized growth. Fungal Biology 115 (6), 446–474.

Roberson, R. W., Abril, M., Blackwell, M., Letcher, P., McLaughlin, D., Mouriño Pérez, R., Riquelme, M., Uchida, M., 2010. Hyphal structure. In: Borkovich, K. A., Ebbole, D. J. (Eds.), Cellular and Molecular Biology of Filamentous Fungi. Whasington DC, USA, pp. 8–24.

Robinson, C. H., 2001. Cold adaptation in arctic and antarctic fungi. New phytologist 151 (2), 341–353.

Romão-Dumaresq, A. S., Dourado, M. N., de Lima Favaro, L. C., Mendes, R., Ferreira, A., Araújo, W. L., 2016. Diversity of cultivated fungi associated with conventional and transgenic sugarcane and the interaction between endophytic *Trichoderma virens* and the host plant. PloS one 11 (7), e0158974.

Rorrer, G. L., Cheney, D. P., 2004. Bioprocess engineering of cell and tissue cultures for marine seaweeds. Aquacultural Engineering 32 (1), 11–41.

Rosenfeld, A., Thurston, M., 1971. Edge and curve detection for visual scene analysis. IEEE Transactions on Computers 100 (5), 562–569.

Rosin, P. L., 2001. Unimodal thresholding. Pattern Recognition 34 (11), 2083–2096.

Rouchdy, Y., Cohen, L. D., 2013. Geodesic voting for the automatic extraction of tree structures. Methods and applications. Computer Vision and Image Understanding 117 (10), 1453–1467.

Sahasrabudhe, N. A., Sankpal, N. V., 2001. Production of organic acids and metabolites of fungi for food industry. Applied Mycology and Biotechnology 6, 387–425.

Saltelli, A., Tarantola, S., Campolongo, F., Ratto, M., 2004. Sensitivity Analysis in Practice: a Guide to Assessing Scientific Models. John Wiley and Sons, Chichester, UK.

Samapundo, S., Devlieghere, F., De Meulenaer, B., Geeraerd, A., Van Impe, J., Debevere, J., 2005. Predictive modelling of the individual and combined effect of water activity and temperature on the radial growth of *Fusarium verticilliodes* and *F. proliferatum* on corn. International Journal of Food Microbiology 105 (1), 35–52.

Samapundo, S., Devlieghere, F., Geeraerd, A., De Meulenaer, B., Van Impe, J., Debevere, J., 2007. Modelling of the individual and combined effects of water activity and temperature on the radial growth of *Aspergillus flavus* and *A. parasiticus* on corn. Food Microbiology 24 (5), 517–529.

Samson, R., 1989. Filamentous fungi in food and feed. Journal of Applied Bacteriology 67 (27–35).

Samson, R. A., 2011. Ecology and general characteristics of indoor fungi. In: Adan, O. C., A, S. R. (Eds.), Fundamentals of mold growth in indoor environments and strategies for healthy living. Wageningen Academic, Wageningen, The Netherlands, Ch. 5, pp. 101–116.

Schnepf, A., Roose, T., Schweiger, P., 2008. Impact of growth and uptake patterns of arbuscular mycorrhizal fungi on plant phosphorus uptake - a modelling study. Plant and Soil 312 (1-2), 85–99.

Schubert, M., Fink, S., Schwarze, F. W., 2008. Evaluation of *Trichoderma spp.* as a biocontrol agent against wood decay fungi in urban trees. Biological Control 45 (1), 111–123.

Schwarze, F. W., 2007. Wood decay under the microscope. Fungal Biology Reviews 21 (4), 133–170.

Secor, G. A., Gudmestad, N. C., 1999. Managing fungal diseases of potato. Canadian Journal of Plant Pathology 21 (3), 213–221.

Sherif, S., Shukla, M., Murch, S., Bernier, L., Saxena, P., 2016. Simultaneous induction of jasmonic acid and disease-responsive genes signifies tolerance of american elm to dutch elm disease. Scientific Reports 6, 21934.

Shui, P.-L., Zhang, W.-C., 2012. Noise-robust edge detector combining isotropic and anisotropic Gaussian kernels. Pattern Recognition 45 (2), 806–820.

Shui, P.-L., Zhang, W.-C., 2013. Corner detection and classification using anisotropic directional derivative representations. IEEE Trans. on Image Processing 22 (8), 3204–3218.

Simonin, A., Palma-Guerrero, J., Fricker, M., Glass, N. L., 2012. Physiological significance of network organization in fungi. Eukaryotic Cell 11 (11), 1345–1352.

Siripatrawan, U., Makino, Y., 2015. Monitoring fungal growth on brown rice grains using rapid and non-destructive hyperspectral imaging. International Journal of Food Microbiology 199, 93–100.

Sluimer, I., Schilham, A., Prokop, M., van Ginneken, B., 2006. Computer analysis of computed tomography scans of the lung: A survey. IEEE Trans. on Medical Imaging 25 (4), 385–405.

Sobol, I. M., 2001. Global sensitivity indices for nonlinear mathematical models and their monte carlo estimates. Mathematics and Computers in Simulation 55 (1), 271–280.

Soddell, F., Soddell, J., 2005. Of lindenmayer systems, fungi and music. ACMC05 Generate and Test: Proceedings of the Australasian Computer Music Conference, 143–148.

Staal, J., Abramoff, M., Niemeijer, M., Viergever, M., van Ginneken, B., 2004. Ridge based vessel segmentation in color images of the retina. IEEE Trans. on Medical Imaging 23 (4), 501–509.

Stacey, A., Truscott, J., Gilligan, C., 2001. Soil-borne fungal pathogens: scaling-up from hyphal to colony behaviour and the probability of disease transmission. New Phytologist 150 (1), 169–177.

Stacey, A. J., Truscott, J. E., Asher, M. J., Gilligan, C. A., 2004. A model for the invasion and spread of rhizomania in the united kingdom: implications for disease control strategies. Phytopathology 94 (2), 209–215.

Steinberg, G., 1998. Organelle transport and molecular motors in fungi. Fungal Genetics and Biology 24 (1), 161–177.

Steinberg, G., 2007. Hyphal growth: a tale of motors, lipids, and the Spitzenkörper. Eukaryotic Cell 6 (3), 351–360.

Stutz, J. C., Copeman, R., Martin, C. A., Morton, J. B., 2000. Patterns of species composition and distribution of arbuscular mycorrhizal fungi in arid regions of southwestern North America and Namibia, Africa. Canadian Journal of Botany 78 (2), 237–245.

Sun, X., Guo, L.-D., 2012. Endophytic fungal diversity: review of traditional and molecular techniques. Mycology 3 (1), 65–76.

Sundari, S. K., Adholeya, A., 2003. Growth profile of ectomycorrhizal fungal mycelium: emphasis on substrate ph influence. Antonie van Leeuwenhoek 83 (3), 209–214.

Thornton, C., 2011. Environmental fungi as a cause of human mycoses. Biomedical Scientist 55 (10), 716.

Tindemans, S. H., Kern, N., Mulder, B. M., 2006. The diffusive vesicle supply center model for tip growth in fungal hyphae. Journal of Theoretical Biology 238 (4), 937–948.

Tlalka, M., Bebber, D., Darrah, P., Watkinson, S., Fricker, M., 2007. Emergence of self-organised oscillatory domains in fungal mycelia. Fungal Genetics and Biology 44 (11), 1085–1095.

Toffoli, T., 1984. Cellular automata as an alternative to (rather than an approximation of) differential equations in modeling physics. Physica D: Nonlinear Phenomena 10 (1), 117–127.

Tommerup, I., 1983. Temperature relations of spore germination and hyphal growth of vesicular-arbuscular mycorrhizal fungi in soil. Transactions of the British Mycological Society 81 (2), 381–387.

Tongen, A., Goriely, A., Tabor, M., 2006. Biomechanical model for appressorial design in magnaporthe grisea. Journal of Theoretical Biology 240 (1), 1–8.

Torre, V., Poggio, T., 1984. On edge detection. IEEE Trans. on Pattern Analysis and Machine Intelligence 8 (2), 147–163.

Torres, C., Negro, C., Fuente, E., Blanco, A., 2012. Enzymatic approaches in paper industry for pulp refining and biofilm control. Applied Microbiology and Biotechnology 96 (2), 327–344.

Trinci, A., 1969. A kinetic study of the growth of *Aspergillus nidulans* and other fungi. Microbiology 57 (1), 11–24.

Trinci, A., 1974. A study of the kinetics of hyphal extension and branch initiation of fungal mycelia. Microbiology 81 (1), 225–236.

Tupin, F., Maitre, H., Mangin, J.-F., Nicolas, J.-M., Pechersky, E., 1998. Detection of linear features in SAR images: Application to road network extraction. IEEE Trans. on Geoscience and Remote Sensing 36 (2), 434–453.

Valík, L., Baranyi, J., Görner, F., 1999. Predicting fungal growth: the effect of water activity on *Penicillium roqueforti*. International Journal of Food Microbiology 47 (1), 141–146.

van den Bosch, F., Gilligan, C. A., 2008. Models of fungicide resistance dynamics. Annual Reviews of Phytopathology 46, 123–147.

Van den Bulcke, J., Boone, M., Van Acker, J., Van Hoorebeke, L., 2009. Three-dimensional x-ray imaging and analysis of fungi on and in wood. Microscopy and Microanalysis 15 (5), 395–402.

Vázquez, M., Martin, A. M., 1998. Mathematical model for phaffia rhodozyma growth using peat hydrolysates as substrate. Journal of the Science of Food and Agriculture 76 (4), 481–487.

Vicente, G., Bautista, L. F., Rodríguez, R., Gutiérrez, F. J., Sádaba, I., Ruiz-Vázquez, R. M., Torres-Martínez, S., Garre, V., 2009. Biodiesel production from biomass of an oleaginous fungus. Biochemical Engineering Journal 48 (1), 22–27.

Vidal-Diez de Ulzurrun, G., Baetens, J. M., Van den Bulcke, J., Lopez-Molina, C., De Windt, I., De Baets, B., 2015. Automated image-based analysis of spatio-temporal fungal dynamics. Fungal Genetics and Biology 84 (2), 12–25.

Viitanen, H., Toratti, T., Makkonen, L., Peuhkuri, R., Ojanen, T., Ruokolainen, L., Räisänen, J., 2010a. Towards modelling of decay risk of wooden materials. European Journal of Wood and Wood Products 68 (3), 303–313.

Viitanen, H., Vinha, J., Salminen, K., Ojanen, T., Peuhkuri, R., Paajanen, L., Lähdesmäki, K., 2010b. Moisture and bio-deterioration risk of building materials and structures. Journal of Building Physics 33 (3), 201–224.

Vlachos, M., Dermatas, E., 2010. Multi-scale retinal vessel segmentation using line tracking. Computerized Medical Imaging and Graphics 34 (3), 213–227.

Wadsö, L., 1997. Principles of a microcalorimetric technique for the study of mould activity as a function of relative humidity. Journal of Thermal Analysis and Calorimetry 49 (2), 1053–1060.

Wadsö, L., Johansson, S., Pilgård, A., Alfredsen, G., 2013. The activity of rot fungi (*Postia placenta*) during drying and rewetting cycles measured by isothermal calorimetry. Engineering in Life Sciences 13 (6), 536–540.

Wagstaff, J. E., Klapholz, S., Esposito, R. E., 1982. Meiosis in haploid yeast. Proceedings of the National Academy of Sciences 79 (9), 2986–2990.

Watters, M. K., Griffiths, A. J., 2001. Tests of a cellular model for constant branch distribution in the filamentous fungus *Neurospora crassa*. Applied and Environmental Microbiology 67 (4), 1788–1792.

Watters, M. K., Humphries, C., De Vries, I., Griffiths, A. J., 2000. A homeostatic set point for branching in *Neurospora crassa*. Mycological Research 104 (05), 557–563.

Watts, H. J., Veacute, A., Perera, T. H. S., Davies, J. M., Gow, N. A. R., 1998. Thigmotropism and stretch-activated channels in the pathogenic fungus *Candida albicans*. Microbiology 144 (3), 689–695.

Webster, J., Weber, R., 2007. Introduction to fungi. Cambridge University Press, New York, USA.

Weickert, J., 1998. Anisotropic Diffusion in Image Processing. ECMI Series. Teubner-Verlag.

Weickert, J., 1999. Coherence-enhancing diffusion filtering. International Journal of Computer Vision 31 (2-3), 111–127.

Weiner, J., Thomas, S. C., 2001. The nature of tree growth and the age-related decline in forest productivity. Nordic Society Oikos 94 (2), 374–376.

Weinzierl, R., Henn, T., 1991. Alternatives in insect management: biological and biorational approaches. Vol. 401. North Central Regional Extension Publications.

Wendland, J., 2001. Comparison of morphogenetic networks of filamentous fungi and yeast. Fungal Genetics and Biology 34 (2), 63–82.

Wessels, J., 1986. Cell wall synthesis in apical hyphal growth. International Review of Cytology 104, 37–79.

Whittaker, R. H., 1969. New concepts of kingdoms of organisms. Science 163 (3863), 150–160.

Witkin, A. P., 1983. Scale-space filtering. In: Proc. of the International Joint Conference on Artificial Intelligence. Vol. 2. pp. 1019–1022.

Xiao, Y., Kreber, B., Breuil, C., 1999. Localisation of fungal hyphae in wood using immunofluorescence labelling and confocal laser scanning microscopy. International Biodeterioration and Biodegradation 44 (4), 185–190.

Zana, F., Klein, J.-C., 1999. A multimodal registration algorithm of eye fundus images using vessels detection and Hough transform. IEEE Trans. on Medical Imaging 18 (5), 419–428.

Zhang, Y., 1996. A survey on evaluation methods for image segmentation. Pattern Recognition 29 (8), 1335–1346.

Zhdanova, N. N., Zakharchenko, V. A., Vember, V. V., Nakonechnaya, L. T., 2000. Fungi from chernobyl: mycobiota of the inner regions of the containment structures of the damaged nuclear reactor. Mycological Research 104 (12), 1421–1426.

Zhou, K., Gui, M., Li, P., Xing, S., Cui, T., Peng, Z., 2012. Effect of combined function of temperature and water activity on the growth of *Vibrio harveyi*. Brazilian Journal of Microbiology 43 (4), 1365–1375.

Zhuang, X., Tlalka, M., Davies, D. S., Allaway, W. G., Watkinson, S. C., Ashford, A. E., 2009. Spitzenkörper, vacuoles, ring-like structures, and mitochondria of phanerochaete velutina hyphal tips visualized with carboxy-dffda, cmac and $\text{dioc}_6(3)$. Mycological Research 113 (4), 417–431.

Zullinger, E. M., Ricklefs, R. E., Redford, K. H., Mace, G. M., 1984. Fitting sigmoidal equations to mammalian growth curves. Journal of Mammalogy 65 (4), 607–636.

Zwietering, M., Jongenburger, I., Rombouts, F., Van't Riet, K., 1990. Modeling of the bacterial growth curve. Applied and Environmental Microbiology 56 (6), 1875–1881.

Curriculum vitae

Personalia

Name	Guillermo Vidal Diez de Ulzurrun
Gender	Male
Date of birth	29/06/1984
Place of birth	Madrid, Spain
Nationality	Spanish
Marital Status	Married
E-mail	Guillermo.Vidal@UGent.be

Education

2008 - 2009

Post-graduate master in Corporate Finance, Universidad Complutense de Madrid, Spain

2002 - 2008

Licenciatura Matematicas, Universidad Complutense de Madrid, Madrid, Spain

Employment

January 2013 - present

Full-time researcher at the Research Unit Knowledge-Based Systems, Department of Mathematical Modelling, Statistics and Bioinformatics, Faculty of Bioscience Engineering, Ghent University.

March 2010 - December 2012

IT strategy analyst at Accenture Spain.

October 2008 - February 2010

University lecturer at Saint Louis University, Madrid campus.

Scientific output

Publications in international journals (ISI-papers)

G. Vidal-Diez de Ulzurrun, J.M. Baetens, J. Van den Bulcke, B. De Baets (2017). Modelling three-dimensional fungal growth in response to environmental stimuli. Journal of Theoretical Biology 414, 35-49.

G. Vidal-Diez de Ulzurrun, J.M. Baetens, J. Van den Bulcke, C. Lopez-Molina, I. De Windt, B. De Baets (2015). Automated image-based analysis of spatio-temporal fungal dynamics. Fungal Genetics and Biology 84, 12-25.

C. Lopez-Molina, G. Vidal-Diez de Ulzurrun, J.M. Baetens, J. Van den Bulcke, B. De Baets (2015). Unsupervised ridge detection using second order anisotropic Gaussian kernels. Signal Processing 116, 55-67.

Conference proceedings

G. Vidal-Diez de Ulzurrun, J.M. Baetens, J. Van den Bulcke, B. De Baets (2016). Studying fungal growth using automated image analysis and computer simulations 47th Annual Meeting of the International Research Group on Wood Protection (IRG 47), May 2016, Lisbon, Portugal.

Conference Abstracts

G. Vidal-Diez de Ulzurrun, J.M. Baetens, J. Van den Bulcke, B. De Baets (2016). Lattice-free three-dimensional fungal growth modelling with environmental interactions. 10th European Conference on Mathematical and Theoretical Biology, July 2016, Nottingham, UK.

G. Vidal-Diez de Ulzurrun, J.M. Baetens, J. Van den Bulcke, B. De Baets (2016). Studying fungal growth using automated image analysis and computer simulations. 47th Annual Meeting of the International Research Group on Wood Protection (IRG 47), May 2016, Lisbon, Portugal.

G. Vidal-Diez de Ulzurrun, J.M. Baetens, J. Van den Bulcke, B. De Baets (2015). Spatio-temporal monitoring fungal growth dynamics using image analysis and graph theory. XVII Congress of European Mycologists, Sept 2015, Funchal, Portugal.

G. Vidal-Diez de Ulzurrun, J.M. Baetens, J. Van den Bulcke, C. Lopez-Molina, B. De Baets (2015). Extraction of fungal growth features: combining image analysis and graph theory. 20th National Symposium on Applied Biological Sciences, Jan 2015, Louvain-la-Neuve, Belgium.

G. Vidal-Diez de Ulzurrun, J.M. Baetens, J. Van den Bulcke, B. De Baets (2014). Modelling three-dimensional fungal growth: A spatially explicit lattice-free approach. 9th European Conference on Mathematical and Theoretical Biology, June 2014, Gothenburg, Sweden.

G. Vidal-Diez de Ulzurrun, J.M. Baetens, J. Van den Bulcke, B. De Baets (2014). Towards a lattice-free three-dimensional fungal growth model. National Symposium on Applied Biological Sciences, February 2014, Gembloux, Belgium.

G. Vidal-Diez de Ulzurrun, J.M. Baetens, J. Van den Bulcke, B. De Baets (2013). Towards a lattice-free three-dimensional fungal growth model. Workshop 1: Sustainability and Complex Systems, Mathematical Biosciences Institute, Sept 2013, Ohio, USA.